Università degli studi Roma Tre
Ph.D. in Scienze della materia, nanotecnologie e sistemi complessi
XXXVII Cycle

Institut national de la recherche scientifique
Doctorat en sciences de l'énergie et des matériaux

DUAL DEGREE JOINT Ph.D. PROGRAM

Artificial aging of modern organic pigments in presence of reactive inorganic whites

THESIS TITLE

Agnese De Carlo
Ph.D. Candidate: | Signature

Luca Tortora
Tutor: Prof. | Signature

Patrizio Antici
Tutor: Prof. | Signature

Marco Barbieri
Roma Tre Coordinator: Prof. | Signature

Abstract

The investigation of aging processes and degradation mechanisms in the materials that artists commonly use is important for developing the right conservation strategies and preventing aesthetic variations. This Ph.D. focuses on establishing effective artificial aging procedures to study the interactions between modern organic pigments and highly reactive white inorganic pigments.

During the Ph.D., different aging experiments were designed and tested through exposure of pigments to different conditions of light (solar, ultraviolet, visible), temperature, and relative humidity. A multi-technique analytical approach was employed to investigate the surface-level and molecular variations induced by aging. These techniques include colorimetry, Fourier transform infrared spectroscopy, Raman spectroscopy, X-ray diffraction, and time-of-flight secondary ion mass spectrometry. Due to the complexity of the multi-component samples, the use of complementary techniques was fundamental to studying the aging-induced variations.

The study focuses mainly on three modern organic pigments, commonly used in modern and contemporary works of art, belonging to the monoazo, isoindoline, and phthalocyanine classes. Their stability was studied in interaction with three different white inorganic pigments, lead white, titanium dioxide, and zinc oxide.

Two main case studies were reported with the aim of investigating the photostability of selected modern pigments in samples that combine organic and inorganic pigments in paint or powder forms. Surface color variations were the first indicators of chemical and physical degradation. Vibrational techniques were used to investigate molecular changes in pigments and binder, whereas X-ray diffraction analyses provided insight into the role of crystalline nature in the degradation process. In particular, ion mass spectrometry enabled high-sensitivity surface analysis, allowing a detailed investigation of the degradation effects underlying the observed color changes.

This research sheds light on pigment-metal oxide interactions in paint systems, providing valuable insight into their stability over time in modern and contemporary artworks, laying the groundwork for future studies on organic-inorganic pigment mixtures.

Abstract

L'étude des processus de vieillissement et des mécanismes de dégradation des matériaux couramment utilisés par les artistes est importante pour développer les bonnes stratégies de conservation et prévenir les variations esthétiques. Cette recherche de doctorat s'est concentrée sur l'établissement de procédures de vieillissement artificiel efficaces pour étudier les interactions entre les pigments organiques modernes et les pigments inorganiques blancs hautement réactifs.
Pendant le cours de doctorat, différentes expériences de vieillissement ont été conçues et testées par l'exposition à la lumière (solaire, ultraviolet, visible), à la température et à l'humidité relative. Une approche analytique multi-technique a été employée pour étudier les variations moléculaires et au niveau de la surface induites par le vieillissement, y compris la colorimétrie, la spectroscopie infrarouge à transformée de Fourier, la spectroscopie Raman, la diffraction des rayons X et la spectrométrie de masse d'ions secondaires à temps de vol. En raison de la complexité des échantillons multi-composants, l'utilisation de techniques complémentaires était fondamentale pour étudier les variations induites par le vieillissement.
En particulier, trois pigments organiques modernes, couramment utilisés dans les œuvres d'art modernes et contemporaines, appartenant aux classes des monoazoïques, des isoindolines et des phtalocyanines, ont été sélectionnés. Leur stabilité a été étudiée en interaction avec trois pigments inorganiques blancs différents, le blanc de plomb, le dioxyde de titane et l'oxyde de zinc.
Deux études de cas principales ont été rapportées dans le but d'étudier la photostabilité de pigments modernes sélectionnés dans des échantillons combinant des pigments organiques et inorganiques sous forme de peinture ou de poudre. Les variations de la couleur de surface ont représenté les premiers indicateurs de dégradation chimique et physique. Des techniques vibrationnelles ont été utilisées pour étudier les changements moléculaires dans les pigments et les liants, tandis que les analyses par diffraction des rayons X ont permis de comprendre le rôle de la nature cristalline dans le processus de dégradation. En particulier, la spectrométrie de masse d'ions secondaires a permis

une analyse de surface à haute sensibilité, permettant une étude détaillée des effets de dégradation sous-jacents aux changements de couleur observés.
Cette recherche met en lumière les interactions entre les pigments et les oxydes métalliques dans les systèmes de peinture et fournit des informations précieuses sur leur stabilité dans le temps dans les œuvres d'art modernes et contemporaines, jetant les bases d'études futures sur les mélanges de pigments organiques et inorganiques.

Contents

List of Abbreviations

AATCC American Association of Textile Chemists and Colourists

ASTM American Society for Testing and Materials

ATR Attenuated Total Reflection

CIELAB CIE L*a*b*

CIE Commission Internationale de l'Eclairage

CI Colour Index^{TM}

CoPc Cobalt phthalocyanine

DSSC Dye-Sensitized Solar Cell

FoV Field of View

FTIR Fourier Transform Infrared Spectroscopy

IR Infrared

PB75 CI Pigment Blue 75

PL Photoluminescence Spectroscopy

PW1 CI Pigment White 1

PW4 CI Pigment White 4

PW6 CI Pigment White 6

Py-GC Pyrolysis–Gas Chromatography

PY139 CI Pigment Yellow 139

PY1 CI Pigment Yellow 1

RS Raman Spectroscopy

SDC Society of Dyers and Colourists

SEM Scanning Electron Microscopy

SIMS Secondary Ion Mass Spectrometry

SOP Synthetic Organic Pigment

TAG Triacylglyceride

ToF Time-of-Flight

UHV Ultra-High Vacuum

UV Ultraviolet

VIS Visible

XRD X-Ray Diffraction

XRF X-Ray Fluorescence Spectroscopy

General overview

In the field of cultural heritage science, the investigation of material alterations over time plays a pivotal role in the conservation and preservation of artworks, as well as in the accurate reconstruction of their original colors. Color variations are the earliest and most visible signs of degradation in artworks. These visual changes can indicate deeper chemical, physical, and morphological transformations within the materials, influenced by external factors such as exposure to light, relative humidity, and temperature. In particular, ultraviolet (UV) and visible (VIS) radiation can trigger the photodegradation of both binders and pigments, leading to significant changes in their visual appearance and structural integrity. Similarly, fluctuations in humidity and temperature can facilitate oxidative and thermal degradation, particularly affecting the chemical and physical properties of the binders and pigments used in artworks.

The aging process, whether conducted in situ or in a controlled laboratory setting, is essential for understanding the long-term effects of environmental factors on art materials. By simulating these factors and accelerating the aging process, researchers can systematically evaluate the contributions of various external influences to material deterioration. Laboratory experiments, in particular, offer valuable insights into the durability and stability of materials, helping to inform the development of more effective conservation strategies.

This Ph.D. research focuses on the interaction between specific organic and inorganic pigments, examining their stability under different conditions of the aging process. The primary aim of this project is to deepen the understanding of the aging and degradation mechanisms of organic and inorganic materials commonly used by artists, with a particular emphasis on accelerated aging tests. Indeed, a fundamental objective of the Ph.D. is the design and optimization of controlled artificial aging processes aimed at simulating specific environmental stressors and inducing measurable color changes

in testing paint samples. Subsequently, a multi-technique analytical approach was developed, integrating complementary methodologies to investigate the physical and chemical variations induced by the aging process, with a particular focus on surface-level modifications and molecular-level interactions. Depending on the specific case of study, this approach involved the use of colorimetry, Fourier transform infrared spectroscopy, Raman spectroscopy, photoluminescence spectroscopy, and time-of-flight secondary ion mass spectrometry. By analyzing the influence of highly reactive inorganic components on the stability of organic pigments, this research contributes to the existing knowledge in the field of art preservation and advanced methodologies for the conservation of cultural heritage.
Three synthetic organic pigments from different color classes were selected for investigation: monoazo and isoindoline (both yellow pigments) and phthalocyanine (a blue pigment). These pigments were chosen for their prevalence in modern and contemporary artistic practices and for their stability to light exposure. Monoazo and isoindoline pigments are widely used in modern artworks, industrial paints, plastics, and printing inks, while phthalocyanines are employed not only by artists but also in the production of optical devices, electronics, and solar cells. Furthermore, both monoazo and phthalocyanine pigments are frequently used in mural painting formulations, often in combination with inorganic white pigments. These pigments are present in contemporary murals worldwide, including the famous murals *Cinema Airone* (1953) by G. Capogrossi in Italy, the *Polyforum Cultural Siqueiros* (1964) by D.A. Siqueiros in Mexico, and the mural created by K. Haring at the *Necker Hospital* in France (1987)[1].
In modern and contemporary art, inorganic white pigments are generally added to paints to create various hues and shades, expanding artists' palettes and enhancing the durability of their artworks. In addition to their role in color formulation, these pigments can also be employed in underpainting techniques to establish light and contrast, or be used as protective coatings and driers. Notably, titanium dioxide and zinc oxide have been recently employed in the formulation of self-cleaning outdoor paints, exploiting their photocatalytic activity. Indeed, these paints contain photocatalytic pigments which generate reactive oxygen species when exposed to sunlight, decomposing organic compounds (such as smog and atmospheric particulate matter), bacteria, and pollutants (like nitrogen oxides, NO_x). In contrast, lead white (basic lead carbonate) was historically widely used due to its excellent opacity and coverage. However, lead white has largely been replaced by titanium white and zinc white due to its toxicity, with titanium dioxide prized for its superior brightness and opacity, and

[1]DOI: 10.3390/coatings13122044

zinc white for its fine texture and cooler color tone.
The interactions between inorganic white pigments and organic binders are of particular interest, as they can induce different degradation mechanisms. Lead white and zinc white, for example, react with the fatty acids in oil-based paints, leading to the formation of metal soaps and photo-oxidation, which can compromise the mechanical properties of the paint. Titanium dioxide, when exposed to UV light, acts as a photocatalyst, accelerating the degradation of organic materials and resulting in yellowing and weakening of the paint layer.
The degradation of paints that combine colored organic pigments with inorganic white pigments remains an open area of scientific interest, complicated by the wide range of experimental variables and conditions involved. The presence of numerous pigments, specific aging processes, and the occurrence of spurious effects - such as changes in the binder's volume, differential oil absorption by the white pigments, or localized surface degradation - can obscure the targeted effects. Therefore, it is critical to develop valid methodologies for detecting and analyzing these phenomena.
This Ph.D. project was carried out as part of a cotutelle program, in collaboration between the University of Roma Tre - Department of Sciences in Italy and the Institut National de la Recherche Scientifique - Centre Energie Matériaux et Communication (INRS-EMT) in Canada. In Italy, the research activities were conducted under the supervision of Dr. Luca Tortora at the Surface Analysis Laboratory Roma Tre (LASR3), which collaborates with Roma Tre University and the Istituto Nazionale di Fisica Nucleare (INFN, Roma Tre section). In Canada, the research activities were carried out under the supervision of Professor Patrizio Antici, in collaboration with Professor Andreas Ruediger's lab.
The thesis is organized into three parts, each addressing a specific aspect of the research project. The first part provides an overview of the aging of modern pigments and the analytical methods employed. The second part presents the two main case studies, each focusing on different sample types, where the interaction between organic and inorganic art materials is examined through a specific artificial aging process and a multi-technique analytical approach. This part is also detailed in specific publications. Finally, the third part includes the conclusions and future perspectives.

The following is a brief outline of the chapters:

- **Part I:**
  - **Chapter 1 - State of art** introduces the focus of the artificial aging of modern painting materials and the degradation processes involved. It also presents the materials selected for this Ph.D. research, highlighting their properties and relevance to aging studies.
  - **Chapter 2 - Multi-technique approach** outlines the multi-technique approach employed to characterize the materials and study the aging variations induced in the surface of the samples. In addition, in this chapter, the four distinct artificial aging procedures, specifically developed and optimized during this Ph.D. research, are presented.
- **Part II:**
  - **Chapter 3 - Stability of monoazo and isoindoline yellows mixed with white pigments** presents the study of the stability of mixed paint samples composed of yellow synthetic organic pigments combined with inorganic whites. Building on preliminary studies published in the journal *Acta IMEKO*[2], the work examined surface color changes and photodegradation variations induced by artificial UV-VIS aging under controlled conditions of humidity and temperature. A multi-technique approach was employed to analyze the aging-induced variations. Published in the journal *Dyes and Pigments*[3], these results provide valuable insights for future research focused on the interactions and stability of organic-inorganic pigments in paint mixtures.
  - **Chapter 4 - Solar photostability of Co-phthalocyanine with TiO_2 nanopowders** is part of an ongoing collaboration with Professor Andreas Ruediger's lab group at the INRS-EMT. This study focuses on the investigation of powder samples composed of a mixture of cobalt phthalocyanine and titanium dioxide. A multi-technique approach was employed to examine the color fading and degradation processes of the organic-inorganic powder mixture. In this study, different aging processes and sample preparation methods were tested. The results of this study are currently in preparation for submission to a journal.

[2]DOI: 10.21014/actaimeko.v13i3.1791
[3]DOI: 10.1016/j.dyepig.2025.113122

- **Part III:**
  - **Conclusions** summarize the main contributions of this Ph.D. project and propose directions for future research. Additionally, a list of published articles, conference proceedings, ongoing work, and a summary of participation in international conferences are provided.

This Ph.D. project pioneered a new research line within both laboratories (Italy and Canada) and focused on studying the complex interactions and stability of organic and inorganic materials in artistic contexts. The challenges associated with a new research line, along with the open questions it has raised, present opportunities for future research in this field.

Présentation générale

Dans le domaine des sciences du patrimoine culturel, l'étude des altérations matérielles au fil du temps joue un rôle essentiel dans la conservation et la préservation des œuvres d'art, ainsi que dans la reconstitution fidèle de leurs couleurs d'origine. Les variations chromatiques constituent les premiers signes, à la fois précoces et visibles, de dégradation des œuvres. Ces changements visuels peuvent révéler des transformations chimiques, physiques et morphologiques plus profondes des matériaux, influencées par des facteurs externes tels que l'exposition à la lumière, l'humidité relative et la température. En particulier, le rayonnement ultraviolet (UV) et visibles (VIS) peut déclencher la photodégradation des liants et des pigments, entraînant des modifications significatives de leur apparence visuelle et de leur intégrité structurelle. De même, les fluctuations de l'humidité et de la température peuvent favoriser la dégradation oxydative et thermique, affectant notamment les propriétés chimiques et physiques des liants et des pigments utilisés dans les œuvres d'art.
Le processus de vieillissement, qu'il soit étudié in situ ou dans un environnement de laboratoire contrôlé, est fondamental pour comprendre les effets à long terme des facteurs environnementaux sur les matériaux artistiques. En simulant ces facteurs et en accélérant le vieillissement, les chercheurs peuvent évaluer de manière systématique les contributions respectives des différentes contraintes externes à la détérioration des matériaux. Les expériences en laboratoire, en particulier, offrent des perspectives précieuses sur la durabilité et la stabilité des matériaux, contribuant ainsi à l'élaboration de stratégies de conservation plus efficaces.
Cette recherche doctorale se concentre sur l'interaction entre des pigments organiques et inorganiques spécifiques, en examinant leur stabilité dans différentes conditions de vieillissement. L'objectif principal de ce projet est d'approfondir la compréhension des mécanismes de vieillissement et de dégradation des matériaux organiques et inor-

ganiques couramment utilisés par les artistes, avec une attention particulière portée aux tests de vieillissement accéléré. Un objectif fondamental de ce projet de doctorat est la conception et l'optimisation de protocoles de vieillissement artificiel contrôlés, visant à simuler des contraintes environnementales spécifiques et à induire des variations de couleur mesurables sur des échantillons de peinture test. Une approche analytique multi-technique a ensuite été développée, intégrant des méthodologies complémentaires afin d'analyser les modifications physiques et chimiques induites par le vieillissement, en mettant l'accent sur les altérations de surface et les interactions moléculaires. Selon les cas étudiés, cette approche a mobilisé la colorimétrie, la spectroscopie infrarouge à transformée de Fourier (FTIR), la spectroscopie Raman, la spectroscopie de photoluminescence et la spectrométrie de masse par ions secondaires à temps de vol (ToF-SIMS). En analysant l'influence de composants inorganiques hautement réactifs sur la stabilité des pigments organiques, cette recherche contribue à l'avancement des connaissances dans le domaine de la conservation de l'art et au développement de méthodologies avancées pour la préservation du patrimoine culturel.
Trois pigments organiques synthétiques issus de différentes classes chromatiques ont été sélectionnés: des pigments monoazo et isoindoline (jaunes), et un pigment phtalocyanine (bleu). Ces pigments ont été choisis pour leur prédominance dans les pratiques artistiques modernes et contemporaines, ainsi que pour leur stabilité à l'exposition lumineuse. Les pigments monoazo et isoindoline sont largement utilisés dans l'art moderne, les peintures industrielles, les plastiques et les encres d'imprimerie, tandis que les phtalocyanines sont employées non seulement par les artistes, mais aussi dans la fabrication de dispositifs optiques, de composants électroniques et de cellules solaires. De plus, les pigments monoazo et phtalocyanines sont fréquemment présents dans les formulations de peintures murales, souvent en association avec des pigments blancs inorganiques. Ces pigments sont utilisés dans des fresques murales contemporaines à travers le monde, telles que *Cinema Airone* (1953) de G. Capogrossi en Italie, le *Polyforum Cultural Siqueiros* (1964) de D.A. Siqueiros au Mexique, ou encore la fresque réalisée par K. Haring à *Necker Hospital* en France (1987)[4].
Dans l'art moderne et contemporain, les pigments blancs inorganiques sont généralement ajoutés aux peintures pour créer diverses nuances, enrichir la palette des artistes et renforcer la durabilité des œuvres. En plus de leur rôle dans la formulation des couleurs, ces pigments sont aussi utilisés dans les techniques de sous-couche pour créer des effets de lumière et de contraste, ou comme couches protectrices et agents siccatifs. Notamment, le dioxyde de titane et l'oxyde de zinc ont récemment été intégrés dans

[4]DOI: 10.3390/coatings13122044

des peintures d'extérieur autonettoyantes, exploitant leur activité photocatalytique. Ces peintures contiennent en effet des pigments photocatalytiques capables, sous l'effet de la lumière solaire, de générer des espèces réactives de l'oxygène, décomposant les composés organiques (comme les particules de pollution atmosphérique), les bactéries et les polluants (tels que les oxydes d'azote, NO_x). En revanche, le blanc de plomb (carbonate basique de plomb), historiquement très utilisé en raison de son opacité et de son pouvoir couvrant, a été largement remplacé par le blanc de titane et le blanc de zinc en raison de sa toxicité. Le dioxyde de titane est apprécié pour sa brillance et son opacité supérieures, tandis que le blanc de zinc est reconnu pour sa finesse et sa tonalité plus froide.

Les interactions entre les pigments blancs inorganiques et les liants organiques présentent un intérêt particulier, car elles peuvent induire différents mécanismes de dégradation. Le blanc de plomb et le blanc de zinc, par exemple, réagissent avec les acides gras présents dans les peintures à l'huile, conduisant à la formation de savons métalliques et à des phénomènes de photo-oxydation, qui compromettent les propriétés mécaniques de la couche picturale. Le dioxyde de titane, quant à lui, agit comme photocatalyseur lorsqu'il est exposé à la lumière UV, accélérant la dégradation des matériaux organiques, ce qui entraîne un jaunissement et une fragilisation de la peinture.

La dégradation des peintures combinant des pigments organiques colorés et des pigments blancs inorganiques constitue un domaine d'intérêt scientifique encore peu exploré, en raison de la diversité des variables expérimentales en jeu. La présence de multiples pigments, la spécificité des protocoles de vieillissement, et l'occurrence d'effets parasites - tels que les variations de volume du liant, l'absorption différentielle de l'huile par les pigments blancs, ou la dégradation localisée en surface - peuvent masquer les effets ciblés. Il est donc crucial de développer des méthodologies valides pour détecter et analyser ces phénomènes.

Ce projet doctoral a été réalisé dans le cadre d'un programme de cotutelle, en collaboration entre l'Université Roma Tre - Département des Sciences, en Italie, et l'Institut national de la recherche scientifique - Centre Énergie Matériaux Télécommunications (INRS-EMT), au Canada. En Italie, les activités de recherche ont été menées sous la supervision du Dr Luca Tortora au laboratoire d'analyse de surface Roma Tre (LASR3), en collaboration avec l'Université Roma Tre et l'Istituto Nazionale di Fisica Nucleare (INFN, section Roma Tre). Au Canada, la recherche a été encadrée par le professeur Patrizio Antici, en collaboration avec le laboratoire du professeur Andreas Ruediger.

La thèse est structurée en trois parties, chacune abordant un aspect spécifique du projet de recherche. La première partie présente une vue d'ensemble du vieillissement

des pigments modernes et des méthodes analytiques utilisées. La deuxième partie expose les deux principales études de cas, axées sur différents types d'échantillons, dans lesquelles les interactions entre matériaux organiques et inorganiques sont examinées à l'aide de procédés de vieillissement artificiel spécifiques et d'une approche analytique multi-technique. Cette partie est également détaillée dans des publications spécifiques. Enfin, la troisième partie rassemble les conclusions et les perspectives futures.
Un aperçu des chapitres:

- **Partie I:**
  - **Chapitre 1 - État de l'art** introduit le thème du vieillissement artificiel des matériaux picturaux modernes et les processus de dégradation associés. Il présente également les matériaux sélectionnés dans le cadre de cette recherche doctorale, en soulignant leurs propriétés et leur pertinence pour les études de vieillissement.
  - **Chapitre 2 - Approche multi-technique** décrit la stratégie analytique mise en œuvre pour caractériser les matériaux et étudier les variations induites en surface par le vieillissement. Ce chapitre présente également les quatre protocoles de vieillissement artificiel distincts, développés et optimisés au cours de cette recherche.
- **Partie II:**
  - **Chapitre 3 - Stabilité des pigments jaunes monoazo et isoindoline en mélange avec des pigments blancs** présente l'étude de la stabilité des échantillons de peinture composés de pigments organiques jaunes synthétiques et de pigments blancs inorganiques. S'appuyant sur des études préliminaires publiées dans *Acta IMEKO*[5], ce travail analyse les variations colorimétriques et les processus de photodégradation induits par un vieillissement UV-VIS artificiel sous des conditions contrôlées d'humidité et de température. Une approche multi-technique a été employée pour caractériser ces altérations. Publiés dans la revue dans la revue *Dyes and Pigments*[6], ces résultats apportent des éléments précieux pour de futures recherches sur les interactions et la stabilité des pigments organiques/inorganiques dans les mélanges de peinture.

[5]DOI: 10.21014/actaimeko.v13i3.1791
[6]DOI: 10.1016/j.dyepig.2025.113122

- **Chapitre 4 - Photostabilité solaire de la Co-phtalocyanine avec des nanopoudres de TiO_2** fait partie d'une collaboration en cours avec le groupe de laboratoire du Professeur Andreas Ruediger à l'INRS-EMT. Cette étude porte sur des échantillons de poudre composés d'un mélange de cobalt-phtalocyanine et de dioxyde de titane. Une approche multi-technique a été employée pour examiner les processus de décoloration et de dégradation du mélange de poudres organiques et inorganiques. Dans cette étude, différents processus de vieillissement et méthodes de préparation des échantillons ont été testés. Les résultats de cette étude sont actuellement en préparation pour être soumis à une revue.

- **Partie III:**
  - **Conclusions** résume les principales contributions de ce projet doctoral et propose des perspectives de recherche future. En outre, une liste des articles publiés, des actes de conférences, des travaux en cours et un résumé de la participation à des conférences internationales sont fournis.

Ce projet de doctorat a ouvert la voie à un nouvel ligne de recherche au sein des deux laboratoires (Italie et Canada) et xée sur l'étude des interactions complexes et de la stabilité des matériaux organiques et inorganiques dans les contextes artistiques. Les défis liés à cette nouvelle orientation, ainsi que les questions ouvertes qu'elle soulève, offrent de nombreuses opportunités pour de futurs travaux dans ce domaine.

Part I

1 State of art

This chapter introduces the topic of artificial aging in the context of modern painting materials, providing an overview of the degradation processes that affect colorants. Particular attention is given to the chemical and physical mechanisms induced by environmental exposure, such as light, humidity, and temperature. In addition, the chapter emphasizes the importance of studying the aging process of materials commonly used in modern paints, including synthetic organic pigments, white inorganic pigments, and binders. A detailed description of the selected materials and their pigment classes is then presented. These materials were selected for their relevance in artistic practices, such as modern and contemporary paintings or street artworks. The frequent combination of organic and inorganic pigments in such artworks highlights the need to study accelerated aging processes that take into account these interactions. Indeed, the possible interactions between organic and inorganic components when mixed in complex paint formulations can significantly influence their stability and degradation pathways.

1.1 Aging process of colorants

The study of the aging process of colored materials used by artists represents an open problem in the conservation and prevention of the field of cultural heritage. Different factors can influence the aesthetic appearance of a painting, leading to the loss or alteration of colors. The discoloration, or color fading, is a complex phenomenon due to specific degradation factors that depend both on the chemical nature of the materials and the surrounding environmental conditions.
Colorants are classified as either pigments or dyes. Pigments are colored, white, or black powders that are nearly or completely insoluble in the medium in which they are incorporated. Indeed, the pigment coloring effect results from mechanical dispersion within the medium, while the pigments remain chemically and physically unaltered. In contrast, dyes are soluble substances that form stable bonds with the molecules of the material being colored. The stability and insolubility of pigments are fundamental to the creation of artworks and for ensuring their long-term preservation [1].
Among the main factors influencing the aging of colorants is the light source. Light is particularly harmful to art materials, especially organic compounds. UV radiation can induce photodegradation, leading to significant alterations in both the chemical structure and the visual appearance of artworks. Although visible light is less energetic than UV radiation, it can still contribute to degradation, particularly in light-sensitive pigments. Light damage to artworks is induced by photodegradation, known to be a surface-level phenomenon that occurs mainly in the first 5-10 μm of the painting [2]. In addition to light, other important environmental parameters that can induce irreversible degradation of art materials are relative humidity and temperature [3]. Humidity can severely affect the stability of artworks due to the role of oxygen in the photodegradation mechanism. On the other hand, temperature can accelerate the degradation processes by promoting both chemical reactivity and the diffusion of oxygen into organic materials such as binders and pigments. Furthermore, another critical factor is pigment aggregation. The presence of aggregates increases the stability of colorants due to a protective effect, which reduces the exposure of deeper molecules to direct light.
Photodegradation of colorants can occur through different mechanisms, each involving distinct interactions with light:

- Photolysis
- Photooxidation

- Photoreduction
- Photocatalysis

The photolysis process occurs when a molecule absorbs a photon (typically in the UV range), and this energy triggers a chemical reaction that does not depend on the presence of oxygen. In organic colorants, photolysis can lead to the cleavage of chemical bonds, resulting in color degradation or a shift in hue.
According to J. Oakes [4] and N.S. Allen [5], the primary photodegradation mechanisms that affect organic colorants (both dyes and pigments) are photooxidation and photoreduction.
In photooxidation, an organic molecule absorbs light and transitions from the ground state (M) to an excited state (M^*). Photooxidation, in the presence of oxygen, can occur by singlet oxygen ($^1O_2$) or superoxide ($O_2^{-\bullet}$). If the colorant is excited to a triplet state ($^3M^*$), the degradation occurs by triplet-triplet annihilation with oxygen to produce singlet oxygen. Singlet oxygen is a highly reactive species that can interact with the chemical structure of the colorant, causing the breaking of chemical bonds and, consequently, variations in the color or stability of the organic colorant.

$$^3M^* +^3O_2 \rightarrow M +^1O_2$$

$$^1O_2 \ + M \rightarrow degradation$$

In the case of superoxide photooxidation, the excited-state molecule can transfer electrons to molecular oxygen, leading to the formation of superoxide. Superoxide is a reactive radical anion that tends to interact rapidly with other molecules, including colorant bonds.

$$M^* + O_2 \rightarrow M^{+\bullet} + O_2^{-\bullet}$$

$$O_2^{-\bullet} + M \rightarrow degradation$$

In photoreduction, upon light absorption, the colorant in its excited state can accept an electron or a hydrogen atom from nearby molecules, leading to its reduction and the formation of reduced species such as free radicals. These radicals can subsequently interact with the chemical structure of the colorant, contributing to color changes and fading. Degradation can be triggered by both $R^\bullet$ radicals and peroxy radicals $RO_2^\bullet$.

$$R^\bullet/RO_2^\bullet + M \rightarrow degradation$$

However, to initiate radical formation through bond cleavage, the absorption of high-energy light is generally required.
In the case of inorganic compounds, another type of photodegradation that can occur is photocatalysis. The inorganic colorant is a semiconductor that acts as a photocatalyst when exposed to UV or visible radiation, absorbing energy that activates its catalytic properties [6]. The colorant then generates electron-hole pairs, which, by recombining and interacting with nearby molecules, give rise to reactive oxygen species or free radicals. These reactive species can interact with other molecules, leading to alterations in color stability, fading, or changes in surface properties. Photocatalysis requires a specific threshold of light energy to initiate the reaction, which can vary depending on the inorganic component and environmental conditions. Photocatalysis is used in a variety of applications due to its ability to accelerate chemical reactions in the presence of light, especially in the environmental and industrial fields.
Photodegradation of pigments depends on several factors, including the chemical composition of the pigment itself and its interaction with the binder, which can either protect or accelerate the degradation of the pigment when exposed to light. The property that defines the light stability of pigments, as it relates to a binder, is lightfastness. According to Peter A. Lewis [7], the term "lightfastness" refers to a pigment's ability to withstand exposure to light, both direct and indirect, natural and artificial, without suffering any visible change in appearance. The American Society for Testing and Materials (ASTM International or simply ASTM) classifies five different categories of lightfastness based on the degree of color change observed in samples before and after exposure to light. This change is quantified using the color difference units ΔE, calculated according to the CIELAB color difference equation [8].

- Lightfastness I, excellent lightfastness, exhibits a mean color change of less than 4.0 ΔE.
- Lightfastness II, very good lightfastness, exhibits a mean color change of more than 4.0 ΔE but not more than 8.0 ΔE.
- Lightfastness III, fair lightfastness, exhibits a mean color change of more than 8.0 ΔE but not more than 16.0 ΔE.
- Lightfastness IV, poor lightfastness, exhibits a mean color change of more than 16.0 ΔE but not more than 24.0 ΔE.
- Lightfastness V, very poor lightfastness, exhibits a mean color change of more than 24.0 ΔE.

It is important to highlight that color differences are not always perceptible to the human eye. Indeed, quoting W. Mokrzycki and M. Tatol [9]:

"When:

- $0 < \Delta E < 1$ - observer does not notice the difference,
- $1 < \Delta E < 2$ - only experienced observer can notice the difference,
- $2 < \Delta E < 3.5$ - unexperienced observer also notices the difference,
- $3.5 < \Delta E < 5$ - clear difference in color is noticed,
- $5 < \Delta E$ - observer notices two different colors.

These data represent experimentally verified statistics."

The study of degradation mechanisms in organic colorants requires detailed analysis of their molecular structure. In particular, both the nature of the auxochrome groups and their position on the chromophore significantly influence the photophysical and photochemical behavior of the entire molecule [4, 5]. Indeed, some substituent groups can be highly photoreactive in themselves. Specifically, electron-withdrawing substituents tend to promote photoreductive degradation mechanisms, whereas electron-donating substituents facilitate photooxidative processes. A possible alteration of the auxochromic groups can lead to color shifts as shown in Figure 1.1.

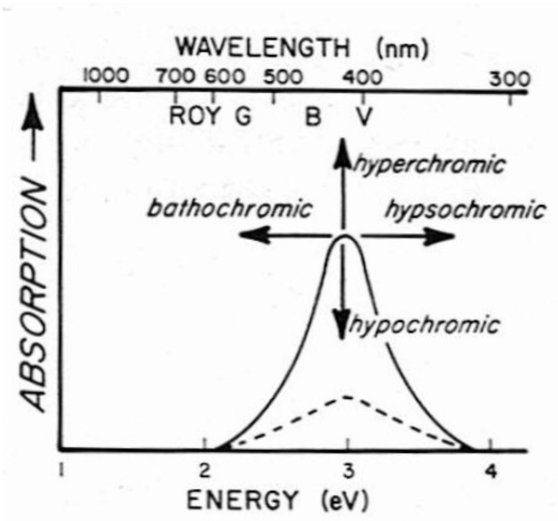

Figure 1.1 Effect of auxochromic groups on the absorption spectrum of a chromophore [10].

These may be bathochromic (red shift), resulting in a shift to a larger wavelength, or hypsochromic (blue shift), resulting in absorption to a shorter wavelength. Moreover, it is possible to find a hyperchromic effect that increases the intensity of the color, or a hypochromic effect that decreases it [10].

Over the past 25 years, scientific interest in pigments has grown significantly, motivated by the need to identify, preserve, and conserve both historical and modern artworks. Analytical studies on pigments have become a central theme within heritage science, intersecting with different disciplines such as archaeometry, conservation science, materials physics, and analytical chemistry. Indeed, this interdisciplinary convergence has led to the application of numerous analytical techniques [11]. For example, spectroscopic techniques, such as ultraviolet-visible reflectance, fluorescence, infrared, and Raman spectroscopy, are widely employed in this field, each offering specific advantages and limitations. For more detailed molecular analysis, liquid chromatography or mass spectrometry are considered the most accurate approaches, although they require sampling. This contributed to a marked increase in scientific publications on this topic, as shown in Figure 1.2 from a bibliometric analysis based on a dataset of 932 articles published between 1999 and 2023.

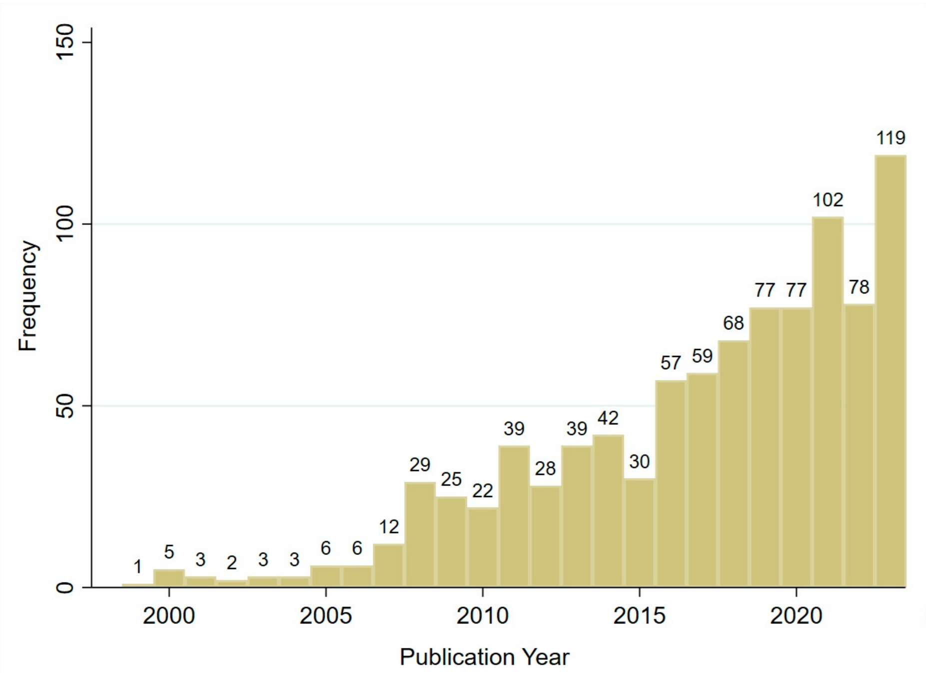

Figure 1.2 Time trend in published studies related to the analytical investigation of pigments in cultural heritage from 1999 to 2023 [11].

In particular, recent studies have focused on the degradation mechanisms affecting pigments, binders, and paint layers. This includes the investigation of chemical and physical degradation processes, as well as the various environmental and material-related factors that influence them, leading to a more dynamic understanding of how these materials change over time. In particular, the study of the degradation process of modern colorants presents significant challenges, such as the high number of existing

colorants and the inherent complexity of these materials. Moreover, distinguishing between synthesis products and true degradation compounds is difficult, as they often exhibit overlapping chemical features [12].
Studying the effect induced by light on paints, the physico-chemical variations of the material may be due not only to the pigment itself but also to the binder and the interaction they have with each other. Recent studies faced up to the synthetic organic pigments considering the aging due to either the powder pigments [13] or to the interaction between pigments and binder, as for example in the formulation of acrylic and alkyd resins [2]. However, scientific literature lacks an extensive study about the stability of the new generation of synthetic organic pigments in the presence of reactive metal oxides. Indeed, studies on paint degradation have primarily focused on the interaction between binders and inorganic pigments [14, 15] or on the impact of the binder on the stability of the paint [16].

1.2 Modern paint systems and degradation mechanisms

The study of the chemical and physical aging variations of modern pigments is essential to assess their long-term stability within complex paint systems and to develop effective conservation strategies and preventive measures.
The composition of paint consists of several key components, including pigments, binders, solvents, fillers, and additives. These elements determine the characteristics of the paint, including its visual appearance, texture, and methods of application. Pigments are the colorant that impart color to the paint, while binders (or media) hold the pigment particles together and ensure their adhesion to the substrate. Solvents facilitate the adjustment of the paint's consistency, thereby facilitating its application. Fillers increase the bulk, opacity, and texture of the paint. Additives improve the paint's stability, enhance its flow, or prevent clumping.
Chromatic changes in paintings, such as fading, darkening, or blanching [17, 18], are the result of photodegradation processes, both physical and chemical, caused by prolonged exposure to light and environmental conditions [3]. Although many synthetic pigments developed in the 20th and 21st centuries demonstrate higher lightfastness than historical pigments, their aging process can vary depending on the type of binder used, the pigment-pigment interactions, and the presence of inorganic components.
The complexity of the aging mechanism in painting materials is further amplified by

the diversity of modern pigments, which originate from various chemical classes, each characterized by different properties in terms of light stability, solubility, polarity, and chemical reactivity. Furthermore, the interaction between organic pigments and inorganic compounds can significantly influence degradation processes. These interactions are particularly significant in the case of reactive mixtures, such as commercial spray paints, varnishes, or protective coatings commonly used in contemporary practices [19–21]. Indeed, white inorganic pigments are widely employed in these mixtures for primer preparations, to create various shades of color, and as protective coatings or drying agents. For this reason, it is important to consider the interaction between organic and inorganic pigments in the degradation process of paints.
In the following, the two main categories of painting materials are presented, describing their degradation process: pigments (synthetic organic and white inorganic pigments) and binders. Specifically, the materials used in this Ph.D. were selected from these categories based on their relevance to artistic practices, as well as their use in artworks and other applications.

1.2.1 Modern pigments

Pigments have long been essential to human expression and artistic creation, translating vision into visual form across historical periods. Based on their chemical composition, pigments are typically classified as inorganic or organic [1].
Inorganic pigments are not carbon-based compounds and are typically derived from minerals or metal-based compounds. These pigments are often more stable and durable than organic ones, offering excellent lightfastness and resistance to fading. They can be further classified into natural and synthetic categories. For example, one of the main white pigments in use since antiquity is lead white, an inorganic pigment synthetically prepared as basic lead carbonate, whereas the native mineral is cerussite. Several inorganic pigments are semiconductors, and it is possible to totally characterize all the steps that lead to photooxidative and photodegradation mechanisms. For example, the aging processes of n-type semiconductor pigments, such as red mercury sulfide (HgS) and cadmium yellows (CdYs), have been extensively studied due to their light-induced redox reactions, which may compromise the original coloration and visual integrity of artworks [22–24]. The darkening of chrome yellow pigments due to the photoreduction process, as well as the degradation phenomenon in azurite pigments, have also been subjects of considerable study [25, 26].
In particular, white inorganic pigments are widely used not only for their white coloring properties but also to lighten colored pigments, thereby creating different hues and

shades [27]. The white color of inorganic pigments results from the optical properties of these materials, primarily their low absorption of visible light and high nonselective light-scattering capacity [28, 29]. These pigments are also employed as a covering base in underpainting techniques, wherein a preliminary layer of white paint is applied to establish light and contrast before the coat of colored layers [30]. Concurrently, the employment of white inorganic pigments enhances the durability of paints due to their high chemical stability.

Organic pigments are carbon-based compounds that can be further subdivided into two main groups: natural pigments, which are derived from sources such as plants, animals, or insects, and synthetic pigments, which are produced through chemical processes in laboratories to achieve specific colors and properties.

Specifically, natural pigments have been employed in art and textiles for centuries. However, their use is limited by the availability of the raw materials from which they are derived. Light-induced damage to natural organic pigments has been widely studied, particularly with respect to color changes, as these pigments are considered susceptible to fading over time [22]. Notably, indigo blue stands out as one of the oldest known pigments, in use for over 4,000 years, with its light-induced degradation being well-documented [31]. Additionally, other studies have focused on the photoinduced aging mechanisms of anthraquinone-based red dyes, such as alizarin and cochineal, which were widely used in ancient times [32, 33].

Consequently, traditional natural pigments have been almost completely replaced by industrial chemical-derived synthetic alternatives in the modern colorant market. This is due to the enhanced reliability, cost-effectiveness, and performance of the synthetic pigments, which provide a more extensive range of colors and improved stability compared to their natural counterparts [34].

In particular, synthetic organic pigments (SOPs) are composed of complex organic molecules comprising a distinctive group of atoms known as chromophores (from Ancient Greek *χρῶμα* (chrōma) "color" and *φορός* (phoros) "carrier of"). The chromophore group imparts color to a molecule by absorbing specific wavelengths of light radiation within the UV-VIS spectral range, due to electron transitions between the molecular orbitals generally resulting from n$\rightarrow \pi^*$ or $\pi \rightarrow \pi^*$ transitions [4]. In general, chromophores are unsaturated functional groups that contain double bonds (such as –N=O, –N=N–, C=O, or C=C), triple bonds (such as –C≡C– or –C≡N), or aromatic rings. Furthermore, SOPs may comprise metal ions or auxochromes (from Ancient Greek *αὐξάνω* (auxanō) "increase" and *χρῶμα* (chrōma) "color"). While auxochromes themselves do not impart color, they enhance the color intensity of the chromophore by

donating nonbonding electron pairs (such as $–NH_2$, $–OH$ or $–CH_3$), or by withdrawing electron density through the acceptance of nonbonding electron pairs (such as $–NO_2$, –Br or –Cl). Additionally, organic pigments may include materials whose color is due not to a single group, but to several chromophores which give rise to a conjugation system [7, 10].
The development of synthetic pigments has resulted in a vast array of colorants, which are systematically recorded in systems such as the Colour Index^{TM} (CI) [35]. First published in 1924 by the Society of Dyers and Colourists (SDC) and the American Association of Textile Chemists and Colourists (AATCC), this comprehensive catalog assigns unique identifiers to colorants, including the CI generic name and CI constitution number, based on their chemical composition and molecular structure. For pigments, the CI Generic Name describes the class (e.g., Pigment - P), with its chromatic hue (e.g., Yellow - Y, Orange - O, Red - R, Violet - V, Blue - B, etc.), followed by a serial number corresponding to the chronological order registered in the Colour Index. The use of this standardized index across both the art and industrial sectors facilitates the consistent identification and application of pigments. Following the classification proposed by Herbst and Hunger [1], the SOPs can be divided into three main categories, as outlined below:

- Azo pigments
  - Monoazo Yellow and Orange
  - Disazo
  - β-Naphthol
  - Naphthol AS
  - Azo Pigment Lakes
  - Benzimidazolone
  - Disazo Condensation
  - Metal Complex
  - Isoindolinone and Isoindoline
- Polycyclic Pigments
  - Phthalocyanine
  - Quinacridone
  - Perylene and Perinone
  - Diketopyrrolo-Pyrrole
  - Thioindigo
  - Anthraquinone
  - Dioxazine
  - Triarylcarbonium
  - Quinophthalone
- Miscellaneous Pigments

Azo pigments are the largest class of organic pigments, characterized by the presence of one or more azo groups (-N=N-) in their molecular structure. They are known for their vibrant hues, ranging from yellows and oranges to deep reds, and are widely used due to their excellent color strength and versatility. Polycyclic pigments, on the other hand, include a range of complex molecular structures. These pigments are valued for their exceptional lightfastness, chemical stability, and broad spectrum of intense colors, making them indispensable in various artistic and industrial applications. All pigments that do not belong to one of these two groups are classified as miscellaneous. These include a variety of synthetic pigments with unique structures that play important roles in various applications.

In this Ph.D. project, three colored SOPs were selected from different classes within the full range of existing categories. The selected pigments include two yellow pigments belonging to the monoazo and isoindoline classes and one blue pigment belonging to the phthalocyanine class. The CI Generic Names assigned to these pigments are CI Pigment Yellow 1 (PY1), CI Pigment Yellow 139 (PY139), and CI Pigment Blue 75 (PB75), respectively.

In addition, three white inorganic pigments were selected for their significant role in artistic and decorative applications: lead white (basic lead carbonate, $2PbCO_3{\cdot}Pb(OH)_2$), titanium white (titanium dioxide, TiO_2), and zinc white (zinc oxide, ZnO).

The objective is to investigate the stability of these colored modern pigments, both individually and in combination with binders or inorganic pigments, by analyzing the chemical and physical variations occurring after aging processes. In the following, a comprehensive overview of the specific classes and the selected pigments is provided.

Monoazo pigments

Monoazo pigments constitute an important class of SOPs, defined by a single azo group, as illustrated by their general molecular structure in Figure 1.3.

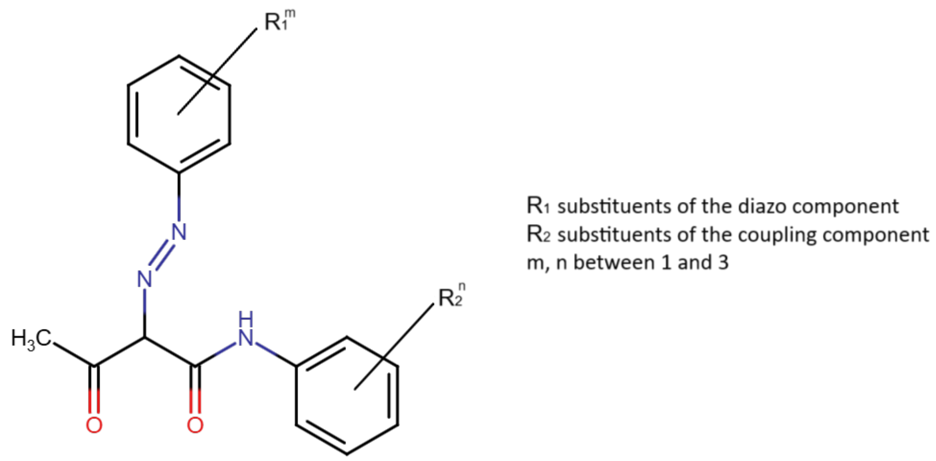

Figure 1.3 Schematic representation of the structure of monoazo pigments [36]. R_1 and R_2 represent substituents, which may include CH_3, OCH_3, OC_2H_5, Cl, Br, NO_2, CF_3.

The azo pigments are widely used in modern and contemporary paints, including mural spray paints, due to their bright yellow to orange hues and cost-effectiveness, often in combination with titanium dioxide [37, 38]. First discovered in 1909 by the historic German company Meister Lucius & Brüning, they were commercialized in 1910 under the name "Hansa Yellows". The most common Hansa Yellow pigments are PY1 and PY3. The PY1 pigment is characterized by a warm and brilliant hue, rendering it particularly suitable for interior decorative paints. The PY3 pigment, compared with PY1, has auxochromes -Cl on the aromatic rings, which impart a redder hue and improve chemical stability. The PY74 and PY97 pigments are also prevalent in the market and offer good weather resistance, making them ideal for industrial paints and outdoor applications [1, 34, 39].

Among the monoazo pigments, PY1 was selected. Introduced under the commercial name "Hansa Yellow G", PY1 is a bright yellow pigment that presents a nitro (-NO_2) and a methyl (-CH_3) substituents in the diazo component R_1, in ortho- and para-position relative to the azo bridge, respectively, and no R_2 substituents.

Specifically, PY1 belongs to the yellow arylide class, a subgroup of the larger monoazo category, with the chemical structure of the 2-[(4-methyl-2-nitrophenyl)diazenyl]-3-oxo-N-phenylbutanamide. It can be present in different tautomeric forms due to the presence of the single (-N-NH-) group instead of the traditional azo (-N=N-) linkage [1]. In such a class of pigments, the azo bond between two aromatic groups represents the chromophore center of the molecule. The equilibrium between the azo and hydrazone forms depends on the chemical environment (solvent polarity, pH, and adjacent functional groups), and the shift between azo and hydrazone forms can alter the absorption spectrum of the pigment, affecting lightfastness and degradation.

Isoindoline pigments

Isoindoline yellow pigments represent a relatively recent class of lightfast and weatherfast SOPs. The molecular structure of isoindoline pigments is characterized by the presence of an isoindole ring, as illustrated in Figure 1.4.

Introduced in the mid-1960s, this high-quality pigment class rapidly gained popularity due to its bright hues and good chemical stability. Consequently, these pigments are frequently employed in various applications, including industrial coatings, exterior paints, printing inks, and artistic compositions, frequently in conjunction with white inorganic pigments. Depending on the substitution pattern X_1 e X_3, isoindoline pigments can be either azomethine derivatives or methine derivatives. Isoindoline pigments exhibit hues ranging from yellow (PY109, PY110, PY139, PY173, PY185) to orange (PO61, PO66, PO69), red (PR260), and brown (PBr38). Other isoindoline pigments with different shades have not achieved significant commercial success [1, 34, 40].

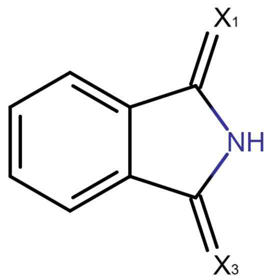

Figure 1.4 Schematic representation of the structure of isoindoline pigments [36]. X_1 and X_3 represent substituents, defining azomethine (X_1 = O or N–, X_3 = N–) or methine (X_1 = X_3 = C linked to heterocyclic rings) derivatives.

Among the isoindoline pigments, PY139 was selected. In more detail, PY139 presents a symmetric configuration of methine type, wherein the isoindoline chromophore is attached to two identical heterocyclic rings of barbituric acid $C_4H_4N_2O_3$, with the chemical structure of the 5-[3-(6-hydroxy-2,4-dioxo-1H-pyrimidin-5-yl)isoindol-1-ylidene]-1,3-diazinane-2,4,6-trione. This pigment provides a reddish-yellow shade with excellent lightfastness and weatherfastness properties, making it suitable for use in plastics, paints, and printing inks.
The isoindoline ring leads to the presence of two different tautomeric forms, involving the two heterocyclic ring systems attached through a carbon bond. In its crystalline form, PY139 is organized in a two-dimensional network, benefiting from hydrogen bonding interactions [41]. Notably, the high number of hydrogen bond donors and acceptors contributes to strong intermolecular attractive forces, promoting the formation of a tightly packed structure. The influence of physical properties, such as particle size and shape, on color behavior is particularly pronounced in isoindoline pigments.
The ASTM lists these two yellow pigments among those exhibiting high stability and good lightfastness when combined with oil [42, 43]. Although the extensive characterization of monoazo and isoindoline pigments in modern and contemporary paintings and the investigation of photoaging within the same molecular class [16, 44], a comprehensive understanding of their lightfastness in the case of powder pigments or paints interacting with white inorganic pigments is still lacking.

Phthalocyanine pigments

Phthalocyanine pigments are one of the most important classes of synthetic organic pigments. The excellent chemical and physical properties of phthalocyanines, and their low production cost, make them the largest fraction of blue and green organic pigments on the market [1]. For this reason, these pigments are widely used in the artistic field in modern paintings [45, 46], or as organic pigments in street artwork paints [21].
Phthalocyanines are distinguished by a highly conjugated macrocyclic structure comprising four isoindole units linked through nitrogen atoms, with a central metal ion typically present to stabilize the complex, as shown in Figure 1.5.

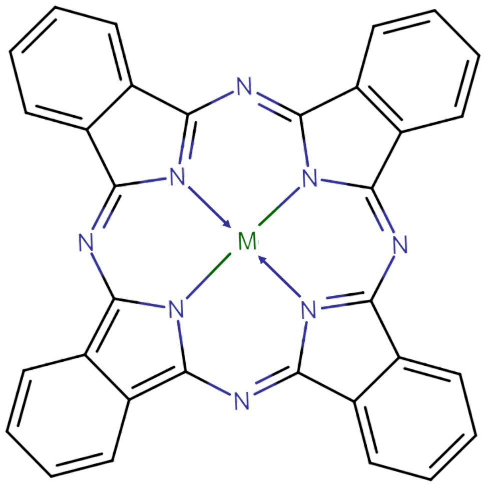

Figure 1.5 Schematic representation of generic metal phthalocyanine structure [36]. In the center, M represents the metal ion (M = Cu, Co, Ni, Zn, Fe, Mn, etc.)

The stability and rigidity of this structural configuration permit extensive electron delocalization across the entire macrocycle. The delocalized π-electrons are primarily responsible for light absorption, particularly within the ultraviolet and visible light region, contributing to the vivid coloration and excellent lightfastness that typify phthalocyanines. These pigments typically display shades of blue and green. The exact color depends on the different coordination of the metal ions at their center (or lack thereof in the case of the metal-free phthalocyanine H_2Pc), which enhances their chemical and physical properties, as well as the specific auxochrome groups attached to the macrocyclic structure. The central metal ion determines the pigment's electronic properties, significantly influencing its light absorption behavior. Copper is the most common central metal in phthalocyanine pigments, producing the intense phthalo blue pigment in five distinct polymorphic forms. The presence of other central metals can result in variations in color and chemical reactivity. Moreover, the presence of auxochrome groups, such as chlorine (-Cl) and bromine (-Br), shifts the pigment's hue towards green, contributing to the synthesis of pigments such as phthalo green. The versatility of phthalocyanines, combined with their low production cost, has enabled their rapid adoption across artistic and industrial applications [1, 34, 47].

Among the various phthalocyanine pigments, cobalt phthalocyanine (CoPc or PB75) was selected as one of the SOPs investigated in this Ph.D. research project. The central cobalt ion within the macrocycle is responsible for the distinctive dark blue color with red and violet undertones. In addition to its color, CoPc exhibits the characteristic properties of phthalocyanines, including chemical stability and lightfastness. Indeed, the different oxidation states and coordination abilities of cobalt induce shifts in the electronic structure of the pigment, thereby influencing its stability and light absorption properties. These attributes make CoPc pigments highly suitable for a wide range of applications, including paints, coatings, plastics, and printing inks. Moreover, the exceptional light stability of cobalt phthalocyanine is attracting considerable interest as a potential component for various advanced applications. These include, for instance, its deployment as a material in optical, electronic, and photoelectronic devices, as well as in gas sensors and solar cells [48–50].

The stability of phthalocyanines in solutions is widely investigated as light-induced photobleaching/photodegradation [51], in combination with different solvents: organic [52], ionic liquids, acids [53], or water [54]. In addition, the chemical and structural stability of phthalocyanine and its influence on the photodegradation of acrylic and alkyd paints have been extensively studied [55, 56].

The high stability of cobalt phthalocyanine during this Ph.D. was studied only in interaction with titanium dioxide, which was found to be the most reactive inorganic pigment. Although the conjugated molecular structure of phthalocyanine exhibits excellent solidity, and the titanium dioxide shows high performance to UV and visible light, the stability of the combination of these two pigments is not well known. At the macroscopic level, the solid-state interaction of these two powder pigments is lacking, and the physical/chemical effect of TiO_2 on the stability of phthalocyanine pigments, in powder form without binder, is not entirely clear.

Lead white

Lead white, historically known as "biacca" and classified as CI Pigment White 1 (PW1), is one of the oldest white pigments, used in painting, sculpture, and decorative arts since ancient times. Traditionally produced synthetically by reacting metallic lead with vinegar, lead white occurs naturally as the rare minerals cerussite ($PbCO_3$) and hydrocerussite ($2PbCO_3{\cdot}Pb(OH)_2$).
Its exceptional opacity, brightness, and warm undertone make lead white the predominant white pigment until modernity, widely used in classical European oil paintings [57]. However, since the ’60s, due to concerns over lead toxicity and the advent of alternative white pigments in contemporary markets, lead white has gradually been replaced by the more modern pigments based on zinc and titanium compounds [29, 58]. Lead white was thus restricted or banned in many countries but continued to be available for more than a couple of decades after the issuance of regulations limiting its use, still in the restoration and conservation of historic artworks and buildings. Although lead white is not strictly considered a modern inorganic pigment, its well-known degradation mechanism was helpful to validate our simulated aging process.
Lead white is highly reactive in oil-based media, forming a strong bond with the binder that contributes to the overall durability and flexibility of paint films. Moreover, lead white functions as an effective siccative, accelerating the thermooxidative polymerization and subsequent degradation of drying oils by promoting the formation of cross-linked networks within the matrix [59]. Beyond its role in film formation and drying, lead white can also initiate chemical degradation processes. Specifically, it can react with free fatty acids generated through the hydrolysis of triglycerides in the oil medium, triggering a saponification process. This reaction results in the formation of lead soaps (lead carboxylates). Over time, these soaps may migrate through the layers, aggregate, and crystallize, significantly impacting the stability and appearance of painted surfaces. The accumulation of lead soaps has been associated with surface protrusions, increased opacity, translucency, or delamination [60–62].

Titanium white

Titanium dioxide, classified as CI Pigment White 6 (PW6), is one of the most widely used white inorganic pigments of the 20th century. Its popularity has surpassed that of traditional white pigments due to its high stability, non-toxicity, and low cost. TiO_2 exists in three natural crystalline forms: anatase, rutile, and brookite. Brookite, a rare mineral, is not employed in pigment production. The anatase and rutile forms are, however, synthesized to yield white pigments [28, 63].

The primary application of titanium dioxide is as a white pigment, extensively used in various commercial products, including paints, paper, pastels, plastics, inks, and cosmetics. Beyond its role as a pigment, TiO_2 has also found interest in the scientific research field thanks to its photocatalytic properties, such as material for energy generation and storage, environmental protection, catalyst, and biomedical applications [64–66]. Titanium dioxide can also be studied in combination with colorant, for example, an important application concerns the use of phthalocyanines in combination with titanium dioxide for the study of photocatalysis and the creation of dye-sensitized solar cells (DSSC) [50, 67], in which the active material consists of the colorant that transfers electrons to the TiO_2 following the absorption of photons. In addition, titanium dioxide has attracted new interest in the field of cultural heritage for its use in "anti-smog" paints applied to outdoor artworks [68, 69]. These paints take advantage of the photocatalytic activity of TiO_2 to break down harmful pollutants under sunlight, thus helping reduce air pollution.

Despite its widespread use and advantageous properties, titanium dioxide in paints can interact with the organic binder, potentially leading to erosion or oxidative degradation of the binder [70–72]. These interactions are primarily attributed to the photocatalytic activity of TiO_2, which can generate reactive oxygen species under light exposure, breaking down binder molecules and accelerating the aging process of the paint film, thus resulting in discoloration and fading. This phenomenon is not the only problem associated with titanium dioxide interactions in painted systems. Several studies have documented visible degradation processes in wall paintings and murals, possibly resulting from the physical migration of TiO_2 powders toward the surface [37, 73]. In addition, in the context of modern and contemporary artworks, the interaction between TiO_2 and synthetic organic pigments adds further complexity, leading to color differences in the paints [16, 74]. To counteract these effects, commercially available TiO_2 pigments are often surface-coated with inert materials such as aluminum, zirconium, or silicon oxides, which effectively decrease the photocatalytic activity of TiO_2 [75]. These materials help preserve pigment stability even under prolonged exposure to UV radiation. The presence or absence of these treatments must be carefully considered when evaluating the photostability of modern pigments subjected to environmental conditions. However, it is important to note that, as previously discussed, the photocatalytic activity of titanium dioxide is intentionally exploited in various technological and artistic applications, including protective coatings, mural paints, solar cells, photocatalytic systems, and more.

Zinc white

Zinc oxide, classified as CI Pigment White 4 (PW4), has been known since ancient times, though its use as a pigment became widely recognized only in the late 18th century. It is highly valued for its non-toxicity, fine particle quality, cool transparent tone, and exceptional long-term stability. Industrial-scale production began in France around 1780, but it was not until 1834 that it emerged under the name "Chinese White" as a true alternative to the toxic lead white. Derived from the mineral zincite, zinc white is now exclusively produced synthetically through the combustion of zinc metal, using either the direct process (American) or the indirect process (French) [28, 76].
Zinc oxide is the subject of considerable scientific research for its antimicrobial properties and resistance to environmental factors. It is widely used in various industries, including cosmetics, ceramics, plastics, and pharmaceuticals [77, 78].
Zinc white can contribute to different degradation processes in paintings, affecting both the mechanical and chemical stability of painted surfaces. Similarly to lead white, it can promote the saponification of the oil binder, leading to the formation of zinc soaps (zinc carboxylates). These compounds may migrate through the paint layers, crystallize, and accumulate, resulting in physical damage such as brittleness, cracking, and increased transparency of the paint layers [61, 79]. In addition to soap formation, zinc oxide is known to exhibit photocatalytic activity under light exposure, particularly in the presence of UV radiation. Interestingly, this photocatalytic property has been intentionally exploited in recent applications, where zinc oxide is incorporated into the formulation of self-cleaning paints for outdoor use. In these modern materials, ZnO nanoparticles help degrade organic pollutants deposited on surfaces by triggering oxidative degradation under light exposure [80, 81]. However, this reactivity, similar to that observed in titanium dioxide, can initiate or accelerate photooxidative degradation processes of both the oil binder and other pigments, further compromising the stability and appearance of the paint film.

1.2.2 Binders

Binders are of fundamental importance in paint formulations, as they act as the medium that binds pigment particles together and facilitates their adherence to the substrate. Beyond their role in cohesion, binders contribute to the texture, gloss, elasticity, and stability of the paint.

Throughout art history, binders have evolved significantly, aligning with the technical and artistic demands. The main binders employed in painting can be divided into three types [82], as outlined below:

- tempera, derived from protein-based materials (such as egg yolk or animal glue) or polysaccharide-based materials (such as vegetable gums);
- oils, valued for their ability to form transparent, flexible, and durable films;
- synthetic polymers, such as alkyd and acrylic resins.

Notwithstanding the advent of synthetic binders in the 20th century, siccative oils remain the most widely used medium in painting techniques, with applications also in modern and contemporary art.

From antiquity to the present, linseed, walnut, and poppy oil have been the most common drying oils employed in painting [83]. These oil binders are a complex mixture of triacylglycerides (TAGs), which consist of glycerol molecules esterified with three fatty acids. The fatty acids typically present in siccative oils include saturated acids (such as myristic, palmitic, and stearic acids) and polyunsaturated acids (such as oleic, linoleic, and linolenic acids), which are differentiated by the number of conjugated double bonds. A distinguishing feature of these oils is their high concentration of polyunsaturated fatty acids, which renders them highly susceptible to oxidation and polymerization, leading to the formation of durable and elastic paint films.

The drying process of siccative oils is characterized by oxidation and polymerization reactions, resulting in chemical and physical variations of the paint film [84, 85]. Known as curing, this process involves the absorption of atmospheric oxygen and the crosslinking of unsaturated fatty acids. The result of these reactions is the formation of a high-molecular-weight, three-dimensional polymer network, leading to a strong and stable paint film. However, external factors such as light, temperature, and humidity can accelerate the aging processes. Over time, these conditions may lead to yellowing and a loss of elasticity, thereby compromising the film's properties. The drying and aging of oils are subjects of significant interest in the scientific literature. Indeed, a comprehensive understanding of these processes is fundamental for the conservation and restoration of painted artworks.

Linseed oil

Among all drying oils, linseed oil is known for its excellent drying properties and mechanical strength, making it the most widely used binder in the artistic field. Linseed oil is extracted from the seeds of *Linum usitatissimum*, and the high content of polyunsaturated fatty acids characterizes it. In particular, α-linolenic acid ($C_{18:3}$), a triply unsaturated fatty acid with an 18-carbon chain and three double bonds, constitutes approximately 48-60% of linseed oil composition. Other significant saturated fatty acids present are oleic acid ($C_{18:1}$, 14-24%) and linoleic acid ($C_{18:2}$, 14-19%), which contain one and two double bonds, respectively. Additionally, smaller amounts of saturated fatty acids, such as palmitic acid ($C_{16:0}$, 6-7%) and stearic acid ($C_{18:0}$, 3-6%), contribute to the overall structure of the oil [86, 87].
Figure 1.6 illustrates the molecular structure of the main fatty acids of linseed oil.

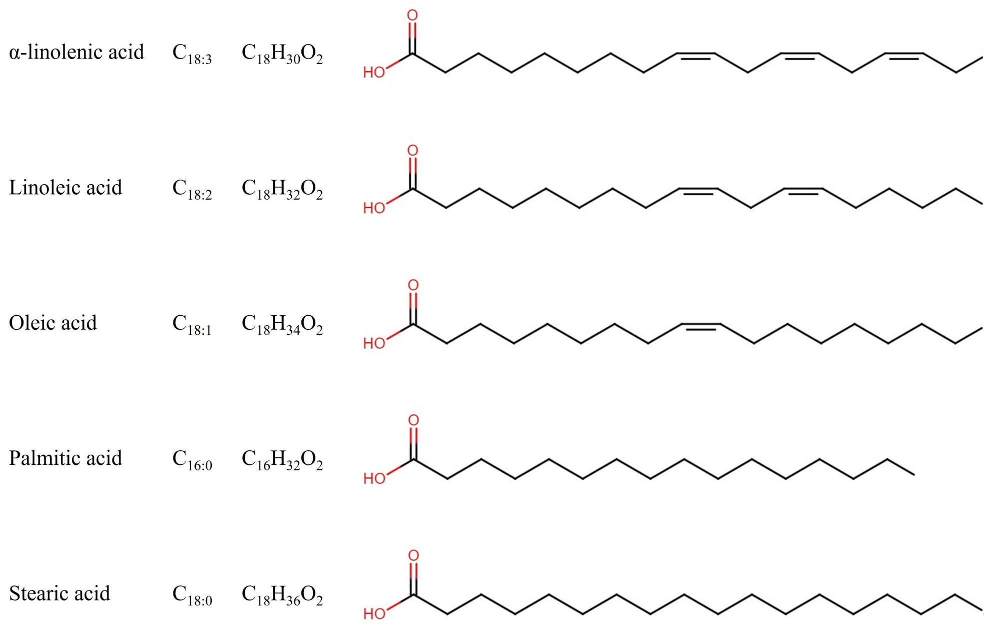

Figure 1.6 Schematic representation of the molecular structures of the main fatty acids present in linseed oil [36]. From top to bottom: α-linolenic acid, linoleic acid, oleic acid, palmitic acid, and stearic acid.

2 Multi-technique approach

This chapter provides an overview of the techniques employed both to characterize the materials used in the sample preparation and to investigate the variations induced by artificial aging processes. The analysis of materials in the field of cultural heritage, including pigments, binders, and paints, requires a multidisciplinary approach that incorporates different analytical techniques. Specifically, the multi-technique approach ensures the acquisition of detailed information regarding the chemical composition, structural characteristics, and state of conservation of the artworks while preserving their integrity. The methodologies employed in this field can be classified into non-invasive and invasive techniques, with invasive methods further divided into non-destructive and micro-destructive methods [82].

- Non-invasive techniques enable the analysis of materials without requiring sampling or direct contact, making them essential for studying artworks and artifacts of significant historical value. These methods preserve the integrity of the object while providing detailed information. They operate based on electromagnetic radiation, with specific wavelengths selected according to the type of information required. Among the most common techniques in this field are photography under various lighting conditions, UV fluorescence, and infrared reflectography.
- Invasive non-destructive techniques enable material analysis without altering the sample, even though some require direct contact. These methods, widely employed in cultural heritage studies, are based on the interaction between electromagnetic radiation and matter to obtain elemental and chemical information. Some of the most commonly used techniques are scanning electron microscopy

(SEM), X-ray fluorescence (XRF), and photoluminescence spectroscopy (PL). Molecular spectroscopy techniques, such as Fourier transform infrared (FTIR) and Raman spectroscopy, are particularly valuable in this field. Identifying functional groups and comparing spectra with reference databases provides insight into the molecular composition of both organic and inorganic materials.

- Invasive micro-destructive techniques, on the other hand, involve the collection of small quantities of material, chemical treatment, or partial removal of the sample during analysis. Commonly applied micro-destructive techniques in cultural heritage studies include thermal methods as well as mass spectrometry. In particular, secondary ion mass spectrometry (SIMS) is used to identify organic materials such as polymers, synthetic pigments, and oils, providing high surface sensitivity. SIMS is considered a micro-destructive technique because it bombards the sample with a beam of primary ions, resulting in surface ablation and material removal at the nanometric scale. Furthermore, because this technique requires small sample sizes, it often involves the sampling of material from the artwork.

To gain a comprehensive understanding of the interactions and degradation processes occurring between organic and inorganic pigments under aging processes, a multi-technique approach was designed, using a combination of the techniques outlined below. The choice of the most suitable technique depends on both the material and the type of information to be obtained. In the context of studies on the artificial aging of pigments and paints, an important factor in the selection of the technique is the depth of analysis, or penetration depth (d_p), which refers to the ability of the instrument to probe the surface layers or the deeper internal layers of the material. Table 2.1 provides the penetration depth of the analytical techniques used in this Ph.D., with the main factors that can influence it, excluding the material type.

Table 2.1 Comparison of penetration depth of the analytical techniques employed.

Technique	**Penetration depth d_p**	**Main influencing factors**
FTIR-ATR	0.5 – 10 μm	IR wavelength ATR crystal (Ge < Si < ZnSe)
Raman	10 nm – 5 μm	Laser wavelength (UV < VIS < near-IR)
ToF-SIMS	1 – 10 nm	Energy of the primary ions Acquisition time

2.1 Colorimetry

Colorimetry is a non-invasive technique used for color measurement based on objective methods that quantify the color perceived by the human eye. It employs instruments called colorimeters that detect the intensity of light reflected from a surface across different wavelengths. The measured data are expressed in standardized color spaces that provide a quantitative representation of color perception. In the field of cultural heritage, the most commonly used color space is the CIE L*a*b* (commonly referred to as CIELAB), developed in 1976 by the Commission Internationale de l'Éclairage (CIE, International Commission on Illumination) [9, 88]. With this technique, the color of an object is represented as a point in the three-dimensional CIELAB color space through three chromatic coordinates:

- L^*, the luminosity, is the z-axis ranging from black ($L^* = 0$) to white ($L^* = 100$);
- a^*, the red-green chromatic, is the abscissa axis, from $+a^*$ (red) to $-a^*$ (green);
- b^*, the yellow-blue chromatic, is the ordinate axis, from $+b^*$ (yellow) to $-b^*$ (blue).

This color space exhibits non-uniform distributed color domains, as schematically illustrated in Figure 2.1 [89], and is based on the opponent color model, in which colors located on the same axis but with opposite coordinates (such as green-red on the a^* axis and blue-yellow on the b^* axis) cannot be perceived simultaneously.

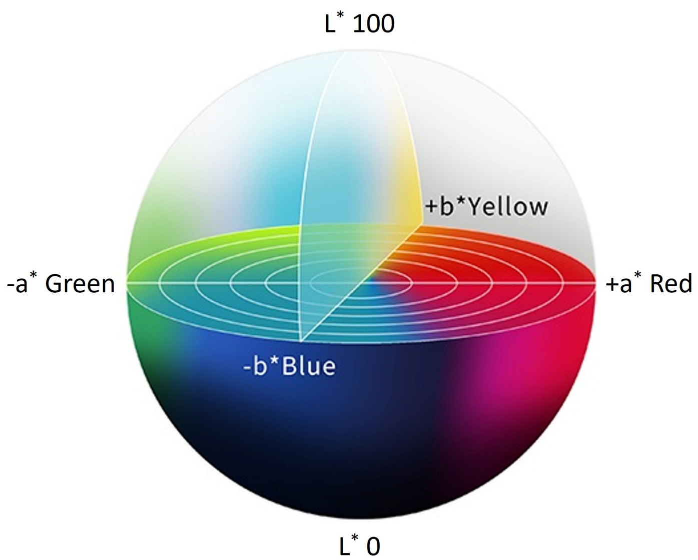

Figure 2.1 1976 CIELAB color space [89].

The nature of illumination significantly influences the perception and quantification of the color of an object [90]. The CIE recommended standard illuminants and optical geometries for use in colorimetry. Illuminant A represents the spectral distribution of a tungsten filament incandescent light source (color temperature 2856 K). Illuminants B and C are derived from Illuminant A by applying appropriate filters to simulate, respectively, noon sunlight (B) and average daylight conditions (C). The D series represents daylight simulants under different conditions: D75 (7500 K) corresponds to northern daylight, D65 (6500 K) to average daylight, and D55 (5500 K) to a combination of direct sunlight and skylight. Finally, the F series represents various types of fluorescent lamps, although none are classified as standard illuminants. In addition, two standard geometries are recommended: the 2° geometry, which simulates foveal (central) vision for focused color perception, and the 10° geometry, which represents peripheral vision with a wider field of view. The D65 illuminant and the 10° standard observer geometry are generally preferred for most applications.
Colorimetry has been used to quantify the first variations observed after artificial aging in terms of color perception, thereby providing numerical data on color variations. The total color change (ΔE) between two color points is calculated as the Euclidean distance between these points in the CIELAB color space:

$$\Delta E = \sqrt{(\Delta L^*)^2 + (\Delta a^*)^2 + (\Delta b^*)^2}$$

where Δ refers to the difference in color parameters between the aged sample and the unaged reference. When the value of ΔL^* is positive, the luminosity of the aged sample is lighter than the reference, and when ΔL^* is negative, the aged sample appears darker. A positive value of Δa^* indicates that the aged sample is redder than the reference, while a negative value suggests that it is greener. A positive value of Δb^* indicates that the aged sample is yellower, while a negative value indicates that it is bluer.

2.2 Fourier transform infrared spectroscopy

FTIR spectroscopy is an analytical technique that utilizes the absorption of infrared (IR) radiation by molecules to study the chemical composition of various materials. Molecules absorb infrared radiation at specific wavelengths corresponding to the vibrations of their chemical bonds [91]. This absorption generates a specific infrared spectrum, characteristic of the analyzed compound, providing valuable information about its chemical structure.
When a molecule absorbs an IR photon with a specific frequency ν_m, it transitions from its ground state to an excited vibrational energy state. The energy released by the IR radiation is thus converted into vibrational energy. For energy to be transferred from an IR photon to a molecule through absorption, the molecular vibration must induce a change in the dipole moment of the molecule [92, 93]. The intensity of the IR absorption I_{IR} is proportional to the square of the change in the dipole moment μ, caused by the change in the vibrational amplitude Q:

$$I_{IR} \propto \left(\frac{\partial \mu}{\partial Q}\right)^2$$

Only under these conditions, the alternating electric field of the IR radiation interacts with the molecule, causing changes in the amplitude of one of its vibrational motions. For this reason, not all molecular vibrations are IR-active, particularly in highly symmetrical molecules, where these vibrations do not produce a change in the dipole moment. The condition required for absorption is:

$$\left(\frac{\partial \mu}{\partial Q}\right) \neq 0$$

A typical IR spectrometer emits infrared radiation across a broad spectrum, conventionally divided into three regions:

- near-IR 14000-4000 cm^{-1},
- mid-IR 4000–400 cm^{-1},
- far-IR 400–0 cm^{-1}.

The mid-IR region, particularly useful for identifying a wide range of organic and inorganic materials, including binding media, pigments, paints, and varnishes, is further divided into two subregions, each providing specific information about the composition and structure of the analyzed materials. The region 4000-2000 cm^{-1}, known as the functional group region, contains absorption frequencies characteristic of organic functional groups, such as C=O, C=C, C–H, and O–H. These functional groups exhibit distinct absorption peaks at specific frequencies, regardless of the overall molecular structure. The region 2000-400 cm^{-1}, known as the fingerprint region, contains absorption peaks influenced by the overall skeletal structure of the molecule. The IR signals in this region are characteristic to each molecule, as even minor structural variations alter the distribution of absorption peaks. For this reason, no two molecules have the same IR features, making infrared spectroscopy a powerful tool for compound identification through database comparisons.

Molecular vibrations in IR spectroscopy can be classified as stretching and bending. Stretching vibrations involve changes in bond length along the axis connecting two atoms and can occur in either a symmetric or asymmetric mode. Bending vibrations, on the other hand, involve changes in bond angles and can also be classified as symmetric or asymmetric. These deformations can occur in-plane or out-of-plane, commonly referred to as rocking, scissoring, wagging, and twisting. A schematic representation of these vibrational modes is shown in Figure 2.2.

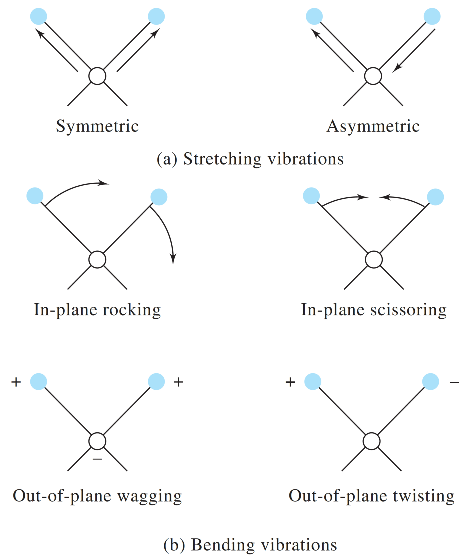

Figure 2.2 Types of molecular vibrations: (a) stretching and (b) bending vibrations. In out-of-plane vibrations, the + symbols + and - indicate the movement towards the reader and the page, respectively [91].

FTIR spectroscopy was performed in different modes, including transmission, reflection, and attenuated total reflection (ATR). The following section specifically examines the ATR mode, as it was the main method used in our experiments.

2.2.1 Attenuated total reflection mode

ATR is a widely used modality in FTIR spectroscopy that enables the direct analysis of solid, liquid, and semi-solid samples with minimal preparation. This technique relies on the principle of total internal reflection, allowing infrared radiation to interact with the sample at the surface of a high-refractive-index crystal, such as diamond, germanium (Ge), or zinc selenide (ZnSe) [94]. Specifically, infrared radiation propagates from the optically denser ATR crystal to the less dense sample, which is in direct contact with the crystal. As the angle of incidence increases, a fraction of the incident beam is reflected until it exceeds a certain threshold, known as the critical angle, and total internal reflection occurs. The beam penetrates a small distance into the medium until the reflection occurs, creating an evanescent wave, an electromagnetic field that extends into the sample. During the reflections, the evanescent wave interacts with the sample, resulting in partial absorption of its energy. The corresponding intensity attenuation is measured by the detector. A schematic principle of the ATR mode is shown in Figure 2.3.

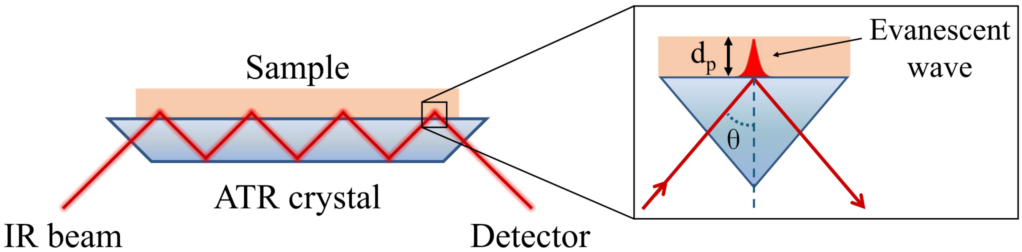

Figure 2.3 Schematic representation of the ATR mode (left), and a graphical detail of a single reflection with the evanescent wave, the penetration depth d_p, and the angle θ (right).

The depth of penetration d_p of the evanescent wave, which varies from a fraction of a wavelength to several wavelengths, determines the interaction between the infrared radiation and the sample, and is approximated as:

$$d_p = \frac{\lambda}{2\pi[n_c^2 \sin\theta - n_s^2]^{1/2}}$$

where λ is the wavelength of light, n_c is the refractive index of the ATR crystal, n_s is the refractive index of the sample, and θ is the angle between the incident IR beam and the surface normal of the crystal, as illustrated in Figure 2.3. Typical penetration depth in ATR ranges from approximately 0.5 to 10 μm, depending on the wavelength of the incident infrared light, the refractive index of the ATR crystal, and the sample under investigation.

2.3 Raman spectroscopy

Raman spectroscopy is an analytical technique based on the inelastic scattering of light by matter. When a sample is irradiated with a monochromatic light source, the light scatters in all directions, giving rise to the Raman effect [91]. In Raman experiments, this monochromatic light is provided by a laser source with an excitation wavelength in the UV, VIS, or near-IR spectral region (248-1064 nm).
In the Raman process, a molecule can absorb an incident photon with energy $h\nu_{ex}$, exciting the system from the ground vibrational state $\nu = 0$ to a virtual energy level j. After excitation, the molecule relaxes by emitting a photon from the virtual state, either elastically or inelastically. In elastic scattering, called Rayleigh scattering, the emitted photon has the same frequency (ν_{ex}) as the incident photon. In inelastic scattering, the wavelength of the scattered light shifts towards lower frequencies ($\nu_{ex} - \nu_{vib}$) or higher frequencies ($\nu_{ex} + \nu_{vib}$) compared to the incident radiation, where ν_{vib} represents the molecular vibration frequency. These shifts are known as Stokes and anti-Stokes scattering, respectively. Specifically, Stokes scattering occurs when molecules in the ground vibrational state are excited to the virtual state, while anti-Stokes scattering arises from molecules already in an excited vibrational state. A schematic diagram of the energy levels involved in the Raman process, using a simplified system with two vibrational energy levels $\nu = 0$ and $\nu = 1$, is illustrated in Figure 2.4.

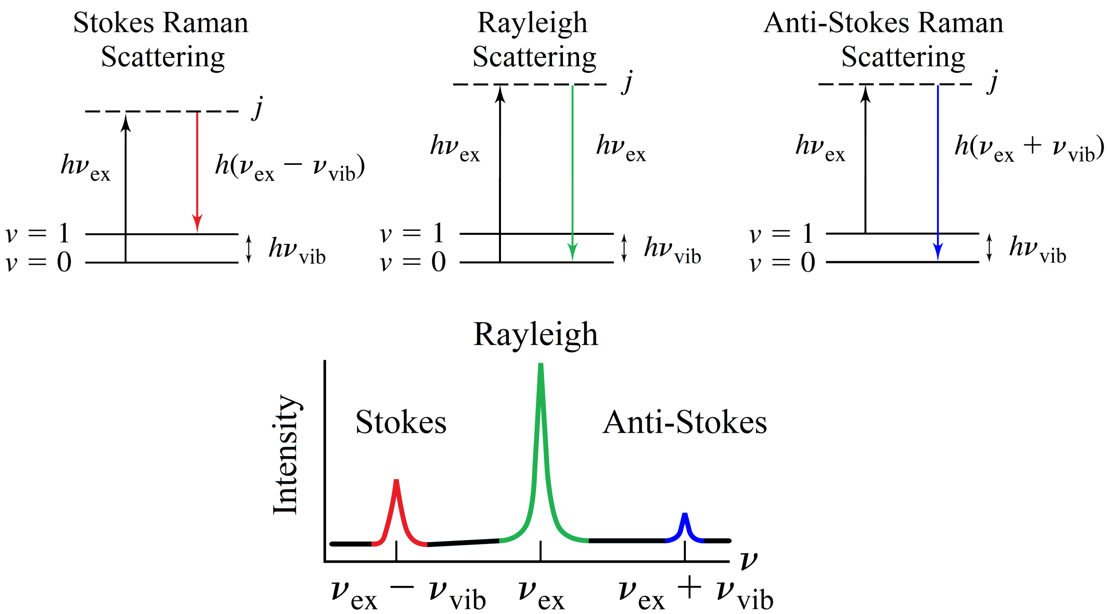

Figure 2.4 Energy levels diagrams of the vibrational transitions involved in the Raman scattering [91].

Rayleigh scattering is the most probable event, with its observed intensity being approximately 10^{-3} times lower than that of the original incident radiation. Stokes and anti-Stokes Raman scattering are considerably less intense, around 10^{-6} of the incident intensity. Additionally, at ambient temperature, Stokes transitions are typically more intense than the corresponding anti-Stokes transitions, as most molecular vibrations are in the ground vibrational state [92, 93].
The intensity of the Raman scattering I_R is proportional to the square of the variation of the polarizability α, with respect to the variation in the vibrational amplitude Q:

$$I_R \propto \left(\frac{\partial\alpha}{\partial Q}\right)^2$$

Only the molecular vibrational modes that cause a change in polarizability are Raman-active, such that they satisfy the condition:

$$\left(\frac{\partial\alpha}{\partial Q}\right) \neq 0$$

In Raman spectroscopy, the penetration depth is strongly influenced by both the optical properties of the material and the selected excitation wavelength, generally following the trend: $d_p(\text{UV}) < d_p(\text{VIS}) < d_p(\text{near-IR})$. Indeed, shorter wavelengths, such as UV lasers, result in less deep penetration, whereas longer wavelengths in the VIS and near-IR regions allow for deeper light penetration into the sample [95]. For example, in silicon, the penetration depth ranges from 3 μm with a 633 nm laser, approximately 300 nm with a 485 nm laser, to $\sim$15 nm with a 364 nm UV laser [96].
Raman spectroscopy is a widely used technique in the field of cultural heritage. While both Raman and IR spectroscopy are employed to study molecular vibrations, they provide different but complementary information. When comparing Raman and FTIR spectra, similarities can be observed, particularly in the functional groups and fingerprint regions, which are essential for identifying specific compounds. However, the types of molecular vibrations that are Raman- or IR-active differ significantly. As already seen, in Raman spectroscopy, the active vibrations are related to changes in the polarizability of the molecule, whereas in IR spectroscopy, a change in the dipole moment is required. This distinction generally means that non-polar or symmetrical molecules are typically Raman-active, while polar and asymmetrical molecules are predominantly IR-active.

2.4 Time-of-flight mass spectrometry

ToF-SIMS is a highly sensitive surface analytical technique, widely used in both industrial and research applications, including the analysis of materials in the cultural heritage field, such as ceramics, polymers, paints, coatings, and more [97]. This technique provides detailed elemental and molecular information about the surface of materials, making it invaluable for characterizing complex surfaces and thin films.

This technique offers two modes of analysis: static and dynamic SIMS mode. The static SIMS mode provides detailed chemical information from the surface layers of the material through surface spectrometry or high-resolution spatial imaging via surface imaging. This mode generates a mass spectrum and chemical maps of the surface distribution of the elements or compounds detected in the spectrum. The dynamic SIMS mode, on the other hand, enables the analysis of the material at different depths by sputtering the surface. This results in depth profiling measurements, as well as in-plane (2D) and in-depth (3D) ToF-SIMS data set reconstruction. Depending on the selected SIMS mode, different characteristics of the material can be explored, from surface composition to depth-dependent variations [91, 98].

Figure 2.5 illustrates the operating principle of the ToF-SIMS technique, which includes the primary ion gun, the secondary ion beam in orange analyzed by the ToF analyzer, the detector, the sputter ion gun for depth profiling, and the electron flood gun.

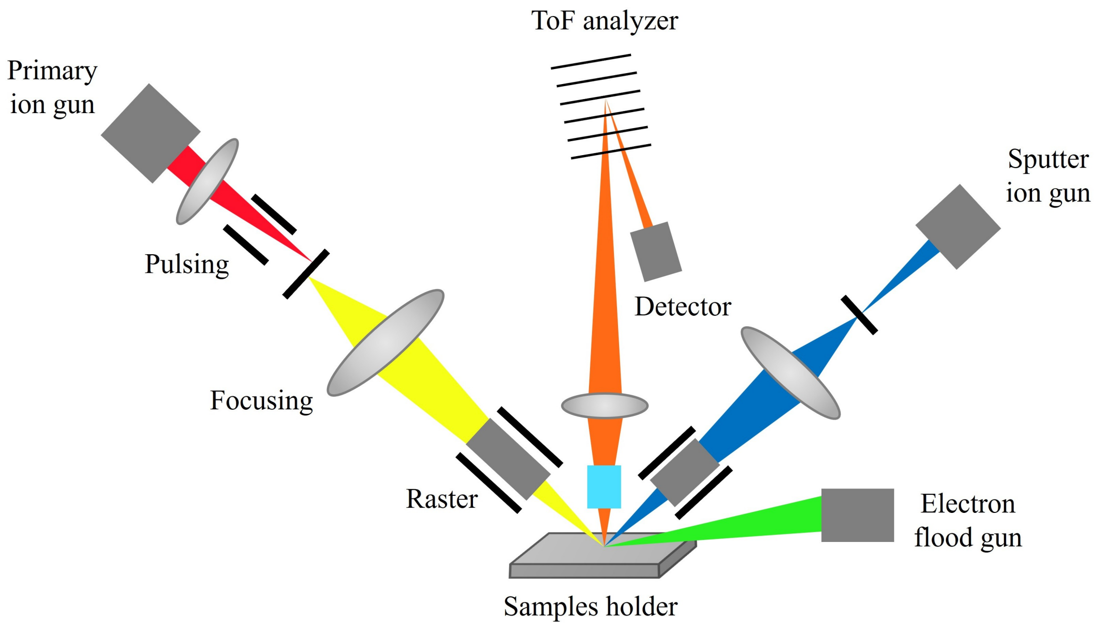

Figure 2.5 Schematic representation of the main components of the ToF-SIMS system.

The primary ion beam consists of high-energy ions (typically 1–30 keV), which are directed onto the sample surface under ultra-high vacuum conditions (UHV). This primary ion beam is pulsed, providing a well-defined start signal for the measurement of the flight time of the secondary ions. Upon striking the surface, the primary ions transfer energy to the atoms in the outermost atomic layers of the sample, leading to the ejection of surface atoms, molecules, fragments, and clusters.

Among the species ejected from the surface, only a small fraction are ionized, typically less than 1%. These ionized species form the secondary ion beam. The secondary ions are extracted and accelerated into the mass analyzer, where, upon reaching the detector, a mass spectrum is generated, plotting the mass-to-charge ratio (m/z) versus the intensity, expressed in counts. This spectrum allows for the identification of the various species present on the surface, providing high-precision chemical analysis and detailed insights into the composition of the materials.

In dynamic mode, a sputter ion gun is used to study the underlying layers of a material. The sputter ion gun bombards the surface with a high-energy ion beam, causing controlled erosion (or sputtering) of the sample, which is combined with static surface analysis. By repeatedly sputtering and analyzing the secondary ions emitted from each successive layer, ToF-SIMS generates a depth profile that reveals how the chemical composition varies with distance from the surface. Dynamic analysis is crucial for applications that require the study of multi-layered structures, such as coatings, composite materials, and thin films.

Another main component of the ToF-SIMS system is the electron flood gun, which is used to compensate for the electrostatic charge that can accumulate on insulating or non-conductive materials during SIMS analysis. The flood gun is an electron source that emits low-energy electrons (0-21 eV) to neutralize the surface charge while preventing any damage to the sample between primary ion pulses.

The penetration depth of ToF-SIMS in static mode depends mainly on the type of material, the primary ion beam used, and the specific conditions of the analysis, such as the acquisition time. Generally, the penetration depth is limited to the uppermost surface layers, providing chemical information from the top 1 to 10 nm of the material.

ToF-SIMS was employed to investigate the potential degradation of organic pigments in the presence of inorganic white pigments, as well as their possible interactions, after artificial aging. By comparison of the mass spectra acquired before and after the aging process, it was possible to assess the stability of the pigment within the outermost surface layers probed by ToF-SIMS.

2.4.1 Time-of-flight analyzer

The basic principle of a ToF detector, as schematized in Figure 2.6, is the separation of secondary ions based on their mass-to-charge ratio (m/z) [99].

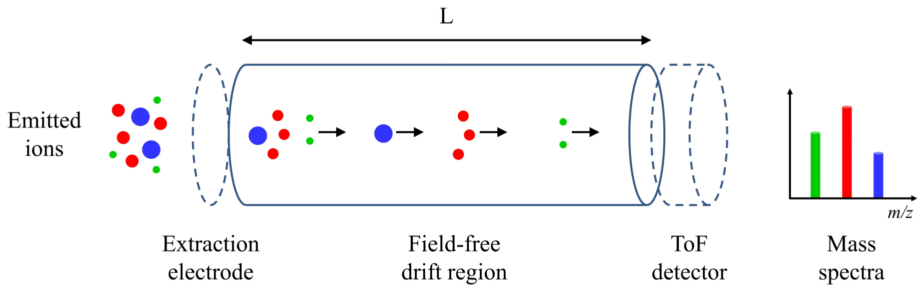

Figure 2.6 Schematic illustration of the working principle of a ToF detector [99].

When ions are subjected to an extraction electric potential V, the ions generated by bombardment acquire a fixed kinetic energy, $E_k = zeV$, where z is the ion charge and e is the electronic charge ($1.6 \cdot 10^{-19} C$). These ions then travel through a field-free drift tube of known length L at a certain velocity v. The kinetic energy of the emitted ions with mass m is given by:

$$E_k = ezV = \frac{1}{2}mv^2$$

Since all ions enter the field-free region with the same kinetic energy, their velocity is inversely proportional to their mass. Therefore, lighter ions have higher velocities, arriving at the detector earlier than heavier ions. The time of flight t is directly proportional to the m/z ratio, according to the following equation:

$$t = \frac{L}{v} = L\sqrt{\frac{m}{2zeV}}$$

In ToF-SIMS, mass separation takes place along the spectrometer axis. A fundamental factor determining the quality of the mass spectrum is the mass resolution, expressed as $m/\Delta m$. Two adjacent masses, m_0 and $m_0 + \Delta m$, reach the detector at different times, t_0 and $t_0 + \Delta t$, respectively. To resolve these two masses, the difference in their arrival times at the detector, Δt, must be sufficiently large. The ToF system is equipped with a reflectron-type mass analyzer. It consists of a series of electrostatic lenses that focus the ions and reverse their direction, increasing the total flight time without requiring a physically larger spectrometer. The resulting extended flight path enables better separation of ions with nearly identical masses, thereby enhancing the overall mass resolution. The high resolution of the ToF-SIMS instrument (10000 $m/\Delta m$) allows the precise identification of molecular fragments and minimizes spectral interferences.

2.5 X-Ray diffraction

X-ray diffraction (XRD) is an analytical technique widely employed to characterize crystalline materials. Its fundamental principle relies on the interaction between incident X-rays and the periodic atomic planes within a crystal lattice, resulting in diffraction patterns characteristic of the material [100, 101], as illustrated in Figure 2.7.

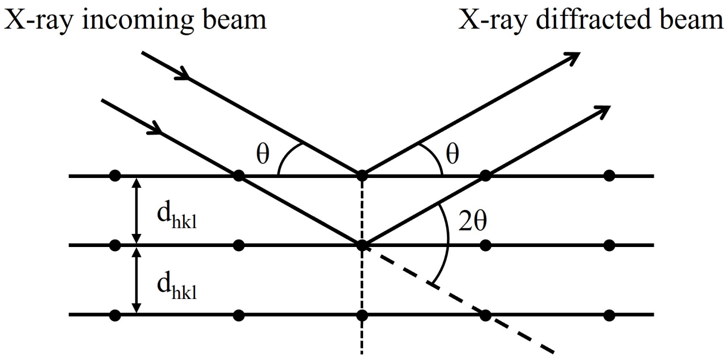

Figure 2.7 Schematic view of X-ray diffraction within a crystal lattice planes.

The condition for constructive diffraction is described by Bragg's Law:

$$n\lambda = 2d_{hkl}\sin\theta,$$

where n is the order of diffraction, λ is the wavelength of the incident X-rays, d_{hkl} is the lattice spacing corresponding to the Miller indices (hkl), and θ is the diffraction angle. In polycrystalline materials, diffraction occurs from multiple crystallographic planes that simultaneously satisfy the Bragg condition.

Each crystalline phase present in the sample generates a distinct diffraction pattern that is uniquely determined by its atomic arrangement and space group symmetry. Therefore, the analysis of these diffraction patterns enables qualitative phase identification of the material. In multiphase systems, the resulting diffraction pattern is a superposition of the individual phase patterns. For this reason, XRD is extensively used for phase identification through comparison with standard diffraction data or crystallographic databases. Furthermore, the relative intensities of the diffraction peaks associated with each phase are proportional to their respective concentrations in the sample, enabling quantitative phase analysis as well. Therefore, XRD are widely used both for qualitative and quantitative analysis.

XRD is a powerful technique not only for the identification of crystalline phases but also for the extraction of structural information, such as the average crystallite size.

In particular, the broadening of the diffraction peaks can be analyzed through peak fitting procedures to estimate the crystallite size D through the following equation, known as the Scherrer equation:

$$D = \frac{k\lambda}{FWHM \cos\theta}$$

where k is a dimensionless shape factor or Scherrer constant, λ is the wavelength of the incident X-rays, $FWHM$ is the full width at half maximum of the XRD peaks in radians, and θ is the diffraction angle.
This technique was applied to the characterization of inorganic pigment powders, specifically titanium dioxide and zinc oxide, to identify the crystalline phases present and estimate the average crystallite size. The structural information obtained through XRD provided valuable information on the photocatalytic activity of these oxides during the aging process.

2.6 Aging processes

During this Ph.D. research, four distinct accelerated aging processes were examined to investigate the stability of the selected synthetic organic pigments when combined with inorganic white pigments. These methods simulate stresses and conditions, including UV, UV-VIS or solar radiation, relative humidity, and temperature. In the following sections, the four aging processes developed and applied in this study will be described in detail, highlighting their specific conditions.

2.6.1 UV- and humidity-related aging

A custom-designed aging chamber was designed and built to simulate a UV- and humidity-related aging process, reported in Figure 2.8a. The aging chamber was equipped with four Philips Lighting TL 20W/12 RS SLV/25 UVB broadband lamps [26]. The emitted radiation was exclusively in the UV spectrum, ranging from 270 to 420 nm, with a peak intensity of around 320 nm within the "B" bandwidth of the UV spectrum. The lamps were arranged to ensure a uniform distribution of radiation via a custom-made holder.
The samples were subjected to UVB radiation for a total exposure duration of 665 hours. During the aging process, the samples were placed in two lines, exactly under the central lamps at a distance of 1.5 cm, as illustrated in Figure 2.8b. The total UV irradiance emitted was estimated through Keitz's formula [102, 103]:

$$E = \frac{I\cos^2\theta(\alpha + \sin\alpha\cos\alpha)}{\pi^2 hL}.$$

I is the UV flux of the lamp in Watt, h and L are the distance of the point P from the lamp and its length respectively, α is the half angle under which the source is observed in all its extension at the point P in radians, and θ is the angle orientation of the point P respect to the plane parallel to the lamp in radians, as schematically illustrated in Figure 2.8c. At this distance, the total UV irradiance emitted was 50.264 W/m^2, considering the contributions of all lamps. This measurement is in agreement with the data obtained using a ThorLabs S302C Thermal Power Sensor Head on the surface of the aging chamber.
The relative humidity inside the chamber was maintained within the range of 70-90% RH by employing a saturated solution of NaCl in distilled water [104, 105]. Both temperature and relative humidity were continuously monitored throughout the aging process using a Grove Temperature and Humidity Sensor DHT11. The sensor was

connected by Arduino hardware and software to a PC, providing data at regular intervals throughout the experiment. Based on the measurements, the average temperature was approximately 30°C, and the relative humidity was maintained within the range of 70-90%. This aging process was employed to evaluate preliminary variations and assess the response of the materials under UV- and humidity-related conditions.

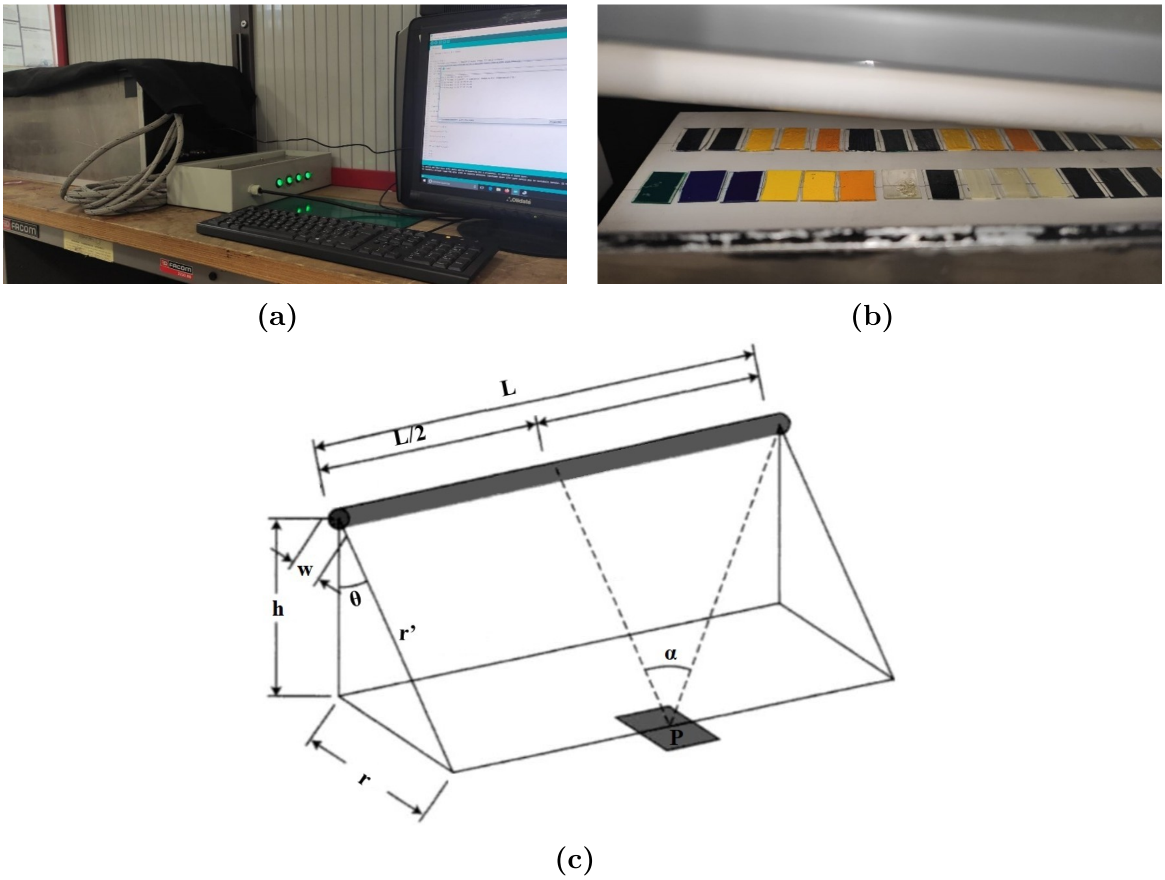

Figure 2.8 (a) Custom-designed aging chamber with PC monitoring. (b) A detailed view of samples under the UVB lamps before the aging process. (c) Schematic geometry for the radiance calculation system at point P used in the Keitz method.

2.6.2 UV-VIS artificial aging

The UV-VIS artificial aging process was conducted in a climate chamber under controlled conditions to simulate long-term material degradation. The chamber is an ACS Angelantoni climatic chamber (Model DY200C, Angelantoni Test Technologies Srl, Italy) with reflective walls, equipped with a high-power 125W Hg lamp. The lamp emits radiation in all directions, ranging from 220 nm to 630 nm, from the UV to the visible range. This radiation source is commonly employed for aging tests on paints,

plastics, rubbers, and other polymer-based products.
The irradiation measurements provided by the manufacturer in UVA, UVB, and UVC range, in contact with the lamp's quartz, are:
UVA - 430 W/m^2, UVB - 356 W/m^2, and UVC - 224 W/m^2.
The samples were exposed to high and controlled temperature and humidity conditions to accelerate aging, simulating environmental stress conditions. The temperature was set at 30°C, and the relative humidity was maintained between 60-70% RH.
Depending on the case study, the aging processes were carried out in the climatic chamber under controlled conditions with the samples positioned under the lamp to ensure uniform irradiation, as illustrated in Figure 2.9. Specifically, the aging processes were carried out under controlled conditions of radiation, temperature, and relative humidity, for a specific period: 30°C, 60%RH for 410 hours for yellow paint samples (Chapter 3); 30°C, 70% RH for three steps of 50 hours, for cobalt phthalocyanine powder samples (Chapter 4).
The use of the climatic chamber led to an improvement in the aging procedure, enabling a time-controlled mechanism that considers radiation, temperature, and humidity. Specifically, the implementation of a more powerful UV-VIS lamp, in comparison to the previous aging setup, combined with precise and consistent control over both temperature and relative humidity, ensures an accurate and reproducible aging simulation.

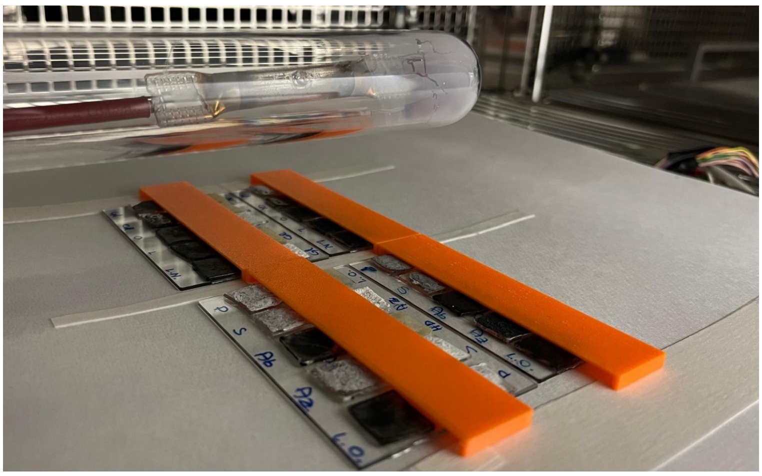

Figure 2.9 A detailed view of the samples positioned under the UV-VIS lamp inside the climatic chamber, before the artificial aging process.

2.6.3 Solar natural aging

The solar natural aging was performed exclusively on powder samples containing mixtures of organic and inorganic pigments (Chapter 4). Special attention was given to the design of the "solar box", which was constructed using a specific polymer transparent to most UV radiation from the sun. Specifically, a transparent UVD plexiglass with a thickness of 2 mm (Tomea Materie Plastiche Srl, Italy) and a high light transmittance above 300 nm was selected. The samples were placed inside the solar box with a custom-made support that ensured adequate spacing and prevented contamination between them during the process. As illustrated in Figure 2.10, half of the samples were covered to exclude the radiation component, providing unaged reference samples. The box was equipped with holes to allow airflow and prevent humidity condensation while ensuring the exclusion of external contaminants through the use of cotton.
All the samples were exposed to natural solar radiation for 40 days during the summer period, from 28 July to 6 September, in Rome (University of Roma Tre - 41°51'24''N latitude and 12°28'01''E longitude), with a southward orientation. The average temperature and relative humidity, measured both day and night, were 27°C and 67% RH, respectively, as recorded by the "atlante italiano della radiazione solare", an online service of ENEA [106].

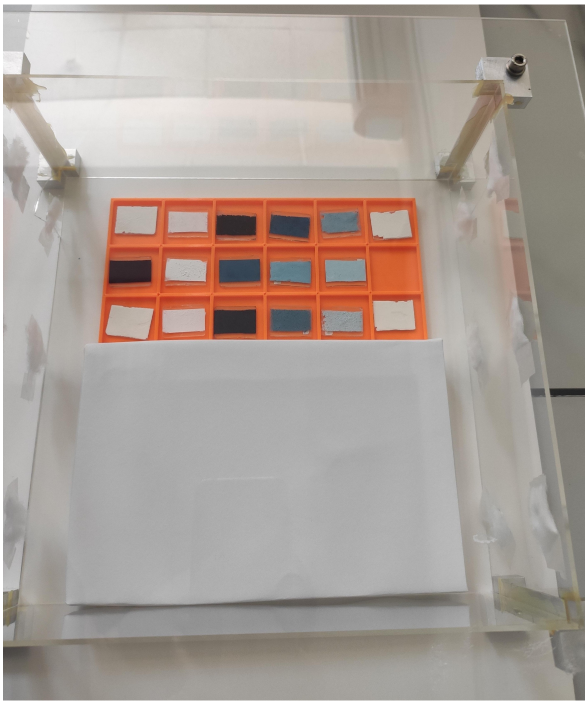

Figure 2.10 Powder samples exposed to natural solar aging inside the aging box, positioned on the custom-designed sample holder.

2.6.4 Solar simulator aging

The solar simulator aging was conducted in collaboration with Professor Andreas Ruediger's research group at INRS-EMT in Canada, where an advanced solar simulation system was employed to accelerate the aging process of powder samples (Chapter 4). In this experimental setup, the samples were directly exposed to irradiation for a total duration ranging between 50 and 100 hours. The solar simulator used is a SS50AAA 150-Watt Solar Simulator (Photo Emission Tech, Inc.), equipped with a Xenon Short Arc lamp. The device model is presented in Figure 2.11, showing also the touch screen panel used for controlling the lamp parameters. The total light irradiance on the samples was nominally of about 1000 W/m^2, corresponding to 1 sun, with an illuminated area of 50 mm $\times$ 50 mm. The solar simulator used in this study operates under the global solar irradiation standard AM 1.5 G, which simulates sunlight passing through the Earth's atmosphere at an oblique angle, similar to the Sun at approximately 48° from the zenith, typical of midday on a clear day in many temperate regions.
The high power output of the solar simulator provided valuable insights into the long-term photostability of a highly stable pigment, a cobalt phthalocyanine, in combination with titanium dioxide.

Figure 2.11 Solar simulator SS50AAA device used for the aging process, with the light intensity control panel.

Part II

3 Stability of monoazo and isoindoline yellows mixed with white pigments

This chapter presents the main results of the study on the stability of paints containing modern yellow pigments in interaction with inorganic white pigments.
The long-term stability and degradation mechanisms of synthetic organic pigments in combination with reactive white inorganic pigments represent a research topic of significant relevance in both materials science and cultural heritage conservation.
In particular, this study investigates the effect of UV-VIS radiation on the stability of two yellow synthetic organic pigments, commonly used in modern artistic practices, the monoazo pigment PY1 and the isoindoline pigment PY139. The effects of artificial aging were studied on three-component paint samples composed of a yellow pigment, linseed oil as a binder, and a white pigment, realized as simplified paint model samples to replicate the main components and interactions in artworks. Three inorganic white pigments were tested: lead white ($2PbCO_3{\cdot}Pb(OH)_2$), zinc white (ZnO), and titanium white (TiO_2). This study extends a preliminary work published in the *Acta IMEKO* journal to a deeper investigation into the interactions between organic and inorganic components in painted systems. Specifically, in this case, organic-inorganic mixed paint samples, rather than bilayer configurations, were prepared to promote greater interaction between the organic pigment and the inorganic compound. Indeed, the reactive inorganic pigments are frequently combined with colored synthetic and organic pigments, both in traditional paintings and in contemporary street art, where exposure to light and environmental factors can significantly impact the stability of pigments.
This study investigated the visible color changes induced by a UV-VIS aging process under controlled conditions. A multi-technique approach was employed to investigate the physical and chemical modifications occurring at the sample surfaces, selecting

methods with different sampling depths, including colorimetry, Fourier transform infrared spectroscopy in attenuated total reflectance mode (ATR-FTIR), micro-Raman spectroscopy (μ-RS), and time-of-flight secondary ion mass spectrometry (ToF-SIMS). The aging process was performed under controlled conditions, and the integration of a highly surface-sensitive technique like ToF-SIMS into the multi-technique approach enabled a detailed investigation of the degradation processes occurring at the surface of the samples.

The results obtained from ATR-FTIR and μ-RS support the hypothesis that light-induced degradation occurred on the samples in the presence of the inorganic whites, as evidenced by the decrease in the signal intensities of the binder and the yellow pigments. ToF-SIMS provided further insights, confirming the photodegradation of the yellow pigments related to the uppermost surface levels following the interaction with UV-VIS radiation, according to the different penetration depths characteristic of the employed techniques.

A key aspect of this work is the rapid color fading induced by the effective aging. Through the multi-technique approach, it was possible to understand these color variations as the degradation process affecting the organic pigments on the surface of the samples, due to the combined action of reactive white pigments and UV-VIS radiation. This work was published with the *Dyes and Pigments* journal. Supplementary materials are provided in Appendix A.

3.1 Materials and methods

3.1.1 Materials

Monoazo (commercial names: Studio Yellow, Pigment Yellow 1 - PY1, C.I. 11680) and isoindoline (commercial names: Isoindole Yellow-Orange, Pigment Yellow 139 - PY139, C.I. 56298) pigments have been selected for the aging process, both purchased by Kremer (Kremer Pigmente GmbH & Co. KG, Aichstetten, Germany) and labeled as PY. The three inorganic white pigments are labeled as W and provided by Sigma-Aldrich/Merck (Merk Life Science S.r.l. | Italy - Sigma-Aldrich) as standard materials: titanium dioxide (634662 - titanium (IV) oxide, a mixture of rutile and anatase in nanopowder form with <100nm particle size (BET), 99.5% trace metal basis), zinc oxide (96479 - zinc oxide, puriss. p.a., ACS reagent, ≥99.0% (KT)), and basic lead carbonate (243582 - lead (II) carbonate basic -325 mesh). The whites have been used in interaction as a mixture with the yellows, using linseed oil (Linseed oil, cold-pressed, #73054) by Kremer (Kremer Pigmente GmbH & Co. KG, Aichstetten, Germany) as a binder for the formulation of samples. The materials and their classifications are shown in Figure 3.1a.

3.1.2 Samples preparation

In order to have reference samples to be compared with the different multi-component paintings, three typologies of samples were prepared as follows (see also Table 3.1):

1. Reference samples of pure materials: solo yellow pigment powders (PY), solo white pigment powders (W), and solo linseed oil (oil), prepared through isopropyl alcohol deposition [13] (6 samples).
2. Reference samples of two-component paint for each yellow (PY + oil) and the inorganic pigments (W + oil), with a binder-to-powder mass ratio of 1:2; the paints obtained were cast on glass slides, creating a homogeneous layer by doctor blade method [107], obtaining quite homogeneous film of about 1 mm (5 samples).
3. Main samples of three-component paint (PY + W + oil) were obtained through the same method and binder-to-powder mass ratio as above; for each combination, two mass ratios between the pigments (PY:W) were tested: 1:10 and 1:100 (6+6 samples).

All the paint samples were dried at room conditions for 1 month. The resulting thickness of each sample was estimated to be around 1 mm. During the aging process, half of each prepared sample was covered by an aluminum foil to obtain a reference for the unaged parts. The schematic representation of the sample preparation is reported in Figure 3.1b.

Table 3.1 Description of the samples with the corresponding labels used for their identification. The samples are categorized as reference pure materials, binary mixtures of single yellow or white pigments in oil, and ternary mixtures combining yellow and white pigments in oil. The white pigments are abbreviated as Pb (lead white), Zn (zinc white), and Ti (titanium white). For ternary mixtures, the two mass ratios between the yellow pigment and white pigment (PY:W) are shown; in these cases, the oil component is implicit and omitted from the labels.

	Reference pure materials	**Binary mixtures PY/W + oil**	**Ternary mixtures PY + W + oil**	
			PY:W 1:10	**PY:W 1:100**
PY	PY1	PY1 + oil	PY1 + Pb 1:10 PY1 + Zn 1:10 PY1 + Ti 1:10	PY1 + Pb 1:100 PY1 + Zn 1:100 PY1 + Ti 1:100
	PY139	PY139 + oil	PY139 + Pb 1:10 PY139 + Zn 1:10 PY139 + Ti 1:10	PY139 + Pb 1:100 PY139 + Zn 1:100 PY139 + Ti 1:100
W	$2PbCO_3 \cdot Pb(OH)_2$	Pb + oil		
	ZnO	Zn + oil		
	TiO_2	Ti + oil		
Oil	Oil			
Tot	6	5	6	6

3.1.3 Accelerated aging

All the samples were exposed to an accelerated aging process in an ACS Angelantoni climatic chamber (Model DY200C, Angelantoni Test Technologies S.r.l., Italy) equipped with a 125W Hg lamp (see Chapter 2.6.2). As reported by the manufacturer, the aging lamp has a spectrum extending from ultraviolet to visible, with emission from 220 nm to 630 nm (Figure A.1), commonly used for aging tests on paints, plastic materials, rubber, etc. The aging process was conducted under controlled conditions of radiation, temperature, and relative humidity, for a specific period: 30°C, 60% RH for 410 hours. The schematic representation of the aging process is reported in Figure 3.1c.

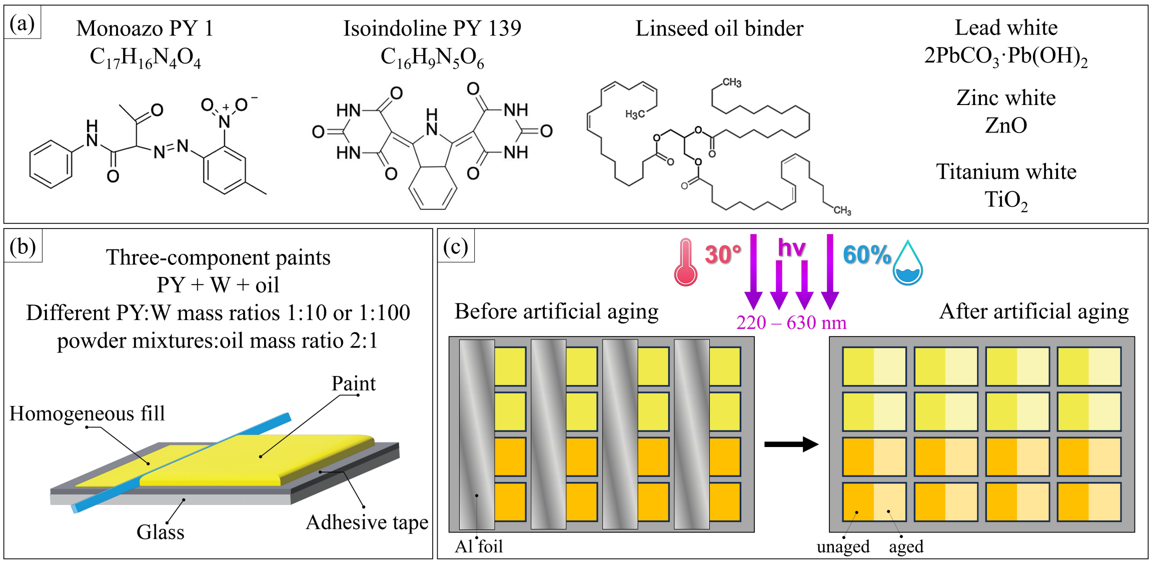

Figure 3.1 Schematic representation of materials and methods considered in our experiments. (a) Pure compounds used to obtain the samples: formulas and molecular structures of yellow organic pigments PY1 and PY139, linseed oil binder with its main component fatty acids, and inorganic white pigments of basic lead carbonate, zinc oxide, and titanium dioxide with their respective chemical formulas. (b) Sample preparation of the three-component paints deposited on glass support through the doctor-blade technique. (c) Artificial aging process-controlled parameters (temperature and relative humidity) and the resulting two unaged and aged halves of the samples.

3.1.4 Methods

Stereomicroscope. High-definition images were acquired with a Leica EZ4 Digital Stereo Microscope (Leica Microsystems S.r.l., Milan, Italy) integrated with a 5-megapixel HD camera. The microscope has a 4.4:1 zoom, with a magnification range from 8x to 35x, and 7-way LED illumination. The samples were photographed with 35x magnification and radial LED lighting and collected with LAS EZ software 3.0 (Leica Microsystems S.r.l., Milan, Italy).

Colorimetry. Colorimetry was performed with an Eoptis CLM-194 portable digital tristimulus colorimeter (Eoptis S.r.l., Trento, Italy) using a standard D65 daylight illuminant and 10° standard observer. Sample geometry and measurement area were kept fixed at 45° and 10 mm, respectively. Data were measured in the CIE 1976 L*a*b* color space with CLM-19X software licensed by Eoptis S.r.l. The colorimetric coordinates L*a*b* were calculated as the average of 5 measurements acquired for each sample, obtaining the standard deviation. The total color change ΔE between the unaged and aged parts of the samples was calculated according to the CIELAB equation:

$$\Delta E = \sqrt{(\Delta L^*)^2 + (\Delta b^*)^2 + (\Delta a^*)^2}. \tag{3.1}$$

Fourier-Transformed Infrared Spectroscopy. Fourier-Transformed Infrared Spectroscopy in ATR mode was carried out with a Thermo Scientific™ Nicolet™ iS50 FTIR Spectrometer (Thermo Fisher Scientific, Waltham, MA, USA), coupled with a DTGS ATR detector. The ATR module is equipped with a built-in, all-reflective diamond crystal with a 45° incident beam, and a KBr beamsplitter in the MID-IR spectral range and a solid substrate beamsplitter in the FAR-IR spectral range. The spectra were acquired in the range of 4000 a 450 cm^{-1}, for the MID-IR range, and 1800-100 cm^{-1}, for the FAR-IR range, performing a total of 120 scans with a spectral resolution of 4 cm^{-1}. The optical velocity and optical aperture were fixed at 0.4747 cm/s and 150, respectively. Several spectra were acquired for each sample at different random points. IR spectra were collected and elaborated with OMNIC™ software 6.0 (Thermo Fisher Scientific, Waltham, MA, USA), for acquisition, subtraction of the contribution of CO_2, mathematical average of different spectra, and baseline correction, and graphed with OriginPro® 2023 software (OriginLab Corporation, Northampton, MA, USA).

Micro-Raman Spectroscopy. A ®Renishaw Raman InVia Qontor micro-Spectrometer (Renishaw plc, Wotton-under-Edge, UK), equipped with a CCD detector (10240×256 pixels, Peltier cooled cells at -70°C) and with a high pass Edge filter, was employed. Analyses were performed in backscattered configuration under a Leica DM 2700 M confocal microscope. A diode laser in the near IR region with a wavelength of 785 nm and a nominal output power of 180 mW was used since the investigation of the samples with the laser at 532 nm caused fluorescence. The spectra were acquired at room temperature both in extended and static mode, with a nominal spectral resolution of about 1 cm^{-1}, by using a long working distance 50× objective, providing a laser spot size of about 2 μm^2. The laser power was filtered at about 0.5-50% of the output power by using neutral density (ND) absorptive filters. In extended mode, the spectra were acquired in the 100-3800 cm^{-1} spectral range, setting the laser power at 18 mW for the samples with PY1 and 0.9 mW for the samples with PY139, with an integration time of 10 seconds, and 5 accumulations. In static mode, the spectra were acquired by selecting a limited spectral range centered on the fingerprint region, to enhance spectral resolution and signal intensity, setting the laser power at 90 mW, with an integration time of 1 second, and 100 accumulations. Using the static acquisition mode, a semi-quantitative analysis was performed on the three-component samples. The percentage variation in the signal intensity of the yellow pigments before and after the aging process was calculated according to the following equation:

$$\%A = \frac{A_u - A_a}{Au} \times 100 \tag{3.2}$$

Where A_u and A_a represent the area under selected Raman bands (specifically, the most intense bands for the yellow pigments, at 1623 cm^{-1} for PY1 and 1564 cm^{-1} for PY139), calculated by a fitting procedure for the unaged and aged spectra, respectively. A preliminary investigation was carried out to verify homogeneity over the sample surface by exploring the Raman response. Afterward, at least three acquisitions were obtained randomly for each sample, and a representative one was here reported. Raman spectra were collected and elaborated with WiRE software 5.6 licensed by Renishaw, for measurement set-up, acquisition, subtraction of systematic errors (i.e., cosmic rays), and baseline correction. Data fitting and graphing were performed using OriginPro® 2023 software (OriginLab Corporation, Northampton, MA, USA).

Time-of-Flight Secondary Ion Mass Spectrometry. Ion bombardment mass spectrometry was performed using a TOF.SIMS$_5$ (ION-TOF GmbH, Münster, Germany) secondary ion mass spectrometer, equipped with bismuth Bi LMIG (liquid metal ion gun) and cesium Cs^+ ion sputter gun. Static surface analysis data were acquired, both in positive and negative polarity, using Bi_3^{++} gun (60 keV) with a pulse width of 18.4 ns and a current emission of 0.35 pA. The surface areas were analyzed in random mode, acquiring 256×256 pixels, and selecting a field of view (FoV) of 500×500 μm^2. Depth profiling measurements were performed in dual-beam mode using Bi_3^{++} as primary gun and Cs^+ (3 keV, current of about 155 nA) as sputter beam. The analysis area (250×250 μm^2) was set at the center of the sputter region (400×400 μm^2). Secondary ions were extracted at 2 kV and detected with a ToF mass analyzer with a cycle time of 150 μs [(1÷1000) m/z mass range]. Charge compensation was achieved using low-energy electrons (20 eV) with the electron flood gun. Mass spectra were user-calibrated using H^+, H_2^+, C^+, CH^+, CH_2^+, CH_3^+, and $Ti^+/Zn^+/Pb^+$ in positive ion mode and H^-, H_2^-, C^-, CH^-, CH_2^-, CH_3^-, O^-, OH^-, and $TiO^-/ZnO^-/PbO^-$ in negative mode. The analysis was repeated at least three times on different areas for each sample. All ToF-SIMS data were acquired, calibrated, normalized, and processed using SurfaceLab 6.5 software (ION-TOF GmbH, Munster, Germany). Specifically, the mass spectra were normalized to total counts and graphed with OriginPro® 2023 software (OriginLab Corporation, Northampton, MA, USA), and the chemical maps were normalized to the total ion image to reduce possible topographic effects.

X-Ray Diffraction. XRD analyses were carried out to study the crystalline structure and phase composition of the pure inorganic white pigments. A Rigaku Geiger-Flex

X-ray diffractometer (Rigaku Holdings Corporation, Tokyo, Japan) with a Co Kα radiation (1.7902 Å), current range 0-30 mA, and voltage 30 kV was used. The crystallite size D was calculated with the Scherrer equation:

$$D = \frac{k \cdot \lambda}{FWHM \cdot \cos\theta} \tag{3.3}$$

where k is the shape factor 0.94 for spherical crystallites, λ the X-ray wavelength (1.7902 Å), θ the Bragg angle, and FWHM the full width at half maximum calculated by a fit procedure of the main peaks with OriginPro® 2023 software (OriginLab Corporation, Northampton, MA, USA). Phase identification and quantification were performed with Profex 5.4.1 software [108] using Rietveld XRD powder refinement.

Scanning Electron Microscopy. SEM analysis was conducted to investigate the surface morphology of the white powder pigments using a Sigma 300 Carl Zeiss microscope (ZEISS AG, Oberkochen, Germany) under high vacuum conditions (10^{-6}–10^{-7} mbar) with a secondary electron detector at a 3 keV accelerating voltage and a working distance of 6mm. Dispersions of a few milligrams of white pigment in 1.5 mL of distilled water were prepared, sonicated for 10 minutes, drop-cast onto pure silicon substrates, and left to dry. The dried powders were then gold-coated with a thickness of 20 nm before SEM analysis.

Stylus Profiler. Topographic maps were acquired with a KLA-Tencor® P-7 Stylus Profiler (KLA Corporation, CA, USA), using a constant force of 0.50 mg, a scan speed of 10 μm/s, and a sampling rate of 200 Hz, with Profiler 7.45 software (KLA Corporation, CA, USA).

3.2 Results

3.2.1 Pure materials characterization

The pure materials characterization through a multi-technique approach enabled an in-depth investigation of the selected pigments and binder, but above all, supported the identification and interpretation of potential chemical variations, degradation pathways, and physical modifications that may occur due to the artificial aging process. Such information was fundamental to evaluating modern pigments' stability in complex, multi-component samples.

ATR-FTIR

The characterization analyses of the two yellow pigments, three inorganic whites, and linseed oil with ATR-FTIR spectroscopy are reported.
The ATR-FTIR spectrum of the monoazo PY1 is illustrated in Figure 3.2 in the wavenumber range of 4000-450 cm^{-1}.

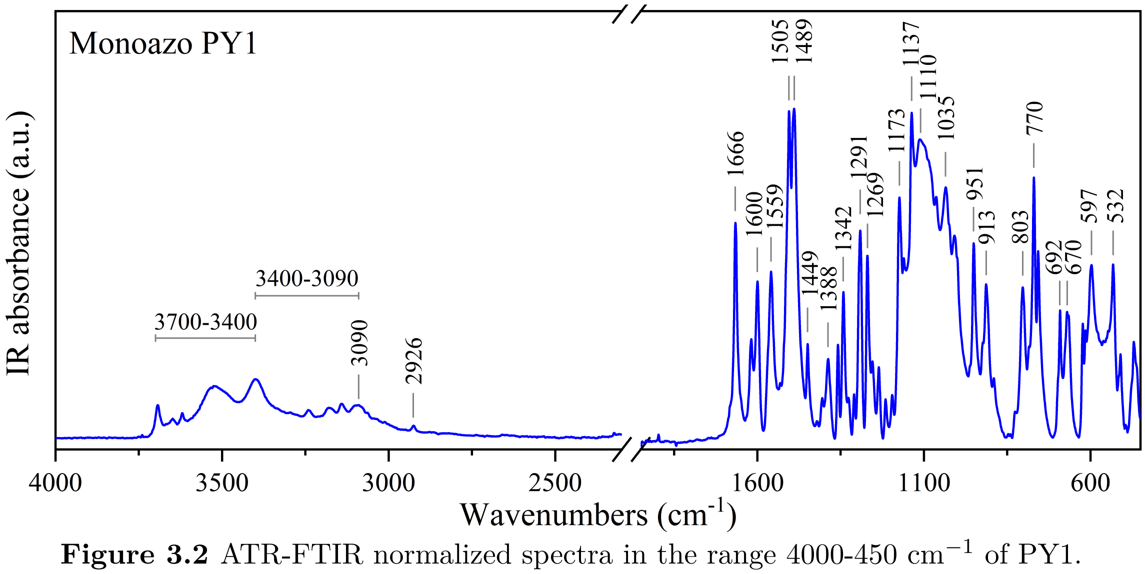

Figure 3.2 ATR-FTIR normalized spectra in the range 4000-450 cm^{-1} of PY1.

The monoazo pigment PY1 exhibits several characteristic bands in the FTIR spectrum. In the functional groups region (4000-2300 cm^{-1}), broad and weak bands of the O-H stretching vibrations within the 3700-3400 cm^{-1} range, signals of the N-H stretching in the amide group between 3400-3090 cm^{-1}, C-H stretching signals at 3090 cm^{-1} in the aromatic ring and 2926 cm^{-1} in the methyl substituent, are identified. Moreover, numerous intense and sharp peaks characterize the fingerprint region (1800-450 cm^{-1}).

Very intense peaks are identified in the spectrum at 1505, 1489, 1137, and 1110 cm^{-1}. The signals at 1505 and 1489 cm^{-1} are indicative of the contribution of C=C stretching in the aromatic ring and C-N stretching, and the skeletal vibrations of the benzene ring, respectively. The other two intense peaks are both associated with the C-N stretching and C-H bending out-of-plane vibrations. The stretching vibrations of double bonds C=O and C=C in conjugated aromatic rings are observed at 1666 and 1600 cm^{-1}, respectively. The N=N stretching in the azo group is detected at 1559 cm^{-1}, thereby confirming the presence of the azo-chromophore in the PY1 structure. Furthermore, C-H in-plane bending vibrations are observed at 1449 cm^{-1}. The substituents present within the aromatic ring of the pigment are identified in the signals recorded at 1388 cm^{-1} of the C-H bending in methyl group and at 1342 cm^{-1} of the N=O symmetric stretching mode in nitro substituent. The strong bands observed at 1291 and 1269 cm^{-1} are attributed to a combination of C-N stretching and C-H bending vibrations, while the band at 1173 cm^{-1} corresponds to additional C-N stretching, and the band at 1035 cm^{-1} is attributed to C-H stretching vibrations. At low wavenumbers, bending modes of C-H deformations are observed, as evidenced by the bands observed at 951, 913, 692, and 670 cm^{-1}, corresponding to C-H out-of-plane bending in the substituted aromatic ring. Additional out-of-plane modes are identified at 803 and 770 cm^{-1} for specific substitutions in para- and ortho-position, respectively. The bands at 597 and 532 cm^{-1} are attributed to C-H rocking in methyl and aromatic groups.

The ATR-FTIR spectrum of the isoindoline PY139 is illustrated in Figure 3.3 in the wavenumber range of 4000-450 cm^{-1}.

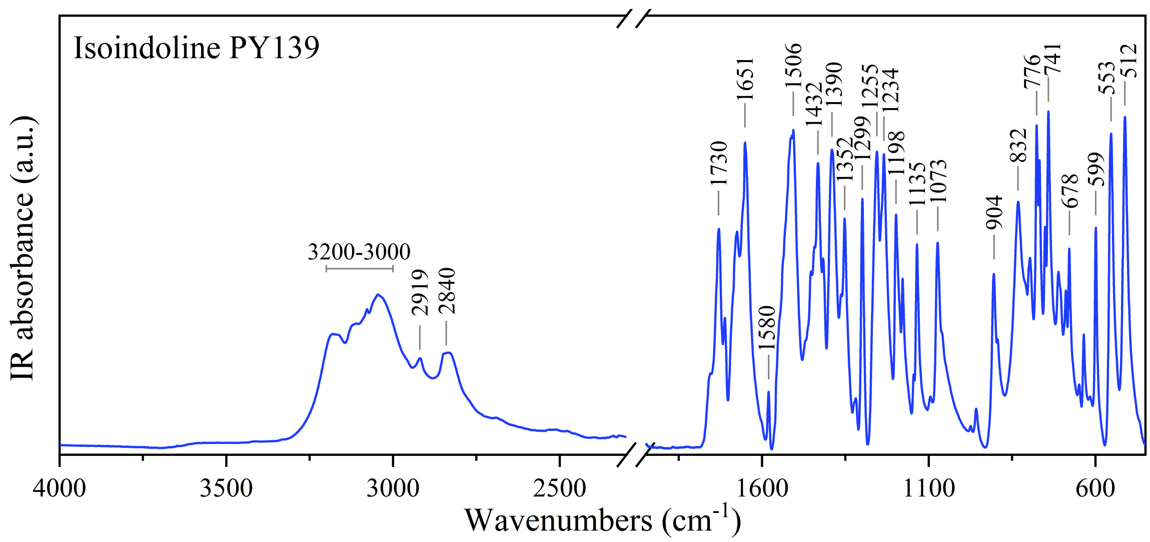

Figure 3.3 ATR-FTIR normalized spectra in the range 4000-450 cm^{-1} of PY139.

The infrared spectrum of the isoindoline pigment PY139 reveals characteristic vibrational modes associated with its molecular structure. In particular, in the region of functional groups, the broad bands between 3200 and 3000 cm^{-1} are attributed to N-H stretching vibrations, which are characteristic of amide groups. Furthermore, weaker bands observed at 2919 and 2840 cm^{-1} correspond to the asymmetric and symmetric stretching of C-H bonds, respectively. In the high-wavenumber fingerprint region, spectroscopic vibrations due to double bonds present in the pigment at 1730, 1651, and 1580 cm^{-1} are observed. These signals are attributed to the stretching vibration of the unconjugated C=O groups, the conjugated C=O stretching, and the -C=C stretching vibrations within the aromatic rings. Intense bands at 1506, 1432, 1390, and 1352 cm^{-1} are identified as indicators of in-plane C-H bending deformations in aromatic rings. The spectral region between 1300 and 1000 cm^{-1} exhibits several strong bands related to the C-N stretching vibrations within the amide groups of the pigment. Specifically, these signals are observed at 1299, 1255, 1234, 1135, 1073, and 1198 cm^{-1}. The peak at 1255 cm^{-1} may also include contributions from N-H bending vibrations. Out-of-plane bending vibrations are observed in the region below 1000 cm^{-1}. The bands at 904, 832, 776, 741, and 678 cm^{-1} are attributed to out-of-plane C-H bending in the aromatic rings. The bands at 599, 553, and 512 cm^{-1} are assigned to out-of-plane C-N bending vibrations.

The characteristic signals of the two yellow pigments were characterized according to the existing literature and databases [42, 109–112]. The main IR vibrational modes of these pigments with their assignments are summarized in Tables 3.2 and 3.3, for the monoazo PY1 and isoindoline PY139, respectively.

Table 3.2 Assignment of the main IR bands for monoazo PY1.

Wavenumber (cm^{-1})[a]	**IR assignment**[b]
3700-3400 (w)	ν(O–H)
3400-3090 (w)	ν(N–H) in amide group
3090 (w)	ν(C–H) aromatic ring
2926 (vw)	ν_s(C–H) in methyl substituent
1666 (s)	ν(C=O)
1600 (m)	ν(C=C) in conjugated aromatic rings
1559 (m)	ν(–N=N–) in azo group
1505 (vs)	ν(C=C) in aromatic ring / ν(C–N)
1489 (vs)	benzene ring skeleton
1449 (w)	δ(C–H) in-plane
1388 (w)	δ(C–H) in methyl substituent
1342 (m)	ν_s(N=O) in nitro substituent
1291 (s) 1269 (s)	ν(C–N) / δ(C–H)
1173 (s)	ν(C–N)
1137 (vs) 1110 (vs)	ν(C–N) / δ(C–H) out-of-plane
1035 (s)	ν(C–H) aliphatic/aromatic
951 (s) 913 (m)	δ(C–H) out-of-plane in substituted aromatic ring
803 (m)	δ(C–H) out-of-plane in methyl para-substituted
770 (s)	δ(C–H) out-of-plane in nitro ortho-substituted
692 (m) 670 (m)	δ(C–H) out-of-plane in substituted aromatic ring
597 (m) 532 (m)	ρ(C–H) in methyl and aromatic groups

[a] Relative intensities - very strong (vs), strong (s), medium (m), weak (w), very weak (vw).
[b] Types of vibrations - ν: stretching, δ: bending, ρ: rocking, $_s$: symmetric.

Table 3.3 Assignment of the main IR bands for isoindoline PY139.

Wavenumber (cm^{-1})[a]	**IR assignment[b]**
3200-3000 (m)	ν(N–H)
2919 (w)	ν_{as}(C–H)
2840 (w)	ν_s(C–H)
1730 (m)	ν(C=O) unconjugated
1651 (s)	ν(C=O) conjugated
1580 (vw)	ν(–C=C) in aromatic rings
1506 (vs) 1432 (s) 1390 (s) 1352 (m)	δ(C–H) in-plane in aromatic rings
1299 (s)	ν(C–N) in amide groups
1255 (s) 1234 (s)	ν(C–N) in amide groups / δ(N–H)
1198 (m) 1135 (m) 1073 (m)	ν(C–N) in amide groups
904 (m) 832 (s) 776 (vs) 741 (vs) 678 (m)	δ(C–H) out-of-plane in aromatic rings
599 (m) 553 (s) 512 (vs)	δ(C–N) out-of-plane

[a] Relative intensities - very strong (vs), strong (s), medium (m), weak (w).
[b] Types of vibrations - ν: stretching, δ: bending, $_s$: symmetric, $_{as}$: asymmetric.

The ATR-FTIR spectrum of lead white $2PbCO_3{\cdot}Pb(OH)_2$ is dominated by its characteristic absorption signals in the fingerprint spectral region 1800-250 cm^{-1}, as illustrated in Figure 3.4.

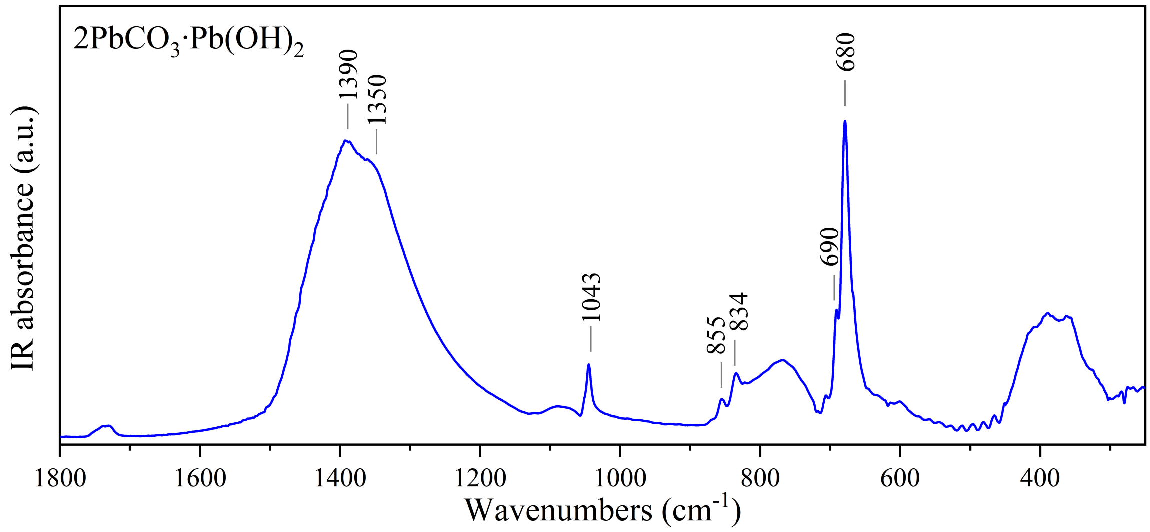

Figure 3.4 ATR-FTIR normalized spectrum in the range 1800-250 cm^{-1} of lead carbonate basic.

According to the literature [113–115], the infrared signals associated with the carbonate group $CO_3{}^{2-}$ exhibit several characteristic signals that are crucial for its identification of lead white in spectroscopic analysis. Specifically, the asymmetric C-O stretching vibrations $\nu_{as}(CO_3{}^{2-})$ appear as a prominent band in the range 1390-1350 cm^{-1}. The symmetric stretching $\nu_s(CO_3{}^{2-})$, give rise to a sharp and well-defined peak at 1043 cm^{-1}, contributing to the distinct spectral fingerprint of the carbonate group. The peaks at 855-834 cm^{-1} are attributable to the out-of-plane bending mode $\delta(CO_3{}^{2-})$, while the intense peak at 680 cm^{-1} is attributable to the out-of-plane rocking bending $\rho(CO_3{}^{2-})$, accompanied by a small shoulder at 690 cm^{-1}. Furthermore, in the high-wavenumber region of the spectrum (not shown), a sharp signal of the hydroxyl stretching vibrations $\nu(OH)$ is observed at 3537 cm^{-1}, which may be associated with hydrated carbonate species.

Titanium dioxide exhibits a distinctive FTIR band within the 380-800 cm^{-1} spectral range, as displayed in Figure 3.5. The extensive band in the spectrum indicates the lattice vibrations of TiO_2 [116], yet no further insights into the crystalline phases can be derived. In addition, no notable absorption signals are discerned above 800 cm^{-1}.

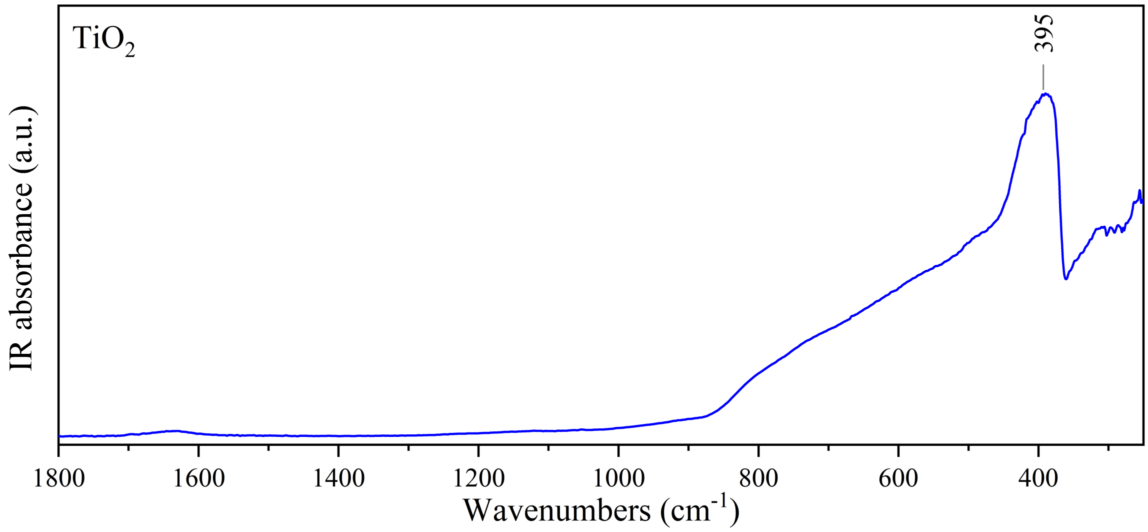

Figure 3.5 ATR-FTIR normalized spectrum in the range 1800-250 cm^{-1} of titanium dioxide.

Zinc oxide exhibits a single broad FTIR band in the 600-250 cm^{-1} spectral range, as shown in Figure 3.6. The low-frequency band in the spectrum is attributed to Zn-O stretching vibrations and serves as a distinctive marker for the inorganic compound ZnO. Additionally, no other significant bands are present above 600 cm^{-1}.

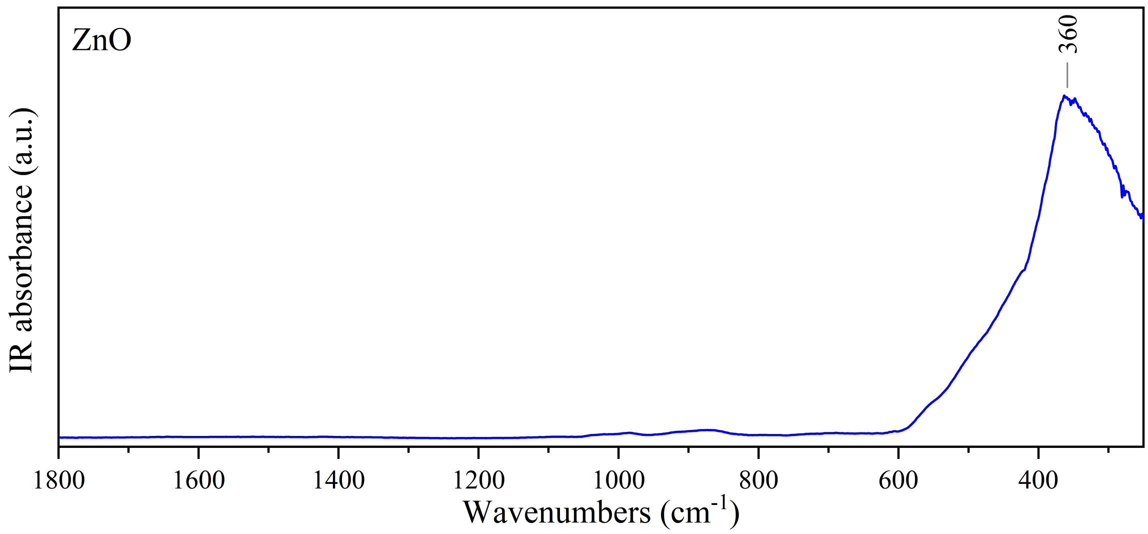

Figure 3.6 ATR-FTIR normalized spectrum in the range 1800-250 cm^{-1} of zinc oxide.

Linseed oil was characterized in fresh and dried forms, as illustrated in Figure 3.7. All the observed FTIR drying variations are consistent with the curing of linseed oil, involving oxidation, polymerization, and isomerization processes.

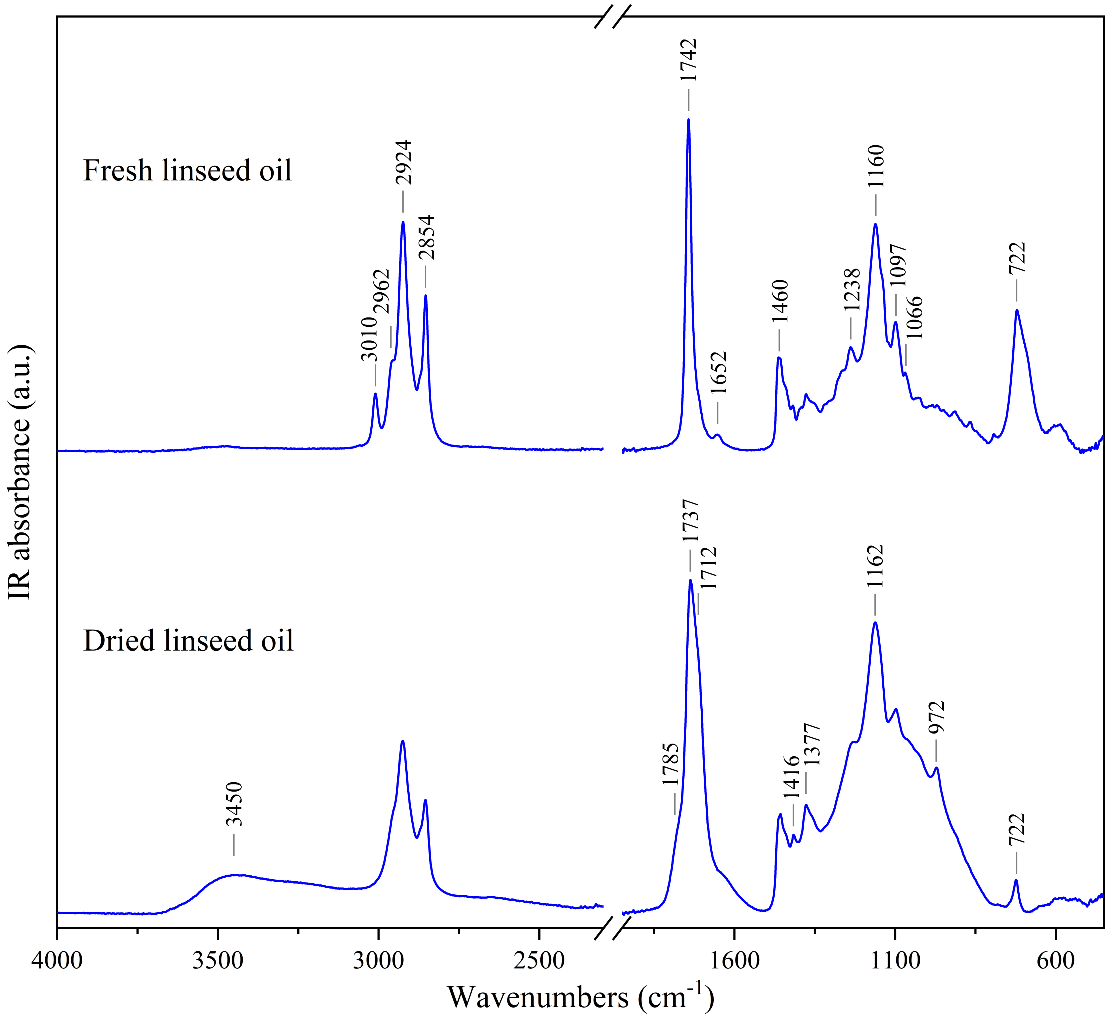

Figure 3.7 ATR-FTIR normalized spectra in the range 4000-450 cm^{-1} of the fresh (top) and dried (bottom) linseed oil.

The broad band observed at approximately 3450 cm^{-1} is attributed to the OH stretching vibrations. This band is absent in the spectrum of fresh oil but appears in the spectrum of dried oil as a result of oxidation occurring during the drying process. The band at 3010 cm^{-1} corresponds to the C-H stretching of *cis* double bonds in unsaturated fatty acids. The total decrease of this band during drying is a key indicator of the isomerization process, whereby the *cis* double bonds in the fresh oil are converted into *trans* configurations in the dried one or are involved in other chemical reactions. Additional bands related to C-H stretching are observed at 2962 cm^{-1} (asymmetric

in CH_3), 2924 cm^{-1} (asymmetric in CH_2), and 2854 cm^{-1} (symmetric in CH_2). The decrease in intensity of these bands during the drying process indicates hydrocarbon loss resulting from chain cleavage reactions that generate volatile oxidation products. In the spectral region below 2000 cm^{-1}, the most intense peak corresponds to the C=O stretching vibrations. This peak, originally located at 1742 cm^{-1}, shifts slightly to 1737 cm^{-1} and shows a broadening effect. The variations in this carbonyl band are further influenced by the formation of shoulders at 1785 cm^{-1}, attributed to ν(C=O) vibrations in secondary oxidation products, and at 1712 cm^{-1}, associated with ν(C=O) vibrations in carboxylic acid products. A small band observed at 1652 cm^{-1} is attributed to the *cis* -HC=CH- stretching vibrations of double bonds. As with the other oil *cis* double bond signals, this band decreases after drying due to the isomerization process. The signal at 1460 cm^{-1} is related to the C-H bending deformation in the methylene and methyl groups. After drying, a slight increase in its intensity is noted, likely reflecting the polymerization and cross-linking of fatty acid chains. Two small signals present at 1416 and 1377 cm^{-1} are attributed to different phenomena: the stretching of C-O bonds in carboxylic acid products (COOH) and the wagging of the methyl groups, respectively. These signals, although very weak in fresh oil, show an increase in intensity upon drying. Furthermore, characteristic C-O stretching vibrations associated with triglyceride ester linkages are identified through peaks at 1238, 1160, 1097, and 1066 cm^{-1}. Although the peaks of this C-O pattern appear to lose definition following the drying of the oil, the observed increase in intensity suggests the oxidative polymerization of the fatty acids. The formation of a small signal at 972 cm^{-1} and the strong decrease of the signal at 722 cm^{-1} during the drying process provide additional evidence of the isomerization process. Indeed, the signals correspond to the out-of-plane deformation of C-H bonds present in unconjugated *trans* and *cis* double bonds, respectively. These spectral changes reflect structural modifications that confirm the conversion from *cis* to *trans* configuration during the drying process.
The assignments of the main characteristic bands and their variations during the oil drying are summarized in Table 3.4, according to the literature [86, 117–119].

Table 3.4 Assignments of the main IR signals for linseed oil with the respective intensity variations observed due to the oil drying.

Wavenumbers (cm^{-1})	**IR assignment**[a]	**Drying variations**
~ 3450	ν(OH)	Formation
3010	*cis* ν(C–H) in C=C–H	Disappear
2962	ν_{as}(C–H) in CH_3	Decrease
2924	ν_{as}(C–H) in CH_2	Decrease
2854	ν_s(C–H) in CH_2	Decrease
1742	ν(C=O)	Shift/broadening
1652	*cis* ν(C=C) in -HC=CH-	Decrease/shoulder
1460	δ(CH) in CH_2, CH_3	Increase slightly
1416	ν(C-O) in COOH	Increase
1377	$\omega(CH_2)$	Increase
1238 1160 1097 1066	ν(C–O)	Increase
972	*trans* δ(C-H) in C=C–H	Formation
722	*cis* δ(C–H) in C=C–H	Decrease

[a] Types of vibrations - ν: stretching, δ: bending, ω: wagging, $_s$: symmetric, $_{as}$: asymmetric.

Raman

The characterization analyses of the two yellow pigments, three inorganic whites, and linseed oil using Raman spectroscopy are presented.
The monoazo yellow pigment PY1 exhibits a complex Raman spectrum in the wavenumber range 100-1800 cm^{-1}, as illustrated in Figure 3.8.

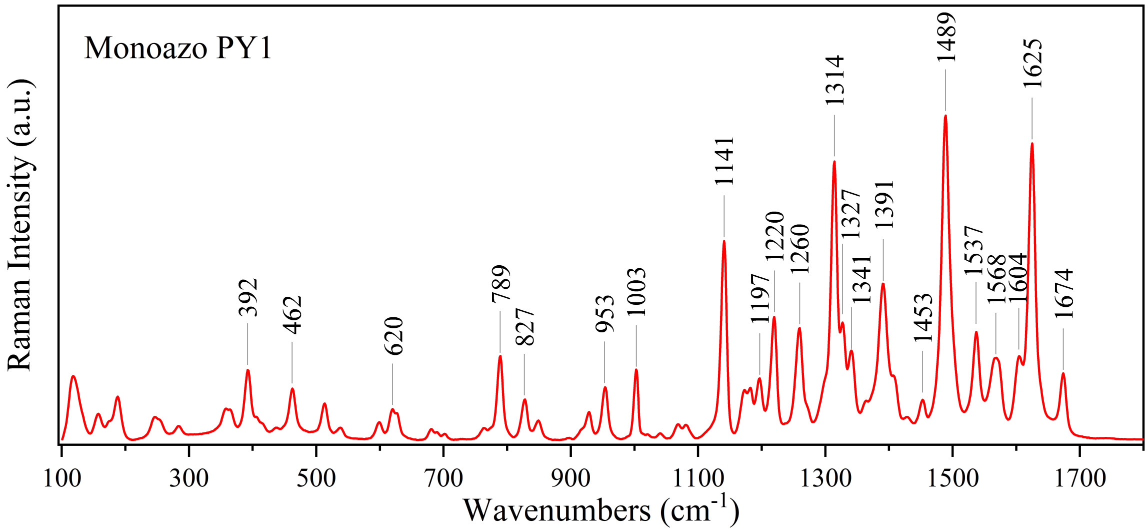

Figure 3.8 Raman normalized spectra in the wavenumber range 100-1800 cm^{-1} of PY1.

Four bands with very strong intensity were observed at 1141 cm^{-1}, 1314 cm^{-1}, 1489 cm^{-1}, and 1625 cm^{-1}. These bands are assigned to the C-N symmetric stretching, the aromatic nitro group modes, the azobenzene ring, and the nitro asymmetric stretching, respectively. The azo chromophore of the pigment is identified by the N=N stretching signal at 1391 $^{-1}$. The bands of the benzenamide vibrations at 953 cm^{-1} (resulting from amide group attached to benzene ring), the amide III band at 1260 cm^{-1}, and the amide I band at 1674 cm^{-1}, are observed. The bands designated as "amide" are characteristic Raman vibrations associated with amide groups within a molecule. An amide group is a functional group constituted by the combination of a carbon atom bonded to an oxygen atom (-C=O) and a nitrogen atom (N-H). Specifically, amide I band is attributed to the C=O stretching vibration influenced by the amide group, amide II band results from C-N stretching with contribution from N-H bending, and amide III band corresponds to the N-H bending with a contribution from C-N stretching. Furthermore, the Raman spectrum of the pigment contains evidence of vibrations attributable to the nitro substituent in the aromatic ring. These vibrations are consistent with the NO_2 aromatic stretching vibrations at 1314-1327-1341 cm^{-1}, the aromatic asymmetric stretching vibrations at 1568 cm^{-1}, and the aromatic scissoring modes at 827 cm^{-1}. The other substituent in the aromatic ring exhibits vibrations at 1453 cm^{-1}, attributed to the C-H deformation of the CH_3 group. Other typical Raman bands attributed to the benzene skeletal vibrations at 392 cm^{-1}, to the C=O bending vibrations at 462 cm^{-1}, to the aromatic C-C ring deformations at 620 cm^{-1}, to the aromatic C-H out-of-plane bending at 789 cm^{-1}, to the benzene ring breathing mode at 1003 cm^{-1}, to the C-N symmetric bending at 1197 and 1220 cm^{-1}, and to the aromatic C=C vibrations in benzene ring at 1537 and 1604 cm^{-1}, were observed. Regarding the isoindoline pigment PY139, the Raman spectrum shows characteristic features in the wavenumber range 100-1800 cm^{-1}, as illustrated in Figure 3.9.

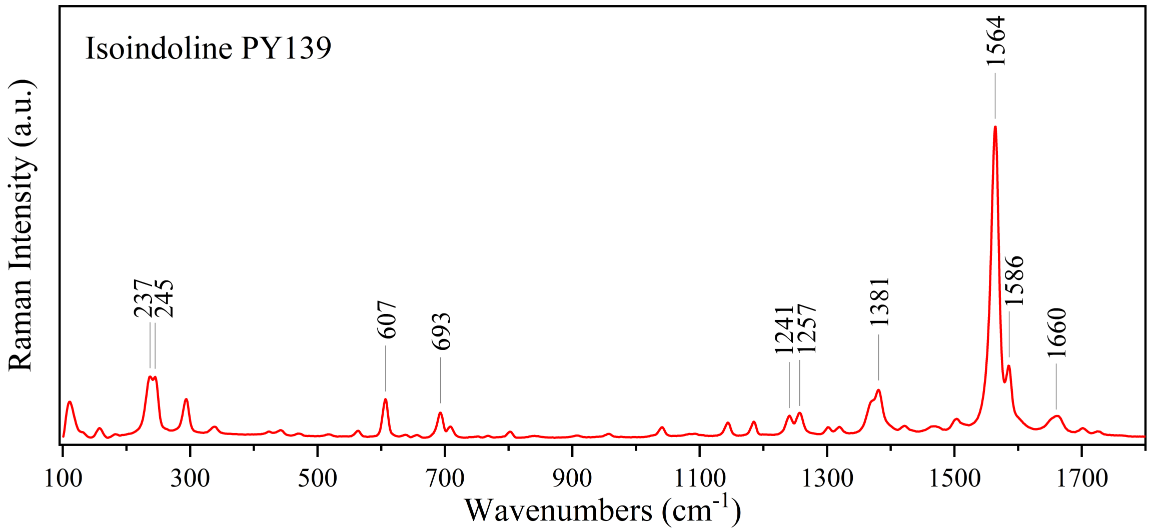

Figure 3.9 Raman normalized spectra in the wavenumber range 100-1800 cm^{-1} of PY139.

The most intense signal at 1564 cm^{-1} is attributed to the amide II band, which helps identify the pigment among others. Confirmation of amide groups in the pigment is also provided by the weak band at 1660 cm^{-1}, corresponding to the C=O stretching in the amide I band. The C-N stretching vibrations in the aromatic rings are detected in the doublet band at 1241 and 1257 cm^{-1}. In addition, the band at 1586 cm^{-1} corresponds to C=C stretching in the aromatic ring, while the band at 1381 cm^{-1} is related to aromatic C-C stretching and C–H bending. The band at 693 cm^{-1} is attributed to out-of-plane C-H deformation, and the band at 607 cm^{-1} is assigned to C–C stretching in the aromatic system. The doublet band at 245 and 237 cm^{-1} corresponds to the molecule's torsional C-C and C-N vibrations.

The characteristic signals of the two yellow pigments were identified according to the existing literature and databases [120–125]. The main Raman bands of these pigments with their assignments are presented in Tables 3.5 and 3.6, respectively, for the monoazo PY1 and isoindoline PY139.

Table 3.5 Main Raman vibrational assignments of monoazo PY1.

Wavenumber (cm^{-1})[a]	**Raman assignment**[b]
392 (m)	Benzene skeletal vibrations
462 (w)	δ(C=O)
620 (w)	δ(C–C) aromatic ring
789 (m)	δ(C–H) aromatic out-of-plane
827 (w)	$\delta(NO_2)$ in-plane aromatic substituent
953 (w)	Benzamide vibrations
1003 (m)	Benzene ring breathing mode
1141 (vs)	ν_s(C–N)
1197 (w) 1220 (s)	δ_s(C–N)
1260 (s)	Amide III
1314 (vs) 1327 (s) 1341 (m)	$\nu(NO_2)$ aromatic substituent
1391 (s)	ν(N=N)
1453 (vw)	δ(C–H) in CH_3 aromatic substituent
1489 (vs)	ν(C=C) azobenzene
1537 (m)	ν(C=C) benzene ring
1568 (m)	$\nu_{as}(NO_2)$ aromatic substituent
1604 (m)	ν(C=C) benzene ring
1625 (vs)	$\nu_{as}(NO_2)$ aromatic substituent
1674 (m)	Amide I

[a] Relative intensities - very strong (vs), strong (s), medium (m), weak (w), very weak (vw).
[b] Types of vibrations - ν: stretching, δ: bending, $_s$: symmetric, $_{as}$: asymmetric.

Table 3.6 Main Raman vibrational assignments of isoindoline PY139.

Wavenumber (cm^{-1})[a]	**Raman assignment**[b]
237 (m) 245 (m)	τ(C–C) / τ(C–N) in conjugated system
607 (w)	ν(C–C) aromatic
693 (w)	δ(C–H) out-of-plane aromatic
1241 (w) 1257 (w)	ν(C–N) aromatic
1370 (sh)	δ(C–H) aromatic
1381 (m)	ν(C–C) in benzene skeletal structure
1564 (vs)	Amide II
1586 (m)	ν(C=C) in conjugated systems
1660 (w)	Amide I

[a] Relative intensities - very strong (vs), medium (m), weak (w), shoulder (sh).
[b] Types of vibrations - ν: stretching, δ: bending, τ: twisting.

Raman spectrum of lead white presents characteristic bands in the wavenumber range 100-1800 cm^{-1}, as illustrated in Figure 3.10.

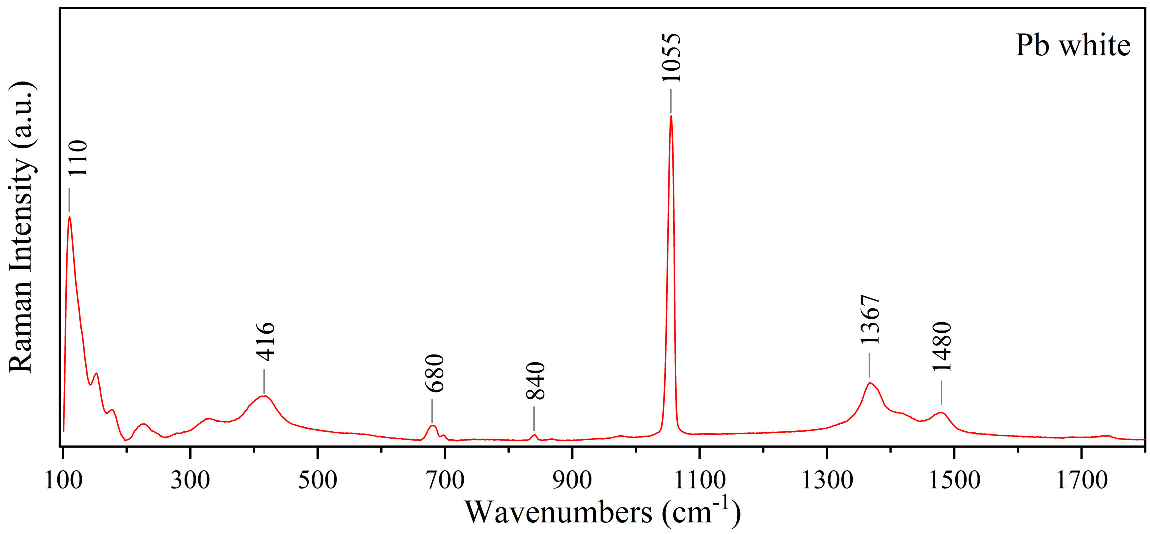

Figure 3.10 Raman normalized spectrum in the wavenumber range 100-1800 cm^{-1} of $2PbCO_3 \cdot Pb(OH)_2$.

According to the literature [126, 127], the intense douplet band at 1055 cm^{-1}, corresponding to the symmetric stretching vibration of the carbonate group $\nu_s(CO_3{}^{2-})$, is a distinctive feature of this white pigment. Additionally, bands of medium intensity were recorded at 110, 416, and 1367 cm^{-1}. These were assigned to the lattice vibrations, the lead oxide stretching mode ν(PbO), and the asymmetric carbonate vibration mode $\nu_{as}(CO_3{}^{2-})$, respectively [128, 129]. These spectral signals are essential for identifying lead white among other lead-based pigments in Raman spectroscopic analysis. Weaker bands were also observed at 680, 840, and 1480 cm^{-1}, attributable to the presence of cerussite and corresponding to the stretching vibrations $\nu(PbCO_3)$ [58].
Titanium white presents characteristic Raman bands within the 100-700 cm^{-1} wavenumber range, as illustrated in Figure 3.11.

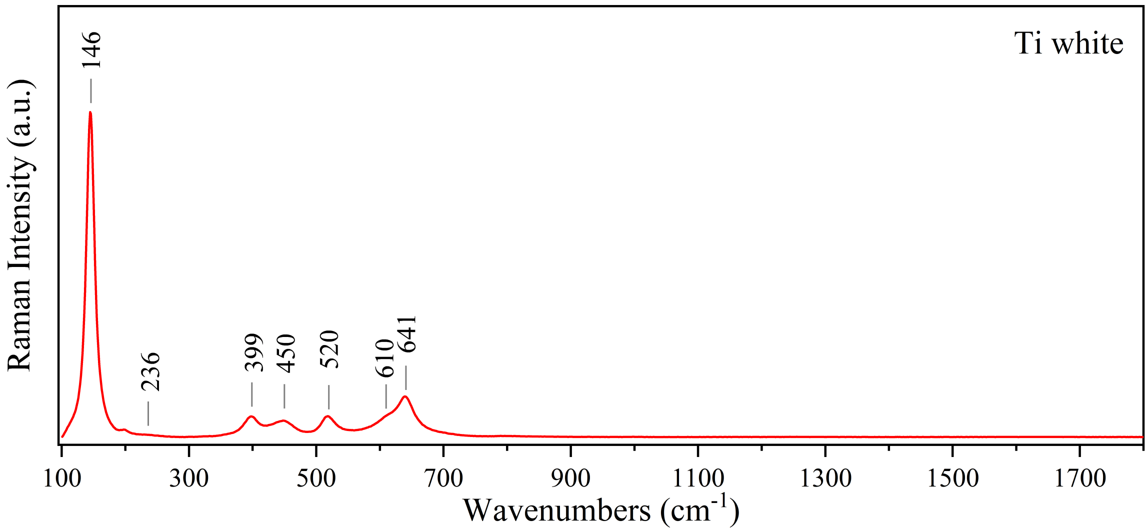

Figure 3.11 Raman normalized spectrum in the wavenumber range 100-1800 cm^{-1} of TiO_2.

The spectrum reveals characteristic Raman bands associated with TiO_2 anatase and rutile phases [130–132]. The anatase structural modes correspond to four well-defined bands at 146, 399, 520, and 641 cm^{-1}, corresponding to the Raman-active modes of E_g, B_{1g}, A_{1g}, and E_g, respectively. Regarding the modes of the rutile phase, although less intense than those of the anatase ones, they are distinguishable at 236, 450, and 610 cm^{-1} (shoulder of the anatase band at 641 cm^{-1}), corresponding to the Raman-active modes of the multi-phonon process, E_g and A_{1g}, respectively. The vibration bands in titanium dioxide are Raman-active vibrational modes that depend on the crystalline symmetry of the material. Specifically, the identified Raman modes of TiO_2 represent the symmetric stretching E_g, symmetric bending B_{1g}, and antisymmetric bending A_{1g} vibrations specific to O-Ti-O bonds [133, 134]. The E_g vibration observed at 146 cm^{-1}, is the most intense band of the anatase phase, and it identifies this white pigment.

Zinc white, although a weak Raman scatterer [135], presents bands in the Raman spectrum characteristic of its crystalline structure, as illustrated in Figure 3.12.

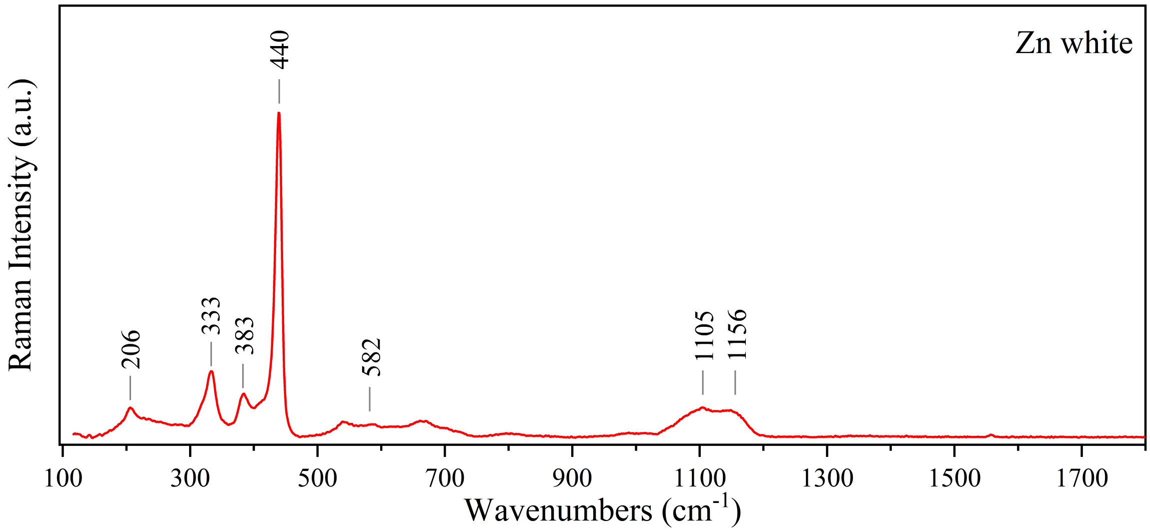

Figure 3.12 Raman normalized spectrum in the wavenumber range 100-1800 cm^{-1} of ZnO.

The most intense peak at 440 cm^{-1} is attributable to the high-frequency E_2^{high} mode, while the expected low-frequency E_2 mode at circa 100 cm^{-1} could not be measured due to the wavenumber range limit [125]. The Raman bands related to the A_1(TO) transverse and E_1(LO) longitudinal phonon modes were recorded at 383 and 582 cm^{-1}, respectively [136]. Furthermore, multi-phonon processes were observed due to the secondary-order Raman spectrum originating from phonons located at the zone boundary: the band at 206, 333 cm^{-1} ($2E_2$ of zinc oxide ZnO), and the broadband with two maximums at 1105 and 1156 cm^{-1} [137, 138].

Figure 3.13 illustrates the Raman spectra of both fresh and dried linseed oil, highlighting the main oil signals and the spectral variations that may occur during the drying process of the oil.

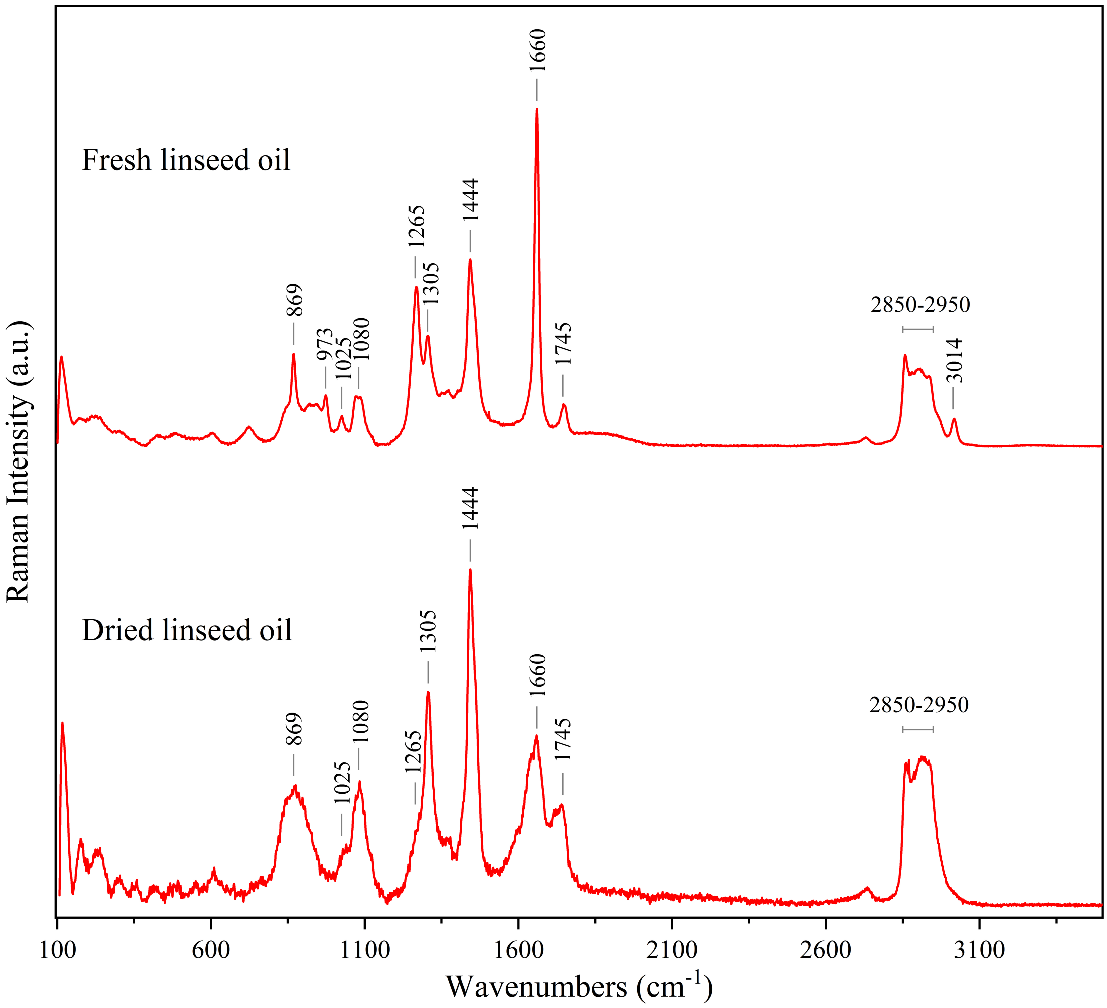

Figure 3.13 Raman normalized spectra in the wavenumber range 100-3500 cm^{-1}, for the fresh (top) and dried (bottom) linseed oil. Spectra were acquired with the 785 nm laser, 7 mW laser power, 10 seconds integration time, and 5 accumulations.

The Raman spectrum of linseed oil reveals characteristic bands that reflect the chemical composition and structure of its predominant unsaturated fatty acids. In particular, in the spectral region below 1800 cm^{-1}, the band at 869 cm^{-1} is attributed to the stretching vibrations of C–C bonds in the aliphatic chains, while the band at 973 cm^{-1} corresponds to the wagging deformation of the CH=CH group, indicative of the *cis* configuration of double bonds. In the dried oil, the first band shows a significant broadening, while the absence of the second band at 973 cm^{-1} is related to the polymerization and oxidation processes of the double bonds. The bands at 1025 cm^{-1}

and 1080 cm^{-1} are associated with the stretching vibrations of C–C bonds, reflecting the structure of the carbon chains. The observed variations in the C-C stretching bands during the drying of linseed oil may be attributed to structural changes that occur with polymerization, cross-linking, or hardening of the molecular matrix. The signal at 1265 cm^{-1} is associated with the rocking motion of CH=CH groups in the *cis* configuration and is visible only in the fresh oil. Due to the natural drying, this band becomes a shoulder and exhibits inverted intensity to its neighbor band at 1305 cm^{-1}, related to the in-phase methylene twisting deformation. The band at 1444 cm^{-1} is also associated with CH deformation of CH_2 groups. During drying, the intensity of this band increases, along with the intensity of the 1305 cm^{-1} band, which can be attributed to structural alterations in the aliphatic chains. Moreover, the band at 1660 cm^{-1} represents the stretching vibrations of C=C *cis* double bonds. After drying, this band decreases in intensity and shows a broadening. This variation is a clear indicator of the progressive cross-linking of the aliphatic chains, resulting in a reduction in the number of double bonds and, consequently, a decrease in the intensity of the Raman band associated with C=C bonds. The band at 1745 cm^{-1} represents the stretching vibrations of C=O bonds. During the drying process, this band exhibits an increase in intensity and a broadening effect. The observed increase in the carbonyl region is a consequence of the oxidation of unsaturated fatty acids, which leads to the formation of C=O groups. Additionally, the spectrum of linseed oil presents a characteristic region around 2900 cm^{-1}, attributable to the symmetric and asymmetric vibrations of the C-H stretching of the methyl -CH_3 and methylene -CH_2- groups. As part of the cross-linking process, the aliphatic chains of fatty acids exhibit increased rigidity and reduced mobility, leading to variations in intensity. In the C-H region, the band at 3014 cm^{-1} is associated with the symmetric =C-H vibrations of the *cis* double bonds. This peak is distinctive to fresh linseed oil, as it is no longer present in the Raman spectrum of dried oil after the natural curing process.

The assignments of the main Raman bands and their variations during the oil drying are summarized in Table 3.7, according to the literature [139–143].

Table 3.7 Main Raman vibrational assignments of linseed oil with the respective intensity variations observed due to the oil drying.

Wavenumbers (cm^{-1})	**Raman assignment**[a]	**Drying variations**
869	ν(C–C)	Broadening
973	*cis* ω(CH=CH)	Disappear
1025	ν(C–C)	Shoulder
1080	ν(C–C)	Broadening
1265	*cis* ρ(CH=CH)	Decrease/shoulder
1305	$\tau(CH_2)$ in-phase	Increase
1444	$\delta(CH_2)$	Increase
1660	*cis* ν(C=C)	Decrease/broadening
1745	ν(C=O)	Increase/broadening
2850-2950	$\nu_{s/as}$(C-H)	Increase
3014	*cis* ν_s(=C–H)	Disappear

[a] Types of vibrations - ν: stretching, δ: bending, ω: wagging, ρ: rocking, τ: twisting (τ), $_s$: symmetric, $_{as}$: asymmetric.

ToF-SIMS

The powder of the monoazo pigment PY1 was also investigated by ToF-SIMS spectrometry in positive and negative ion modes. The resulting mass spectra are presented in Figure 3.14. PY1 was characterized by the identification of its molecular peak: $[M+H]^+$ at *m/z* 341 in positive ion mode and $[M-H]^-$ at *m/z* 339 in negative ion mode. This peak was confirmed by its isotope pattern, which corresponds to the expected molecular composition of PY1 ($C_{17}H_{16}N_4O_4$). In addition to the molecular peak, several fragment ions were identified in both acquisition modes, corresponding to the main molecular breaking points induced by ion bombardment, providing insights into the structural characteristics of the pigment.

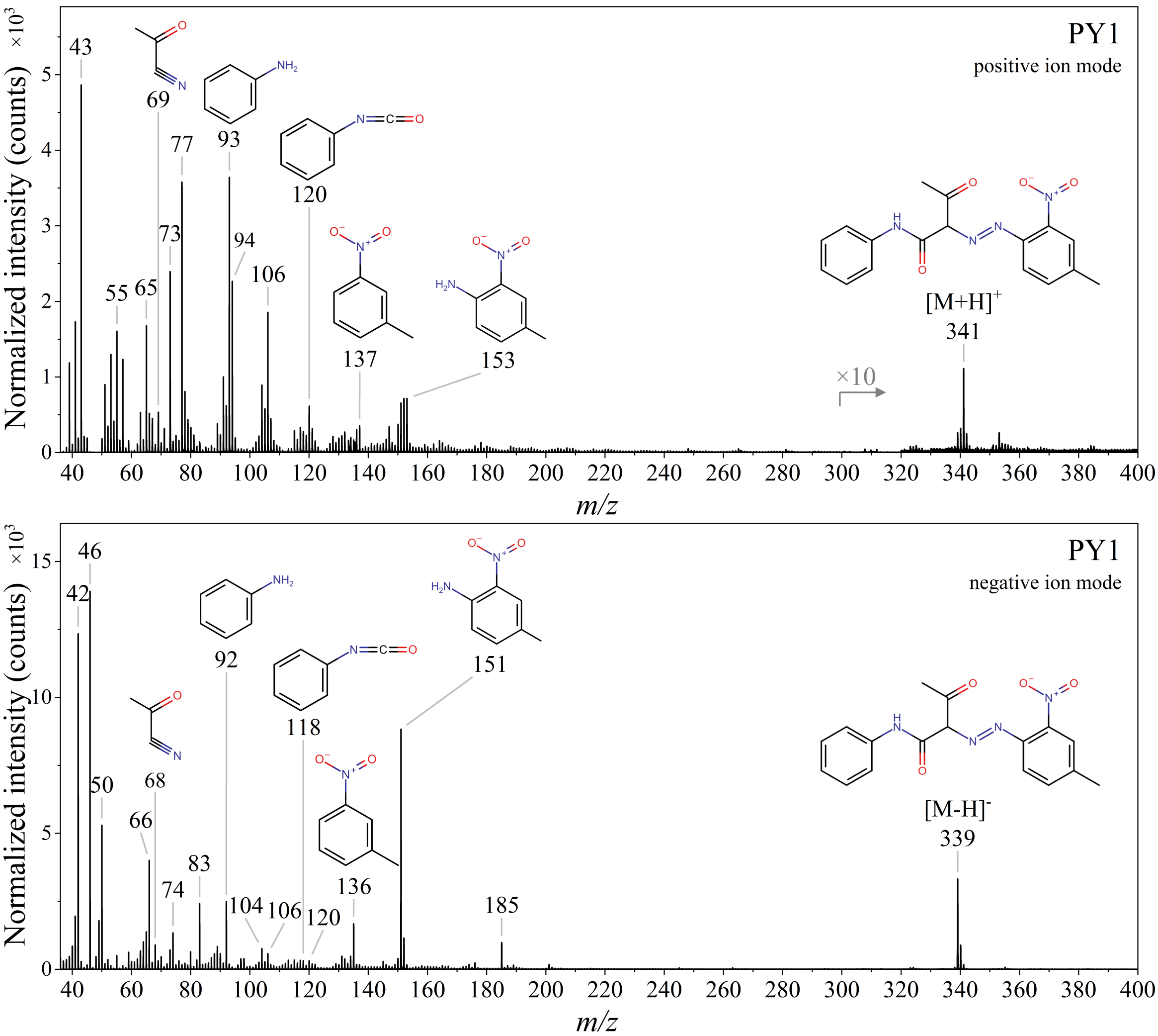

Figure 3.14 ToF-SIMS mass spectra normalized to total counts of PY1 in the mass-to-charge range *m/z* 35-400, acquired in positive (top) and negative (bottom) ion modes. The main molecular fragments and their corresponding chemical structures are highlighted.

In agreement with the scientific literature on both SIMS [144, 145] and Pyrolysis–Gas Chromatography (PyGC) [146, 147], four principal breaking points induced by ion bombardment were identified for PY1, leading to the formation of five characteristic molecular fragments, as illustrated in Figure 3.15.

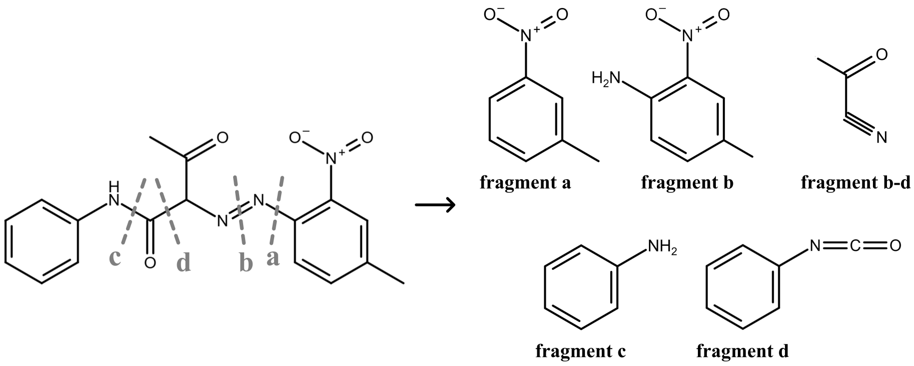

Figure 3.15 Molecular structure of the monoazo pigment showing the principal breaking points (left) and the molecular fragments produced by ion bombardment (right) [36].

The most intense peak in the spectrum appears at *m/z* 93 in positive ion mode, corresponding to fragment c, resulting from the loss of the aniline ion from the molecular structure. Conversely, in negative ion mode, the cleavage of the azo N=N chromophore bond generates a high-intensity signal corresponding to fragment b, detected at *m/z* 151. The strong intensity of these peaks is diagnostic of the monoazo pigment PY1.

In both polarity acquisitions, the following main fragments were recorded:

- fragment a → 1-methyl-nitrobenzene ion $C_7H_7NO_2$ detected at *m/z* 137 in positive ion mode (along with subfragments at *m/z* 73 and 65), and at *m/z* 136 as its deprotonated form in negative ion mode (along with subfragments at *m/z* 120 and 46);
- fragment b → 4-methyl-2-nitroaniline ion $C_7H_8N_2O_2$ detected at *m/z* 153 as its protonated form in positive ion mode, and at *m/z* 151 as its deprotonated form in negative ion mode (along with a subfragment at *m/z* 106);
- fragment c → aniline ion C_6H_7N detected at *m/z* 93 in positive ion mode (along with a subfragment at *m/z* 77), and at*m/z* 92 as its deprotonated form in negative ion mode (along with a dimeric fragment at *m/z* 185);
- fragment d → isocyanatobenzene ion C_7H_5NO detected at *m/z* 120 as its protonated form in positive ion mode (along with subfragments at *m/z* 106 and 94), and at *m/z* 118 as its deprotonated form in negative ion mode (along with subfragments at *m/z* 104, 66, 50 and 42);

- fragment b-d → acetyl cyanide ion C_3H_3NO detected at *m/z* 69 in positive ion mode (along with subfragments at *m/z* 55 and 43), and at *m/z* 68 as its deprotonated form in negative ion mode.

Characteristic intense signals were observed at lower mass-to-charge values. Specifically, in positive mode, peaks at *m/z* 43, corresponding to the acetyl ion ($C_2H_3O^+$), and at *m/z* 77, corresponding to the phenyl ion ($C_6H_5{}^+$), are prominent. In contrast, in negative mode, two intense peaks were detected at *m/z* 42, corresponding to the isocyanate ion (CNO^-), and at *m/z* 46, corresponding to the nitro ion ($NO_2{}^-$). All the molecular fragments identified in positive and negative ion modes are listed in Tables 3.8 and 3.9, respectively.

Table 3.8 List of PY1 molecular signals detected with ToF-SIMS in positive ion mode.

Positive polarity

Molecular signal

ion	*m/z*
$C_{17}H_{17}N_4O_4{}^+$	341.13

Molecular fragments

a		b		c	
ion	*m/z*	ion	*m/z*	ion	*m/z*
$C_7H_7NO_2{}^+$	137.08	$C_7H_9N_2O_2{}^+$	153.08	$C_6H_7N^+$	93.06
$C_2H_3NO_2{}^+$	73.05			$C_6H_5{}^+$	77.04
$C_4H_3N^+$	65.04				

d		b-d	
ion	*m/z*	ion	*m/z*
$C_7H_6NO^+$	120.05	$C_3H_3NO^+$	69.08
$C_7H_8N^+$	106.07	$C_3H_5N^+$	55.06
$C_6H_8N^+$	94.07	$C_2H_3O^+$	43.02

Table 3.9 List of PY1 molecular signals detected with ToF-SIMS in negative ion mode.

Negative polarity	
Molecular signal	
ion	m/z
$C_{17}H_{15}N_4O_4{}^-$	339.11

Molecular fragments

a		b		c	
ion	m/z	ion	m/z	ion	m/z
$C_7H_6NO_2{}^-$	136.04	$C_7H_7N_2O_2{}^-$	151.06	$C_6H_6N^-$	92.05
$C_7H_6NO^-$	120.04	$C_7H_8N^-$	106.06	$C_{12}H_{13}N_2{}^-$	185.11
$NO_2{}^-$	45.99				

d		b-d		other fragments	
ion	m/z	ion	m/z	ion	m/z
$C_7H_4NO^-$	118.03	$C_3H_2NO^-$	68.02	$C_2H_4NO_2{}^-$	74.02
$C_7H_6N^-$	104.05			$C_3HNO_2{}^-$	83.02
C_3NO^-	65.99				
C_3N^-	50.00				
CNO^-	41.99				

About the isoindoline pigment PY139, ToF-SIMS analysis was conducted exclusively in negative ion mode, as the molecular peak of the pigment was undetectable in the positive one. The resulting mass spectrum is shown in Figure 3.16. In particular, the PY139 signal was detected as $[M\text{-}H]^-$ at m/z 366, and more intensely as $[M]^-$ at m/z 367, corresponding to the expected molecular composition ($C_{16}H_9N_5O_6$), as further confirmed by its isotope pattern [145]. In addition to the molecular ion peak, the mass spectrum exhibits several signals associated with organic species. The identification of the molecular fragments was performed by analyzing the m/z values of the detected peaks and their isotopic patterns, taking into account the structure of the PY139 molecule. This approach led to the hypothesis of the main molecular breakpoints induced by the ion bombardment process, suggesting the possible molecular fragments generated, which do not necessarily correspond to stable species.

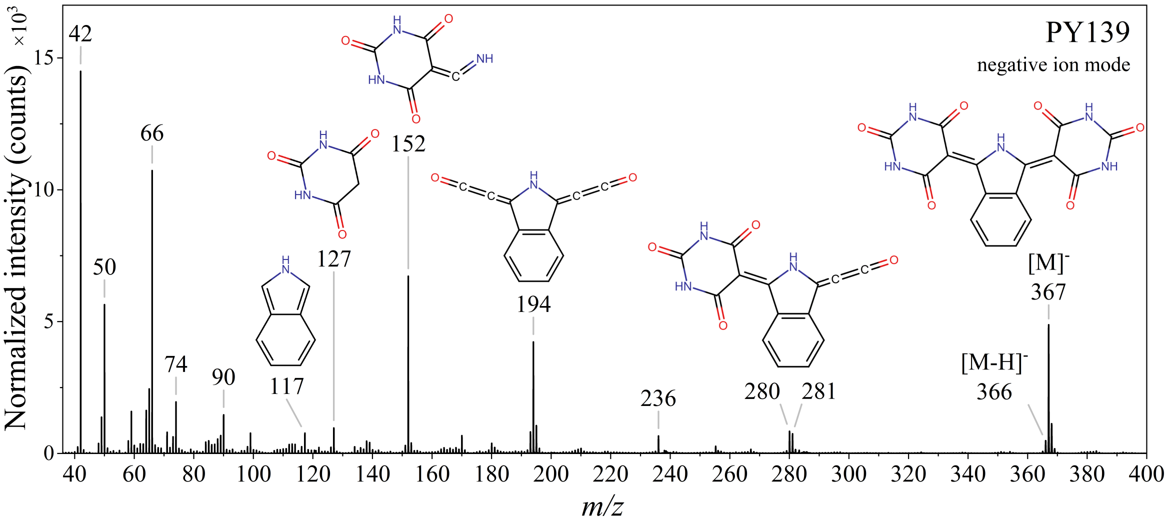

Figure 3.16 ToF-SIMS mass spectrum normalized to total counts of PY139 in the mass-to-charge range m/z 35-400, acquired in negative ion mode. The main molecular fragments and their corresponding chemical structures are highlighted.

Based on the PyGC literature on compounds structurally similar to isoindoline [146, 148], and considering its molecular symmetry, three main breakpoints induced by ion bombardment have been hypothesized for PY139. The resulting fragmentation pattern is expected to generate five molecular fragments, as illustrated in Figure 3.17.

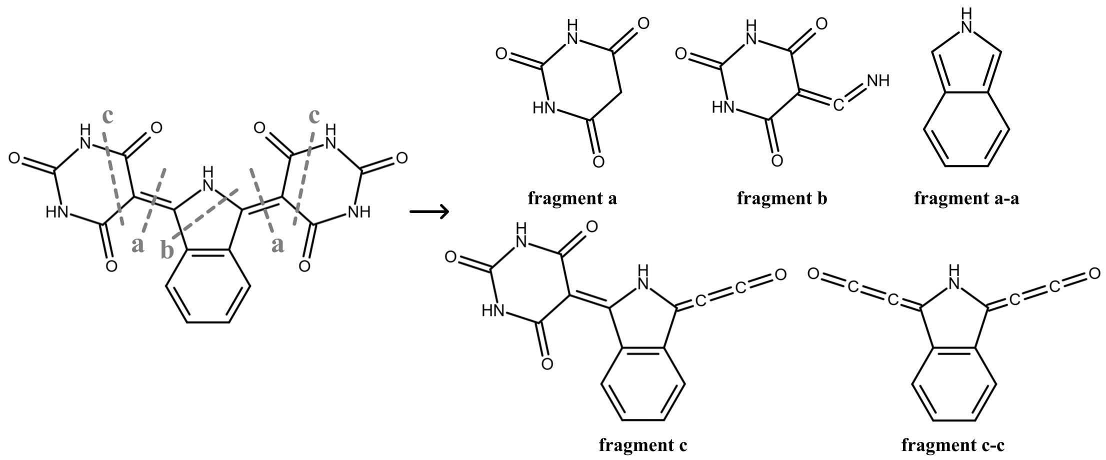

Figure 3.17 Molecular structure of the isoindoline pigment showing the principal breaking points (left) and the molecular fragments produced by ion bombardment (right) [36].

The following main fragments were recorded:

- fragment a → 1,3-diazinane-2,4,6-trione ion in its deprotonated form $C_4H_3N_2O_3$ detected at m/z 127;
- fragment b → intense signal in the mass spectrum detected at m/z 152, corresponding to the deprotonated $C_5H_3N_3O_3$ structure;

- fragment a-a → 2H-isoindole C_8H_7N detected at *m/z* 117 (along with possible dimeric fragment at *m/z* 236);
- fragment c → characteristic signal at *m/z* 281 corresponding to the $C_{14}H_7N_3O_4$ structure (along with its deprotonated form at *m/z* 280);
- fragment c-c → characteristic signal at *m/z* 194 corresponding to the deprotonated $C_{12}H_5NO_2$ structure.

Other characteristic signals of the pigment were observed at lower mass-to-charge values. Specifically, intense peaks were detected at *m/z* 42, corresponding to the isocyanate ion (CNO^-), at *m/z* 50, corresponding to the cyanoethynyl ion (C_3N^-), and at *m/z* 66, corresponding to the 2-isocyanoethynolate ion (C_3NO^-). Two less intense peaks were also observed at *m/z* 74 and 90, corresponding to the $C_2H_4NO_2{}^-$ and $C_2H_4NO_3{}^-$ ions, respectively. All the molecular fragments identified in the negative ion mode are listed in Table 3.10.

Table 3.10 List of PY139 molecular signals detected with ToF-SIMS in negative ion mode.

Negative polarity

Molecular signal

ion	*m/z*
$C_{16}H_9N_5O_6{}^-$	367.06
$C_{16}H_8N_5O_6{}^-$	366.05

Molecular fragments

a		b		a-a	
ion	*m/z*	ion	*m/z*	ion	*m/z*
$C_4H_3N_2O_3{}^-$	127.02	$C_5H_2N_3O_3{}^-$	152.01	$C_8H_7N^-$	117.02
				$C_{16}H_{16}N_2{}^-$	236.13

c		c-c		other fragments	
ion	*m/z*	ion	*m/z*	ion	*m/z*
$C_{14}H_7N_3O_4{}^-$	281.05	$C_{12}H_4NO_2{}^-$	194.02	CNO^-	42.00
$C_{14}H_6N_3O_4{}^-$	280.05			C_3N^-	50.00
				C_3NO^-	66.00
				$C_2H_4NO_2{}^-$	74.02
				$C_2H_4NO_3{}^-$	90.02

The powder of lead white was also investigated using ToF-SIMS spectrometry, acquiring secondary ions in both positive and negative ion polarities, as illustrated in Figures 3.18 and 3.19, respectively. The ability to analyze this compound in both positive and negative modes provided a more comprehensive characterization. Lead is present as a mixture of four stable isotopes: ^{204}Pb (1.40%), ^{206}Pb (24.10%), ^{207}Pb (22.10%), and ^{208}Pb (52.40%). The isotopic pattern of lead facilitated the identification of all lead-containing species within the range of m/z 200-1000, in positive and negative mass spectra. To improve the visualization of all the detected signals, the spectra of both polarities are presented in two separate mass-to-charge ranges.

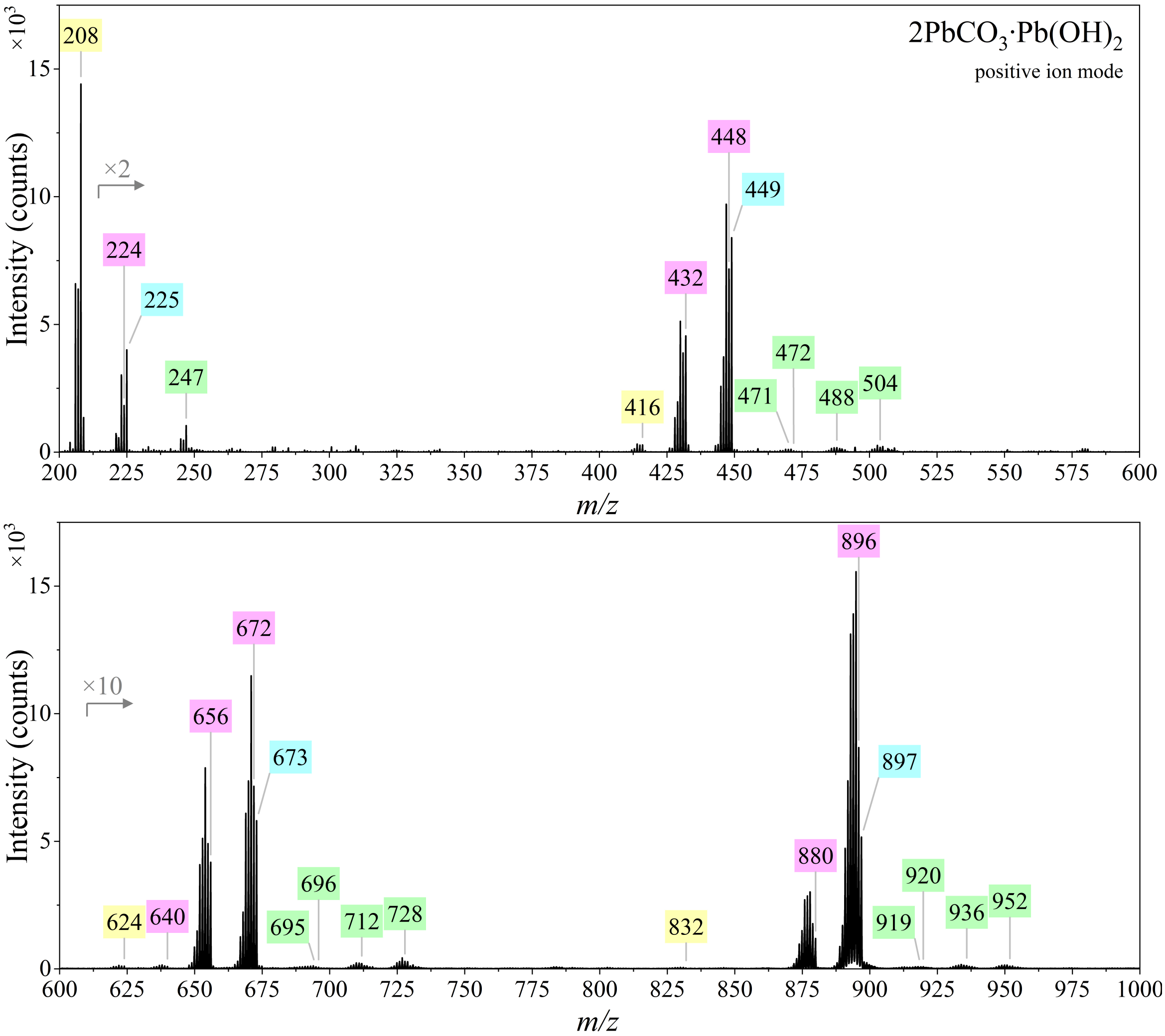

Figure 3.18 ToF-SIMS mass spectra normalized to total counts of lead carbonate basic in the range m/z 200-600 (top) and m/z 600-1000 (bottom), in positive ion mode. The main signals related to lead clusters (yellow), lead oxides (magenta), lead hydroxides (cyan), lead carbonates (green) are highlighted.

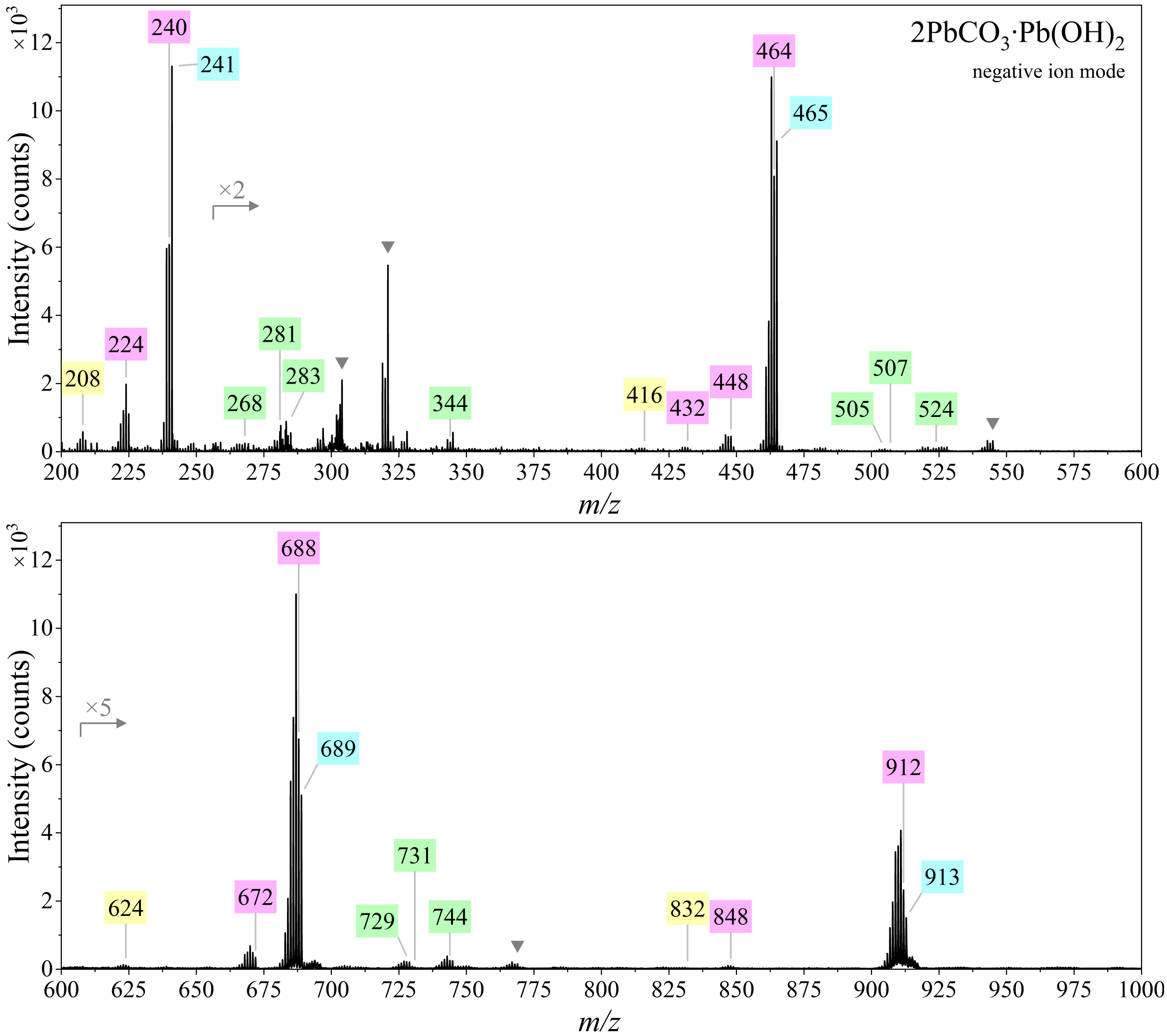

Figure 3.19 ToF-SIMS mass spectra normalized to total counts of lead carbonate basic in the range m/z 200-600 (top) and m/z 600-1000 (bottom), in negative ion mode. The main signals related to lead clusters (yellow), lead oxides (magenta), lead hydroxides (cyan), lead carbonates (green), and lead sulfate species (gray triangles) are highlighted.

According to the literature and database [149–153], all the detected ion signals identified in the mass spectra of lead white are listed in Tables 3.11 and 3.12, corresponding to positive and negative polarity, respectively. The signals are distinguished between lead ion clusters, lead oxides, lead hydroxides, and lead carbonate species.

- Lead clusters Pb_n were observed at m/z 208 for $Pb^{\pm}$, at m/z 416 for $Pb_2^{\pm}$, at m/z 624 for $Pb_3^{\pm}$, and at m/z 831 for $Pb_4^{\pm}$, both in positive and negative ion modes (highlighted in yellow in the mass spectra). These signals are more intense in positive acquisition, as in mass spectrometry Pb-related ions are typically observed in positive polarity.

- Lead oxide signals are clearly visible in both polarities (highlighted in magenta). In particular, in positive ion mode, the most intense signals related to the lead oxides species were detected at *m/z* 224 for PbO^+, at *m/z* 432 for Pb_2O^+, and at *m/z* 448 for $Pb_2O_2{}^+$. At higher mass-to-charge values, less intense signals were observed for Pb_3O^+ at *m/z* 640, $Pb_3O_2{}^+$ at *m/z* 656, $Pb_3O_3{}^+$ at *m/z* 672, $Pb_4O_3{}^+$ at *m/z* 880, and $Pb_4O_4{}^+$ at *m/z* 896. In contrast, in negative mode, among all the signals, those at *m/z* 224 for PbO^-, at *m/z* 240 for $PbO_2{}^-$, at *m/z* 432 for Pb_2O^-, at *m/z* 448 for $Pb_2O_2{}^-$, and at *m/z* 464 for $Pb_2O_3{}^-$ stand out. Less intense signals at higher mass-to-charge values were observed at *m/z* 672, 688, and 912 for $Pb_3O_3{}^-$, $Pb_3O_4{}^-$ and $Pb_4O_5{}^-$, respectively.
- Lead hydroxide ions were identified in conjunction with the most intense signals of lead oxides in both polarities (highlighted in cyan). Specifically, in positive mode, the lead hydroxides recorded are of the type $Pb_nO_nH^+$, with n ranging from 1 to 4: $PbOH^+$ at *m/z* 225, $Pb_2O_2H^+$ at *m/z* 449, $Pb_3O_3H^+$ at *m/z* 673, and $Pb_4O_4H^+$ at *m/z* 897. In negative mode, the hydroxide recorded signals correspond to $Pb_mO_{m+1}H^-$, with m ranging from 1 to 4: PbO_2H^- at *m/z* 241, $Pb_2O_3H^-$ at *m/z* 465, $Pb_3O_4H^-$ at *m/z* 689, and $Pb_4O_5H^-$ at *m/z* 913.
- Lead carbonate species were identified in both polarities, although with relatively low intensity (highlighted in green). Nine combinations of $Pb_nO_m(CO)_2{}^+$ species were recorded in positive mode, with n ranging from 2 to 4 and m assuming the values between *n-2* and *n*. Specifically, for *n=2*: $Pb_2(CO)_2{}^+$ at *m/z* 472, $Pb_2O(CO)_2{}^+$ at *m/z* 488, and $Pb_2O_2(CO)_2{}^+$ at *m/z* 504; for *n=3*: $Pb_3O(CO)_2{}^+$ at *m/z* 696, $Pb_3O_2(CO)_2{}^+$ at *m/z* 712, and $Pb_3O_3(CO)_2{}^+$ at *m/z* 728; for *n=4*: $Pb_4O_2(CO)_2{}^+$ at *m/z* 920, $Pb_4O_3(CO)_2{}^+$ at *m/z* 936, and $Pb_4O_4(CO)_2{}^+$ at *m/z* 952. Lead carbonate signals of the type $Pb_xO_{x-1}C_3H_3{}^+$, with n ranging from 1 to 3, were also observed: $PbC_3H_3{}^+$ at *m/z* 247, $Pb_2OC_3H_3{}^+$ at *m/z* 471, $Pb_3O_2C_3H_3{}^+$ at *m/z* 695, and $Pb_4O_3C_3H_3{}^+$ at *m/z* 919. In negative mode, two types of signals related to lead carbonates were identified. Signals of lead ions linked to the carbonate group (CO_3) were detected at *m/z* 268 for $Pb(CO_3)^-$, at *m/z* 344 for $PbO(CO_3)_2{}^-$, at *m/z* 524 for $Pb_2O_3(CO_3)^-$, and at *m/z* 744 for $Pb_3(CO_3)_2{}^-$. Signals of the type $Pb_yO_yC_2H_zO_2{}^-$, in which y varies from 1 to 3 and z can be 1 or 3, were observed at *m/z* 281/283 for $PbOC_2H_{1/3}O_2{}^-$, at *m/z* 505/507 for $Pb_2O_2C_2H_{1/3}O_2{}^-$, and at *m/z* 729/731 for $Pb_3O_3C_2H_{1/3}O_2{}^-$.

Additionally, in negative ion mode, signals of lead sulfates attributed to the manufacturing process (marked with gray triangles) were detected at *m/z* 304 for $PbSO_4{}^-$, *m/z* 321 for $PbOHSO_4{}^-$, *m/z* 545 for $Pb_2O_2HSO_4{}^-$, and *m/z* 769 for $Pb_3O_3HSO_4{}^-$.

Table 3.11 List of $2PbCO_3{\cdot}Pb(OH)_2$ signals detected with ToF-SIMS in positive ion mode.

Positive polarity							
Pb-clusters		Lead oxides		Lead hydroxides		Lead carbonates	
ion	m/z	ion	m/z	ion	m/z	ion	m/z
Pb^+	207.98	PbO^+	223.98	$PbOH^+$	224.98	$PbC_3H_3{}^+$	246.97
$Pb_2{}^+$	415.95	Pb_2O^+	431.95			$Pb_2OC_3H_3{}^+$	470.93
		$Pb_2O_2{}^+$	447.95	$Pb_2O_2H^+$	448.95	$Pb_2(CO)_2{}^+$	471.93
						$Pb_2O(CO)_2{}^+$	487.88
						$Pb_2O_2(CO)_2{}^+$	503.90
$Pb_3{}^+$	623.93	Pb_3O^+	639.91			$Pb_3O_2C_3H_3{}^+$	694.89
		$Pb_3O_2{}^+$	655.91			$Pb_3O(CO)_2{}^+$	695.88
		$Pb_3O_3{}^+$	671.92	$Pb_3O_3H^+$	672.92	$Pb_3O_2(CO)_2{}^+$	711.83
						$Pb_3O_3(CO)_2{}^+$	727.86
$Pb_4{}^+$	831.91	$Pb_4O_3{}^+$	879.86			$Pb_4O_3C_3H_3{}^+$	918.88
		$Pb_4O_4{}^+$	895.87	$Pb_4O_4H^+$	896.87	$Pb_4O_2(CO)_2{}^+$	919.92
						$Pb_4O_3(CO)_2{}^+$	935.81
						$Pb_4O_4(CO)_2{}^+$	951.81

Table 3.12 List of $2PbCO_3{\cdot}Pb(OH)_2$ signals detected with ToF-SIMS in negative ion mode.

Negative polarity							
Pb-clusters		Lead oxides		Lead hydroxides		Lead carbonates	
ion	m/z	ion	m/z	ion	m/z	ion	m/z
Pb^-	207.98	PbO^-	223.97			$Pb(CO_3)^-$	267.96
		$PbO_2{}^-$	239.97	PbO_2H^-	240.97	$PbOC_2HO_2{}^-$	280.96
						$PbOC_2H_3O_2{}^-$	282.97
						$PbO(CO_3)_2{}^-$	343.98
$Pb_2{}^-$	415.96	Pb_2O^-	431.95			$Pb_2O_2C_2HO_2{}^-$	504.93
		$Pb_2O_2{}^-$	447.95			$Pb_2O_2C_2H_3O_2{}^-$	506.95
		$Pb_2O_3{}^-$	463.95	$Pb_2O_3H^-$	464.95	$Pb_2O_3(CO_3)^-$	523.92
$Pb_3{}^-$	623.92	$Pb_3O_3{}^-$	671.92			$Pb_3O_3C_2HO_2{}^-$	728.90
		$Pb_3O_4{}^-$	687.92	$Pb_3O_4H^-$	688.92	$Pb_3O_3C_2H_3O_2{}^-$	730.89
						$Pb_3(CO_3)_2{}^-$	743.88
$Pb_4{}^-$	831.89	Pb_4O^-	847.85				
		$Pb_4O_5{}^-$	911.88	$Pb_4O_5H^-$	912.88		

Titanium dioxide pigment was also characterized using the ToF-SIMS technique, as illustrated in Figure 3.20. Titanium is composed of five stable isotopes: ^{46}Ti (8.25%), ^{47}Ti (7.44%), ^{48}Ti (73.72%), ^{49}Ti (5.41%), ^{50}Ti (5.18%). The isotopic pattern facilitated the identification of all titanium-containing species within the range of *m/z* 50-350, in the negative mass spectrum. The analysis in positive ion mode did not yield significant findings, as the titanium-based signals were either too weak or undetectable.
According to the literature and database [154–156], all the detected ion signals identified in the mass spectrum of titanium dioxide are listed in Table 3.13, corresponding to negative polarity. The signals are distinguished between titanium oxides, titanium dioxide clusters, and titanium hydroxide species.

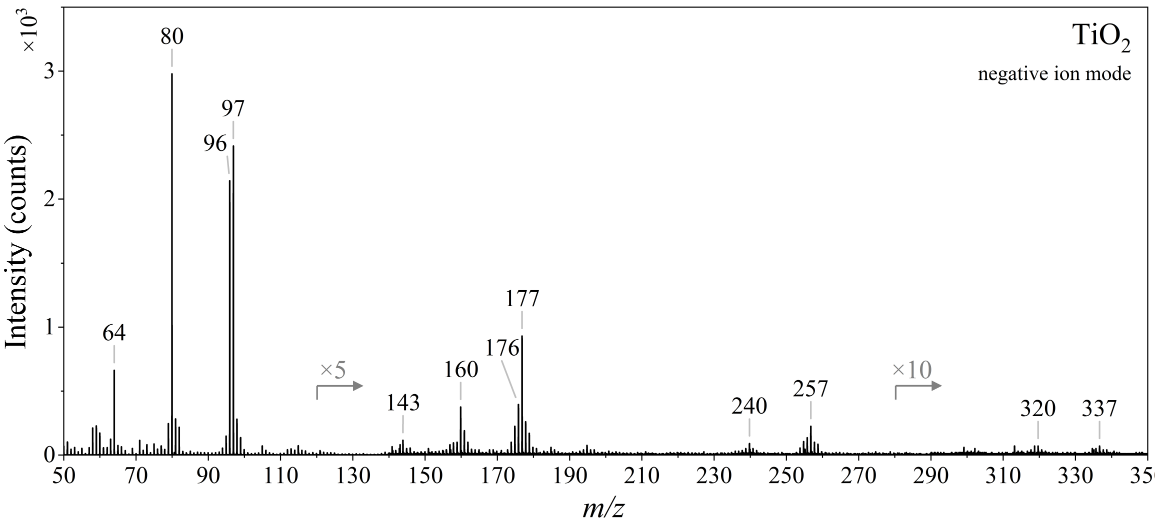

Figure 3.20 ToF-SIMS mass spectra normalized to total counts of titanium dioxide in the mass-to-charge range *m/z* 50-350, acquired in negative ion mode. The main ion signals are highlighted.

Table 3.13 List of TiO_2 signals detected with ToF-SIMS in negative ion mode.

Negative polarity					
Titanium oxides		TiO_2-clusters		Titanium hydroxides	
ion	*m/z*	ion	*m/z*	ion	*m/z*
TiO^-	63.95	$(TiO_2)^-$	79.94	$(TiO_2)OH^-$	96.93
$TiO_3{}^-$	95.92	$(TiO_2)_2{}^-$	159.83	$(TiO_2)_2OH^-$	176.82
$Ti_2O_3{}^-$	143.86	$(TiO_2)_3{}^-$	239.74	$(TiO_2)_3OH^-$	256.73
$Ti_2O_5{}^-$	175.82	$(TiO_2)_4{}^-$	319.65	$(TiO_2)_4OH^-$	336.64

In negative ion mode, SIMS analysis of titanium dioxide powder highlighted the formation of species during the ion bombardment process, including signals indicative of titanium oxides, as well as hydroxides and clusters of titanium dioxide.

- Titanium oxide ions $Ti_nO_m^-$ were observed at *m/z* 64 for TiO^-, and at *m/z* 96 for $TiO_3{}^-$. At higher mass-to-charge ratios, the mass spectrum reveals two other low-intensity signals related to titanium oxide at *m/z* 143 and 176, for $Ti_2O_3{}^-$ and $Ti_2O_5{}^-$, respectively.
- Titanium dioxide ion represents the most intense signal acquired in the mass spectrum at *m/z* 80 for TiO_2^-, confirmed by its theoretical isotopic distribution. In addition, titanium dioxide clusters $(TiO_2)_n^-$, with n ranging from 2 to 4, were observed at *m/z* 160 for *n=2* as $(TiO_2)_2^-$, at *m/z* 240 for *n=3* as $(TiO_2)_3^-$, and at *m/z* 320 for *n=4* as $(TiO_2)_4^-$.
- Titanium hydroxide signals appear as $[(TiO_2)_n{+}OH]^-$ ions, with n ranging from 1 to 4, and are directly associated with the corresponding TiO_2-species. These signals are observed at an *m/z* shift of about 17, corresponding to an OH^- ion, relative to the previously detected titanium dioxide species. Specifically, they are recorded at *m/z* 97 for *n=1* as $(TiO_2)OH^-$, at *m/z* 177 for *n=2* as $(TiO_2)_2OH^-$, at *m/z* 257 for *n=3* as $(TiO_2)_3OH^-$, and at *m/z* 337 for *n=4* as $(TiO_2)_4OH^-$.

Furthermore, the analysis of the mass spectrum at mass-to-charge values greater than *m/z* 350 revealed the presence of other species displaying titanium-based patterns (not shown), including $(TiO_2)_n^-$ accompanied by its hydroxide ion $(TiO_2)_nOH^-$. However, the low intensity of these signals prevented a more detailed analysis.

Finally, ToF-SIMS analysis was performed to analyze zinc white, acquiring secondary ions in negative ion polarity, as illustrated in Figure 3.21. Zinc has five stable isotopes: ^{64}Zn (48.63%), ^{66}Zn (27.90%), ^{67}Zn (4.10%), ^{68}Zn (18.75%), and ^{70}Zn (0.62%). The distinct isotopic pattern of zinc enabled the identification of all zinc-containing species within the range of *m/z* 70-550 in the negative mass spectrum. Notably, the combination of zinc oxide and hydroxide species generates characteristic isotopic patterns, allowing for the characterization of this pigment. As observed for titanium white, the analysis in positive ion mode did not yield significant findings.
According to the literature and database [157, 158], all the detected ion signals identified in the mass spectrum of zinc oxide are listed in Table 3.14, corresponding to negative polarity. The signals are distinguished between zinc oxide clusters, zinc oxides, and zinc hydroxide species.

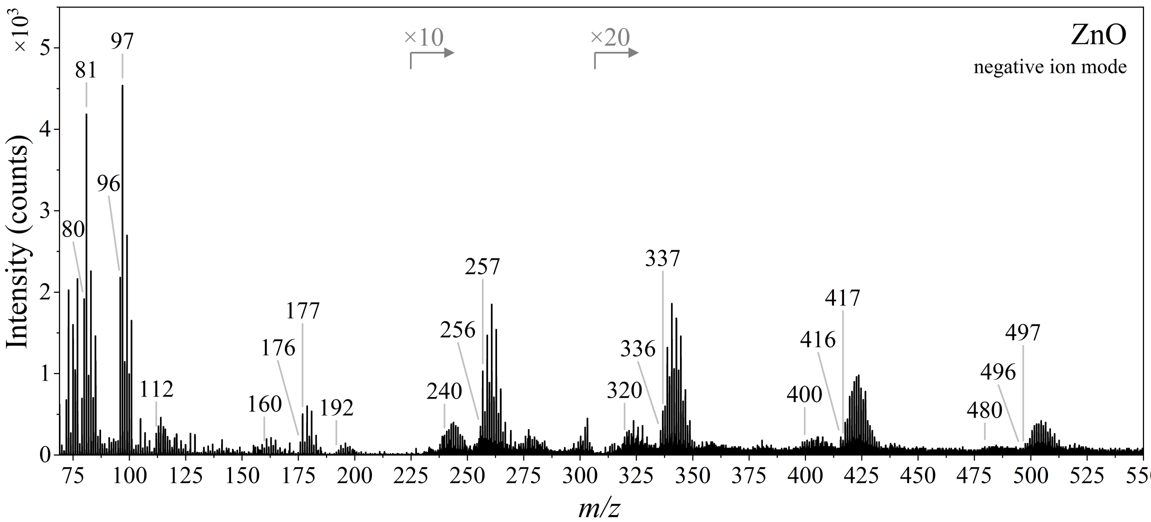

Figure 3.21 ToF-SIMS mass spectra normalized to total counts of zinc oxide in the mass-to-charge range *m/z* 70-550, acquired in negative ion mode. The main ion signals are highlighted.

Table 3.14 List of ZnO signals detected with ToF-SIMS in negative ion mode.

Negative polarity					
ZnO-clusters		Zinc oxides		Zinc hydroxides	
ion	m/z	ion	m/z	ion	m/z
$(ZnO)^-$	79.93			$ZnOH^-$	80.93
		$ZnO_2{}^-$	95.92	ZnO_2H^-	96.93
		$ZnO_3{}^-$	111.92		
$(ZnO)_2{}^-$	159.85	$Zn_2O_3{}^-$	175.85	$Zn_2O_3H^-$	176.86
		$Zn_2O_4{}^-$	191.85		
$(ZnO)_3{}^-$	239.79	$Zn_3O_4{}^-$	255.78	$Zn_3O_4H^-$	256.79
$(ZnO)_4{}^-$	319.72	$Zn_4O_5{}^-$	335.70	$Zn_4O_5H^-$	336.71
$(ZnO)_5{}^-$	399.67	$Zn_5O_6{}^-$	415.64	$Zn_5O_6H^-$	416.65
$(ZnO)_6{}^-$	479.60	$Zn_6O_7{}^-$	495.56	$Zn_6O_7H^-$	496.57

In negative ion mode, SIMS analysis of zinc oxide powder highlighted the formation of different species during the ion bombardment process, including signals of zinc oxide clusters, as well as oxide and hydroxide species.

- Zinc oxide represents one of the most intense signals acquired at m/z 80 for ZnO^-, confirmed by its theoretical isotopic distribution. In addition, zinc oxide clusters of the type $(ZnO)_n^-$, with n ranging from 2 to 6, were observed at m/z 160 for n=*2* as $(ZnO)_2^-$, at m/z 240 for n=*3* as $(ZnO)_3^-$, at m/z 320 for n=*4* as $(ZnO)_4^-$, at m/z 400 for n=*5* as $(ZnO)_5^-$, and at m/z 480 for n=*6* as $(ZnO)_6^-$.
- Among the zinc oxide species detected in the mass spectrum, the signals corresponding to the form $Zn_nO_{n+1}{}^-$, with n ranging from 1 to 6, are particularly distinctive. Specifically, these signals are observed at m/z 96 for $ZnO_2{}^-$, at m/z 176 for $Zn_2O_3{}^-$, at m/z 256 for $Zn_3O_4{}^-$, at m/z 336 for $Zn_4O_5{}^-$, at m/z 416 for $Zn_5O_6{}^-$, and at m/z 496 for $Zn_6O_7{}^-$. Other two signals of zinc oxide species were recorded at m/z 112 for $ZnO_3{}^-$, and at m/z 192 for $Zn_2O_4{}^-$.
- The zinc hydroxide signal $ZnOH^-$ was observed at m/z 81, along with other zinc hydroxide species detected as $Zn_nO_{n+1}H^-$ ions, with n ranging from 1 to 6. These last signals are directly associated with the previously mentioned zinc oxide signals (Zn_nO_{n+1}), forming the distinctive isotopic patterns of zinc white. Specifically, they are recorded at m/z 97 for ZnO_2H^-, at m/z 177 for $Zn_2O_3H^-$, at m/z 257 for $Zn_3O_4H^-$, at m/z 337 for $Zn_4O_5H^-$, at m/z 417 for $Zn_5O_6H^-$, and at m/z 497 for $Zn_6O_7H^-$.

XRD

XRD measurements were performed to analyze the crystalline structure of TiO_2 and ZnO powders. In particular, the percentage of the predominant phases and the crystallite size were quantified by the analysis of peak intensities and positions.
TiO_2 powder reveals the characteristic crystalline phases of titanium dioxide, with the main diffraction peaks corresponding to anatase and rutile phases [159, 160], as illustrated in Figure 3.22. The anatase phase presents diffraction peaks at 2θ of 29.76°, 44.61°, 56.69°, and 65.23°. The rutile phase exhibits diffraction peaks at 2θ of 32.27°, 42.65°, 48.45°, and 63.98°.
The low definition of the XRD pattern suggests that the powder is partially amorphous, indicating an initial stage of crystallinity formation [161]. The crystallite size was measured using the Scherrer formula by fitting the two main peaks, corresponding to the peak reflection of anatase (101) at 29.8° and rutile (110) at 32.3°. The analysis revealed a composition of 79.5% anatase phase and 20.5% rutile phase, with the calculated crystallite sizes ranging from approximately 13 to 17 nm.

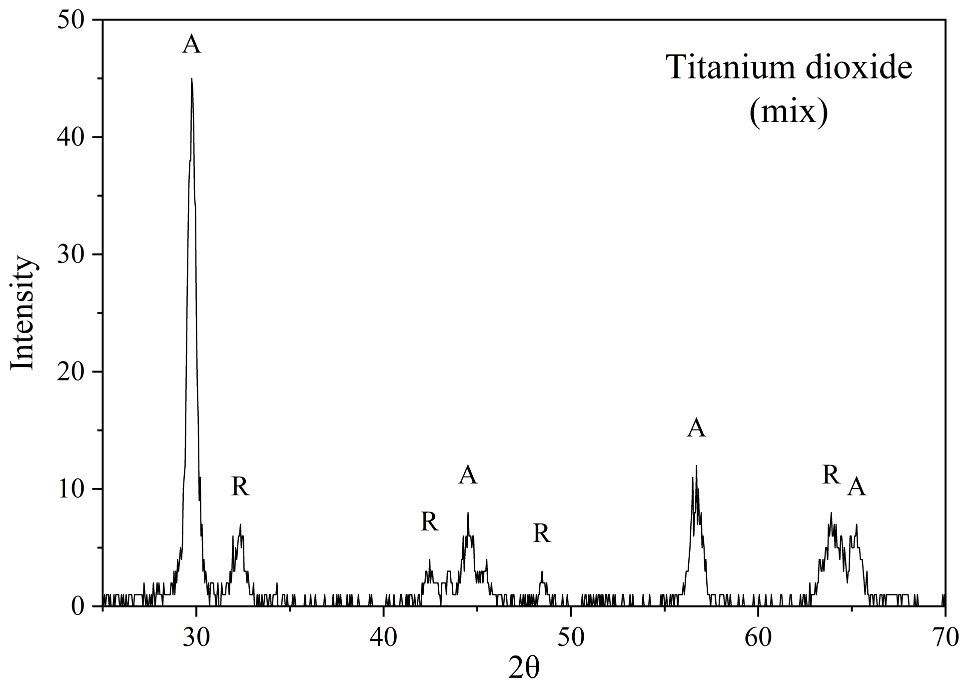

Figure 3.22 XRD patterns of TiO_2 powder acquired with Co-Kα source, with the diffraction peaks corresponding to the anatase (A) and rutile (R) phases indicated.

ZnO powder reveal a hexagonal wurtzite phase, as illustrated in Figure 3.23, according to the literature on XRD analysis using a Cu Kα source [162, 163]. Zinc oxide exhibits distinct diffraction peaks in the 2θ range of 30°-90°, specifically at 37.4°, 40.5°, 42.7°, 56.1°, 67.0°, 74.8°, 79.2°, 81.2°, and 82.6°. These diffraction peaks correspond to the characteristic crystalline planes of ZnO: (100), (002), (101), (102), (110), (103), (200), (112), and (201).

The sharpness and high intensity of the XRD peaks indicate that the powder is highly crystalline. The average crystallite size, determined using the Scherrer formula by fitting the first three main diffraction peaks corresponding to the (100), (002), and (101) planes, is approximately 42 nm.

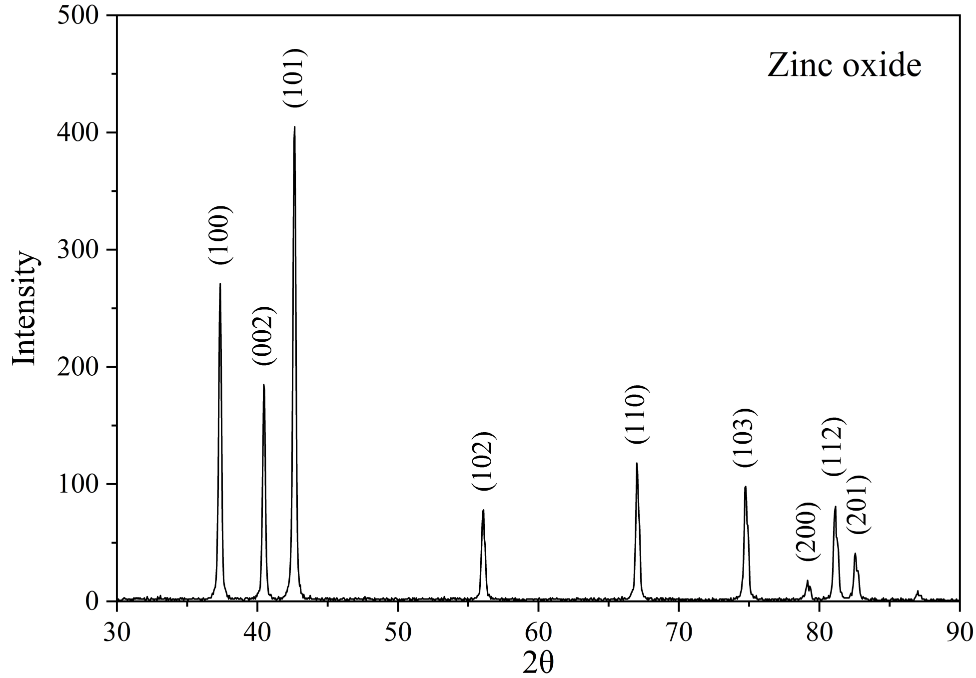

Figure 3.23 XRD patterns of ZnO powder acquired with Co-Kα source, with the main diffraction peaks and the corresponding crystal planes indicated.

3.2.2 Instrumental and visual evaluation of color changes

The stereomicroscope images and the colorimetric variations in the CIELAB a* vs b* and L* diagrams of the three-component paint samples are reported in Figure 3.24. After artificial aging, a general fading of the colors can be easily appreciated by the naked eye for the ternary mixtures, as shown in Figure 3.24a. In detail, the unaged part of the samples displays glossy and broad roughness surfaces, whereas the aged ones exhibit more homogeneous, satin-like, and flattened surfaces, especially in the case of samples with lead white. Samples with higher white pigment content (1:100 ratio) exhibit similar color variations, as reported in Figure A.2a.
The total color changes ΔE of the ternary mixtures range from a minimum of 23 to a maximum of 73 (Figure A.2b). This implies that the color change after aging is far beyond the sensitivity of the human eye (fixed at $\Delta E=3$) and classified as significant ($\Delta E>5$) in literature [164, 165]. In particular, the three-component samples realized with titanium dioxide show the largest color changes ΔE after the artificial aging ($\Delta E = 63.08 \pm 0.95$ for the sample with PY1 and $\Delta E = 73.39 \pm 0.96$ for the sample with PY139); this effect is less marked in the samples containing lead and zinc white. To further interpret the total color change ΔE, variations in the colorimetric coordinates (L*, a*, b*) were examined. In the CIELAB a* vs b* diagram in Figure 3.24b, following aging, the three-component samples present a strong decrease in the b* component (yellowness/blueness), as a higher color variation. This is more evident in the presence of titanium white ($\Delta b^* = -62.93 \pm 0.12$ for the sample with PY1 and $\Delta b^* = -71.57 \pm 0.11$ for the sample with PY139). In contrast, the a* component (redness/greenness) follows a different trend: mock-ups containing PY1 show a slight increase in a* values, whereas those with PY139 display a decrease. Despite the discrepancy in the sign of Δa^*, after the aging, the colors of all three-component mock-ups are in the unsaturated region of the CIELAB diagram, because of the different extent of the gray area at different L* values. Indeed, as shown by the arrows, the colorimetric coordinates of the three-component samples moved towards the white reference samples, close to the center of the CIELAB colour space. Figure 3.24c shows L* values (brightening/darkening) for unaged and aged mixtures paints, the differences being small in the case of samples containing PY1 and larger in the case of the ones containing PY139.
In a general view of the colorimetric results, significant discolorations were observed in the ternary mixtures due to a substantial loss of the yellow component b*, accompanied by an increase in the brightness L* (particularly evident in the samples containing PY139). Both the increase of L* and the decrease of the yellow chromatic component b* towards the center of the axis contributed to a loss of color saturation. Such

desaturation is thus considered evidence of yellow pigment degradation. For the samples containing Pb and Zn white, we argue that the surface texture variation is due to different siccative effects operated by the inorganic pigments, leading to a change in the volumetric shrinkage and, as a consequence, to a different surface light scattering. On the other hand, the loss of color saturation is more evident in the samples with titanium dioxide, which show the most evident discoloration after aging.

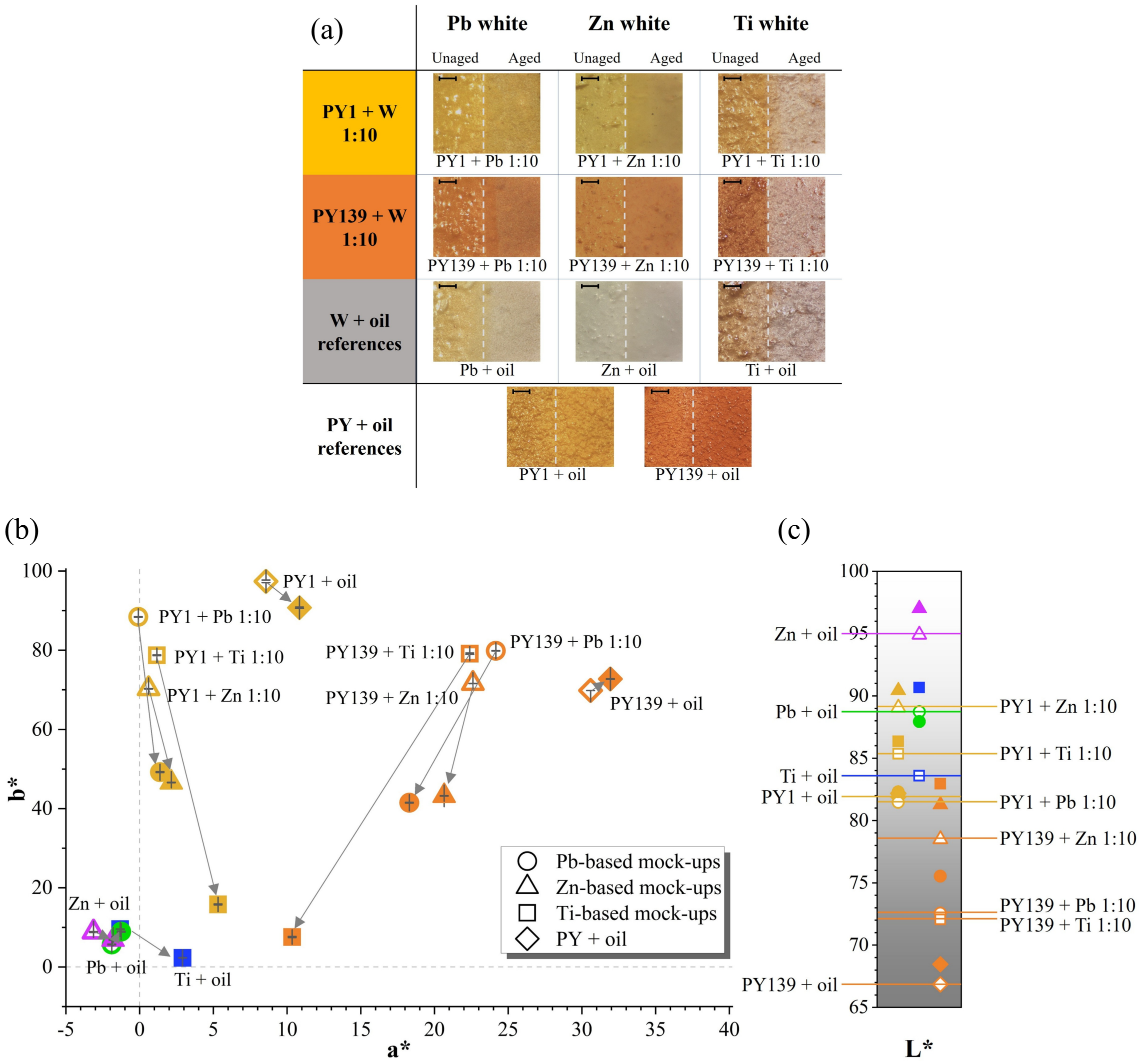

Figure 3.24 (a) Pictures of the ternary (1:10) and binary mixture samples acquired with the stereomicroscope (scale bar denotes 500 µm length). The images show the unaged (left) and aged (right) parts. (b) Diagram a* vs b* and (c) L* component of the CIELAB colour space: unaged (empty symbols) and aged (filled symbols) samples prepared with lead white (circle), zinc white (triangle), titanium white (square), and the reference samples of PY + oil (diamond). Arrows indicate the colorimetric variation from the unaged to the aged condition. Samples prepared with PY1 and PY139 are represented in yellow and orange, respectively.

3.2.3 Sub-surface degradation analysis by vibrational spectroscopies

The samples were then studied through ATR-FTIR and micro-Raman spectroscopies to understand the molecular variations after artificial aging. In Figures 3.25-3.27, FTIR and Raman spectra of the binary and ternary mixtures and the reference spectra of the pure organic pigments, linseed oil, and inorganic whites are reported. In particular, ATR-FTIR spectra were obtained by merging the MID- and FAR-infrared measurements. Only the fingerprint spectral ranges 2000-250 cm^{-1} for ATR-FTIR and 100-2000 cm^{-1} for micro-Raman measurements are reported. For both vibrational spectroscopies, the spectra were normalized in intensity with respect to the most intense signal of the inorganic white pigments to provide a proper qualitative analysis of the observed variations.

$2PbCO_3{\cdot}Pb(OH)_2$ effect

In the lead white-containing mixtures (Figure 3.25a), ATR-FTIR spectra are predominantly characterized by the signals of $2PbCO_3{\cdot}Pb(OH)_2$, including the signal at 3537 cm^{-1} of ν(OH) stretching, the band at 1390-1355 cm^{-1} of the asymmetric C-O stretching vibration of the carbonate group $\nu_{asy}(CO_3{}^{2-})$, the sharp characteristic peaks at 1043 of the symmetric $\nu_{sy}(CO_3{}^{2-})$ and 680 cm^{-1} of the out-of-plane rocking bending $\delta_{rocking}(CO_3{}^{2-})$ [113, 114]. The signal at 680 cm^{-1} was considered as the reference for the intensity normalization. In addition, the intense signals of linseed oil (such as the C-H symmetric and asymmetric stretching at 2929-2856 cm^{-1}, the C=O carbonyl band at 1740-1734 cm^{-1}, and the C-O stretching at 1240-1164-1170 cm^{-1} [118]), can be easily recognized in the unaged sample; a significant decrease in overall signal intensity occurs after the aging indicating the occurrence of different phenomena related to the binder curing process such as bulk polymerization and cross-linking typical of the lead-containing paints [117]. Finally, the peaks with low intensity in the fingerprint region between 1000 and 500 cm^{-1} associated with the yellow pigments PY1 and PY139 (brown and orange line, respectively) can be observed in both unaged (black line) and aged (dotted red line) three-component paint samples.
Raman spectra (Figure 3.25b) were normalized in intensity with respect to the most intense Raman band of the inorganic lead white, located at 1053 cm^{-1}, assigned to the $CO_3{}^{2-}$ symmetric stretching [129]. For the lead white-containing samples, the aging process induced a decrease in the intensity of the oil signals, as highlighted by the grey arrows in the spectra, suggesting an influence mainly on the binding medium.

In particular, the bands located at 1660, 1444, 1307, 1085, and 870 cm^{-1} show a lower intensity in the aged samples, consistent with an increase in oil drying, in agreement with the FTIR analysis. These bands are assigned respectively to the ν(C=C) stretching, to the methylene scissoring $\delta(CH_2)$ bending, to the in-phase methylene twisting $\delta(CH_2)$ bending, and the last two bands to the ν(C-C) stretching [141, 142]. Raman bands assigned to both yellow pigments show a minor intensity in the aged samples, as indicated by the brown and orange arrows. However, such a difference in signal intensity was observed to be strongly dependent on the area analyzed of the sample. Indeed, after the accelerated aging, a significant inhomogeneity of the sample topography and surface distribution of the yellow pigments was observed. Besides intensity variations, no shift or modification in the molecular structure is detected as a consequence of the aging process.

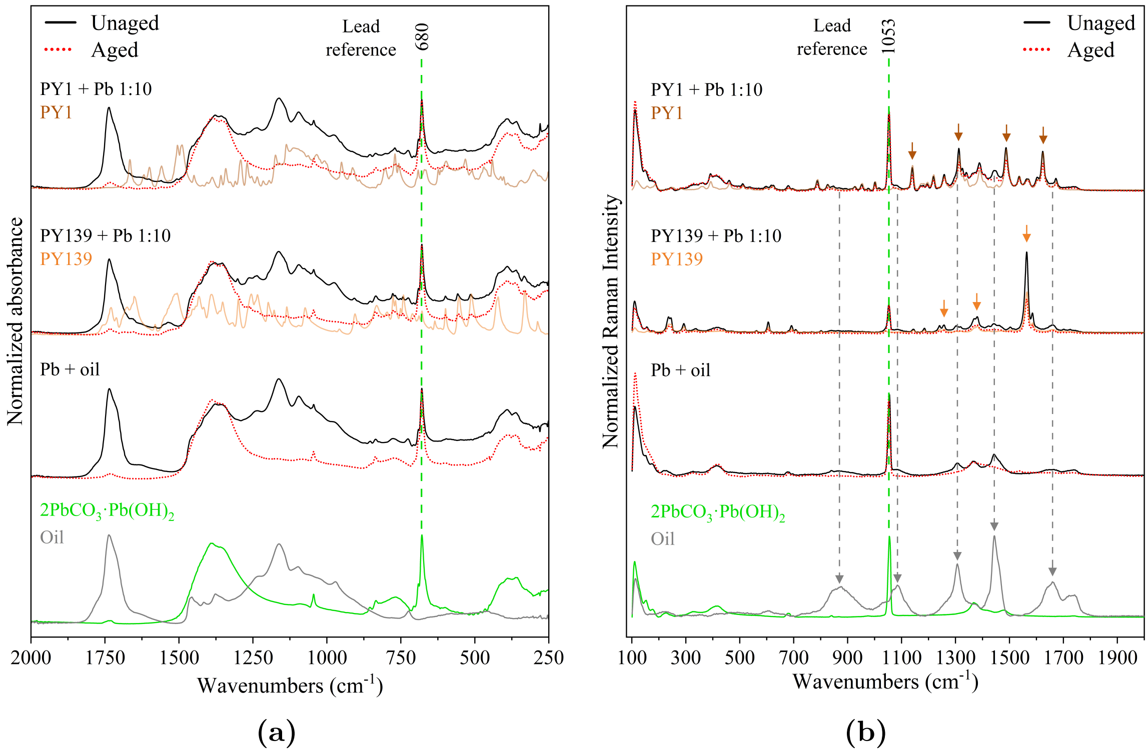

Figure 3.25 Comparison of the unaged (black line) and aged (dotted red line) lead white-based binary and ternary mixtures: (a) ATR-FTIR normalized spectra in the wavenumber range 2000-250 cm^{-1} and (b) Raman normalized spectra in the wavenumber range 100-2000 cm^{-1}. Reference spectra of PY1 (brown line), PY139 (orange line), $2PbCO_3 \cdot Pb(OH)_2$ (green line), and linseed oil (grey line) are also reported.

In the ATR-FTIR spectra acquired for the paints with $2PbCO_3 \cdot Pb(OH)_2$ powder having particles <44 μm (as reported in the data sheet), the peaks attributed to the yellow pigments (1000-500 cm^{-1}) remain evident even after aging. This suggests that the observed color change by colorimetry is probably due to the drying effect of lead white, a phenomenon well-documented in literature [59, 118]. Raman results suggest that the artificial aging in multi-component paint formulations induces mostly physical modifications, with a variation in the homogeneity of the mixture. Indeed, the different relative intensity in the investigated areas, before and after aging, could be due to different local pigment densities. On the other hand, it seems that the chemical stability of the three components (yellow pigment, binder, and white) is different: in particular, the inorganic and organic pigments seem chemically stable after aging, while the oil undergoes an acceleration in drying, as also observed in FTIR results.

ZnO effect

In the FTIR spectra of the ZnO-containing mixture (Figure 3.26a), the absorption band of the ZnO stretching vibration at 367 cm^{-1} is the most intense signal for the inorganic compound, and it was selected as the reference for normalization. Similarly to the samples prepared with lead white, the characteristic peaks of the linseed oil underwent a significant decrease in signal intensity as a consequence of the artificial aging. However, in this case, the unaged and aged samples exhibit a broad band at around 1585 cm^{-1}, assigned to the presence of zinc-carboxylates. As illustrated in Figure A.3 (pink region), this band was previously identified in the unaged samples as the zinc ν_{asy}(COO–) band [166] after the simple drying process of about 1 month. Moreover, in the aged samples, this band shows a broadening and significant shift of about 20 and 30 cm^{-1} for samples containing PY1 and PY139, respectively. These variations suggest a possible formation of metal soaps [79], with a different extent for the two yellow pigments. Indeed, it is known that zinc white promotes the formation of metal carboxylates when carboxylic acids are present [115]. In Figure A.3, it is also possible to see the presence of the characteristic peaks associated with the yellow pigments in the range 1500 and 800 cm^{-1}; despite their relatively low intensity, these peaks are still appreciable after the aging process.

In the Raman spectra of the samples prepared with zinc white (Figure 3.26b), the most intense band of ZnO at 439 cm^{-1}, assigned to the high-frequency E_2 mode [125], was used as the reference band for normalization. Zinc white is known to be a weak Raman scatterer [135]. For this reason, its reference band exhibits a relatively lower intensity with respect to the characteristic bands of yellow pigments and oil when mixed together. This is particularly noticeable in the case of the sample containing PY1, and even more with PY139. Nevertheless, an overall weak decrease of the signal intensity in both oil and yellow pigments following exposure to UV-VIS radiation was revealed. No band shifts were detected in the spectra.

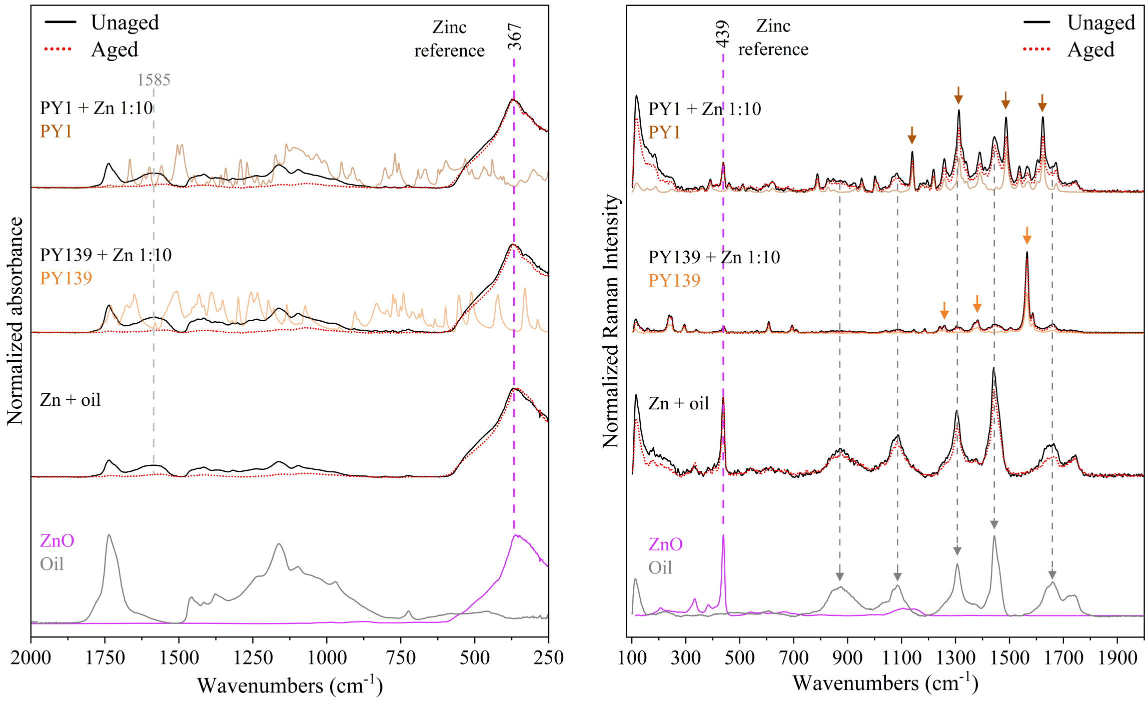

(a) (b)

Figure 3.26 Comparison of the unaged (black line) and aged (dotted red line) zinc white-based binary and ternary mixtures: (a) ATR-FTIR normalized spectra in the wavenumber range 2000-250 cm^{-1} and (b) Raman normalized spectra in the wavenumber range 100-2000 cm^{-1}. Reference spectra of PY1 (brown line), PY139 (orange line), ZnO (pink line), and linseed oil (grey line) are also reported.

The samples containing ZnO show the FTIR spectral features of the yellow pigments even after exposure to the aging lamp. Peaks of low intensity were detected within the range 1500-800 cm^{-1}, indicative of the presence of both monoazo and isoindoline molecules in the first microns of the samples probed by the ATR-FTIR. A photocatalytic reaction mechanism of ZnO was expected to be observed, as zinc white presents a nano-crystalline structure [162], which will be seen in more detail later. In general, the low-intensity Raman signals assigned to the binder could be due to a greater drying process of the oil stimulated by the inorganic white, but a partial degradation of the fatty acids constituting the binding medium cannot be excluded. In the same way, the intensity of the Raman signals attributed to the yellow pigments decreased after UV-VIS exposure. As seen above, the inorganic white and the organic pigments seem chemically stable after aging.

TiO_2 effect

The ATR-FTIR spectra of the samples prepared with TiO_2 (Figure 3.27a) exhibit a dominant feature related to the titanium reference peak, with a maximum at 400 cm^{-1} attributed to the lattice vibrations of anatase [116]. Following aging, this band appears to be more defined and sharper. In addition, three broad bands at 1200, 1070, and 925 cm^{-1}, of uncertain identification, seem to become more evident after the aging treatment (Figure A.4a). The loss of structural resolution within the skeletal vibrations range (1400-800 cm^{-1}) is attributed to the degradation products of the binding medium [117]. In this case, it is important to note that the characteristic FTIR absorption peaks of PY1 and PY139 within the 1800-800 cm^{-1} range are distinctly evident in the unaged samples; after the aging, these peaks completely disappear.
The Raman bands associated with the yellow pigments are very low in intensity after the artificial aging when TiO_2 is used as inorganic white (Figure 3.27b). The most intense band at 147 cm^{-1}, corresponding to the anatase structural mode E_g [131], was selected as the reference band for normalization, while the rutile polymorph is detected with very low intensity (according to XRD 20.5% rutile). This anatase band is very intense, attenuating to all the other organic bands. For this reason, Raman spectra were also collected as static acquisition, focused in the range 550-1690 cm^{-1} and increasing the laser power, in order to exclude the collection of the most intense anatase Raman band at 147 cm^{-1} (Figure A.4b). A new reference band for titanium dioxide was set at 639 cm^{-1}, which is also associated with the E_g structural mode of the anatase phase, though with less intensity [134]. By using this approach, it was possible to calculate the variations in signal intensity for the three-component samples by selecting two representative bands at 1623 cm^{-1} related to the nitro asymmetric stretching for PY1, and at 1564 cm^{-1} related to the amide group for PY139 [120]. The decrease in signal intensity was calculated as the percentage variation between the area under the selected Raman band before and after the aging process, revealing a value greater than 70% after the treatment in the climate chamber for both samples. No shifts or variations in the Raman spectra profiles were recognized, thereby indicating that noticeable new molecular species following aging were not found.
The absence of FTIR spectral features related to PY1 and PY139 in the samples where TiO_2 is present in nanopowder form (<100 nm as reported in the data sheet), as a mixture of rutile and anatase polymorphs, could suggest their possible photocatalytic degradation by the inorganic white. In addition, a drying process catalyzed by this white nanosized pigment could be behind the change in the characteristic oil spectrum in the range 1200-925 cm^{-1}, not observed in the presence of the other two whites.

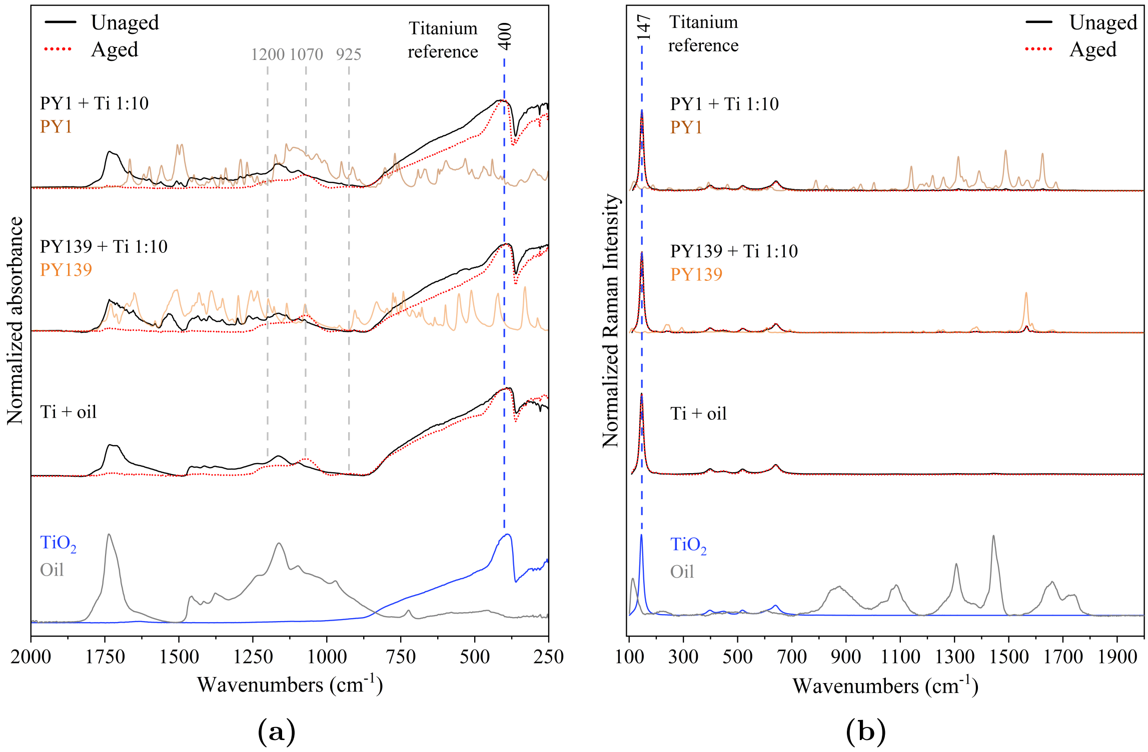

Figure 3.27 Comparison of the unaged (black line) and aged (dotted red line) titanium white-based binary and ternary mixtures: (a) ATR-FTIR normalized spectra in the wavenumber range 2000-250 cm^{-1} and (b) Raman normalized spectra in the wavenumber range 100-2000 cm^{-1}. Reference spectra of PY1 (brown line), PY139 (orange line), TiO_2 (blue line), and linseed oil (grey line) are also reported.

In contrast to the ATR-FTIR results, PY1 and PY139 signals are still recognizable in the Raman spectra after aging. This discrepancy between the two vibrational spectroscopies could be due to a higher limit of detection (LOD) of the ATR-FTIR technique, especially in the case of complex mixtures in which overlapping signals of the different components are observed [167]. Considering that LOD is strongly dependent on sample formulations, the values reported by authors for ATR analyses of linseed oil and pigment mixtures, under experimental conditions similar to the present study, range from 1.5-2.7 wt% [168]. These values, compared with the PY concentration in the samples under investigation (6 wt% of the overall paint composition), would allow the detection of the pigments only in the case of unaged samples; conversely, in the hypothesis of degradation, the concentration could have dropped below the LOD resulting in no signal evidence in the aged samples. However, the Raman results support the hypothesis that such light-induced pigment degradation may have effectively occurred in the presence of TiO_2.

3.2.4 Surface degradation and chemical mapping by ToF-SIMS

Figures 3.28-3.33 show the ToF-SIMS results for the three-component paint samples. Synthetic organic pigments and, more in general, modern colorants and pigments were extensively studied through different mass spectrometry techniques [144, 145]. In this case, ToF-SIMS allows the ionization of the elements and molecules from the first nanometers of the sample surface, providing data as mass spectra and chemical maps. Such kind of investigation is crucial to discriminate against chemical phenomena induced by the UV-VIS radiation occurring on the sample surface. ToF-SIMS measurements on real paint samples are challenging due to different factors, like the inherently non-flat nature of the paint surfaces, the presence of organic and inorganic compounds in the same chemical matrix, and the potential interactions between them. Mass spectra of the reference samples W + oil (Figures A.5 and A.6) and the pure yellow pigments (Figures 3.14 and 3.16) were first collected and then used to correctly attribute the ion peaks present in the mass spectra of the three-component samples. ToF-SIMS measurements were recorded in both polarities but are presented according only to the polarity where the molecular peak of the yellow pigments showed higher ionization yield. Data were acquired separately in the unaged and aged regions, as indicated in all the mass spectra by black and red lines, respectively.

Lead white-based ternary mixtures

Figures 3.28 and 3.29 show ToF-SIMS mass spectra and chemical maps for the samples realized with lead white. PY1 molecular ion signal was recorded in positive ion mode as its protonated molecule $[M+H]^+$ ($C_{17}H_{17}N_4O_4^+$ m/z 341.12), PY139 molecular ion signal was detected in negative ion mode $[M]^-$ ($C_{16}H_9N_5O_6^-$ m/z 367.05). Additional characteristic molecular fragments were also identified: $C_7H_9N_2O_2^+$ m/z 153.08 for PY1, $C_5H_2N_3O_3^-$ m/z 152.01 and $C_{12}H_4NO_2^-$ m/z 194.02 for PY139 (Figure 3.28a-b, brown and orange diamonds). The aging process led to a significant decrease in PY1 molecular ion peak intensity; this is less evident for PY139. The intensity of O^- and OH^- signals was observed in the aged samples (not shown).

In the range m/z 200-920, several ion signals of lead white were revealed in both positive (Pb^+, $PbOH^+$, Pb_2^+, Pb_2O^+, $Pb_2O_2H^+$, $Pb_3O_2^+$, $Pb_3O_3H^+$, $Pb_4O_3^+$, $Pb_4O_4H^+$) and negative ion mode (Pb^-, $PbOH^-$, PbO_2H^-, $Pb_2O_2^-$, $Pb_2O_3^-$, $Pb_2O_3(OH)^-$, $Pb_2O_3(CO_3)^-$, $Pb_3O_4^-$, $Pb_3O_4(OH)^-$, $Pb_4O_5^-$) (Figure 3.28a-b, green font) [149–153]. These lead-related signals were recorded in the unaged and aged parts of the samples, although with markedly higher intensities in the aged ones.

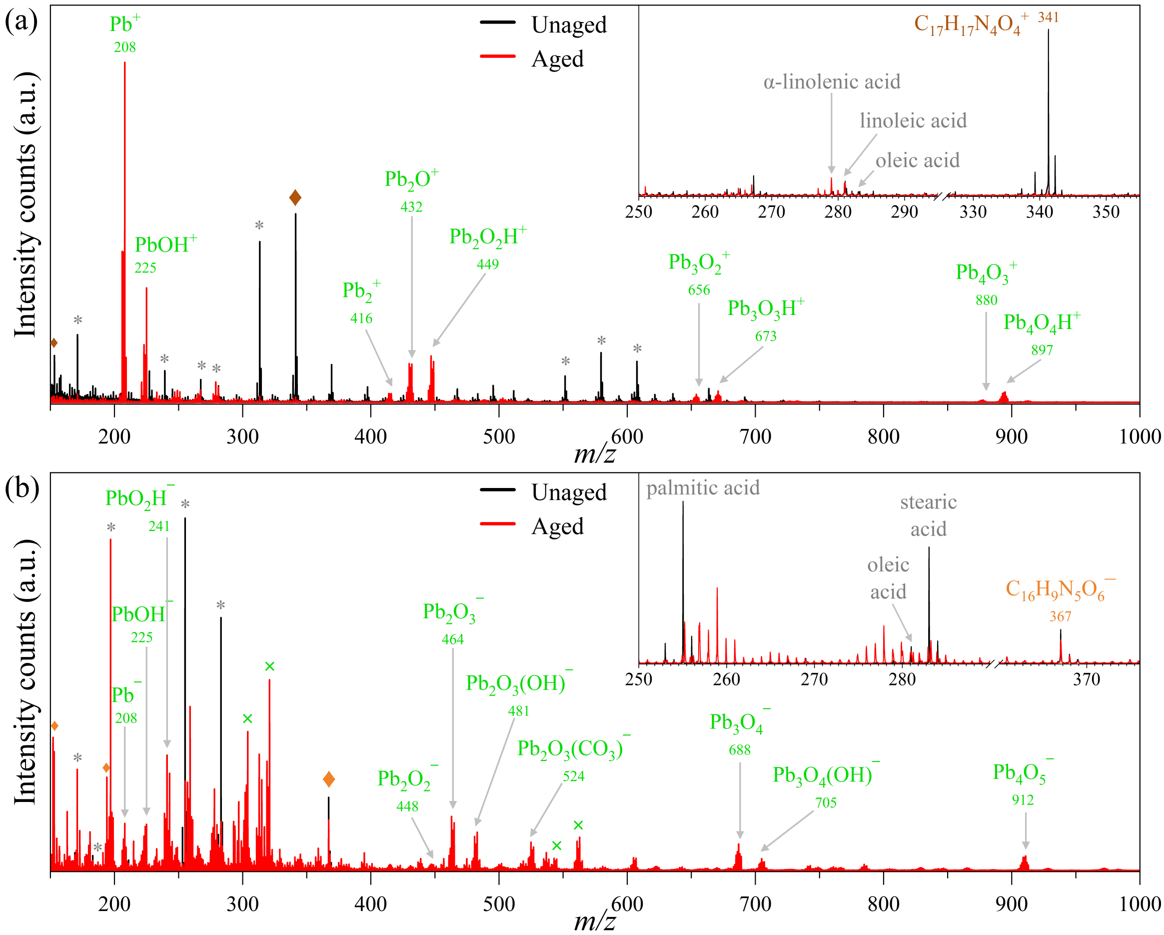

Figure 3.28 ToF-SIMS mass spectra normalized to total counts in the mass-to-charge range m/z 150-1000 acquired for the unaged (black line) and aged (red line) three-component paint samples containing lead white with PY1 (a), in positive ion mode, and with PY139 (b) in negative ion mode. Lead-related signals are written in green, linseed oil fragments are marked with gray asterisks, and the molecular signals of the yellow pigments are marked with diamonds. Marked with × are lead sulfates of the manufacturing process.

For what regards the linseed oil (Figure 3.28a-b, gray asterisks), the mass spectra revealed the presence of protonated fatty acids of α-linolenic ($C_{18}H_{31}O_2^+$ m/z 278.98), linoleic ($C_{18}H_{33}O_2^+$ m/z 280.96), and oleic acid ($C_{18}H_{35}O_2^+$ m/z 283.19) in positive ion mode (inset in Figure 3.28a). Secondary ion yields of protonated palmitic and stearic acids at m/z 257.22 and 285.24 are very low in the spectra. However, distinctive fragments indicative of the drying and aging of the oil were recorded: acylium ions of azelaic, palmitic, and stearic acids (m/z 171.11, 239.23 and 267.27), as well as diacylglycerol ester ions containing palmitic and stearic acids (m/z 551.51, 579.55 and 607.58), and monoacylglycerol ions of palmitic acid (m/z 313.28). In negative ion mode, the predominant signals in the unaged mass spectrum are the deprotonated fatty acids of palmitic ($C_{16}H_{31}O_2^-$ *m/z* 255.27), oleic ($C_{18}H_{33}O_2^-$ *m/z* 281.26), and stearic acid ($C_{18}H_{35}O_2^-$ *m/z* 283.31) (inset in Figure 3.28b). Additionally, signals corresponding to the oxidation and degradation products of the oil were observed: deprotonated decanoic acid ions (*m/z* 170.90), deprotonated azelaic acid ions (*m/z* 187.13 very low intensity), and the aliphatic chain fragments of palmitic acid (*m/z* 196.91). All these fragments are characteristic of the oil binder [150, 151, 169]. The intensity of these signals is higher in the unaged region of the sample with PY1, except for the protonated monocarboxylic fatty acids, which demonstrate almost the same intensity in both regions. In contrast, for the sample with PY139, these signals are more intense in the unaged region for stearic and palmitic acids and in the aged region for the degradation fragments. Lead soaps were not detected, in agreement with FTIR and Raman techniques.

Figures 3.29 and 3.30 show the normalized chemical maps acquired from the unaged and aged regions of the lead-based samples containing PY1 and PY139, respectively. Notable changes were observed in the intensity distributions of the molecular ion signals ($C_{17}H_{17}N_4O_4^+$ for PY1 and $C_{16}H_9N_5O_6^-$ for PY139). The ion distribution of PY1 and PY139 signals seems to be homogeneous in the unaged part of the samples (Figures 3.29a.1 and 3.30a.1), while the yellow pigment signals are distributed in rounded spots of some tens of microns in the aged parts (Figures 3.29b.1 and 3.30b.1). This kind of inhomogeneity in the distribution of the yellow pigments was previously also detected through Raman microscopy. Additionally, in the unaged samples, the chemical maps of the fatty acid signals of the oil (protonated linoleic acid $C_{18}H_{33}O_2^+$ in Figure 3.29a.2 and deprotonated stearic acid $C_{18}H_{35}O_2^-$ in Figure 3.30a.2) showed a homogeneous distribution across the surface areas analyzed. After aging, a higher intensity is observed in the spot regions where the yellow pigment intensity is also concentrated (Figures 3.29b.2 and 3.30b.2), probably due to the localized effect of oil absorption by the granules themselves. Conversely, the intensity distribution of lead-related signals ($PbOH^+$ in Figure 3.29a.3 and $PbOH^-$ in Figure 3.30a.3) in both samples was non-homogeneous and complementary to that observed for the pigment molecular signals, with higher intensity counts in the aged parts (Figures 3.29b.3 and 3.30b.3).

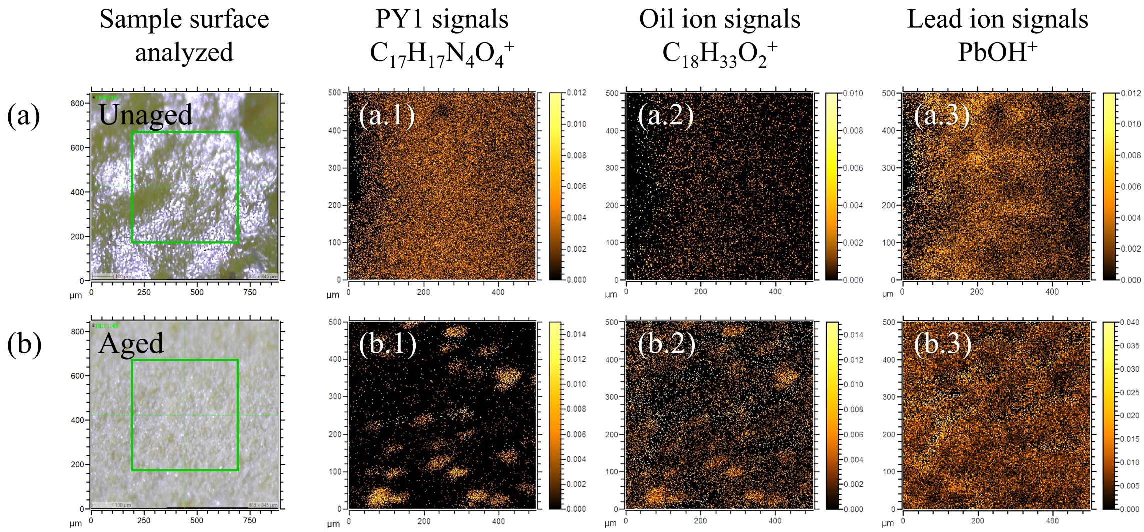

Figure 3.29 Images of the analyzed surface areas and the corresponding normalized ToF-SIMS ion maps (FoV: 500×500 μm^2) acquired in positive ion mode for the (a) unaged and (b) aged three-component sample containing $2PbCO_3{\cdot}Pb(OH)_2$ with PY1. The normalized chemical maps provide the ion signals of: the yellow pigments PY1 ($C_{17}H_{17}N_4O_4^+$, panels a.1 and b.1), protonated linoleic acid from the oil binder ($C_{18}H_{33}O_2^+$, panels a.2 and b.2), and lead hydroxide ($PbOH^+$, panels a.3 and b.3).

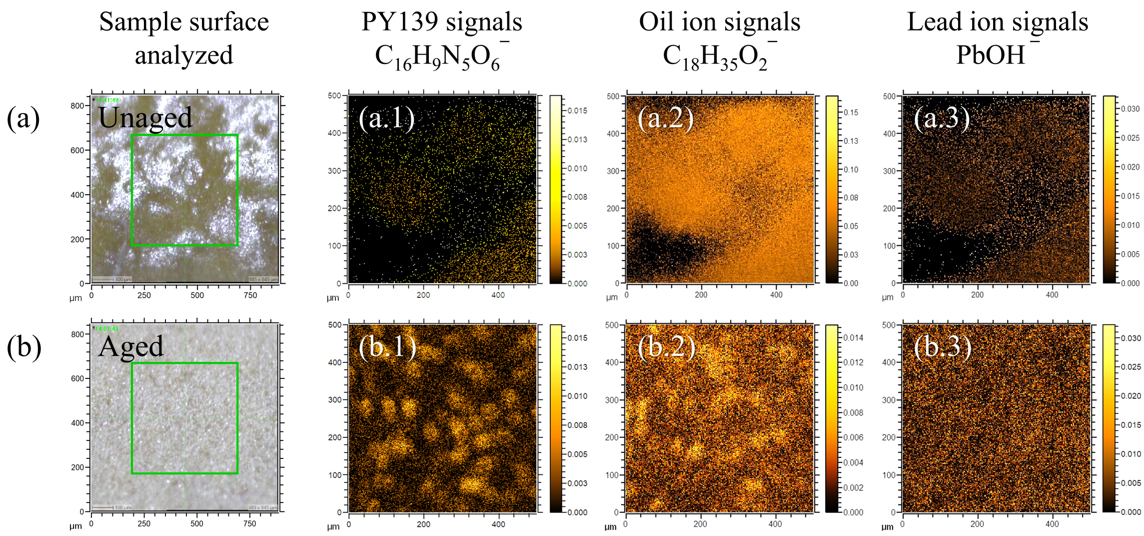

Figure 3.30 Images of the analyzed surface areas and the corresponding normalized ToF-SIMS ion maps (FoV: 500×500 μm^2) acquired in negative ion mode for the (a) unaged and (b) aged three-component sample containing $2PbCO_3{\cdot}Pb(OH)_2$ with PY139. The normalized chemical maps provide the ion signals of: the yellow pigments PY139 ($C_{16}H_9N_5O_6^-$, panels a.1 and b.1), deprotonated stearic acid from the oil binder ($C_{18}H_{35}O_2^-$, panels a.2 and b.2), and lead hydroxide ($PbOH^-$, panels a.3 and b.3).

In a general view, ToF-SIMS results showed that after the aging process, the ion signals associated with $2PbCO_3{\cdot}Pb(OH)_2$ are more intense, and the signals related to the oil binder, such as the monoacylglycerol and diacylglycerol ions, strongly decrease in intensity, indicating a chemical modification of the binding medium. This was also observed in the corresponding unaged/aged reference samples (Pb + oil, Figure A.5). In particular, the increase of the signal intensity ratio between the two ion species O^-/OH^- suggests the auto-oxidation of oils catalyzed by the presence of metals [170], in this case operated by lead [59]. From a mechanical point of view, the drying and aging of the oil lead to the hardening and shrinking of the paint and as a consequence to a reorganization at the molecular scale, exposing the pigment granules on the surface. This would explain the increased detection of lead-related signals, as well as those of yellow pigments (especially PY139). More in detail, the normalized chemical maps of the aged surfaces in Figures 3.29 and 3.30 revealed a spot intensity distribution for the yellow pigments (panels a.1). For this reason, ToF-SIMS analysis evidences that the granules of non-well-dispersed pigment underwent reduced interaction with other components during UV-VIS exposure. Complementarily, outside the pigment granules, low-intensity and homogeneous distribution in the chemical maps was observed as a consequence of aging. It may therefore be concluded that the surface degradation of the yellow pigments in these samples is partial but wider than the area covered by granules, resulting in an overall alteration in the perceived color of the samples. The presence of pigment granules also explains the detection of yellow pigment signals after aging, as previously indicated by the two vibrational spectroscopies, as well as the heterogeneity observed in the Raman analysis. Finally, lead soap formation was not observed in the ToF-SIMS analysis, which may be attributed to either the short timing of the aging process or the low intensity of these signals.

Zinc white-based ternary mixtures

The three-component paint samples prepared with zinc white were also analyzed using ToF-SIMS. The ToF-SIMS analysis was initially conducted in static mode to investigate surface chemistry. Given that the pigment was previously detected before and after the aging process using FTIR and Raman spectroscopy, our goal was to further characterize its surface composition. However, the generation of secondary ions from the surface proved to be challenging, likely due to charging effects or matrix effects inherent to the sample. The molecular ion peak of the pigment was not detected in the sample containing PY1, neither in the unaged nor in the aged part (Figure A.7a). Similarly, for the sample containing PY139, the molecular peak was observed only in the unaged part with extremely weak intensity (Figure A.7b). For both the samples, no additional characteristic molecular ion peaks at high mass values related to the pigments were observed in the aged part. Also, the characteristic isotopic patterns of ZnO, typically observed for this white pigment under ion bombardment (Figure 3.21), were not recorded [157, 158]. These limitations hindered the direct assessment of surface molecular distribution and required an alternative analytical approach. Considering that FTIR and Raman spectroscopy have a sampling depth range of a few microns, we opted to perform depth profiling experiments to investigate the molecular distribution beneath the surface using a different ion as a tracking signal. Depth profiling experiments were conducted for the sample containing PY1, selected as a representative case, by using the Cs^+ sputtering source to produce a crater >10 μm (Figure 3.31), as estimated by the stylus profiler (Figure A.8), and following the ion signal distribution of CN^- (m/z 26.01).

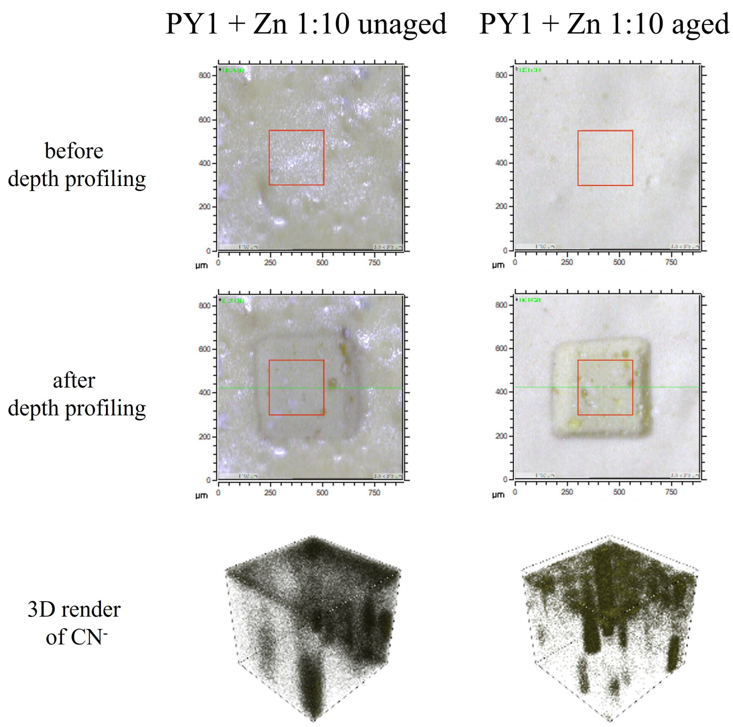

Figure 3.31 Images of the analyzed surfaces with ToF-SIMS before and after the depth profiling acquisition for the three-component samples containing zinc white with PY1 (top), and the resulting 3D renderings of CN^- ions (bottom). On the left is the unaged sample, and on the right is the aged one.

As reported in the 3D renderings of CN^- ions (Figure 3.31, bottom), we observed that such a characteristic ion signal, common to both pigment molecules, is distributed in well-defined granules at the surface but also in depth. This finding is similar to some aspects of what was observed for the three-component lead white samples, but in this case, the pigment is clearly present also on the surface, suggesting that the organic material had not undergone significant degradation during the artificial aging process. The stability of the yellow pigments in the presence of zinc white in these conditions was unexpected, as zinc oxide is commonly reported to exhibit photocatalytic activity comparable to titanium dioxide, which often leads to the degradation of organic components [171].

Titanium white-based ternary mixtures

Figures 3.32 and 3.33 illustrate ToF-SIMS mass spectra and chemical maps for the three-component paint samples prepared with titanium white. In the mass spectra collected in negative ion mode, it was possible to detect the deprotonated molecular ion peak $[M\text{-}H]^-$ at *m/z* 339.06 ($C_{17}H_{15}N_4O_4^-$) for PY1 and the molecular ion peak $[M]^-$ at *m/z* 367.05 ($C_{16}H_9N_5O_6^-$) for PY139. As in the case of lead-based samples, additional characteristic fragments of the molecular ion peaks were also reported in the mass spectra: $C_7H_7N_2O_2^-$ *m/z* 151.06 for PY1, $C_5H_2N_3O_3^-$ *m/z* 152.01, and $C_{12}H_4NO_2^-$ *m/z* 194.02 for PY139 (Figure 3.32a-b, brown and orange diamonds). It is interesting to note that after the aging process, the molecular ion peaks of both pigments, as well as the characteristic fragments, are nearly absent in the mass spectra.

Secondary ion signals corresponding to the titanium white pigment (TiO_2^- *m/z* 79.94, $(TiO_2)OH^-$ *m/z* 96.94, $Ti_2O_3^-$ *m/z* 143.85, and $(TiO_2)_2OH^-$ *m/z* 176.85) [154, 155] were identified in the mass spectra of both samples (Figure 3.32a-b, blue font). These TiO_2-related signals were detected in both the unaged and aged parts of the samples, with higher signal intensity observed in the unaged regions. Also in this case, in the mass spectra, the intensity of O^- and OH^- signals increased after aging (not shown).

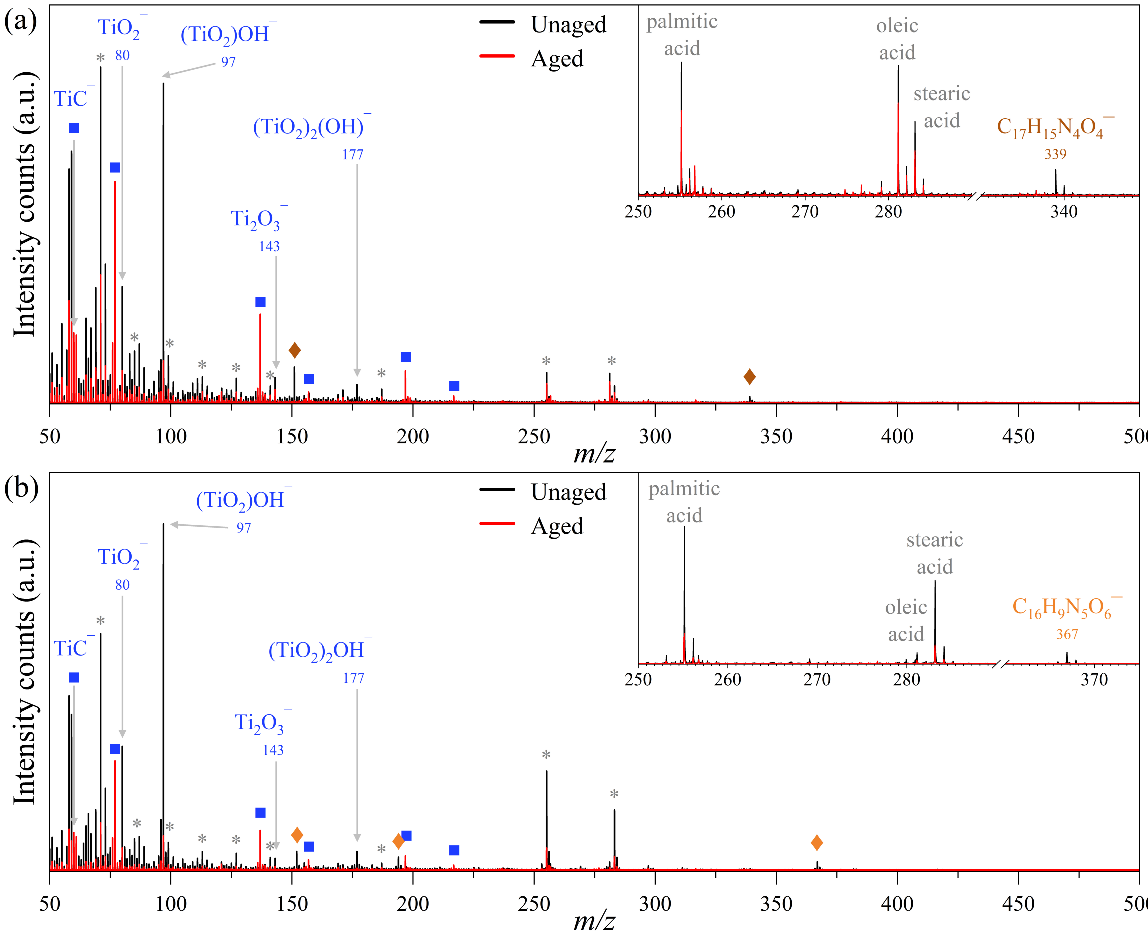

Figure 3.32 ToF-SIMS mass spectra normalized to total counts in the mass-to-charge range m/z 50-500 acquired for the unaged (black line) and aged (red line) three-component paint samples containing titanium white with PY1 (a) and with PY139 (b) in negative ion mode. TiO_2-related signals are written in blue, linseed oil fragments are marked with gray asterisks, TiC-adducts are marked with blue squares, and the molecular peaks of the yellow pigments are marked with diamonds.

Characteristic peaks were also identified for the binding medium (Figure 3.32a-b, grey asterisks). In particular, deprotonated fatty acids of palmitic, oleic, and stearic acid were recorded (Figure 3.32a-b, insets). For both unaged samples, the relatively weak intensity of the azelaic acid ions and of some aliphatic chain fragment ions coming from the fatty acids with chemical structure $C_2H_3(CH_2)_xCOO^-$, where x ranges from 0 to 5, were detected (Figure 3.32a-b, grey asterisks at low mass values). The intensity of these ion signals related to linseed oil decreases after aging, indicating a degradation process that also affects the binding medium. In addition, it is important to highlight that the ion signal ratio between the oleic and stearic acid is different for the sample prepared with PY1 and PY139 but it remains constant in both the unaged and aged part of the samples. This is reported in literature being indicative of a different oxidation state of the oil leading to a different oleic-stearic acid ratio [172].

The interaction of titanium with the carbon present in the organic component (oil and pigment) may result in the formation of TiC adduct ions. Two distinct adducts were identified in the mass spectra (Figure 3.32a-b, blue squares). The first group of adducts contains different titanium-carbon units ionized together with a hydroxyl group, with general structure $(TiC)_nOH^-$, where n, ranging from 1 to 3, represents the number of repeated units: $(TiC)OH^-$ *m/z* 76.95, $(TiC)_2OH^-$ *m/z* 136.91, and $(TiC)_3OH^-$ *m/z* 196.86. The second group of ion adducts presents the chemical structure $TiO_2(TiC)mOH^-$, with m corresponding to 1 and 2, composed by the following signals: $TiO_2(TiC)OH^-$ *m/z* 156.89, and $TiO_2(TiC)_2OH^-$ *m/z* 216.84. These TiC adducts were observed only after the artificial aging process, further confirming the occurrence of a chemical degradation of the organic matter.

Figures 3.33 and 3.34 show the normalized chemical maps acquired from the unaged and aged regions of the titanium-based samples containing PY1 and PY139, respectively. The surface color change is appreciable by the naked eye in the ToF-SIMS micro camera image, showing the analysis area (Figures 3.33 and 3.34, left side). The chemical distribution of the molecular ion peaks of the yellow pigments PY1 ($C_{17}H_{15}N_4O_4^-$, Figure 3.33a) and PY139 ($C_{16}H_9N_5O_6^-$, Figure 3.34a) clearly indicate that after the artificial aging, the yellow pigments are not present in their original form. The same effect, to a lesser extent, can also be appreciated for the linseed oil (deprotonated stearic acid $C_{18}H_{35}O_2^-$, Figures 3.33b and 3.34b). In addition, the unaged area of the samples initially including the oil-pigments mixture provides more intense TiO_2^- signals that become less intense in the aged area (Figures 3.33c and 3.34c). The degradation of the organic material in these three-component samples is observed by the presence of TiC adduct ions in the aged area of the samples (Figures 3.33d and 3.34d); such adducts were not detected in the unaged parts for both the three-component paints and the reference sample (Ti + oil, Figure A.6).

ToF-SIMS results confirm that the artificial aging process induced a photodegradation on the surface of the samples, operated by the TiO_2-based inorganic white.

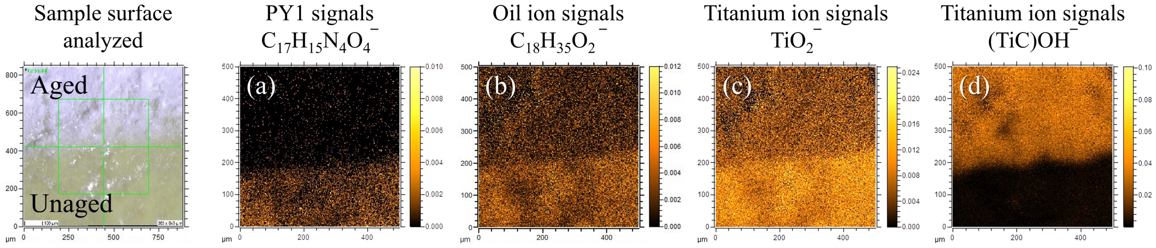

Figure 3.33 Images of the analyzed surface areas and the corresponding normalized ToF-SIMS ion maps (FoV: 500×500 μm^2) for the three-component sample containing TiO_2 with PY1. The measurements were acquired in negative ion mode in the middle region between the aged and unaged areas of the sample. The normalized chemical maps show the ion signals of: (a) the yellow pigments PY1 ($C_{17}H_{15}N_4O_4^-$), (b) deprotonated stearic acid from the oil binder ($C_{18}H_{35}O_2^-$), (c) titanium dioxide (TiO_2^-), and (d) a TiC-adduct ($(TiC)OH^-$).

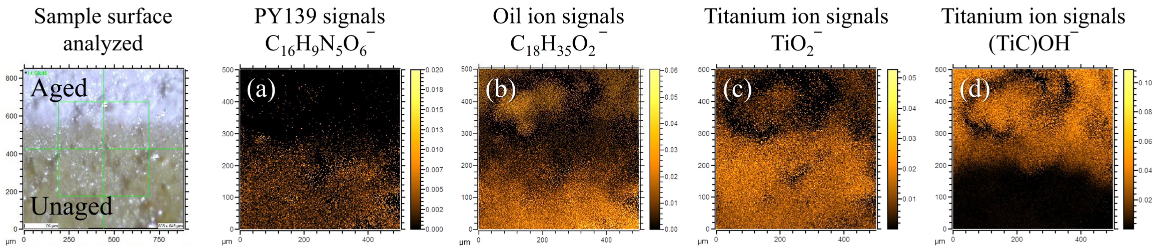

Figure 3.34 Images of the analyzed surface areas and the corresponding normalized ToF-SIMS ion maps (FoV: 500×500 μm^2) for the three-component sample containing TiO_2 with PY139. The measurements were acquired in negative ion mode in the middle region between the aged and unaged areas of the sample. The normalized chemical maps show the ion signals of: (a) the yellow pigments PY139 ($C_{16}H_9N_5O_6^-$), (b) deprotonated stearic acid from the oil binder ($C_{18}H_{35}O_2^-$), (c) titanium dioxide (TiO_2^-), and (d) a TiC-adduct ($(TiC)OH^-$).

3.2.5 The importance of crystallographic and morphological analysis in reactive inorganic pigments

To assess the nature of the zinc white used in our samples, an XRD analysis on pure ZnO powder was performed, which confirmed that the pigment consisted predominantly of the wurtzite phase (Figure 3.23). The photocatalytic activity of zinc oxide is strongly dependent on its shape, crystallinity, particle size, and aggregation state [163]. Specifically, bulk or aggregated ZnO exhibits significantly lower photocatalytic efficiency compared to its nanostructured counterparts. The crystallite size calculated with the Scherrer formula for ZnO powder is about 40-44 nm. Additional characterization through SEM analysis (Figure A.9a) revealed that the crystal size ranges from approximately 180 nm to 400 nm (with isolated large-sized crystals of about 800 nm),

further supporting the classification of this ZnO as aggregated material. The large particle size of ZnO likely contributed to pigment aggregation, also considering that the viscosity of the PY + oil mixture is much higher, and the dispersion is significantly lower, therefore resulting in a reduction of the effective surface area available for photocatalysis. Since the degradation of organic molecules by ZnO is typically more efficient when the material is in nanometric form [163], the low photocatalytic activity observed in our samples can be attributed to the aggregation of the pigment. This suggests that the stability of the organic components of the paint during aging was not significantly impacted by ZnO-related photocatalytic degradation. These findings highlight the importance of ZnO particle morphology in dictating its reactivity and its potential effects on the long-term preservation of painted surfaces.
XRD analysis was also performed on pure TiO_2 powder. It is well known in literature that TiO_2 in nanosized form is able to induce the degradation of organic molecules [173]. The powder of TiO_2 used in this work is characterized by particles with an average size <100 nm, as also confirmed by SEM (Figure A.9b). At the same time, the percentage of 79.5% anatase phase and 20.5% rutile phase, with crystallite sizes around 13-17 nm calculated from XRD analysis (Figure 3.22), presents a relatively lower crystallinity degree than ZnO powder. Therefore, such a combination of nanosized, low crystalline titanium dioxide with the organic pigments PY1 and PY139 could induce the discoloration of the paint under high relative humidity and UV-VIS light exposure [2, 174]. In conclusion, the resulting photodegradation occurred in the uppermost layers of the samples containing TiO_2, as evidenced by a surface-sensitive technique like ToF-SIMS. The progressive surface-sensitivity of the techniques (ToF-SIMS > μ-RS 785 nm > ATR-FTIR) would also explain the detection of yellow pigment signals after aging with μ-RS (despite the significant decrease in intensity), whereas the high LOD of ATR-FTIR prevents their observation.

3.3 Conclusions

This study employed a multi-technique approach aiming to highlight the impact of artificial aging on organic-inorganic mixtures, namely three-component paints containing linseed oil, selected yellow pigments (PY1 and PY139), and different white pigments: lead carbonate basic, zinc oxide, and titanium dioxide. The findings provide valuable insights into the degradation mechanisms affecting both the binding medium and the yellow pigments. The three analytical techniques with different degrees of surface sensitivity confirmed the photodegradation of the yellow molecules at the surface levels as a consequence of their interaction with UV-VIS radiation. This study stresses the need to consider color fading as a complex result due to many factors, in part depending on the chemical reactivity of the mixture components and in part on physical properties, such as morphology, granulometry, degree of dispersion, oil absorption ratio, and drying power (mainly influenced in this work by the choice of inorganic white pigment). In such complex systems, the multi-technique approach showed that significant composition changes can occur only at the very uppermost layers of the samples and thus that bulk and surface must be properly differentiated, in view of a more comprehensive understanding of paint stability when both organic and inorganic pigments are included.

Specifically, in the case of lead white, the degradation observed is primarily attributed to the drying process of the oil, leading to changes in its optical properties, and the discoloration of only the fine fraction of the yellow pigments dispersed in the binder. Rather than undergoing significant chemical changes, massive yellow granules remained unaltered, although being more exposed, likely as a consequence of the reorganization of the oil. Conversely, zinc oxide exhibited less evident discoloration. Although ZnO is known for its potential as a photocatalytic agent under UV-VIS exposure, the particle size can reduce its effectiveness in catalyzing the degradation of the binding medium or pigment molecules. This indicates that the use of a similar type of bulk ZnO does not pose a severe risk for the photodegradation of oil-based paints in modern and contemporary formulations. On the other hand, titanium dioxide demonstrated a markedly different behavior. Even with a low degree of crystallinity, if present in nanometric form, TiO_2 effectively induced photodegradation of the organic matrix. This finding raises concerns regarding the formulation of paints containing nano-TiO_2, as its strong photocatalytic activity can lead to unintended degradation of the binding medium and pigments. This serves as a cautionary note for conservators and paint manufacturers when formulating artworks and coatings, especially in environments with prolonged UV-VIS and humidity exposure. From a practical perspective, these results offer key takeaways for both conservators and modern paint manufacturers. For restoration professionals, understanding the distinct behaviors of these pigments under aging conditions can inform preservation strategies, particularly when dealing with historical artworks. For those working with eco-friendly paints, the high photocatalytic efficiency of TiO_2 could be leveraged for environmental applications, such as the degradation of pollutants in air-purifying coatings. However, careful consideration is needed to balance the benefits of this functionality with the potential risks of premature degradation in artistic and protective coatings.

4 Solar photostability of Co-phthalocyanine with TiO_2 nanopowders

This chapter reports the results of the study on aging processes in powder samples of mixed organic and inorganic pigments.

The stability of modern organic pigments with excellent lightfastness, such as phthalocyanine molecules, in presence of inorganic compounds, represents a research area of interest in both the fields of cultural heritage and industrial applications, including for example, the fabrication of photoelectronic devices and solar cells. In particular, this study investigates the stability of a cobalt phthalocyanine (CoPc) pigment in presence of titanium dioxide (TiO_2) under different aging processes.

This work considers a pigment more stable to light than the two yellows of monoazo and isoindoline pigments, as classified by the ASTM. In this case, only titanium dioxide was considered as the inorganic component, since the previous Chapter demonstrated that it exhibited the highest reactivity under aging. Furthermore, powder samples were investigated without the addition of a binder, thereby limiting the interaction to the two main components: organic and inorganic pigment.

Preliminary studies were carried out on samples of CoPc+TiO_2 powder mixtures subjected to both artificial UV-VIS aging and exposure to natural sunlight. The objective was to examine the variations induced by aging through a multi-technique approach by colorimetry, Fourier transform infrared (FTIR), and Raman spectroscopy. In this case, the color changes observed following these specific aging processes were mainly attributed to physical variations in the powders rather than chemical degradation.

Subsequently, a solar simulator was employed to induce a more accelerated and intense aging method compared to the previous ones, monitoring the aging variations via Raman spectroscopy and time-of-flight secondary ion mass spectrometry (ToF-SIMS).

Initial promising results indicated a color change confined exclusively to the edge of the sample, attributed to a CoPc photodegradation process. As a result of a drying effect, a greater dispersion of the phthalocyanine molecules could be present on the edge of the sample. This would allow titanium dioxide to interact more effectively with the organic molecule under solar irradiation.
Consequently, two different sample preparation methods were tested: CoPc dispersed in water (H_2O) and CoPc dissolved in tetrahydrofuran (THF). The photostability of CoPc was also evaluated by testing different crystalline phases of titanium dioxide (anatase, rutile, mixture of anatase and rutile, and P25 nanopowders). From Raman and ToF-SIMS analyses, it was observed that the choice of solvent significantly influenced the stability of the pigment. Indeed, the samples prepared with the dispersion in H_2O showed slight degradation, with pigment aggregates still present after solar aging. This reflects a strong intermolecular interaction between the phthalocyanine molecules. Conversely, the samples prepared with THF exhibited significant degradation following solar exposure, likely due to the increased separation of the molecule aggregates. This suggests that decreasing the CoPc intermolecular interaction may promote degradation by Ti_2O under solar simulation exposure.
This ongoing research, conducted in collaboration with Professor Andreas Ruediger's group at INRS-EMT, has shown promising results so far. Nevertheless, further investigation is necessary, for example, to assess the effect of the different crystalline phases of TiO_2 nanopowders on the solar photostability of the Co-phthalocyanine pigment.

4.1 Materials and methods

4.1.1 Materials

Cobalt phthalocyanine ($C_{32}H_{16}CoN_8$ - CoPc - cobalt(II) phthalocyanine, β-form, dye content 97%), also known as chromofine blue and classified as Pigment Blue 75 (PB 75), was used. Four different crystalline phases of titanium dioxide nanopowder were tested (see Table 4.1): anatase (637254 - titanium(IV) oxide, anatase - nanopowder, <25 nm particle size, 99.7% trace metals basis), rutile (637262 - titanium(IV) oxide, rutile - nanopowder, <100 nm particle size, 99.5% trace metals basis), a mixture of rutile and anatase (634662 - titanium(IV) oxide, a mixture of rutile and anatase in nanopowder form with <100 nm particle size (BET), 99.5% trace metal basis), and commercial nanopowder P25 (US3500 - titanium oxide nanopowder - TiO_2, 80% anatase/20% rutile, 99+%, 20nm). The samples were prepared with dichloromethane (CH_2Cl_2 - DCM - suitable for HPLC, ≥99.8%, contains amylene as stabilizer), pure water (H_2O - Millipore system), or tetrahydrofuran (C_4H_8O - THF - contains 250 ppm BHT as an inhibitor, puriss. p.a., ACS reagent, reag. Ph. Eur., ≥99.9%). All the powders and solvents were purchased from Sigma-Aldrich (Merck Life Science S.r.l), except P25 from US Research Nanomaterials, Inc.

Table 4.1 Summary of the titanium dioxide powders employed in this study, including the particle size characteristics and their main crystalline phases content.

TiO_2 phase	Particle size	Crystalline phase
Anatase (A)	<25 nm	100% A
Rutile (R)	<100 nm	traces ≥10% A
Mixture of rutile and anatase (mix)	<100 nm	79.5% A / 20.5% R
Nanopowder (P25)	20 nm	80% A / 20% R

4.1.2 Samples preparation

To investigate the effect of titanium dioxide on the stability of Co-phthalocyanine under different aging processes, three sample preparation procedures were tested:

- Powder samples of CoPc mixed with titanium dioxide were prepared in molar ratios CoPc:TiO_2 of 1:10, 1:100, and 1:1000. Specifically, the two pigments were ground and mixed in a ceramic mortar to obtain a fine and homogeneous powder.

This powder mixture was then momentarily suspended in dichloromethane (DCM), and the resulting suspension was deposited dropwise onto glass slides and left to dry at room conditions. Reference samples of pure TiO_2 and CoPc were also prepared. These powder samples were subjected to both artificial UV-VIS and natural sunlight aging.

- "Dispersed" samples CoPc:TiO_2 were obtained using water as the solvent to deposit the powder mixtures, testing different molar ratios. In particular, the two pigments are ground and mixed in 1 mL of water to create a dispersion, then dropped and cast on a glass slide as a thick layer. Afterward, the slides were dried in a hot air oven at 80°C for 60 min to evaporate the water. These powder samples were subjected to simulated solar irradiation.
- "Solution" samples CoPc:TiO_2 were obtained using tetrahydrofuran (THF) as the solvent, testing only the 1:1000 molar ratio, which was selected as a reference case due to its color variation observed in the dispersed samples. This procedure involves the preparation of a solution of CoPc in THF, calculating the solution concentration in mol·L^{-1}. The correct amount of TiO_2 for the 1:1000 molar ratio was added to the solution, and the samples were prepared and dried as in the previous procedure. These powder samples were subjected to simulated solar irradiation. Appendix B outlines the procedure for the preparation of cobalt phthalocyanine solutions.

All the samples were prepared in duplicate: half were kept in the dark to have a reference, and half were subjected to the specific aging process.

4.1.3 Aging processes

UV-VIS accelerated aging. The samples were exposed to an accelerated aging process in an ACS climatic chamber equipped with a 125W Hg lamp (see Chapter 2.6.2), under controlled conditions: 30°C, 70% RH for three steps of 50 hours.
Solar natural aging. The samples were exposed to natural solar exposure for 40 days during the summer period in Rome (see Chapter 2.6.3), with a southward orientation, average temperature of 27°C, and relative humidity of 67% RH.
Solar simulator aging. The samples were exposed to solar irradiation for 56-96 hours by a Xenon Short Arc lamp (SS50AAA 150-Watt Solar Simulator - Photo Emission Tech, Inc.) (see Chapter 2.6.4). The total light irradiance on the samples is nominally 100 mW/cm^2, corresponding to 1 sun.

4.1.4 Methods

Colorimetry. Colorimetry was performed with Eoptis CLM-194 (Eoptis S.r.l., Trento, Italy), a portable digital colorimeter, using a standard D65 daylight illuminant and 10° standard observer. The geometry and the measurement area on the sample were fixed at 45° and 10 mm, respectively. Data were measured in the CIE 1976 L*a*b* color space by the CLM-19X software licensed by Eoptis. The CIE L*, a*, and b* parameters in the color space were calculated as the average with the standard deviation of four measurements acquired for each sample, both before and after aging. The total color change ΔE was calculated according to the equation:

$$\Delta E = \sqrt{(\Delta L^*)^2 + (\Delta b^*)^2 + (\Delta a^*)^2} \tag{4.1}$$

Fourier-transformed infrared spectroscopy. FTIR spectra were acquired in reflectance mode using a ThermoFisher ®Nicolet Continuum Infrared Microscope (Thermo Fisher Scientific, Waltham, MA, USA). A 15× objective on the Microscope equipped with an MCT/A detector cooled with liquid nitrogen was used. The spectra were acquired in the range 4000-650 cm^{-1}, as a sum of 120 scans with a spectral resolution of 8 cm^{-1} and a reflected infrared beam with a 150×150 μm^2 aperture and 0° angle. Spectra were collected and elaborated with OMNIC™ software 6.0 and then graphed with OriginPro® software (OriginLab Corporation, Northampton, MA, USA).
Raman spectroscopy - 532 nm laser. A ®Renishaw Raman InVia Qontor micro-spectrometer (Renishaw plc, Wotton-under-Edge, UK), equipped with a CCD detector (10240×256 pixels, Peltier cooled cells at -70°C) in backscattered configuration and with a high-pass edge filter, was employed. Analyses were performed under a Leica DM 2700 M confocal microscope (10× and 50×). A green diode laser with a wavelength of 532 nm and a nominal output power of 100 mW was used. The spectra were recorded at room temperature in the spectral range between 100-3800 cm^{-1}, with a nominal spectral resolution of about 1 cm^{-1}, filtering the laser power at 1% of the output power by using neutral density (ND) absorptive filters, with an integration time of 10 seconds, and 5 accumulations. Raman spectra were collected and elaborated with WiRE 5.6 software licensed by Renishaw and then graphed with OriginPro® software (OriginLab Corporation, Northampton, MA, USA).
Raman spectroscopy - 473 nm laser. Raman spectra were acquired in backscattering geometry in a confocal setup. The excitation source is a single mode (TEM00), linearly polarized, CW laser with a wavelength of 473 nm (2.6 eV photon energy), coupled as an open beam into a customized Olympus IX71 inverted, confocal microscope equipped with a 100× objective with a numerical aperture of 0.9. This

provides a focal spot diameter of approx. 650 nm and a solid angle of approx. 56° for enhanced collection efficiency. The backscattered light passes through a triple Optigrate holographic notch filter to suppress the Rayleigh line and is then guided through a polarization-scrambling multimode fiber towards the entrance slit of an Horiba iHR320 spectrometer with 320 mm focal length. We operated the spectrometer with a grating of 2400 l/mm, yielding a spectral resolution of 1 cm^{-1} per pixel at an entrance slit of 50 μm, adjusted for maximum spectral resolution. The detector is a thermoelectrically cooled back-illuminated deep depletion CCD (Horiba Synapse BIDD) with UV-antireflection coating and anti-etaloning function. The operating temperature of the detector was -90°C to reduce thermal noise during acquisition. All spectra are calibrated via the positions of the Rayleigh line and the first-order Raman peak of a high-resistivity single-crystalline silicon sample, while the drift stability is actively monitored through a superimposed emission spectrum from a krypton light source. Raman spectra were graphed with OriginPro® software (OriginLab Corporation, Northampton, MA, USA).

Time-of-flight secondary ion mass spectrometry. Mass spectra and chemical maps were obtained using a $TOF.SIMS_5$ (ION-TOF GmbH, Munster, Germany) mass spectrometer, equipped with a bismuth liquid metal ion gun (Bi LMIG) in positive polarity. Surface analysis data were acquired in high lateral resolution mode using Bi_3^{++} (30 keV) with a pulse width of 18.4 ns and a current emission of 0.35 pA. The randomly analyzed area is equal to 500×500 μm^2, 128×128 pixels. Secondary ions were extracted at 2 kV and detected with a ToF mass analyzer with a cycle time of 100-150 μs [(1÷800) *m/z* mass range]. The mass spectra were user calibrated using H^+, H_2^+, C^+, CH^+, CH_2^+, CH_3^+, and TiO^+ in positive ion mode. All data were acquired, calibrated, normalized to total counts, and processed using SurfaceLab 6.5 software (ION-TOF GmbH, Munster, Germany). Mass spectra were normalized to total counts and plotted using OriginPro® software (OriginLab Corporation, Northampton, MA, USA). Chemical maps were normalized to total ion image to avoid topographic effects.

4.2 Results

4.2.1 CoPc characterization

A detailed characterization of the CoPc pigment was conducted using ATR-FTIR, Raman, and ToF-SIMS analytical techniques.

ATR-FTIR

The IR vibrational modes of cobalt phthalocyanine result in the formation of a distinctive fingerprint region within the FTIR spectrum, characterized by a considerable number of peaks, as illustrated in Figure 4.1.

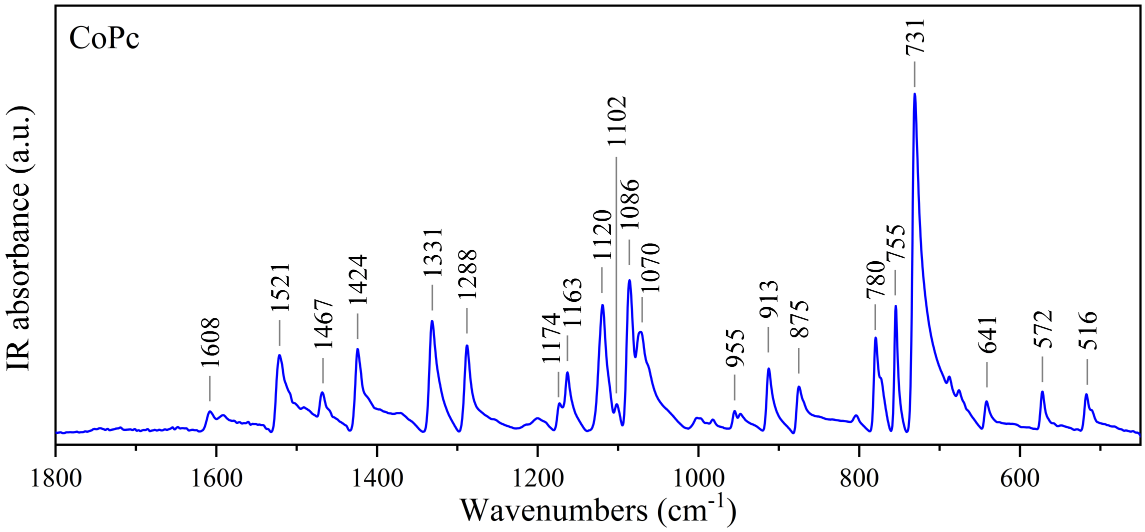

Figure 4.1 ATR-FTIR normalized spectrum in the range 1800-450 cm^{-1} of the CoPc pigment.

The weak band observed at 1608 cm^{-1} is associated with the C=C stretching vibration, indicative of the conjugated aromatic structure of the phthalocyanine macrocycle. The band at 1521 cm^{-1} corresponds to the stretching of C=N bonds, highlighting the nitrogen coordination within the ring system. At 1467 cm^{-1}, the signal is attributed to the in-plane C-H bending, while the band at 1424 and 1331 cm^{-1} correspond to the C-C stretching in the isoindole units of the molecule. Additional confirmation of nitrogen-carbon linkages is provided by the C-N= stretching vibration at 1288 cm^{-1}, as well as by the in-plane C-N= bending at 1163 cm^{-1} with a shoulder at 1174 cm^{-1}. Characteristic in-plane bending vibrations of aromatic C-H bonds are observed at 1120, 1102, 1086, and 1070 cm^{-1}. The weak peak at 955 cm^{-1} is related to the total symmetry vibrations of the benzene rings within the phthalocyanine structure. The peaks observed at 913 and 875 cm^{-1} are indicative of metal-ligand absorption bands and are markedly influenced by the metal ion Co^{2+} present in the central position of the macrocycle [175]. The most intense signal in the spectrum is indicative of the out-of-plane C-H deformation at 731 cm^{-1}, in conjunction with the signals at 780 and 755 cm^{-1}. These peaks correspond to vibrations involving the aromatic rings within the phthalocyanine system. At low wavenumbers, the absorption signals at 641, 572, and 516 cm^{-1} are assigned to the out-of-plane deformation of the C-C bonds in the macrocycle ring. An important finding from the FTIR spectrum is the identification of the specific phthalocyanine polymorphism [176, 177]. In particular, the presence of bands at 875, 780, and 731 cm^{-1} indicate the β-form of the phthalocyanine pigment. Furthermore, two additional signals of the β-polymorphism are observed in the shoulder at 1174 cm^{-1} and in the small band present at 1102 cm^{-1}, characteristic of two different bending in-plane vibrations.

All the assignments of the vibrational modes of the main IR bands detected for the CoPc pigment are presented in Table 4.2, according to the literature [178–181].

Table 4.2 Assignment of the main IR bands for CoPc pigment.

Wavenumbers (cm^{-1})[a]	**IR assignment**[b]
1608 (vw)	ν(C=C) macrocycle
1521 (m)	ν(C=N)
1467 (w)	δ(C—H) in-plane
1424 (m) 1331 (s)	ν(C–C) in isoindole
1288 (m)	ν(C–N=) in isoindole
1174 (sh) 1163 (m)	δ(C–N=) in-plane
1120 (s) 1102 (wv) 1086 (s) 1070 (m)	δ(C–H) in-plane
955 (vw)	Total symmetry benzene
913 (m) 875 (w)	Metal ligand (Co–N) vibration
780 (m) 755 (s) 731 (vs)	δ(C–H) out-of-plane deformation
641 (w) 572 (w) 516 (w)	δ(C–C) out-of-plane ring deformation

[a] Relative intensities - very strong (vs), strong (s), medium (m), weak (w), very weak (vw), shoulder (sh).
[b] Types of vibrations - ν: stretching, δ: bending.

Raman

Cobalt phthalocyanine presents characteristic Raman signals in the spectral range 100–1800 cm^{-1}, as shown in Figure 4.2.

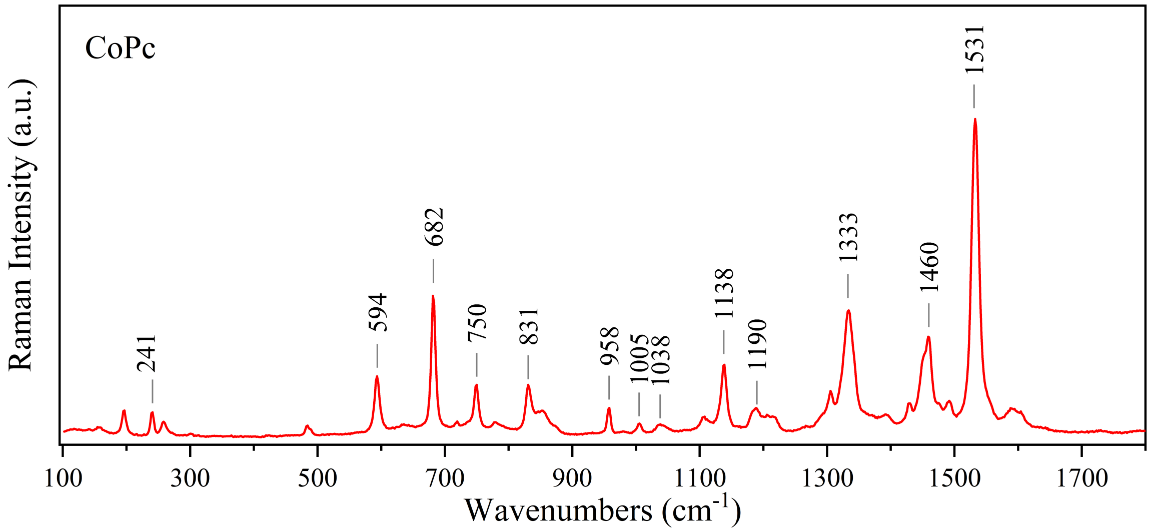

Figure 4.2 Raman normalized spectrum in the wavenumber range 100-1800 cm^{-1} of the phthalocyanine pigment CoPc.

The most intense band at 1531 cm^{-1} is associated with Raman modes involving C-N=C bridge bonds, indicative of fundamental vibrations within the macrocyclic structure. The position of this band contributes to the discrimination between different coordinated metals within the phthalocyanines. Other intense signals are observed at 682, 1333, and 1460 cm^{-1}. These bands are indicative of specific vibrations, including the symmetric breathing and deformation of the macrocycle, the in-plane C-H bending in benzene rings/pyrrole breathing, and the isoindole stretching, respectively. In addition to these bands, the CoPc pigment exhibits other significant Raman absorptions characteristic of its organometallic and aromatic structure. A distinctive band at 241 cm^{-1} is attributed to the Co–N stretching vibration, thus confirming the coordination of the cobalt ion with the nitrogen atoms in the phthalocyanine ligand. The isoindoline ring deformation is evident at 594 cm^{-1}, while the C-H wagging mode appears at 750 cm^{-1}. At 831 cm^{-1}, a combination of C-N stretching and macrocycle deformation is observed, and the benzene breathing mode is prominent at 958 cm^{-1}. For the high-wavenumber range, significant Raman absorptions include the C-H bending vibrations at 1005 and 1190 cm^{-1}, the macrocycle vibrations combined with C-H bending at 1038 cm^{-1}, and the symmetric C-C stretching at 1138 cm^{-1}.

The main Raman bands detected for the CoPc pigment are presented in Table 4.3, according to the literature [55, 182–184].

Table 4.3 Main Raman vibrational assignments of CoPc.

Wavenumbers (cm^{-1})[a]	**Raman assignment**[b]
241 (w)	Co–N, organometallic complex
594 (m)	Isoindole ring deformation
682 (s)	Macrocyle symmetric breathing and deformation
750 (m)	ω(C–H)
831 (m)	ν(C–N) / macrocyle deformation
958 (w)	Benzene breathing
1005 (vw)	δ(C–H)
1038 (vw)	Macrocyle / δ(C–H)
1138 (m)	ν_s(C–C)
1190 (w)	δ(C–H)
1333 (s)	δ(C–H) in-plane in benzene / pyrrole breathing
1460 (s)	Isoindole stretching
1531 (vs)	ν(C-N=C) in bridge bonds

[a] Relative intensities - very strong (vs), strong (s), medium (m), weak (w), very weak (vw).
[b] Types of vibrations - ν: stretching, δ: bending, ω: wagging, $_s$: symmetric.

ToF-SIMS

Cobalt phthalocyanine powder was finally characterized using ToF-SIMS in positive ion mode. The resulting mass spectrum is illustrated in Figure 4.3. The molecular ion signal of the pigment was detected as $[M]^+$ at m/z 571 with high intensity, corresponding to its molecular composition ($C_{32}H_{16}N_8Co$), and further confirmed by its isotopic pattern. In addition to the main molecular peak, similar ion patterns attributed to the addition or loss of small hydrocarbon fragments were identified, resulting from the ion bombardment. Specifically, the signals $[M–C_2H_2]^+$ at m/z 545, $[M–CH_2]^+$ at m/z 557, $[M+CH]^+$ at m/z 584, and $[M+C_2H]^+$ at m/z 596, were observed. In the lower m/z region of the mass spectrum, other fragment ions were identified, taking into account the symmetric structure of the phthalocyanine molecule and its potential fragmentation pathways.

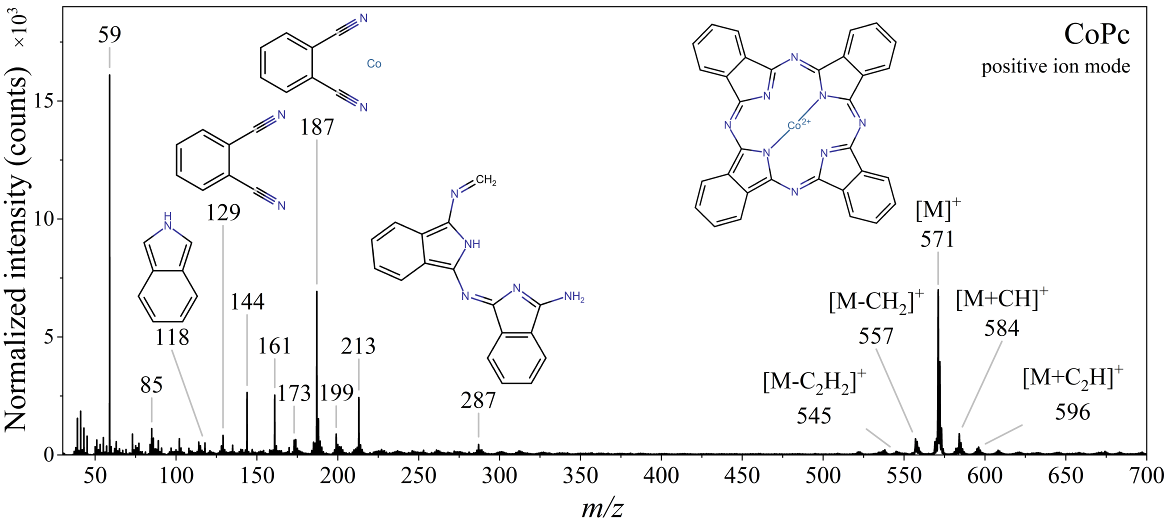

Figure 4.3 ToF-SIMS mass spectrum normalized to total counts of cobalt phthalocyanine CoPc in the mass-to-charge range m/z 30-700, acquired in positive ion mode. The main molecular fragments and their corresponding chemical structures are highlighted.

Based on the scientific literature of SIMS [144, 185] and PyGC [146, 148], three main molecular fragments characteristic of phthalocyanine pigments were identified, as illustrated in Figure 4.4.

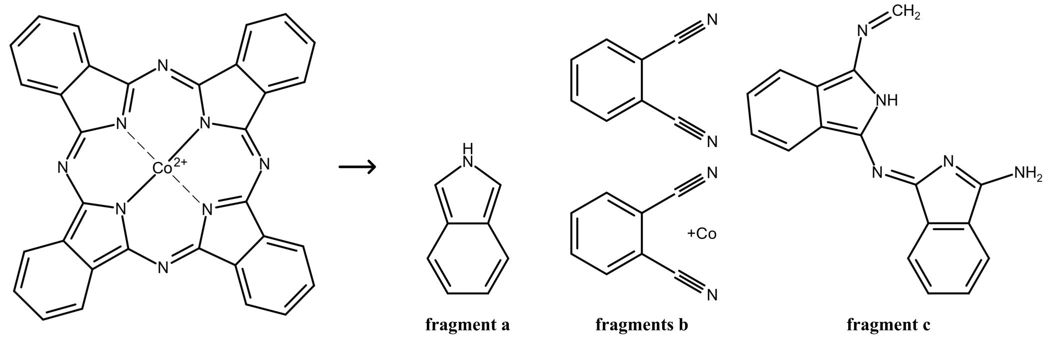

Figure 4.4 Molecular structure of cobalt phthalocyanine pigment (left) with the principal molecular fragments produced by ion bombardment (right) [36].

The most intense peak in the mass spectrum appears at *m/z* 59, corresponding to the cobalt ion Co^+, the central metal atom of the phthalocyanine molecule. In addition, the following main fragments were recorded:

- fragment a → 2H-isoindole ion C_8H_7N detected at *m/z* 118 as its protonated form, with low intensity.
- fragment b → benzene-1,2-dicarbonitrile ion $C_8H_4N_2$ (consisting of a benzene ring with two nitrile groups) detected at *m/z* 129 as its protonated form. This ion is characteristic of the fragmentation pattern of phthalocyanine under ion bombardment. Cobalt-benzene-1,2-dicarbonitrile ion $C_8H_4N_2Co$ at *m/z* 187 was also observed and represents the second most intense peak in the spectrum. This signal is accompanied by other smaller peaks resulting from the addition or loss of C, N, CH, and CN at *m/z* 161, 173, 174, 199, and 213.
- fragment c → ion $C_{17}H_{13}7N_5$ detected at *m/z* 287, corresponds to approximately half of the phthalocyanine macrocycle, resulting from symmetric fragmentation of the molecule and the loss of the central cobalt ion.

Other characteristic pigment signals were detected at *m/z* 85 and 144, corresponding to the fragment ions $CNCo^+$ and $CNCo_2{}^+$, respectively, formed through the coordination of cobalt atoms with the cyanide group during ion bombardment. All the molecular fragments identified in positive ion mode are listed in Table 4.4.

Table 4.4 List of CoPc molecular signals detected with ToF-SIMS in positive ion mode.

Positive polarity

Molecular signal

ion	m/z
$C_{32}H_{16}N_8Co^+$	571.08
$[M-C_2H_2]^+$	545.04
$[M-CH_2]^+$	557.05
$[M+CH]^+$	584.09
$[M+C_2H]^+$	596.06

Molecular fragments

a		b		c	
ion	m/z	ion	m/z	ion	m/z
$C_8H_8N^+$	118.09	$C_8H_5N_2{}^+$	129.05	$C_{17}H_{13}N_5{}^+$	287.10
		$C_8H_4N_2Co^+$	186.99		
		$[C_8H_4N_2Co-CN]^+$	160.98		
		$[C_8H_4N_2Co-N]^+$	172.99		
		$[C_8H_4N_2Co-CH]^+$	174.00		
		$[C_8H_4N_2Co+C]^+$	198.99		
		$[C_8H_4N_2Co+CN]^+$	212.99		

Other fragments

ion	m/z
Co^+	58.94
$CNCo^+$	84.95
$CNCo_2^+$	143.88

4.2.2 UV-VIS and natural solar aging of CoPc mixed with TiO_2

Mixed powder samples of CoPc and TiO_2 with different molar ratios were subjected to both UV-VIS aging and natural sunlight exposure, monitoring the aging-induced variations with colorimetry, FTIR, and Raman spectroscopy.
Figure 4.5 displays the total color change ΔE for all the powder samples after each of the three UV-VIS aging steps of 50 hours. Specifically, Figure 4.6 shows the

CIELAB diagram of the colorimetric values a* vs b* and L* before and after each aging step, and Table 4.5 presents all the colorimetric variations in lightness/darkness ΔL*, redness/greenness Δa*, yellowness/blueness Δb*, and the corresponding total color changes ΔE measured after each step of light exposure.

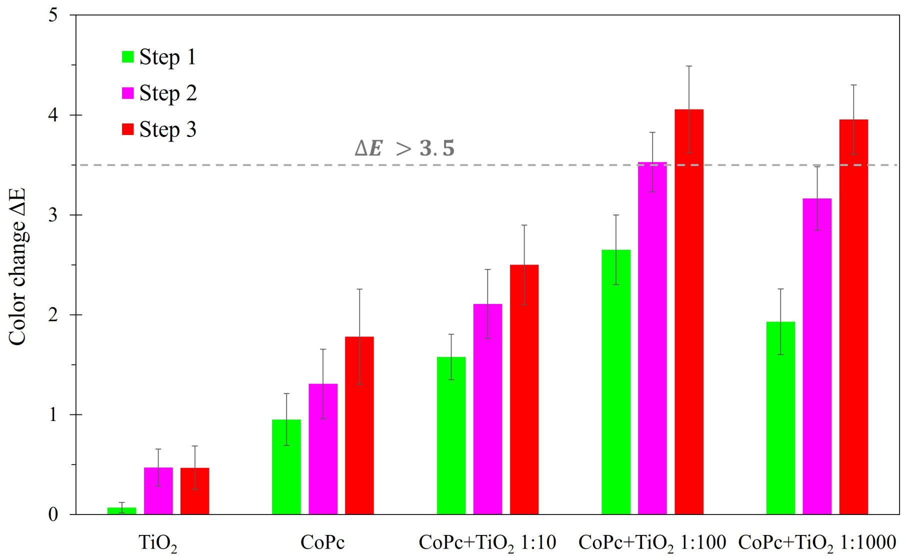

Figure 4.5 Total color change ΔE for the $CoPc+TiO_2$ and reference samples after each UV-VIS aging step.

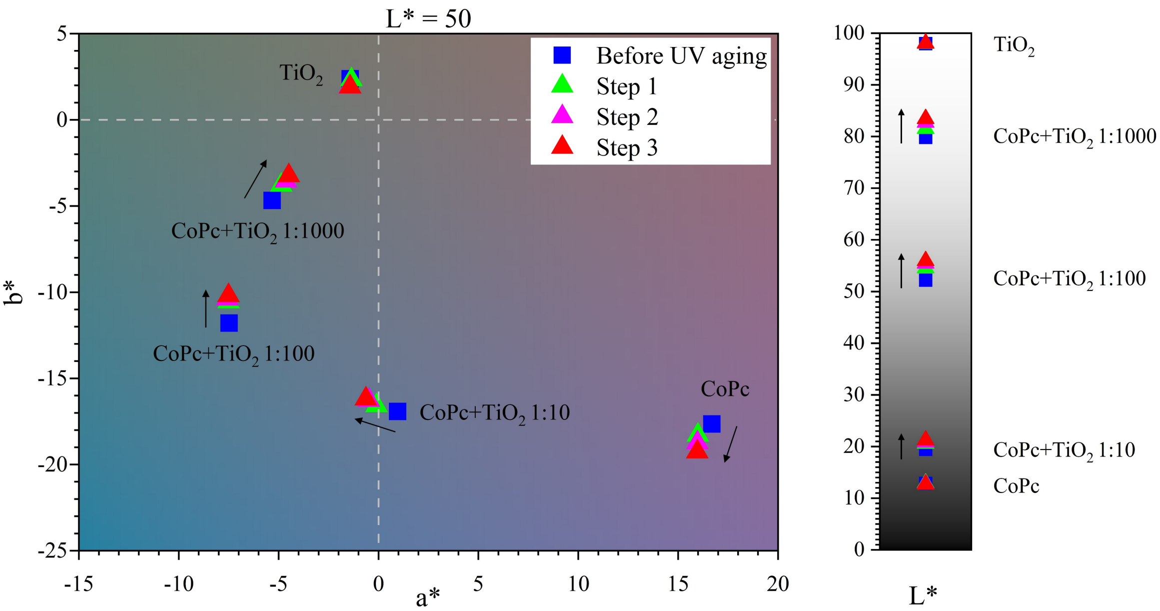

Figure 4.6 Diagram a* vs b* for the fixed L*=50 (left) and L* values (right) of the CIELAB colour space of the samples investigated before and after the three 50-hour steps of UV-VIS light exposure. The arrows highlight the colorimetric variations.

Table 4.5 List of colorimetric variations ΔL*, Δa*, Δb*, and the total color changes calculated ΔE, after the three 50-hour steps of UV-VIS aging for the powder samples. In bold are the values ΔE>3.5.

	Step	ΔL^*	Δa^*	Δb^*	ΔE
TiO_2	1	-0.01±0.14	0.05±0.05	-0.04±0.14	0.07±0.05
	2	0.05±0.13	-0.03±0.05	-0.47±0.13	0.47±0.18
	3	0.06±0.16	-0.01±0.05	-0.47±0.16	0.47±0.22
CoPc	1	0.03±0.07	-0.70±0.03	-0.64±0.19	0.95±0.26
	2	-0.10±0.05	-0.73±0.04	-1.08±0.29	1.31±0.35
	3	-0.20±0.03	-0.73±0.09	-1.61±0.19	1.78±0.48
CoPc+TiO_2 1:10	1	1.11±0.10	-1.07±0.06	0.34±0.15	1.58±0.23
	2	1.40±0.14	-1.44±0.06	0.65±0.21	2.11±0.35
	3	1.78±0.14	-1.59±0.06	0.74±0.20	2.50±0.40
CoPc+TiO_2 1:100	1	2.34±0.10	-0.03±0.08	1.25±0.12	2.65±0.35
	2	3.23±0.07	-0.09±0.08	1.41±0.11	**3.53±0.30**
	3	3.72±0.10	-0.03±0.07	1.61±0.14	**4.06±0.43**
CoPc+TiO_2 1:1000	1	1.66±0.14	0.46±0.08	0.89±0.05	1.93±0.33
	2	2.88±0.09	0.69±0.07	1.13±0.06	3.16±0.32
	3	3.59±0.09	0.83±0.06	1.44±0.05	**3.95±0.35**

The reference powders of TiO_2 and CoPc showed limited color changes ΔE, confirming the strong lightfastness of these pigments. In particular, the white pigment demonstrated excellent stability under UV-VIS light exposure, with total color changes ΔE below 1 and negligible colorimetric variations. For the CoPc pigment, small decreases in the a*, b*, and L* parameters were observed, although these colorimetric variations were not significant, with total color changes being less than 2. The CoPc+TiO_2 samples with different molar ratios showed increases in both b* and L* values. These colorimetric variations indicate a slight color shift from blue to yellow and a brightening effect, as evidenced by the increase of the luminosity L*. Regarding the a* values, the sample with the 1:10 ratio exhibited a small decrease, indicating a shift from red to green. In contrast, in the sample with the 1:100 ratio, the a* value remained unchanged, whereas the sample with the 1:1000 ratio showed a small increase in the red component a*. Notably, the sample prepared with the 1:100 molar ratio exhibited the largest total color change ΔE after the UV-VIS aging process (ΔE>3.5 [9]), followed by the sample with the ratio 1:1000.

The same samples were realized and subjected to natural sunlight exposure. In the same way, Figure 4.7 shows the CIELAB diagram of the colorimetric values a* vs b* and L*, and Table 4.6 presents the colorimetric variations.

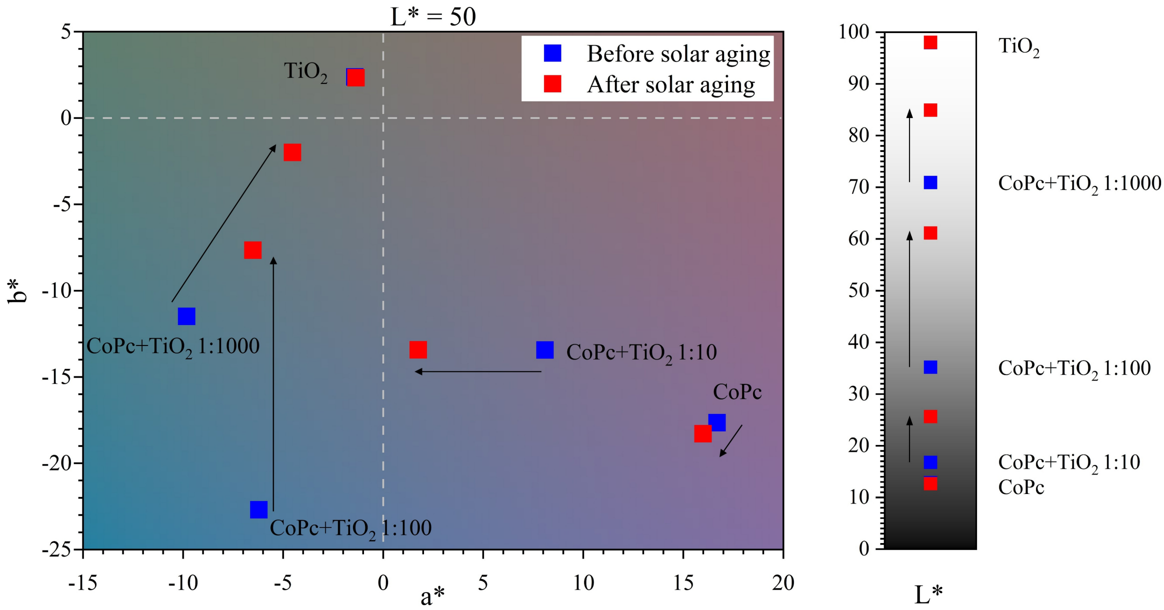

Figure 4.7 Diagram a* vs b* for the fixed L*=50 (left) and L* values (right) of the CIELAB colour space of the samples investigated before and after the natural sunlight aging. The arrows highlight the colorimetric variations.

Table 4.6 List of colorimetric variations ΔL*, Δa*, Δb*, and the total color changes calculated ΔE,after the natural sunlight aging for the powder samples. In bold are the values ΔE>3.5.

	ΔL^*	Δa^*	Δb^*	ΔE
TiO_2	-0.41±0.09	-0.05±0.05	-0.04±0.04	0.42±0.11
CoPc	-0.04±0.16	-0.84±0.07	-0.52±0.12	0.99±0.18
CoPc+TiO_2 1:10	8.84±0.16	-6.33±0.05	0.01±0.07	**10.87±0.88**
CoPc+TiO_2 1:100	25.98±0.53	-0.30±0.22	15.05±0.38	**30.0±5.5**
CoPc+TiO_2 1:1000	14.00±0.03	5.29±0.04	9.50±0.09	**17.72±0.47**

In this case, the colorimetric variations observed are consistent with those previously observed for the same samples aged under UV-VIS light, but are significantly more evident. As a result, exposure to natural sunlight leads to larger color changes, as indicated by ΔE values. The pure CoPc and TiO_2 powders showed no significant color variation (ΔE<1), confirming their stability under light exposure, whereas the sample with the 1:100 molar ratio proved to be the most susceptible to color variation after aging.

Vibrational spectroscopy analyses (FTIR and Raman) were carried out to investigate the origin of the color variations observed after both aging processes. A comparison of the FTIR spectra before and after aging revealed no significant variations other than a general decrease in signal intensity. In contrast, Raman spectroscopy and microscopic observations highlighted a variation in the CoPc+TiO_2 1:100 sample, following both UV-VIS and natural solar aging. Specifically, lighter and darker areas were noted, whereas the unaged sample displayed a uniformly colored surface. Therefore, different points on the surface of the sample were analyzed. In the darker regions, stronger signals associated with the phthalocyanine pigment were detected, as is evident from the stronger intensity of the most characteristic peak of CoPc at 1540 cm^{-1}, associated with the C-N-C bridge bond of the macrocycle [183]. In the lighter areas, titanium dioxide-related signals were more intense, and the characteristic anatase bands were dominant in the spectrum [130]. This could explain the color variations observed by colorimetric analysis.

Figure 4.8 shows the Raman spectra acquired before and after the aging processes, highlighting the lighter and darker areas on the surface. The observed variations were more significant in the sample aged under natural sunlight compared to the same sample under UV-VIS exposure. These results suggest that the color changes detected by colorimetric analysis are predominantly physical, most likely resulting from surface redistribution or reorganization of the powder components, rather than from chemical degradation.

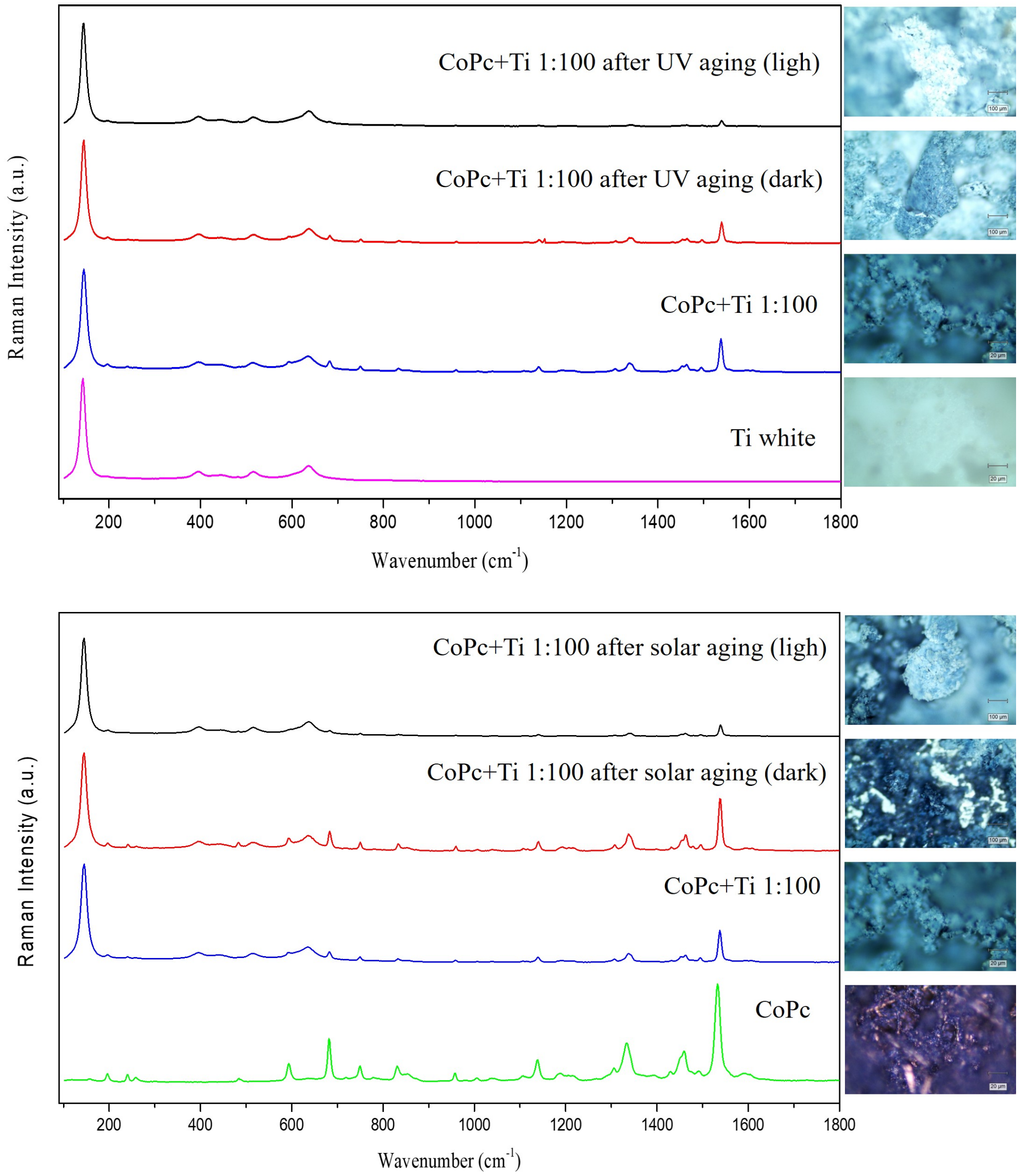

Figure 4.8 Raman normalized spectra of the CoPc+TiO_2 1:100 sample in the range 100-1800 cm^{-1}, acquired with the laser at 532 nm, laser power at 1 mW, integration time 10 seconds, and 5 accumulations. The spectra of the lightest and darkest areas after the UV-VIS aging (top) and natural solar aging (bottom) were reported with the reference spectra of the unaged sample and the pure CoPc and TiO_2 powders.

4.2.3 Artificial solar aging of CoPc dispersed in water mixed with TiO_2

The second phase of the study involved a more intense aging process using a solar simulator, and the samples were prepared by dispersing the powder mixture in water. The interaction between CoPc and TiO_2 was tested for different molar ratios, from 1:10 to 1:20000. Among the various CoPc:TiO_2 molar ratios tested, only the most reactive one of 1:1000 is taken into consideration, for which the largest color change was observed under solar radiation. In particular, this 1:1000 ratio presents a very light blue color, as shown in Figure 4.9. Samples were prepared in duplicate: half were kept in the dark to have a reference, and half were subjected to the solar simulator irradiation for 96 hours (4 days).

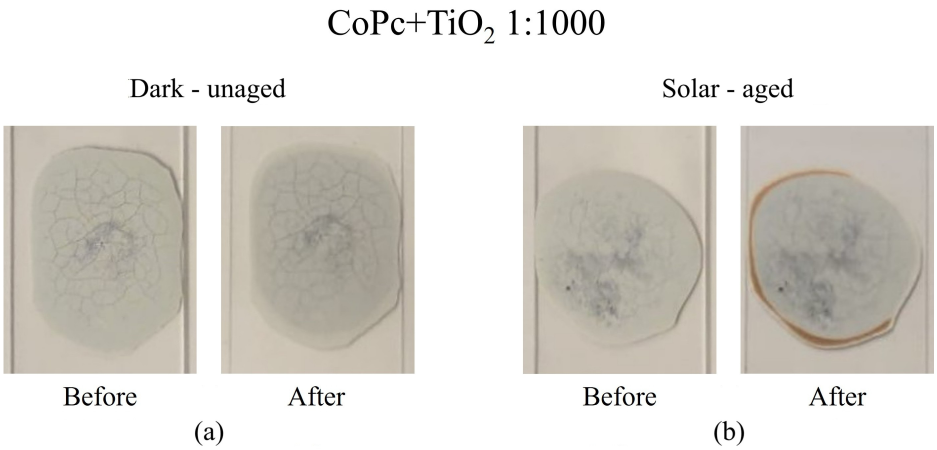

Figure 4.9 Photographs of CoPc+TiO_2 1:1000 samples before and after 4 days under two different conditions: (a) storage in the dark and (b) exposure to solar simulator irradiation.

As is immediately evident from images in Figure 4.9a, after 4 days, a noticeable difference appeared in the sample kept in the dark between the middle area and the edge, which appeared whiter. This contrast became significantly more evident after solar simulator aging in Figure 4.9b, where the edge changed color from white to orange, while the central area remained unchanged. These variations were studied using ToF-SIMS to analyze the differences in surface composition between the two regions, both in the sample kept in the dark (dark-unaged) and in the one subjected to solar irradiation (solar-aged).

Figure 4.10 shows the ToF-SIMS mass spectra acquired for the dark-unaged sample, comparing the middle and edge areas.

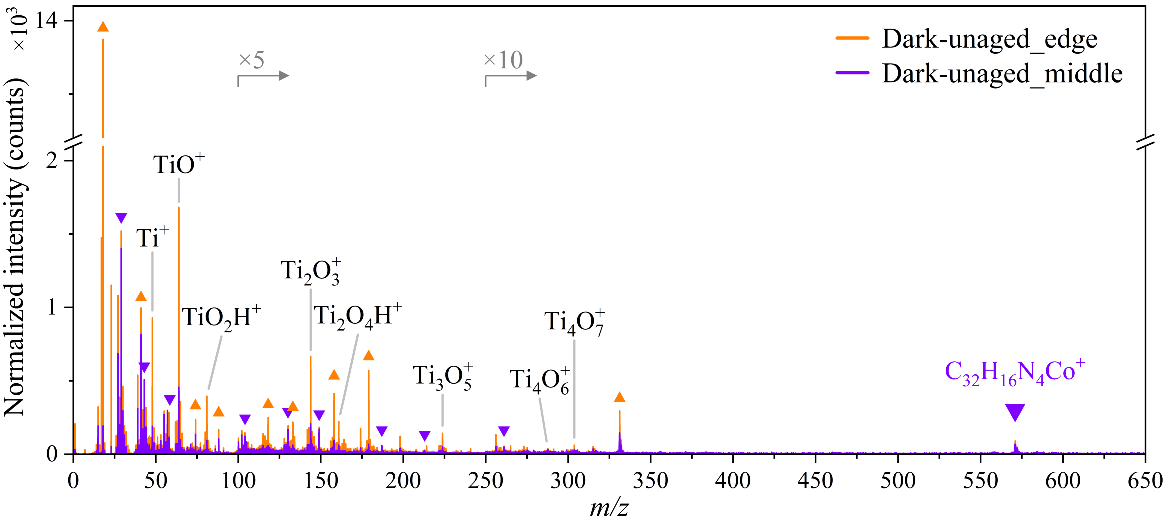

Figure 4.10 ToF-SIMS mass spectra normalized to total counts in the mass-to-charge range *m/z* 1-650 for the dark-unaged sample CoPc+TiO_2 1:1000 in the edge (orange line) and in the middle (purple line) region. TiO_2-related signals are reported, whereas phthalocyanine fragments are marked with triangle symbols.

Ion signals associated with titanium dioxide were identified in the mass spectra: Ti^+ (*m/z* 47.95), TiO^+ (*m/z* 63.94), TiO_2H^+ (*m/z* 80.95), $Ti_2O_3{}^+$ (*m/z* 143.88), $Ti_2O_4H^+$ (*m/z* 160.88), $Ti_3O_5{}^+$ (*m/z* 223.80), $Ti_4O_6{}^+$ (*m/z* 287.80), and $Ti_4O_7{}^+$ (*m/z* 303.8) [154]. The intensity of these signals is higher at the edge of the sample compared to the middle region. The intensity increase of titanium signals could be due to an evaporation effect during drying, leading to a large concentration of titanium at the edge. The molecular peak corresponding to cobalt phthalocyanine ($C_{32}H_{16}N_8Co^+$ *m/z* 571.10) [185] was detected in both regions of the sample, although with lower intensity at the edge, along with characteristic ion fragments produced by the ion bombardment [144, 146]. These ion signals generated by the ToF-SIMS fragmentation of CoPc pigment will hereafter be referred to as "CoPc fragments". The CoPc fragments (Figure 4.10, purple triangle), including for example, Co^+ (*m/z* 58.93), $C_7H_6N^+$ (*m/z* 104.05), $C_8H_4N_2{}^+$ (*m/z* 128.04), $C_8H_6N_2{}^+$ (*m/z* 130.05), $C_8H_4N_2Co^+$ (*m/z* 187.00), and $C_{16}H_{13}N_4{}^+$ (*m/z* 261.10), present lower intensity at the edge of the sample. Additional signals of the ToF-SIMS fragmentation of the CoPc pigment (Figure 4.10, orange triangle), including for example, $C_8H_8N^+$ (*m/z* 118.07), $C_8H_7NO^+$ (*m/z* 133.05), $C_9H_8N_3{}^+$ (*m/z* 158.07), and $C_{16}H_{10}N_5Co^+$ (*m/z* 331.02), were detected in both regions in the mass spectra with higher intensity at the edge of the sample. These ion signals correspond to fragments of the isoindole units in the phthalocyanine macromolecule and will hereafter be referred to as "isoindole fragments". Although both the CoPc fragments and isoindole fragments originate from the ion bombardment of the CoPc pigment, this distinction will be useful in the following sections for identifying possible degradation processes.

All ion signals identified in the mass spectra are listed in Table 4.7, and are distinguished between fragments related to the inorganic component of the white pigment (TiO_2 fragments) and those resulting from ToF-SIMS fragmentation of the organic component of the cobalt phthalocyanine pigment (CoPc fragments and isoindole fragments).

Table 4.7 List of main fragments signals detected with ToF-SIMS in positive ion mode, divided into TiO_2, CoPc, and isoindole fragments.

TiO_2 fragments		**CoPc fragments**		**Isoindole fragments**	
Peaks	m/z	Peaks	m/z	Peaks	m/z
Ti^+	47.9	$CNH_3{}^+$	29.1	$NH_4{}^+$	18.0
TiO^+	63.9	$CN_2H_3{}^+$	43.1	CN_2H^+	41.1
TiO_2H^+	80.9	Co^+	58.9	$CoNH^+$	73.9
$Ti_2O_3{}^+$	143.9	$[C_7H_5N + H]^+$	104.1	CoN_2H^+	87.9
$Ti_2O_4H^+$	160.88	$C_8H_4N_2{}^+$	128.1	$C_8H_8N^+$	118.1
$Ti_3O_5{}^+$	223.8	$C_8H_6N_2{}^+$	130.1	$C_8H_7NO^+$	133.1
$Ti_4O_6{}^+$	287.8	$[C_8H_4N_2Co - C_2N]^+$	149.1	$C_9H_8N_3{}^+$	158.1
$Ti_4O_7{}^+$	303.7	$[C_8H_4N_2Co]^+$	187.0	$C_6H_6N_3Co^+$	179.0
		$[C_8H_4N_2Co + CN]^+$	213.0	$C_{16}H_{10}N_5Co^+$	331.2
		$[C_{16}H_{12}N_4 + H]^+$	261.1		
		$C_{32}H_{16}N_8Co^+$	571.1		

Figure 4.11 shows the normalized chemical maps of selected signals, illustrating the surface intensity distribution of different types of detected species, in the middle (top) and edge regions (bottom) of the dark-unaged sample. Specifically, the molecular ion signals of cobalt phthalocyanine ($C_{32}H_{16}N_8Co^+$, Figure 4.11a) are localized in spots, corresponding to pigment aggregates visible in the analyzed areas, as also confirmed by the chemical maps of cobalt ions (Co^+, Figure 4.11b). Isoindole fragments ($C_8H_8N^+$, Figure 4.11c) showed a low and uniform distribution throughout the analyzed area, whereas the CoPc fragments ($C_8H_4N_2Co^+$, Figure 4.11d) highlighted the same spot intensity distribution as the main CoPc molecular peak, further supporting the spatial localization of the pigment. Titanium-related signals (TiO^+, Figure 4.11e) appear spatially complementary to those of cobalt phthalocyanine, indicating no interaction between the two pigments on the sample surface.

By comparing the normalized chemical maps acquired in the two different regions of the sample, a lower intensity of the ion signals can be observed in the edge region. In particular, the signals related to the CoPc pigment show lower intensity and a reduced spot distribution, whereas the signals associated with titanium are more intense.

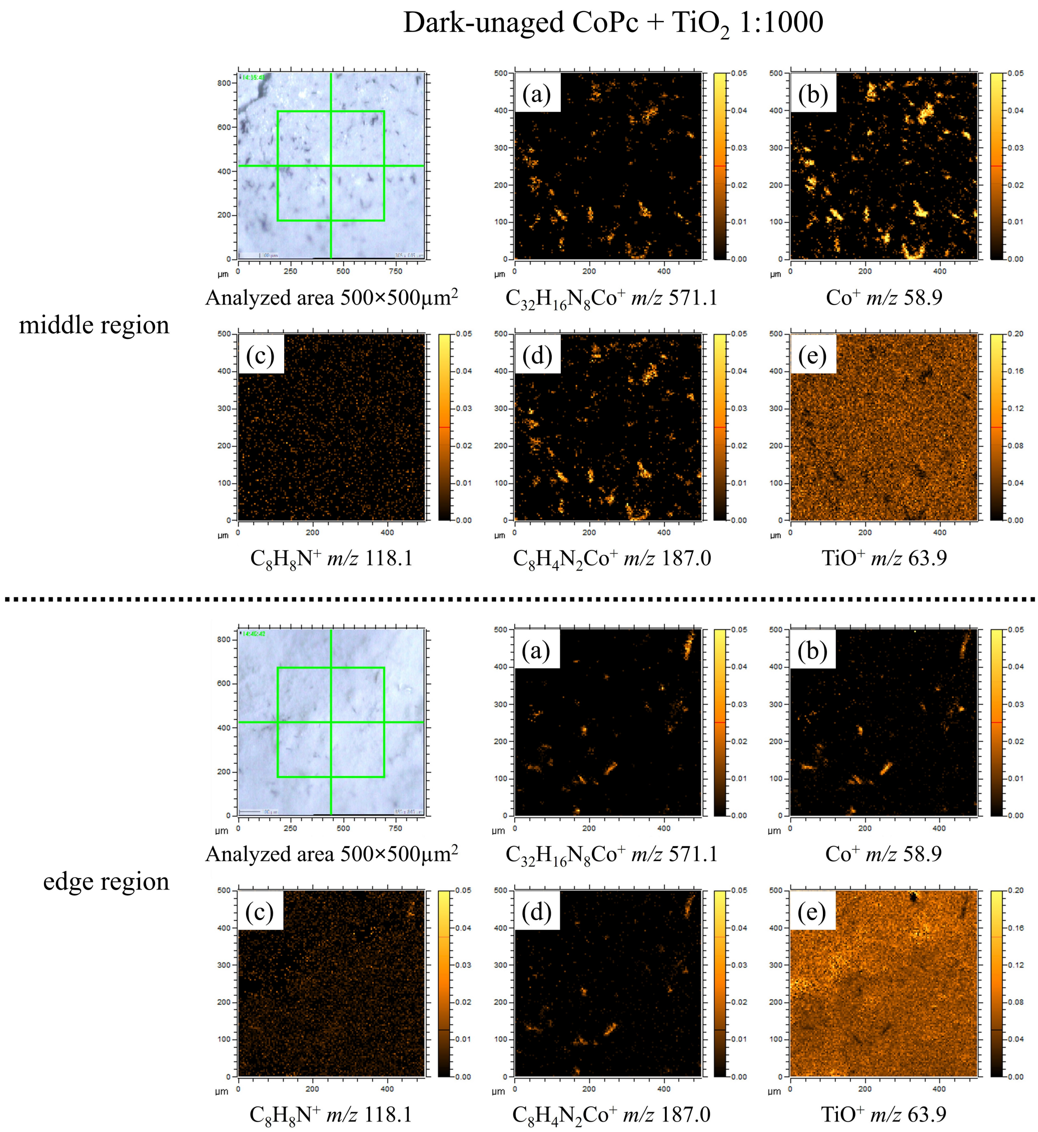

Figure 4.11 Images of the analyzed 500×500 μm^2 surface areas of the dark-unaged sample CoPc + TiO_2 1:1000, with the corresponding normalized ToF-SIMS ion maps. The chemical maps, acquired in positive ion mode in the middle region (top) and edge region (bottom), show the ion signals of: (a) cobalt phthalocyanine ($C_{32}H_{16}N_8Co^+$), (b) cobat (Co^+), (c) an isoindole fragment ($C_8H_8N^+$), (d) a CoPc fragment ($C_8H_4N_2Co^+$), and (e) titanium oxide (TiO^+).

In the same way, Figure 4.12 shows the ToF-SIMS mass spectra acquired for the solar-aged sample, comparing the middle and edge areas.

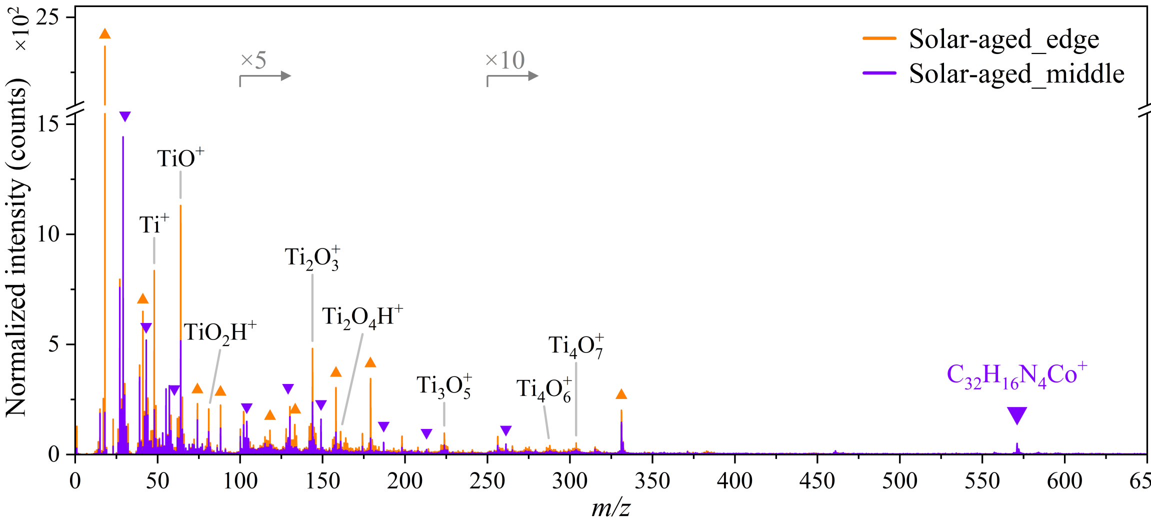

Figure 4.12 ToF-SIMS mass spectra normalized to total counts in the mass-to-charge range *m/z* 1-650 for the solar-aged sample CoPc+TiO_2 1:1000 in the edge (orange line) and in the middle (purple line) region. TiO_2-related signals are reported, whereas phthalocyanine fragments are marked with triangle symbols.

In the solar-aged sample, the same characteristic signals observed in the dark-unaged sample were detected (Table 4.7). Titanium-related signals appeared significantly more intense at the edge of the sample, as shown in the mass spectra. The molecular ion peak of cobalt phthalocyanine was only detected in the middle region and was completely absent at the edge. Similarly, signals corresponding to CoPc fragments were detected with substantially lower intensity in the edge region. In contrast, isoindole fragment signals were more intense at the edge compared to the middle area.
This difference between the middle and edge regions of the solar-aged sample is clearly visible in the normalized chemical maps in Figure 4.13. Signals related to the cobalt phthalocyanine pigment are completely absent in the edge part (Figure 4.13a), whereas cobalt ions exhibit a marked decrease in intensity but remain detectable (Figure 4.13b). Of particular interest is the intensity distribution of isoindole fragments (Figure 4.13c), which appear intense and uniformly distributed at the edge. CoPc fragments are nearly absent in this area (Figure 4.13d), and titanium-related signals are significantly more intense at the edge compared to the middle region (Figure 4.13e).
It is important to emphasize that the isoindole signals recorded at the edge cannot be attributed to the fragmentation of CoPc molecules during ion bombardment. Indeed, if the molecular ions of CoPc are not detected, their characteristic fragment ions should not be present either. This suggests that the isoindole-related signals at lower

m/z values are probably the result of degradation products, indicating that cobalt phthalocyanine underwent chemical degradation when mixed with titanium dioxide exclusively in the edge region. This interpretation is also consistent with the observed color change, as isoindole molecules exhibit an orange coloration.

The promising preliminary results obtained in this phase led to the conclusion that the edge of the solar-aged sample contains a lower amount of cobalt phthalocyanine, likely due to the drying effect. In this region, titanium dioxide could interact more effectively with the phthalocyanine, leading to its degradation following solar irradiation. In contrast, no degradation occurred in the middle area of the sample, which may be due to the strong van-der-Waals intermolecular interactions within the phthalocyanine aggregates [186, 187]. The chromatic variation observed at the edge was systematically investigated by repeating the aging procedure with shorter irradiation time (approximately 50 hours, compared to 96 hours).

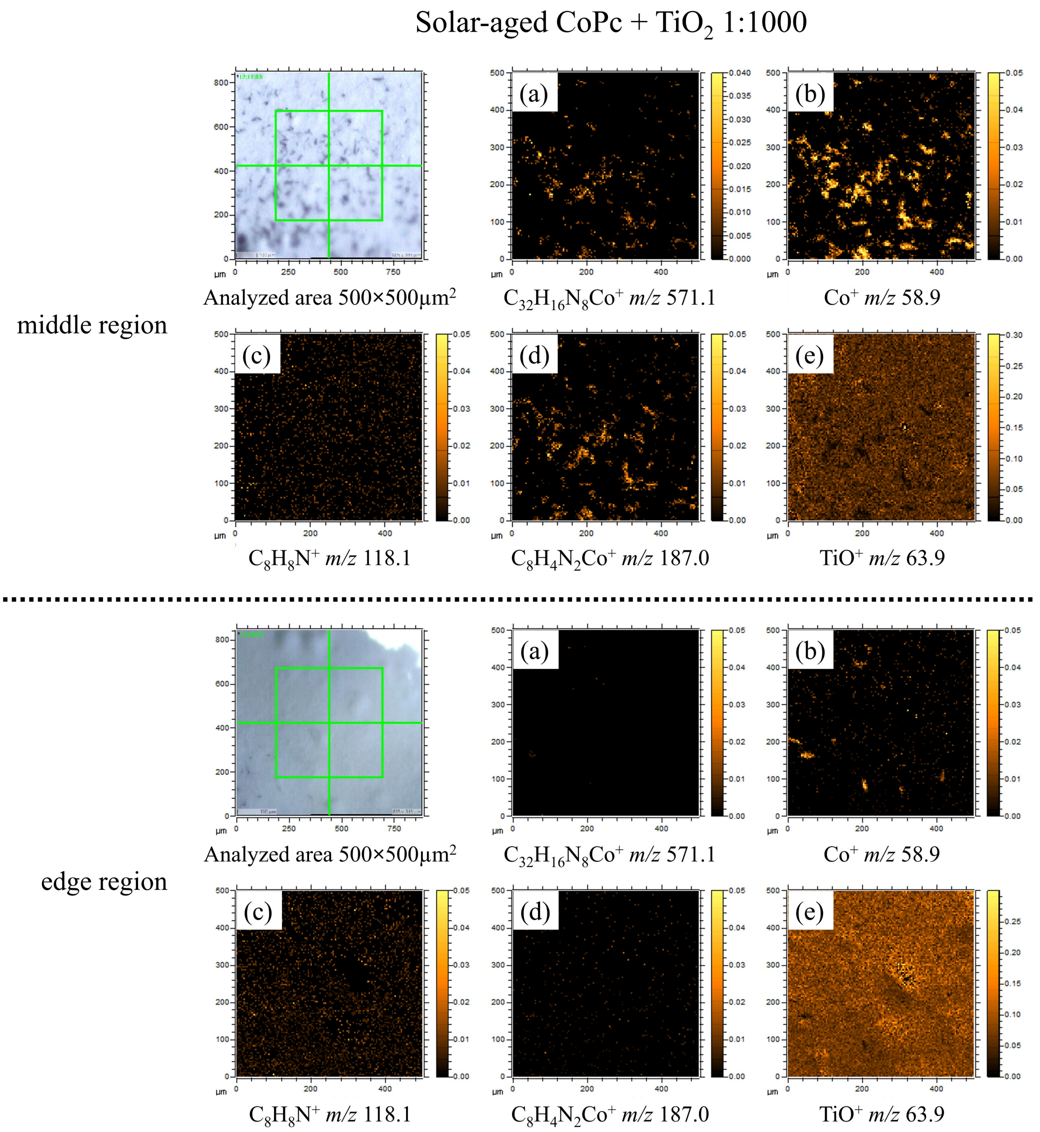

Figure 4.13 Images of the analyzed 500×500 μm^2 surface areas of the solar-aged sample CoPc + TiO_2 1:1000, with the corresponding normalized ToF-SIMS ion maps. The chemical maps, acquired in positive ion mode in the middle region (top) and edge region (bottom), show the ion signals of: (a) cobalt phthalocyanine ($C_{32}H_{16}N_8Co^+$), (b) cobat (Co^+), (c) an isoindole fragment ($C_8H_8N^+$), (d) a CoPc fragment ($C_8H_4N_2Co^+$), and (e) titanium oxide (TiO^+).

4.2.4 Artificial solar aging of CoPc dissolved in organic solvent in presence of TiO_2 with different crystalline phases

As shown in Figure 4.14, CoPc+TiO_2 1:1000 powder samples were prepared in two modalities. Specifically, CoPc solution in THF was realized to solubilize the phthalocyanine molecules, reducing the strong pi-bonds between the molecules, whereas water was used as a medium to disperse the CoPc and TiO_2 powders and deposit them onto a glass slide. In addition, the photostability of cobalt phthalocyanine was studied in combination with four different TiO_2 nanopowders: anatase, rutile, a mixture of anatase and rutile, and P25. The prepared samples were subject to solar irradiation for 56 hours under room laboratory conditions. The light-induced changes were studied with Raman spectroscopy and ToF-SIMS spectrometry.

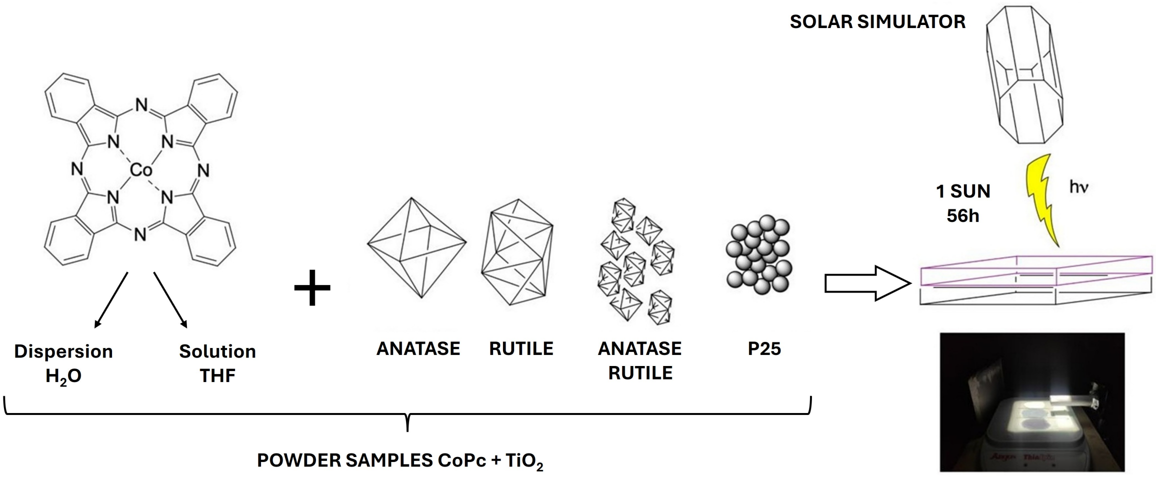

Figure 4.14 Schematic diagram of the preparation of cobalt phthalocyanine and titanium dioxide powder samples, studied under simulated solar irradiation.

The Raman spectra on the degradation of CoPc against different phases of TiO_2 (anatase, rutile, mixture, and P25) were acquired in water (H_2O) and tetrahydrofuran (THF) before and after irradiation for 56 hours under simulated solar irradiation.

In Figure 4.15, the Raman spectra of the anatase TiO_2 with CoPc in H_2O and THF show bands at 144 cm^{-1}, 399 cm^{-1}, 513 cm^{-1}, and 640 cm^{-1}, which correspond to the E_g, B_{1g}, A_{1g}, and E_g modes, respectively [131, 134, 188]. These findings indicate that the anatase phase of TiO_2 is present. The broadened signals in Figure 4.15b observed between 1600 cm^{-1} and 1700 cm^{-1} are attributed to C=C and C=N stretching within the phthalocyanine macrocyclic ring. These signals are the most intensely observed in CoPc in both THF and H_2O. The powder of CoPc in mixture with anatase TiO_2 did not show a significant decrease in signal intensities, indicating that the CoPc pigment is photostable even at a high molar ratio of 1:1000 of CoPc+TiO_2 after the solar irradiation of 56 hours.

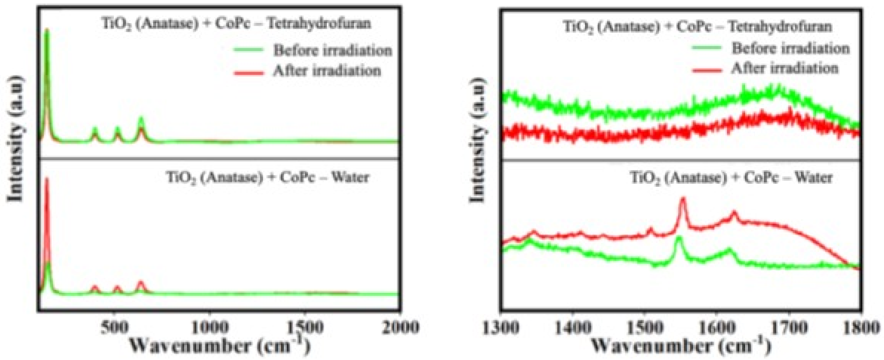

(a) (b)

Figure 4.15 (a) Raman spectra of TiO_2-anatase and CoPc (1:1000 molar ratio) before and after irradiation for 56 hours. (b) Zoom of the spectral range 1300–1700 cm^{-1}.

To further assess the photostability of CoPc, the same experiment was conducted using rutile TiO_2 (Figure 4.16). The Raman signals observed at 237 cm^{-1}, 447 cm^{-1}, and 612 cm^{-1} correspond to the second-order Raman scattering, the E_g, and the A_{1g} mode, respectively [189–191]. The signals associated with the CoPc pigment are as shown in Figure 4.15. Even though the results indicated that the powder of CoPc in mixture with rutile TiO_2 did not reveal a significant decrease after solar irradiation in the CoPc bands within the range of 1300–1700 cm^{-1} in THF, the specific change of the Raman signature in water suggests at least a partial transformation of the pigment (Figure 4.16b). In both solvents, the Raman signal of C=N vibration at 1543 cm^{-1} is decreasing, even though barely detectable above the noise floor.

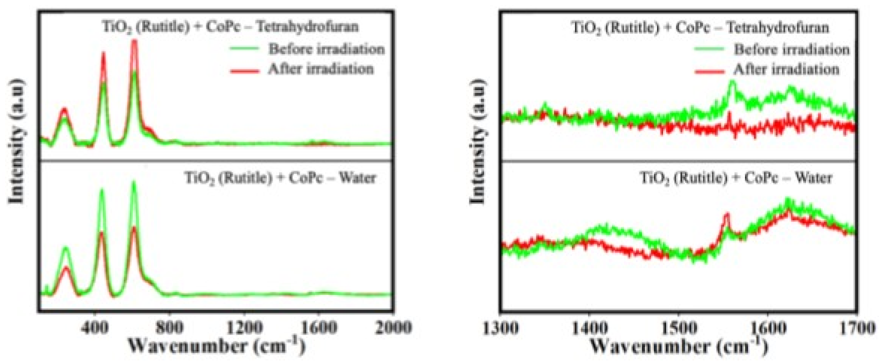

(a) (b)

Figure 4.16 (a) Raman spectra of TiO_2-rutile and CoPc (1:1000 molar ratio) before and after irradiation for 56 h. (b) Zoom of the spectral range 1300–1700 cm^{-1}.

For the TiO_2 mixture of rutile and anatase, the Raman spectra revealed bands corresponding to both anatase and rutile phases of TiO_2 (Figure 4.17). Broadened signals between 1330–1370 cm^{-1} (C–N stretching) and 1600–1700 cm^{-1} (C=C and C=N stretching within the phthalocyanine macrocyclic ring) are visible before irradiation. After 56 hours of solar irradiation, these signals are still present in the Raman spectra of the sample prepared in H_2O with a decrease in intensity, whereas in THF showed the disappearance of CoPc signals, indicating the degradation of the pigment under solar irradiation in the presence of the TiO_2 mixture (Figure 4.17b).

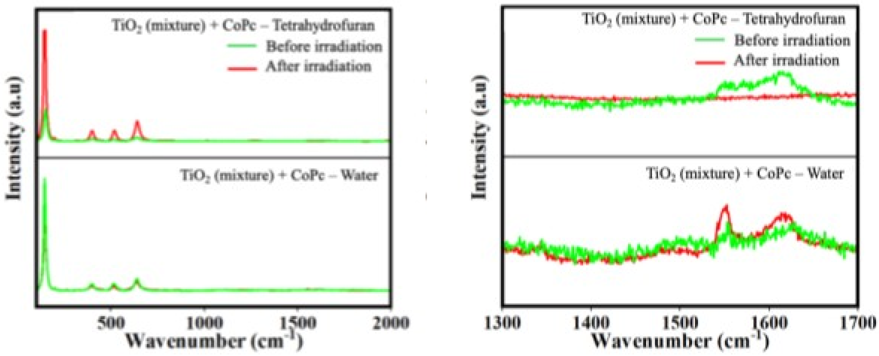

(a) (b)

Figure 4.17 (a) Raman spectra of TiO_2-mixture and CoPc (1:1000 molar ratio) before and after irradiation for 56 h. (b) Zoom of the spectral range 1300–1700 cm^{-1}.

The effects of commercially available photocatalytic nanopowder were also investigated. The Raman spectra revealed bands corresponding to both the anatase and rutile phases of TiO_2 (Figure 4.18). After irradiation in both H_2O and THF, the disappearance of the broadened signal at 1330–1370 cm^{-1} (C–N stretching) and 1600–1700 cm^{-1} (C=C and C=N stretching within the macrocyclic ring) was observed (Figure 4.18b).

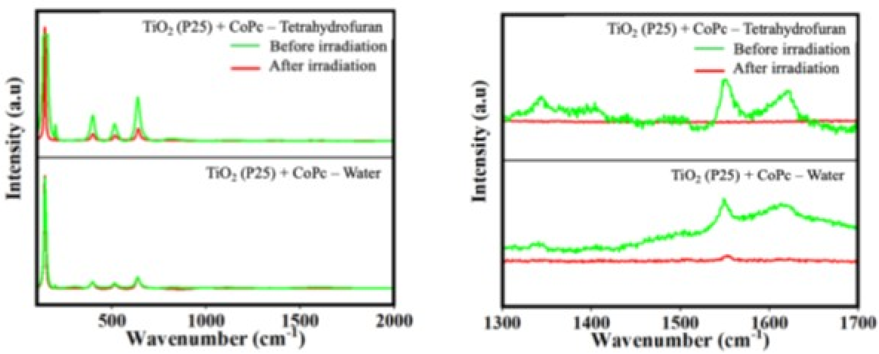

(a) (b)

Figure 4.18 (a) Raman spectra of TiO_2-P25 and CoPc (1:1000 molar ratio) before and after irradiation for 56 h. (b) Zoom of the spectral range 1300–1700 cm^{-1}.

In conclusion, Raman spectra of the samples with pure TiO_2 anatase and rutile did not exhibit significant variations after 56 hours of solar irradiation. On the contrary, a higher photocatalytic activity of the two nanopowder mixtures selected (mixture and P25) was observed, especially in the case of the samples prepared with CoPc solutions in THF, indicating that the pigment is not photostable under these conditions. For this reason, the samples prepared with the two TiO_2 phase mixtures (mixture and P25) were also studied with the TOF-SIMS technique, as reported below.
Figures 4.19 and 4.20 show the ToF-SIMS mass spectra and chemical maps, respectively, acquired in positive ion mode for the sample CoPc+TiO_2 prepared with the mixture of anatase and rutile and with the dispersion in H_2O, before and after the solar irradiation.

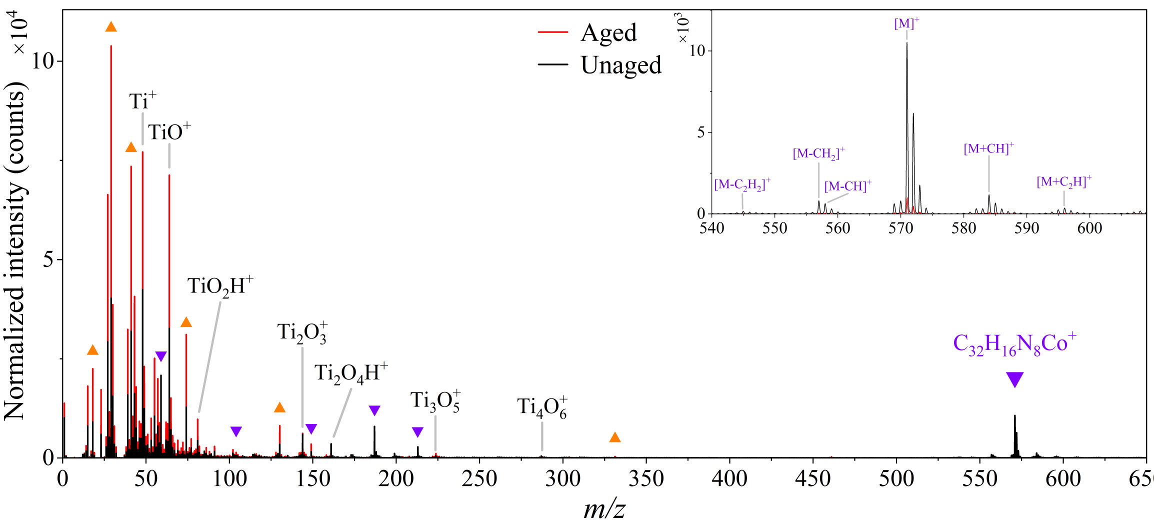

Figure 4.19 ToF-SIMS mass spectra normalized to total counts in the mass-to-charge range m/z 1-650 for the unaged (black line) and aged (red line) CoPc+TiO_2 (mix) samples prepared in H_2O dispersion. TiO_2-related signals are reported, and CoPc fragments are marked with triangle symbols. Inset: mass spectra in the range m/z 540-610.

In the unaged sample, the molecular peak of CoPc ($[M]^+$ $C_{32}H_{16}N_8Co^+$ m/z 571.1) was detected with high intensity and resolution, with its characteristic isotopic pattern. Additional ion patterns, spaced by m/z 13, 14, 25, or 26 to the main molecular peak, were also observed and are attributed to the addition or loss of small hydrocarbon fragments such as CH, CH_2, C_2H, and C_2H_2, respectively, resulting from ion bombardment (Figure 4.19, inset). After solar irradiation, the intensity of these signals decreased significantly. In the chemical maps (Figure 4.20a), the CoPc signal exhibits a homogeneous intensity distribution in the unaged sample, with pigment aggregates in the analyzed area. The surface of the aged sample appears heterogeneous, with regions where pigment aggregation remains visible.

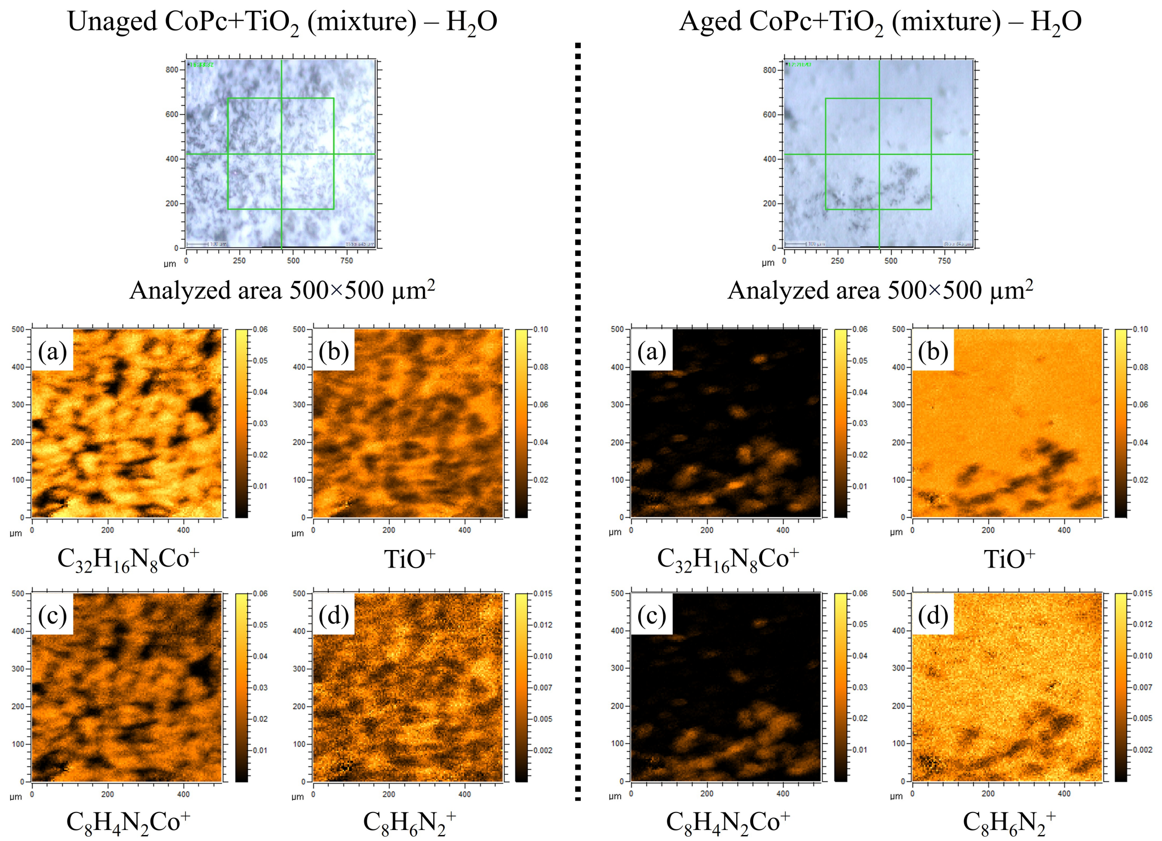

Figure 4.20 Images of the analyzed 500×500 μm^2 surface areas (outlined in green rectangles) for the unaged (left) and aged (right) CoPc+TiO_2 (mix) sample prepared in H_2O dispersion. The corresponding normalized ToF-SIMS chemical maps, acquired in positive ion mode, show the ion signals of: (a) cobalt phthalocyanine ($C_{32}H_{16}N_8Co^+$), (b) titanium oxide (TiO^+), (c) a CoPc fragment ($C_8H_4N_2Co^+$), and (d) a isoindoline fragment ($C_8H_6N_2{}^+$).

Titanium ion signals were detected in both the unaged and aged samples, including Ti^+ at m/z 47.9, TiO^+ at m/z 63.9, TiO_2H^+ at m/z 80.9, $Ti_2O_3{}^+$ at m/z 143.9, $Ti_2O_4H^+$ at m/z 160.9, $Ti_3O_5{}^+$ at m/z 223.8, and $Ti_4O_6{}^+$ at m/z 287.8. After solar irradiation, these signals exhibited higher intensity, especially in the region below 100 m/z. In the chemical maps (Figure 4.20b), TiO^+ ion signals are homogeneously distributed across the analyzed surface, with lower intensity in areas where CoPc aggregates are present, indicating no interaction between the organic and inorganic components.
The fragmentation of the phthalocyanine molecule under ion bombardment is evidenced by the CoPc fragment ions (Figure 4.19, purple triangles), including Co^+ at m/z 58.9, $C_7H_6N^+$ at m/z 104.0, $C_6H_4NCo^+$ at m/z 149.0, $C_8H_4N_2Co^+$ at m/z 186.9, and $C_9H_4N_3Co^+$ at m/z 212.9. The intensity of these fragment ions decreased after solar irradiation, in line with the decrease of the main molecular signal $[M]^+$. This decrease in intensity is also evident in the chemical maps, as demonstrated by a characteristic

CoPc fragment (Figure 4.20c). Additional isoindole fragments were observed in the mass spectra (Figure 4.19, orange triangles), including $C_8H_6N_2^+$ at m/z 130.2, and $C_{16}H_{10}N_5Co^+$ at m/z 331.2. After solar aging, high-intensity ion fragments were also observed in the mass-to-charge region below 100 m/z: NH_4^+ at m/z 18.0, CNH_3^+ at m/z 29.0, CN_2H^+ at m/z 41.0, and $CoNH^+$ at m/z 74.1. These signals exhibit higher intensity in the aged sample, with a uniform distribution across the analyzed area, as evidenced by the chemical maps of a characteristic isoindole fragment (Figure 4.20d). Figures 4.21 and 4.22 show the ToF-SIMS mass spectra and chemical maps, respectively, acquired in positive ion mode for the sample CoPc+TiO_2 prepared with the mixture of anatase and rutile and with the solution in THF, before and after the solar irradiation.

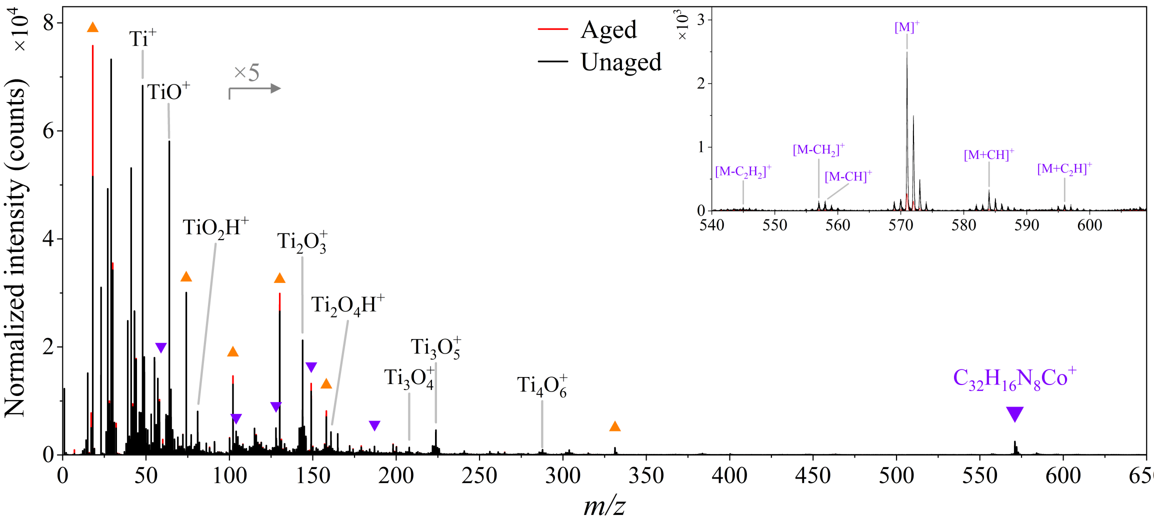

Figure 4.21 ToF-SIMS mass spectra normalized to total counts in the mass-to-charge range m/z 1-650 for the unaged (black line) and aged (red line) CoPc+TiO_2 (mix) samples prepared in THF solution. TiO_2-related signals are reported, and CoPc fragments are marked with triangle symbols. Inset: mass spectra in the range m/z 540-610.

The variations observed for this sample after the simulated solar aging are consistent with those found in the same sample prepared in H_2O. The molecular peak of CoPc ($[M]^+$ $C_{32}H_{16}N_8Co^+$ m/z 571.1) was visible in the unaged sample, where blue-colored shadows were present in the analyzed area. In contrast, in the aged sample, the intensity of this signal decreased significantly and nearly disappeared, as evidenced by the comparison of the acquired chemical maps (Figure 4.22a). Additionally, titanium dioxide signals and the CoPc fragments decreased following irradiation, whereas the fragments corresponding to isoindole structures increased. These variations in intensity are also evident in the chemical maps, as demonstrated by the selected characteristic signals (Figure 4.22b-d). In addition, two more isoindole-related fragments were

recorded, alongside those previously observed: $C_7H_4N^+$ at m/z 102.1, and $C_9H_8N_3{}^+$ at m/z 158.1 (Figure 4.21, orange triangles). The intense $NH_4{}^+$ signal in the aged mass spectrum at m/z 18.0 supports a possible degradation mechanism.
As in the preliminary analyses, the isoindole fragments observed in the aged mass spectra are likely attributed to degradation products rather than ion-induced fragmentation by ToF-SIMS, as the molecular peak of CoPc is not detected. Notably, when a CoPc solution in THF was used, degradation occurred across the whole surface, in contrast to the preliminary results, where it was restricted to the edge, or in the case of the same sample prepared in H_2O, where pigment aggregation is visible even after aging.

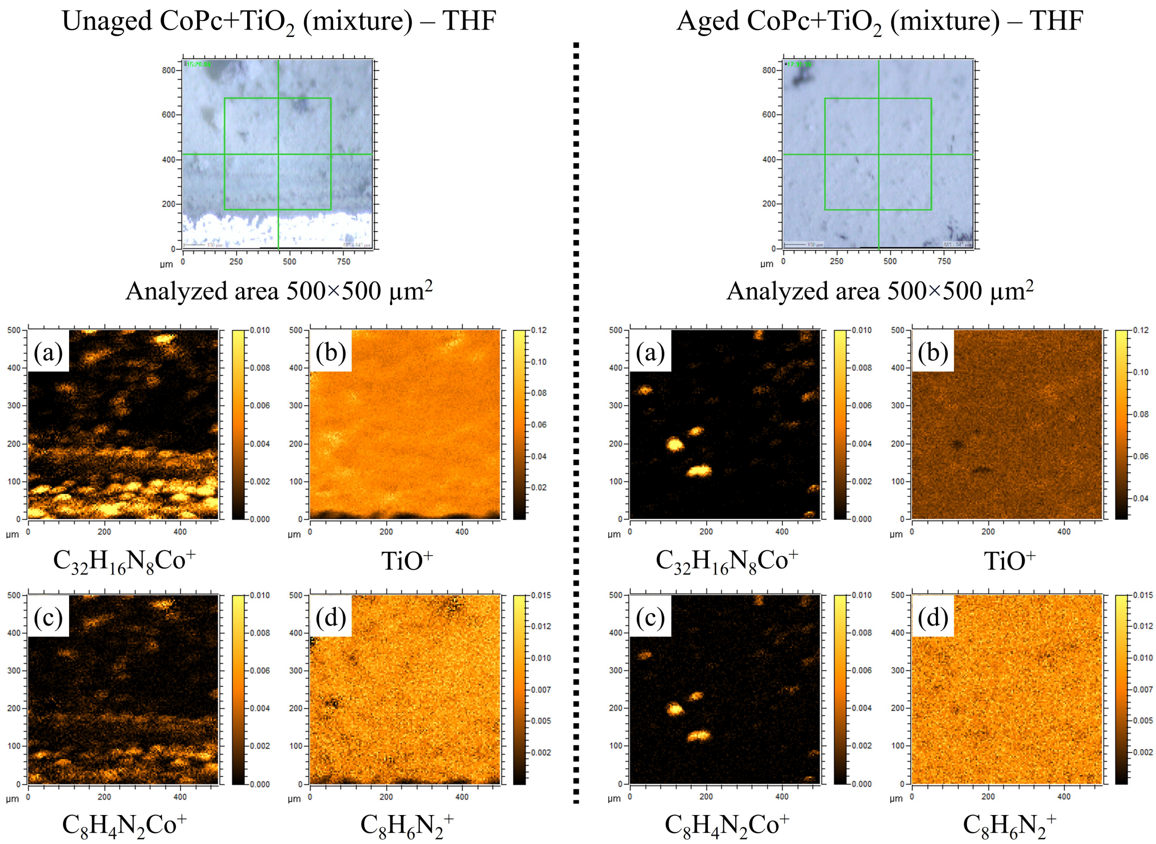

Figure 4.22 Images of the analyzed 500×500 μm^2 surface areas (outlined in green rectangles) for the unaged (left) and aged (right) CoPc+TiO_2 (mix) sample prepared with THF solution. The corresponding normalized ToF-SIMS chemical maps, acquired in positive ion mode, show the ion signals of: (a) cobalt phthalocyanine ($C_{32}H_{16}N_8Co^+$), (b) titanium oxide (TiO^+), (c) a CoPc fragment ($C_8H_4N_2Co^+$), and (d) a isoindoline fragment ($C_8H_6N_2{}^+$).

Similar results were obtained for the samples prepared with titanium dioxide P25 nanopowder, comparing the sample preparation with the dispersion in H_2O and with the solution in THF.

Figures 4.23 and 4.24 show the ToF-SIMS mass spectra and chemical maps, respectively, acquired in positive ion mode for the sample CoPc+TiO_2 prepared with the P25 nanopowder and with the dispersion in H_2O, before and after the solar irradiation.

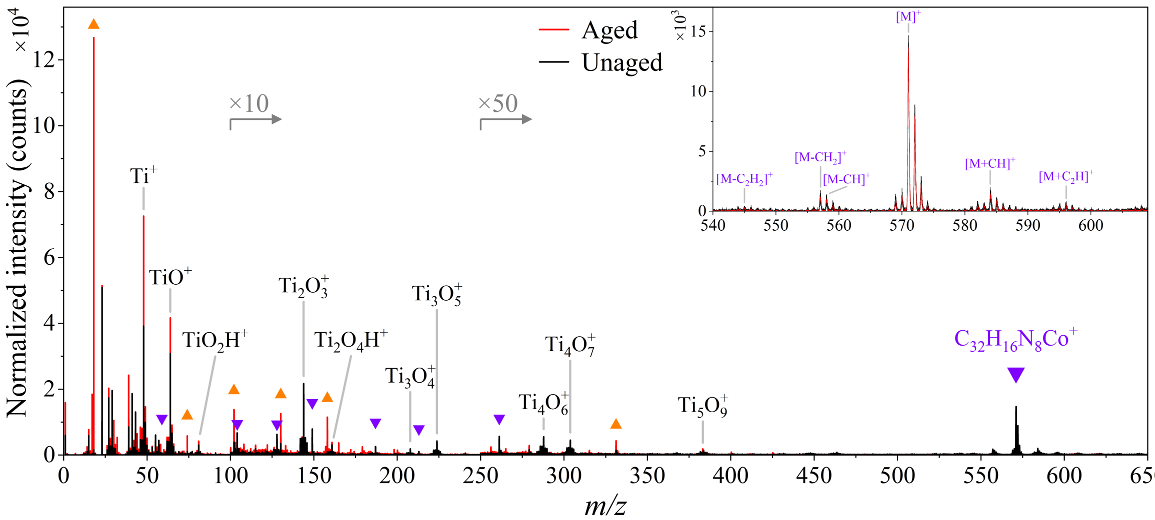

Figure 4.23 ToF-SIMS mass spectra normalized to total counts in the mass-to-charge range m/z 1-650 for the unaged (black line) and aged (red line) CoPc+TiO_2 (P25) samples prepared in H_2O dispersion. TiO_2-related signals are reported, and CoPc fragments are marked with triangle symbols. Inset: mass spectra in the range m/z 540-610.

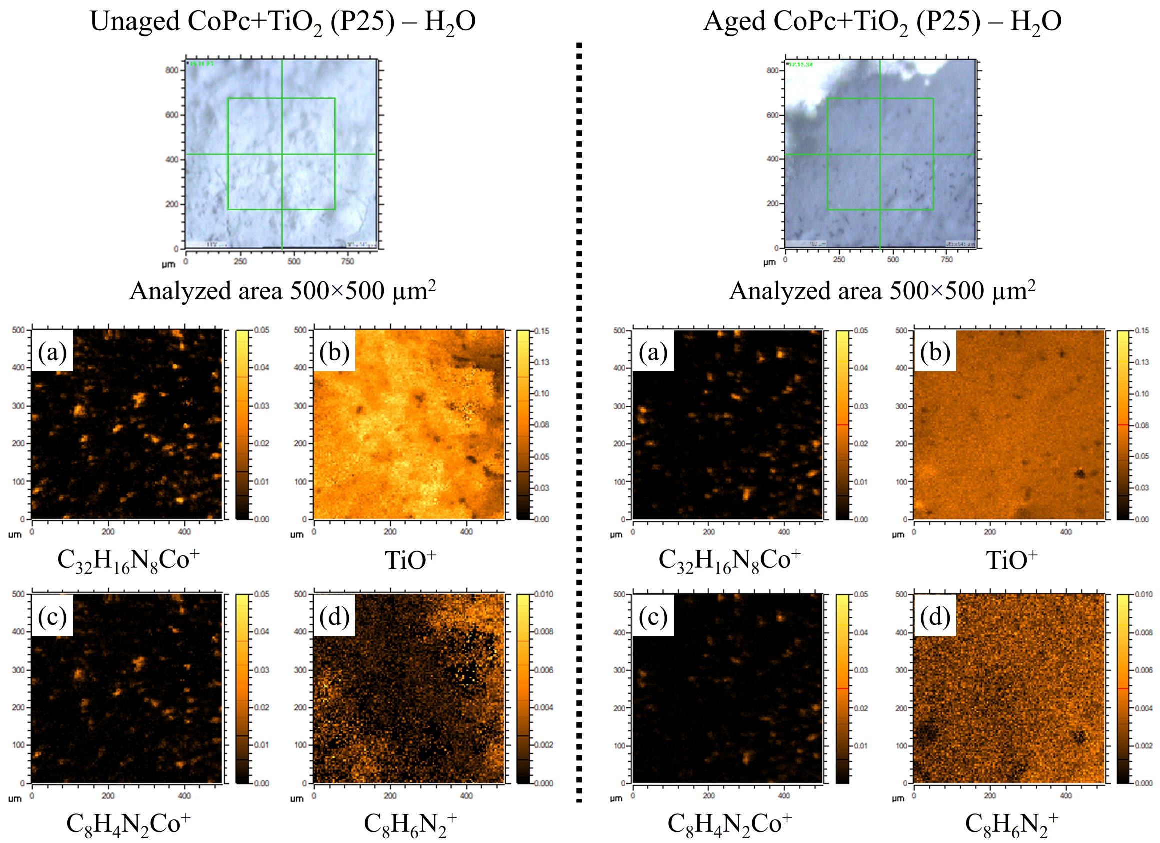

Figure 4.24 Images of the analyzed 500×500 μm^2 surface areas (outlined in green rectangles) for the unaged (left) and aged (right) CoPc+TiO_2 (P25) sample prepared in H_2O dispersion. The corresponding normalized ToF-SIMS chemical maps, acquired in positive ion mode, show the ion signals of: (a) cobalt phthalocyanine ($C_{32}H_{16}N_8Co^+$), (b) titanium oxide (TiO^+), (c) a CoPc fragment ($C_8H_4N_2Co^+$), and (d) a isoindoline fragment ($C_8H_6N_2{}^+$).

Figures 4.25 and 4.26 show the ToF-SIMS mass spectra and chemical maps, respectively, acquired in positive ion mode for the sample CoPc+TiO_2 prepared with the P25 nanopowder and with the solution in THF, before and after the solar irradiation.

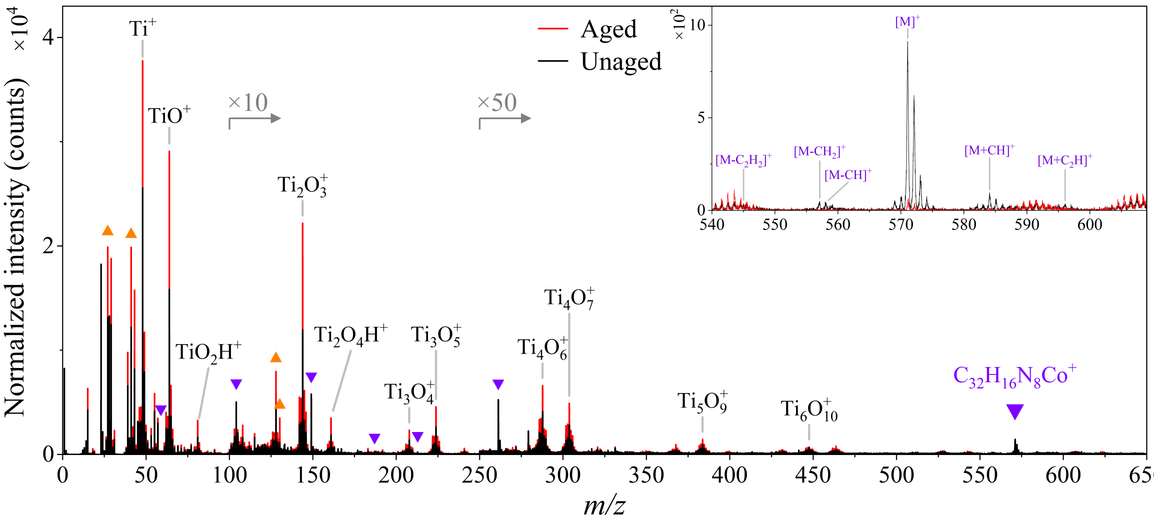

Figure 4.25 ToF-SIMS mass spectra normalized to total counts in the mass-to-charge range *m/z* 1-650 for the unaged (black line) and aged (red line) CoPc+TiO_2 (P25) samples prepared in THF solution. TiO_2-related signals are reported, and CoPc fragments are marked with triangle symbols. Inset: mass spectra in the range *m/z* 540-610.

For the samples prepared with P25, the difference between the two sample preparation methods (CoPc dispersion in H_2O and CoPc solution in THF) is more evident than in the previous case. Specifically, the molecular peak of CoPc in the unaged samples appears as aggregated pigment in the acquired chemical maps (Figures 4.24a and 4.26a). However, in the unaged THF-based sample, the aggregates appear smaller and more homogeneously distributed across the analyzed area, indicating a clear distinction between the CoPc dispersion and solution. After aging, a decrease in the intensity of this signal is observed: only a slight decrease is detected for the sample prepared in H_2O (Figure 4.23, inset), whereas the molecular signal almost completely disappears in the sample prepared in THF (Figure 4.25, inset).

Titanium signals exhibited an increase in intensity in the aged spectrum of the sample prepared with H_2O, particularly in the range below *m/z* 100, as also evidenced by the TiO^+ ion signals in the chemical maps (Figure 4.24b). In contrast, these signals dominated the mass spectra of the sample prepared with THF, both before and after irradiation, showing an additional titanium species (Ti_6O_{10} at *m/z* 447.6) and overall higher intensity in the aged spectrum, as also observed in the corresponding chemical maps (Figure 4.26b). As previously observed, the CoPc fragment ions (Figures 4.23 and 4.25, purple triangles) decreased consistently with the loss of the molecular peak. This decrease in intensity is particularly evident in the chemical maps, as demonstrated by the selected CoPc fragment (Figures 4.24c and 4.26c), especially in the case of the THF-based sample. The isoindole-related fragments (Figures 4.23 and 4.25, orange triangles), already present in the unaged spectra, increased after irradiation and displayed a homogeneous intensity distribution in the chemical maps across the analyzed surface (Figures 4.24d and 4.26d).

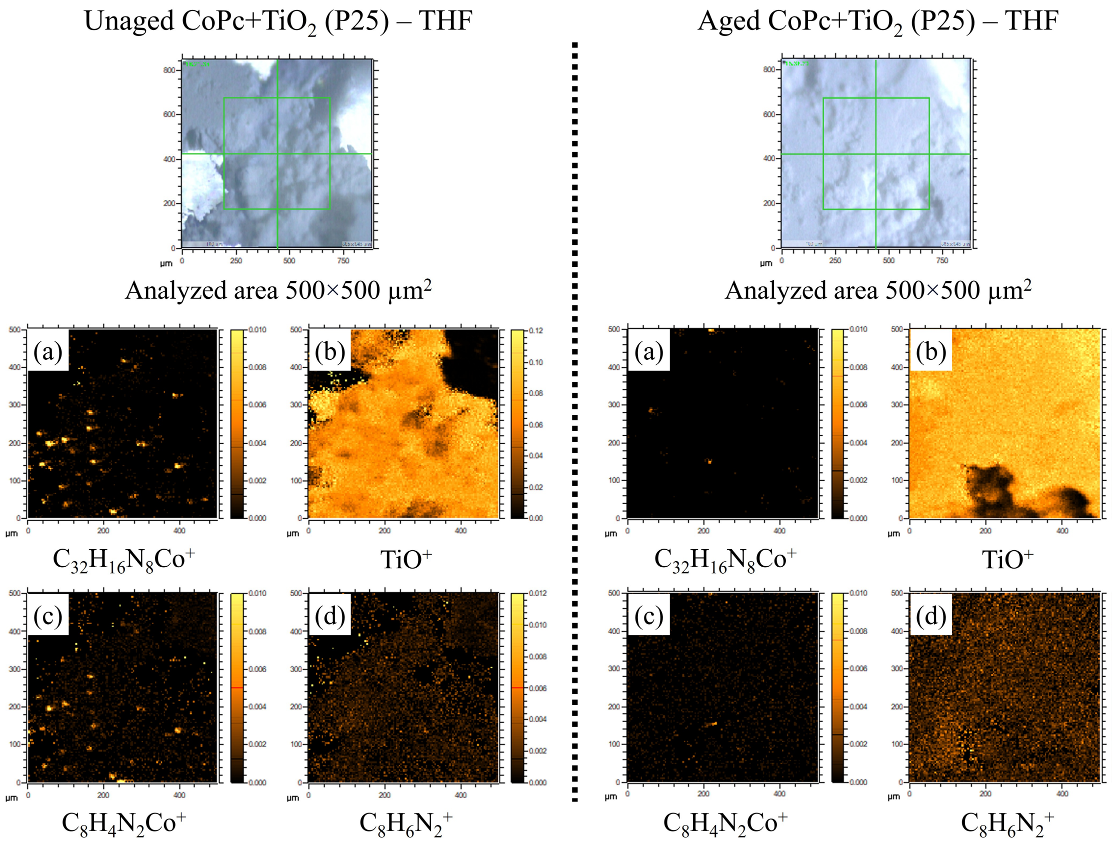

Figure 4.26 Images of the analyzed 500×500 μm^2 surface areas (outlined in green rectangles) for the unaged (left) and aged (right) CoPc+TiO_2 (P25) sample prepared with THF solution. The corresponding normalized ToF-SIMS chemical maps, acquired in positive ion mode, show the ion signals of: (a) cobalt phthalocyanine ($C_{32}H_{16}N_8Co^+$), (b) titanium oxide (TiO^+), (c) a CoPc fragment ($C_8H_4N_2Co^+$), and (d) a isoindoline fragment ($C_8H_6N_2{}^+$).

4.3 Conclusions

In conclusion, the results obtained highlighted how the difference in the preparation of CoPc+TiO_2 powder samples between dispersion and solution significantly influences the stability of the cobalt phthalocyanine pigment under simulated solar irradiation.

The hypothesized degradation process is illustrated in Figure 4.27.

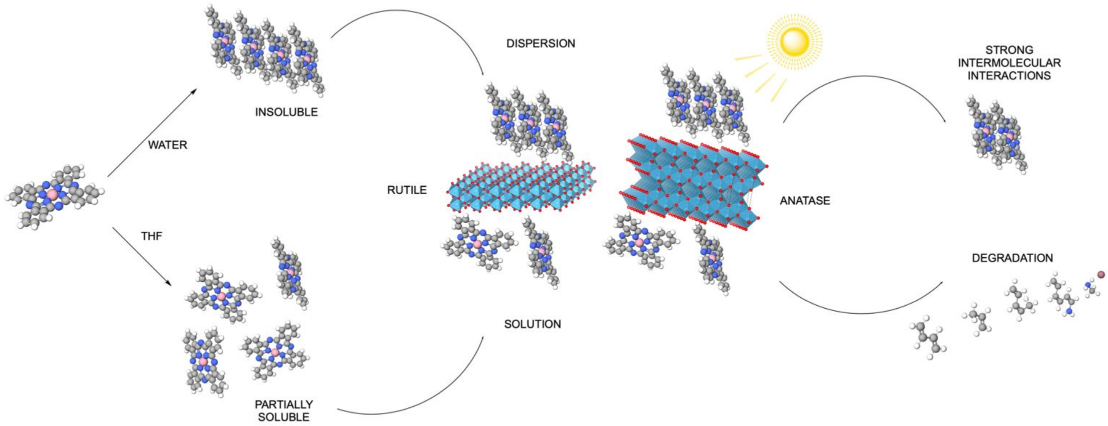

Figure 4.27 Hypothesized degradation mechanism of the CoPc with TiO_2 under solar irradiation, comparing the pigment dispersion in H_2O and the solution in THF.

The dispersion in H_2O did not result in a complete degradation of the CoPc. Indeed, the signals attributed to the CoPc pigment, both in Raman and ToF-SIMS spectra, are still evident after aging, although with decreased intensity. A part of the pigment, perhaps the finer fraction, degraded under solar irradiation, as indicated by the isoindole fragments detected with ToF-SIMS. However, most of the pigment tend to form aggregates, and the strong intermolecular interaction between the phthalocyanine molecules likely determines its stability.

On the contrary, when the samples were prepared with CoPc solution in THF, the solvent more effectively separated the phthalocyanine molecules, and a photodegradation of the pigment under solar irradiation in the presence of TiO_2 was observed. This is confirmed by the absence of the signals related to CoPc, both in Raman and ToF-SIMS measurements. Furthermore, the isoindole fragments in the aged mass spectra are clearly related to the photodegradation of cobalt phthalocyanine.

These results are evident in the powder samples mixing CoPc with the TiO_2 mixture of anatase and rutile, but in particular with the TiO_2 P25 nanopowder. Indeed, the particle size, the surface area, the crystallinity, the crystallite dimension, and the phase composition of TiO_2 significantly affect its reactivity [192, 193]. For this reason, the specific properties of titanium dioxide must be considered in this study.

From an application point of view, these results suggest that both the preparation method and the crystalline phases of the TiO_2 can significantly influence the stability of CoPc pigment in practical applications, such as coatings, solar cells, and photocatalytic systems. Additional studies could investigate different phthalocyanine compounds (CuPc, MgPc, AlPc, ZnPc, etc.) in combination with TiO_2 nanopowders.

Part III

Conclusions

This Ph.D. research focused on the study of the stability of three modern organic pigments in the presence of reactive inorganic whites. Artificial aging experiments were carried out in order to investigate the degradation mechanisms affecting these materials. The first phase of the work thus involved the design and optimization of effective aging processes, applied to multi-component samples prepared in the laboratory by mixing organic and inorganic pigments. These aging processes aimed to accelerate and simulate environmental conditions to which works of art are typically subjected over time, especially in the case of outdoor conditions, such as street art and murals.
A key objective of this research was to set up an analytical methodology based on the integration of complementary techniques with different surface analysis sensitivities. This multi-technique approach enabled both to characterize all the selected materials and to investigate the chemical, physical, and morphological variations induced by the aging process in complex multi-component samples. The combination of colorimetry, Fourier transform infrared spectroscopy, Raman spectroscopy, X-ray diffraction, and time-of-flight secondary ion mass spectrometry was fundamental for identifying and understanding the main degradation effects after aging.
Two case studies were presented as the most relevant results obtained in this Ph.D., illustrating how the presence of white inorganic pigments can significantly accelerate the photodegradation of modern organic pigments, including monoazo, isoindoline, and phthalocyanine.
The results of the first work, "Stability of monoazo and isoindoline yellows mixed with white pigments", showed the influence of three inorganic whites (basic lead carbonate, titanium dioxide, and zinc oxide) on the stability of two modern yellow pigments, PY1 (monoazo) and PY139 (isoindoline). These modern pigments were selected for their use in modern and contemporary art practices, as well as in street art, often combined with

inorganic compounds. The organic and inorganic pigments were mixed with linseed oil as a binder to obtain simplified paint samples that replicate the composition of real paint systems. The findings provide insights into the photodegradation mechanisms affecting both the binder and the yellow pigments at the surface levels, as a result of their interaction with UV-VIS radiation and the reactivity of the inorganic pigments. The visible color changes highlight the impact of metal oxides on the degradation of yellow pigments. Titanium dioxide induces significant surface degradation of the paints, due to its nanopowder form and photocatalytic activity. In contrast, zinc oxide shows limited reactivity, likely due to its larger particle size. Lead carbonate basic, on the other hand, primarily influences the drying of the oil binder and promotes the oxidation of only the finer fractions of the organic pigments. This study investigates the degradation pathways of two modern yellow pigments in the presence of inorganic compounds under UV-VIS artificial aging. The findings enhance the understanding of the long-term stability of these pigments in simplified paint models that simulate artworks exposed to environmental stress.
The results obtained in the second work, "Solar photostability of Co-phthalocyanine with TiO_2 nanopowders", showed the effect of titanium dioxide on the stability of a modern pigment known for its excellent lightfastness (cobalt phthalocyanine). Phthalocyanine and titanium are frequently used together in artistic applications and technological fields, such as coatings, solar cells, and photocatalytic systems. In this case, powder samples were prepared to investigate the stability of this modern pigment in the presence of titanium dioxide alone, previously identified as the most reactive white pigment. The results highlight the importance of the solvent effect during sample preparation. Compared to dispersion in water, the use of tetrahydrofuran solutions significantly enhances the interaction between titanium dioxide and cobalt phthalocyanine, leading to a complete photodegradation of the pigment under solar irradiation. In addition, different crystalline phases of titanium dioxide were tested to evaluate their influence on its photocatalytic activity and, consequently, on the degradation of the cobalt phthalocyanine pigment. Based on these results, the crucial role of the crystalline and morphological properties of TiO_2, such as its crystalline phase (anatase or rutile), the crystallite size, the particle size (and thus the surface area), as well as any surface modifications, becomes evident. For this reason, future studies should include a detailed investigation of the different crystalline phases and particle sizes of titanium dioxide when interacting with cobalt phthalocyanine. This would contribute to a deeper understanding of the degradation mechanisms and the influence that different crystalline nanopowders exert on the stability of the organic

molecule.
In conclusion, this Ph.D. research has opened up a new line of investigation in the two laboratories, laying the foundations for a deeper scientific understanding of the interactions between organic and inorganic pigments, as well as the photostability of modern paints. Indeed, the results highlighted the importance of evaluating the compatibility of organic and inorganic pigment mixtures in paint formulations, providing important data on the long-term stability of selected synthetic organic pigments. Additionally, the findings can offer useful information for the preventive conservation of modern and contemporary works of art.
Future perspectives emerge from these studies. For example, one promising research direction may involve expanding the range of investigated pigments and binders in order to obtain a more complete understanding of current artistic practices and to build a reference database of the main degradation processes involving modern pigments. In addition, it would be interesting to investigate real-world case studies of artworks to better understand how these degradation processes manifest under real environmental conditions, or implement the study through stratigraphic techniques to examine how surface degradation propagates into the deeper layers of the paints. Indeed, by combining stratigraphic analysis with the multi-technique approach developed in this research, an even more complete view of the aging process could be achieved. Another direction could concern studies on kinetic aging, by systematically varying the main parameters of light, temperature, relative humidity, and exposure time. Furthermore, investigating the role of air pollutants and their interaction with photocatalytic pigments may offer insights into the degradation process under real environmental conditions.
The following section includes the scientific publications and participation in international conferences resulting from this Ph.D. research.

List of publications

List of publications:

- A. De Carlo, B. Senthilmurugan, V. Graziani, A. Ruediger, P. Antici, Luca Tortora. Solar photostability of cobalt phthalocyanine with TiO_2 nanopowders. (in preparation).
- A. De Carlo, V. Graziani, A. Privitera, E. Marconi, E. Colantoni, G. Iorio, A. Sodo, P. Antici, L. Tortora. Modern pigments in street art: stability of monoazo and isoindoline yellows mixed with $2PbCO_3{\cdot}Pb(OH)_2$, ZnO, and TiO_2 white pigments. *Dyes and Pigments*, 244:113122, 2026. DOI: 10.1016/j.dyepig.2025.113122.
- A. De Carlo, V. Graziani, A. Privitera, A. Sodo, P. Branchini, P. Antici, L. Tortora. Artificial aging of monoazo and isoindoline yellow pigments. *Acta IMEKO*, 13(3):1–9, 2024. DOI: 10.21014/actaimeko.v13i3.1791.
- A. Mazzinghi, L. Castelli, C. Ruberto, et al. X-ray and neutron imaging for cultural heritage: the INFN-CHNet experience. *The European Physical Journal Plus*, 139:635, 2024. DOI: 10.1140/epjp/s13360-024-05429-z.
- A. De Carlo, V. Graziani, P. Branchini, L. Tortora. Monoazo and Isoindoline Yellow reactivity in presence of Pb, Ti, Zn-based white substrates. In *Proceedings of the 2023 IMEKO TC4 International Conference on Metrology for Archaeology and Cultural Heritage*, pages 485–490, 2023. DOI: 10.21014/tc4-ARC-2023.092.
- A. De Carlo. Photophysical properties changes of organic dyes induced by accelerated UV aging. In *Proceedings of the XII International Conference Diagnosis for the Conservation and Valorization of Cultural Heritage conference*, pages 410–421, 2021. ISBN: 978-88-95609-61-4.

International conferences:

- 2023 IMEKO International Conference "Metrology for Archaeology and Cultural Heritage". Rome (Italy) / October 19-21, 2023.
- XII International AIES Conference "Diagnosis for the Conservation and Valorization of Cultural Heritage". Museo Archeologico Nazionale di Napoli, Naples (Italy) / December 9-10, 2021.

Posters:

- V. Graziani, A. De Carlo, B. Senthilmurugan, A. Ruediger, P. Antici, L. Tortora. Titania nanoparticle-mediated photodegradation in Co-phthalocyanine powder samples. SIMS Europe 2025, Gießen (Germany) / September 7-9, 2025.

A Supplementary Materials - Chapter 3

This appendix provides the supplementary materials supporting the results discussed in Chapter 3: Stability of monoazo and isoindoline yellows mixed with white pigments.

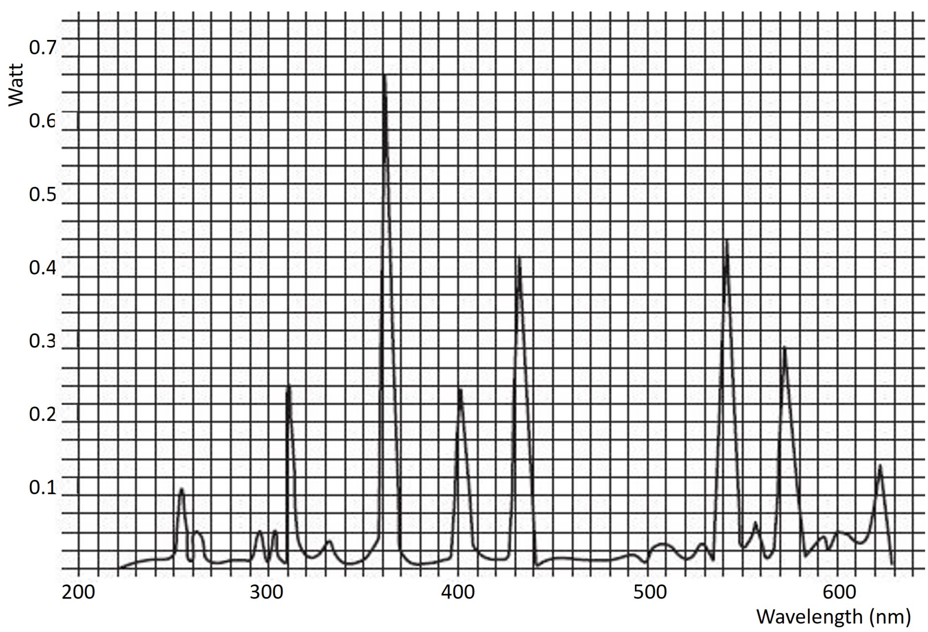

Figure A.1 Spectral power distribution of the 125 W Hg lamp employed for the artificial aging process with emission from 220 nm to 630 nm, provided by Angelantoni manufacturer.

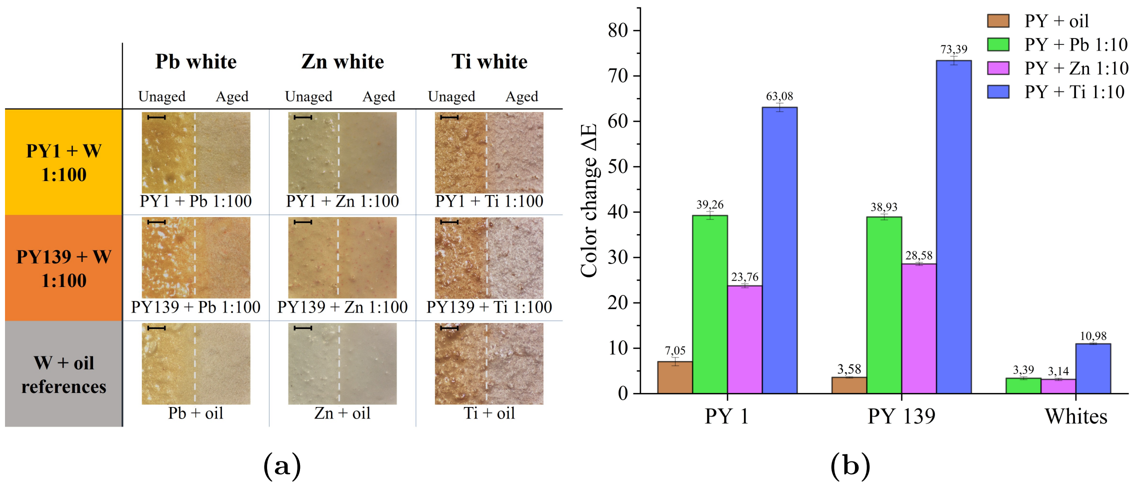

Figure A.2 (a) Images of the three-component paint samples realized with the mass ratio 1:100 between yellow pigment and inorganic white with the reference samples acquired with the stereomicroscope (scale bar denotes 500 μm length). The images show the unaged (left) and artificially aged (right) parts of the samples. (b) Total color change ΔE for the three-component paint and reference samples following artificial aging. On the left are the samples with PY1, on the center are the samples with PY139, and on the right are the W + oil reference samples.

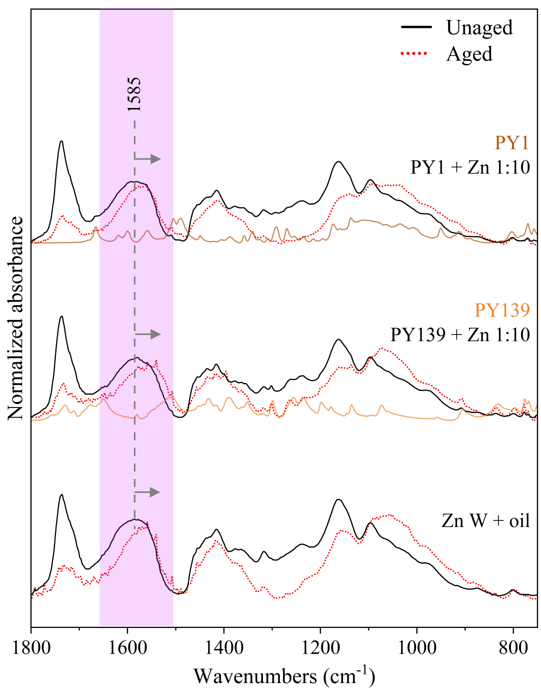

Figure A.3 ATR-FTIR normalized spectra for the unaged (black line) and aged (dotted red line) three-component paint samples with zinc white in the spectral range 1800-750 cm^{-1}.

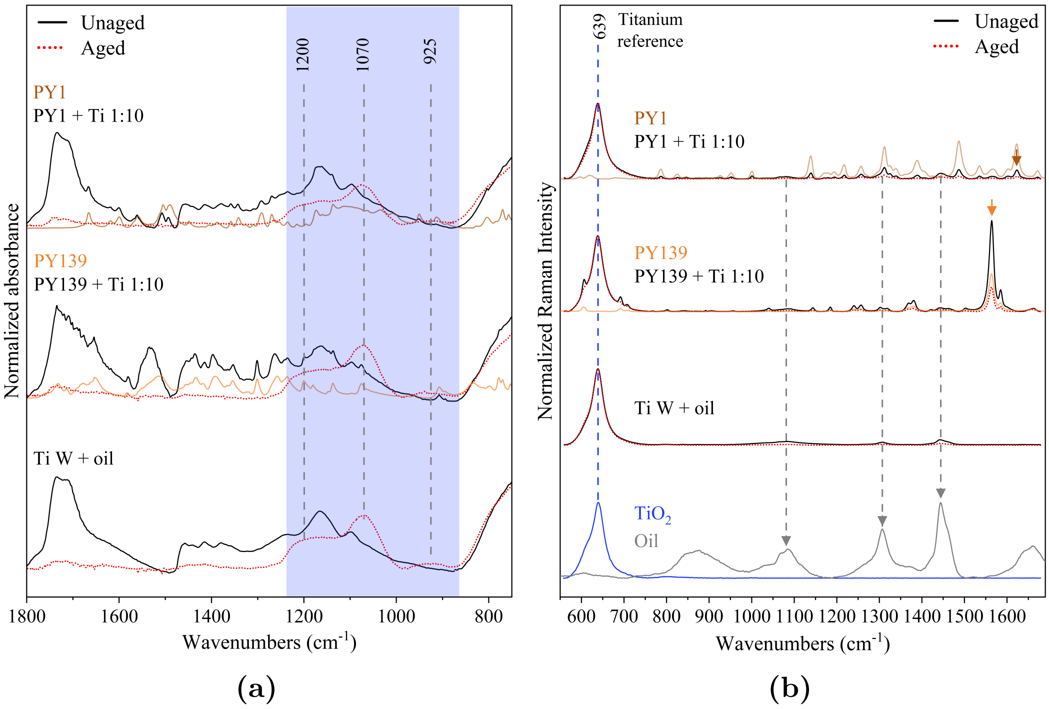

Figure A.4 (a) ATR-FTIR and (b) Raman normalized spectra for the unaged (black line) and aged (dotted red line) three-component paint samples with titanium white in the range 1800-750 cm^{-1} and 550-1690 cm^{-1}, respectively. Raman spectra were acquired in static mode, with laser power 90 mW, integration time 1 s, and 100 accumulations.

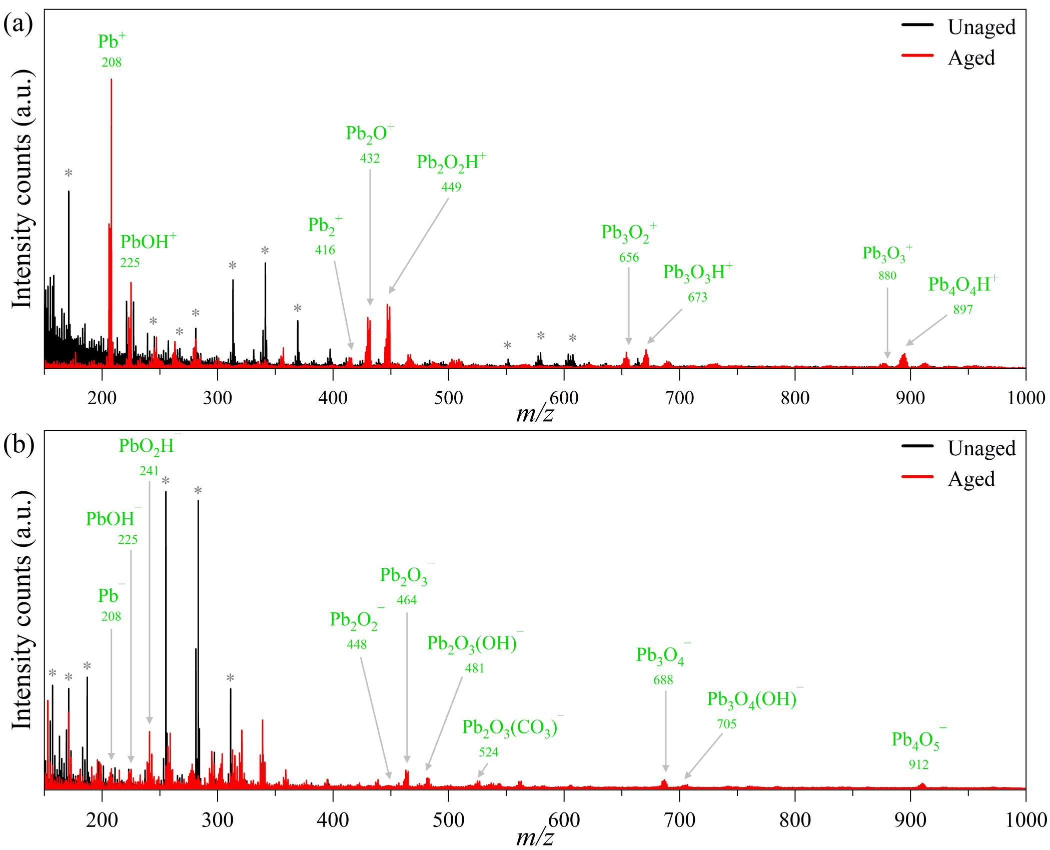

Figure A.5 ToF-SIMS mass spectra normalized to total counts in the mass-to-charge range m/z 150-1000 acquired for the unaged (black line) and aged (red line) reference sample of Pb W + oil in positive (a) and negative (b) ion mode. Lead-related signals are written in green, and linseed oil fragments are marked with gray asterisks.

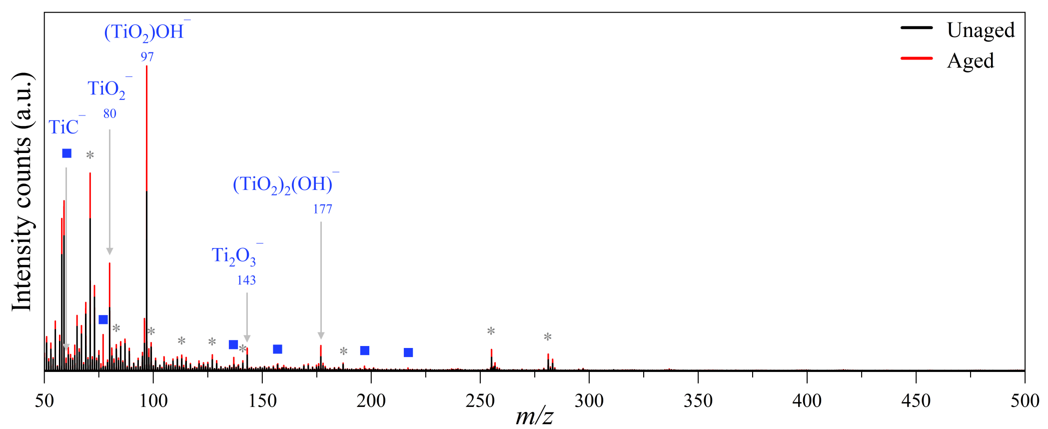

Figure A.6 ToF-SIMS mass spectra normalized to total counts in the mass-to-charge range m/z 50-500 acquired for the unaged (black line) and aged (red line) reference sample of Ti W + oil in negative ion mode. TiO_2-related signals are written in blue, linseed oil fragments are marked with gray asterisks, and TiC-adducts with blue squares.

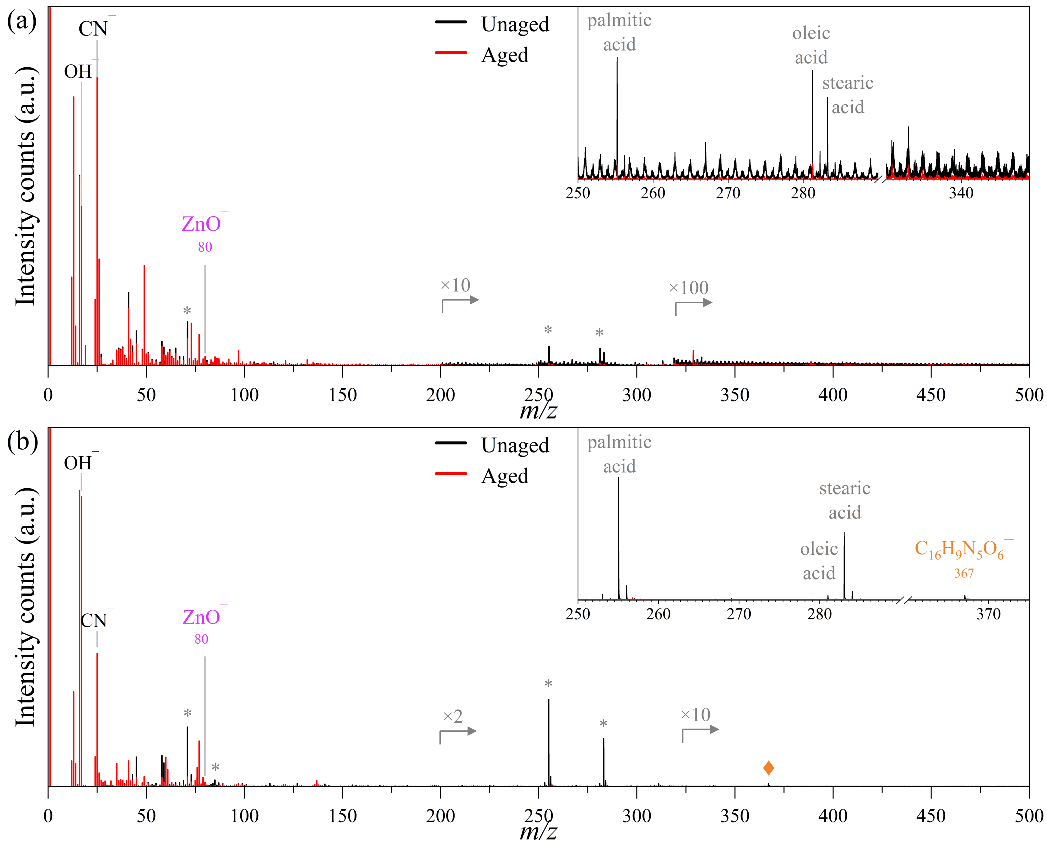

Figure A.7 ToF-SIMS mass spectra normalized to total counts in the mass-to-charge range 1-500 acquired for the unaged (black line) and aged (red line) three-component paint samples containing zinc white with PY1 (a) and PY139 (b) in negative ion mode. ZnO ion signals are written in pink, linseed oil fragments are marked with gray asterisks, and molecular peaks with diamonds.

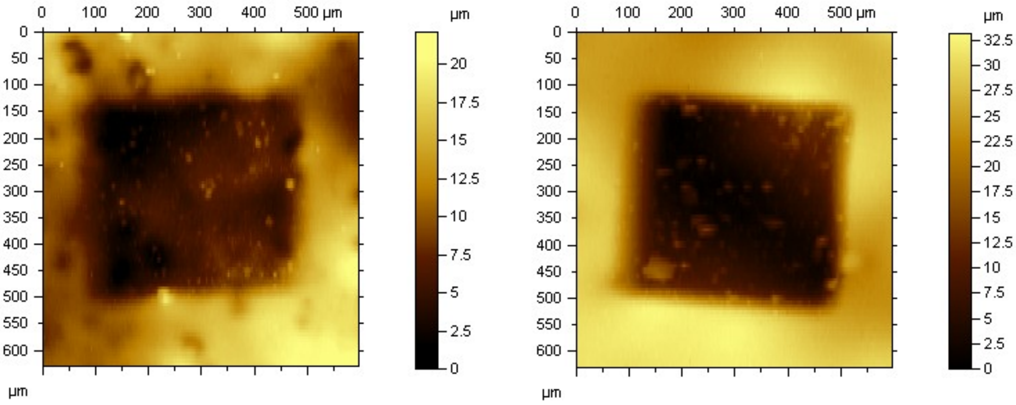

(a) **(b)**

Figure A.8 Surface topography maps acquired using stylus profiler to evaluate the depth profiles obtained by the ToF-SIMS sputtering technique for the unaged (a) and aged (b) three-component PY1 + Zn 1:10 sample.

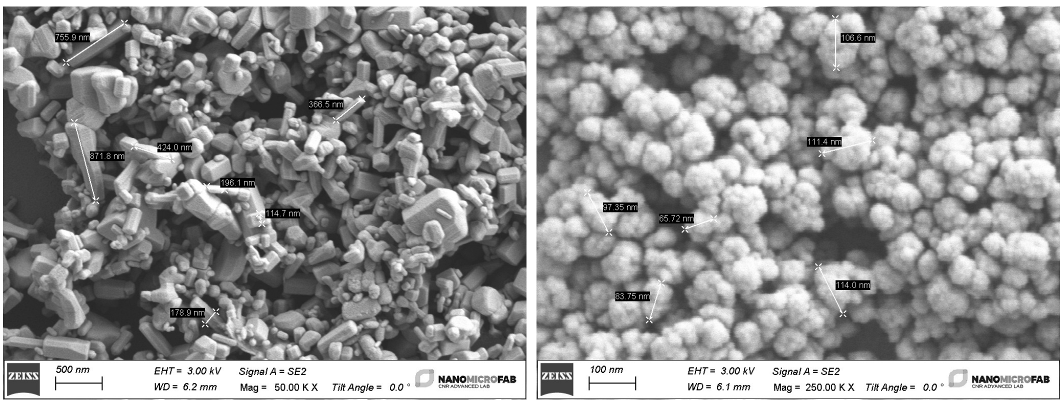

(a) **(b)**

Figure A.9 SEM images of the ZnO powder (a) and TiO_2 powder (b).

B Preparation procedure for CoPc solutions

This appendix describes the preparative procedures for the cobalt phthalocyanine (CoPc) solutions used in the preparation of the samples studied in Ch.4: Solar photostability of Co-phthalocyanine with TiO_2 nanopowders.
CoPc solutions were realized to reduce the strong bonds between the phthalocyanines themselves, and subsequently allow them to interact with titanium dioxide, using tetrahydrofuran (THF) and dichloromethane (DCM) as solvents. The procedure for the preparation of saturated CoPc dissolution consists of three fundamental steps:

1. Finely grind the phthalocyanine powder manually using a ceramic mortar. This step is crucial as it optimizes the process.
2. 10 mg of phthalocyanine powder was weighed with a SARTORIUS balance and dispersed in 100 mL of solvent using a conical flask.
3. The container was immersed for 10 minutes in an ultrasonic tank (Digital Ultrasonic Cleaner DV-32 ARGOLAB) at maximum power and a temperature of approximately 30°C. The suspension was then mixed with vortex agitation, and the ultrasonic procedure was repeated. The dispersion obtained has been left to rest for 24 hours.

Once step 3 is completed, a sediment is observed at the bottom of the beaker. A portion of the powder has dissolved, while another part has settled. At this point, two different methods were attempted to obtain the solutions and calculate their concentration.

Filtration

Cellulose filters were used to filter the solutions (Figure B.1a). The filter was pre-weighed before filtration, then dried in a Memmert vacuum drying oven at T = 80°C and p = 600 mbar for 1 hour and stood for 1 hour under room conditions. In this way, only the amount of powder trapped in the filter can be weighed. However, it was not possible to obtain a correct estimate of the settled powder as the solvent influenced the filter. The effect of solvent on the filter was also studied by a grammage method, increasing the mass of the filter and calculating the grammage as g/m^2. However, no exact validation was found.

Sampling

From the dispersion, $V_f = 32$ mL was taken into a glass vial, carefully using a Pasteur pipette to extract only the supernatant and not the settled powder. The remaining portion of the dispersion in the beaker was evaporated on a hot plate and dried in the vacuum oven. Subsequently, the remaining powder was weighed (as the difference between the weight of the empty beaker and the weight of the beaker with the dried powder). The concentration was then calculated as:

$$C_{CoPc} = \frac{(m_i - m_f)}{MW \cdot V_f},$$

where m_i is the initial mass weighed, m_f is the remained mass of the powder after withdrawal, MW is the molecular weight of CoPc (571.46 g/mol), and V_f is 32 mL. The measured quantity of powder m_f in this sampling method is undoubtedly deficient compared to the quantity of phthalocyanine that does not dissolve in the solvent. Nevertheless, it allowed us to obtain an excess estimate of the concentration of the CoPc solutions as $(9.8 \pm 1.1) \cdot 10^{-5}\ mol \cdot L^{-1}$ in THF and $(6.6 \pm 1.1) \cdot 10^{-5}\ mol \cdot L^{-1}$ in DCM.

UV-Vis analysis

UV-Vis spectra were acquired to characterize the solutions obtained. A ThermoScientific^{TM} Evolution^{TM} Pro UV-Vis Spectrophotometer was employed, using a Hg flash as a light source that emits continuous radiation from 190 nm to 1100 nm and equipped with dual matched silicon photodiodes as detectors. The UV-Vis spectra were collected with Thermo Scientific Insight Pro 1.1.0 software.

UV-VIS absorbance spectra were acquired on the CoPc sampling solutions in the

range 250-900 nm. Two intense regions were observed for the solution in THF. In the higher energy region between 250 nm and 400 nm, it was possible to recognize the B-bands, also called Soret bands, and in the lower energy region, the Q-band shape was recognizable between 600 nm and 750 nm.
The effect of the two different solvents on CoPc is shown in Figure B.1b, where the difference in absorption of the solution in THF compared to the solution in DCM is observed. CoPc solution in THF was then used to prepare the samples, using the correct quantity of TiO_2 to obtain the 1:1000 molar ratio.

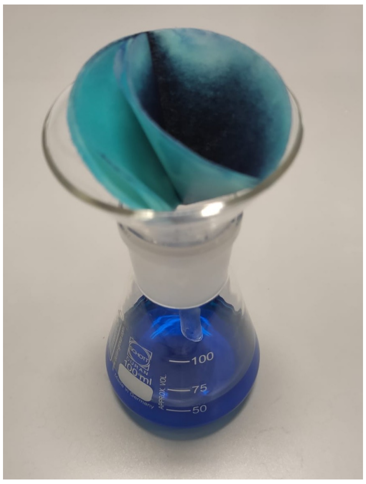

(a)

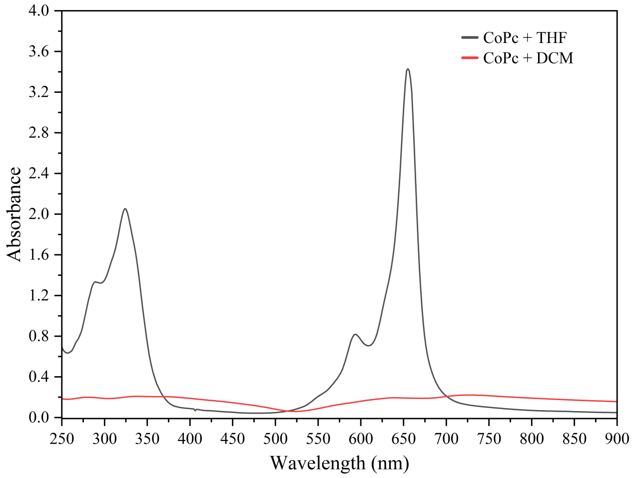

(b)

Figure B.1 (a) Filtration method of a saturated CoPc solution in THF. (b) UV-Vis absorbance spectra in the range 250-900 nm of CoPc solutions in THF (black) and DCM (red).

References

[1] W. Herbst and K Hunger. *Industrial Organic Pigments, Third Edition.* WILEY-VCH Verlag GmbH & Co. KGaA, Weinheim, 2004. ISBN: 3-527-30576-9.

[2] M. Anghelone, V. Stoytschew, D. Jembrih-Simbürger, and M. Schreiner. Spectroscopic methods for the identification and photostability study of red synthetic organic pigments in alkyd and acrylic paints. *Microchemical Journal*, 139:155–163, 2018. DOI: 10.1016/j.microc.2018.02.029.

[3] R.L. Feller. *Accelerated Aging: Photochemical and Thermal Aspects.* Research in Conservation 4, Marina del Rey, CA: Getty Conservation Institute, 1994. ISBN 978-0-89236-125-5.

[4] J. Oakes. Photofading of textile dyes. *Review of Progress in Coloration and Related Topics*, 31(1):21–28, 2008. DOI: 10.1111/j.1478-4408.2001.tb00134.x.

[5] N.S. Allen. Photofading and light stability of dyed and pigmented polymers. *Polymer Degradation and Stability*, 44(3):357–374, 1994. DOI: 10.1016/0141-3910(94)90095-7.

[6] R. Ameta, M.S. Solanki, S. Benjamin, and S.C. Ameta. Photocatalysis. In S.C. Ameta and R. Ameta, editors, *Advanced Oxidation Processes for Waste Water Treatment*, chapter 6, pages 135–175. Academic Press, 2018. ISBN: 978-0-12-810499-6.

[7] P.A. Lewis. *Color for Science, Art and Technology*, chapter 10, pages 283–312. AZimuth. North-Holland, K. Nassau (editor), 1998. ISBN: 978-0-444-89846-3.

[8] ASTM International. *Standard Test Methods for Lightfastness of Colorants Used in Artists' Materials*, 2003. Designation: D4303-03.

[9] W. Mokrzycki and M. Tatol. Color difference Delta E - A survey. *Machine Graphics and Vision*, 20:383–411, 2011. URL: www.researchgate.net/publication/236023905.

[10] K. Nassau. *The Physics and Chemistry of Color: The Fifteen Causes of Color*, chapter 6, pages 107–139. Wiley-Interscience, 1983. ISBN: 0-471-86776-4.

[11] A. Harth. The Study of Pigments in Cultural Heritage: A Review Using Machine Learning. *Heritage*, 7(7):3664–3695, 2024. DOI: 10.3390/heritage7070174.

[12] D. Tamburini, F. Sabatini, S. Berbers, M.R. van Bommel, and I. Degano. An Introduction and Recent Advances in the Analytical Study of Early Synthetic Dyes and Organic Pigments in Cultural Heritage. *Heritage*, 7(4):1969–2010, 2024. DOI: 10.3390/heritage7040094.

[13] E. Ghelardi, I. Degano, M.P. Colombini, J. Mazurek, M. Schilling, H. Khanjian, and T. Learner. A multi-analytical study on the photochemical degradation of synthetic organic pigments. *Dyes and Pigments*, 123:396–403, 2015. DOI: 10.1016/j.dyepig.2015.07.029.

[14] L. Pagnin, R. Calvini, R. Wiesinger, J. Weber, and M. Schreiner. Photodegradation Kinetics of Alkyd Paints: The Influence of Varying Amounts of Inorganic Pigments on the Stability of the Synthetic Binder. *Frontiers in Materials*, 7:2044, 2020. DOI: 10.3389/fmats.2020.600887.

[15] V. Pintus, S. Wei, and M. Schreiner. Accelerated UV ageing studies of acrylic, alkyd, and polyvinyl acetate paints: Influence of inorganic pigments. *Microchemical Journal*, 124:949–961, 2016. DOI: 10.1016/j.microc.2015.07.009.

[16] Z.E. Papliaka, K.S. Andrikopoulos, and E.A. Varella. Study of the stability of a series of synthetic colorants applied with styrene-acrylic copolymer, widely used in contemporary paintings, concerning the effects of accelerated ageing. *Journal of Cultural Heritage*, 11(4):381–391, 2010. DOI: 10.1016/j.culher.2010.02.003.

[17] A. van Loon, P. Noble, and A. Burnstock. *Ageing and deterioration of traditional oil and tempera paints*, pages 216–243. Routledge, 2020. DOI: 10.4324/9780429399916-11.

[18] C. Slottved Kimbriel. Colour Change in Paintings. *Journal of the Institute of Conservation*, 40(3):267–269, 2017. DOI: 10.1080/19455224.2017.1360546.

[19] E.M. Alonso-Villar, T. Rivas, and J.S. Pozo-Antonio. Resistance to artificial daylight of paints used in urban artworks. Influence of paint composition and substrate. *Progress in Organic Coatings*, 154:106180, 2021. DOI: 10.1016/j.porgcoat.2021.106180.

[20] E.C.L. Rigante, C.D. Calvano, R.A. Picca, F. Modugno, and T.R.I. Cataldi. An insight into spray paints for street art: Chemical characterization of two yellow varnishes by spectroscopic and MS-based spectrometric techniques. *Vacuum*, 215:112350, 2023. DOI: 10.1016/j.vacuum.2023.112350.

[21] L. Pagnin, N. Guarnieri, F.C. Izzo, S. Goidanich, and L. Toniolo. Protecting Street Art from Outdoor Environmental Threats: What Are the Challenges? *Coatings*, 13(12):2044, 2023. DOI: 10.3390/coatings13122044.

[22] C. Miliani, L. Monico, M.J. Melo, S. Fantacci, E.M. Angelin, A. Romani, and K. Janssens. Photochemistry of Artists' Dyes and Pigments: Towards Better Understanding and Prevention of Colour Change in Works of Art. *Angewandte Chemie International Edition*, 57(25):7324–7334, 2018. DOI: 10.1002/anie.201802801.

[23] L. Monico, A. Chieli, S. De Meyer, M. Cotte, W. de Nolf, G. Falkenberg, K. Janssens, A. Romani, and C. Miliani. Role of the Relative Humidity and the Cd/Zn Stoichiometry in the Photooxidation Process of Cadmium Yellows ($CdS/Cd_{1-x}Zn_xS$) in Oil Paintings. *Chemistry – A European Journal*, 24(45):11584–11593, 2018. DOI: 10.1002/chem.201801503.

[24] M. Radepont, Y. Coquinot, K. Janssens, J.J. Ezrati, W. de Nolf, and M. Cotte. Thermodynamic and experimental study of the degradation of the red pigment mercury sulfide. *Journal of Analytical Atomic Spectrometry*, 30(3):599–612, 2015. DOI: 10.1039/C4JA00372A.

[25] L. Monico, L. Sorace, M. Cotte, W. de Nolf, K. Janssens, A. Romani, and C. Miliani. Disclosing the Binding Medium Effects and the Pigment Solubility in the (Photo)reduction Process of Chrome Yellows ($PbCrO_4/PbCr_{1-x}S_xO_4$). *ACS Omega*, 4(4):6607–6619, 2019. DOI: 10.1021/acsomega.8b03669.

[26] C. Cardell, A. Herrera, I. Guerra, N. Navas, L. Rodríguez Simón, and K. Elert. Pigment-size effect on the physico-chemical behavior of azurite-tempera dosimeters upon natural and accelerated photo aging. *Dyes and Pigments*, 141:53–65, 2017. DOI: 10.1016/j.dyepig.2017.02.001.

[27] U. Hempelmann, G. Buxbaum, and H.G. Völz. *Industrial Inorganic Pigments. Vol I-Raw Materials and Their Usage, G. Buxbaum and G. Pfaff (editors)*, chapter 1, pages 1–50. WILEY-VCH Verlag GmbH & Co. KGaA, Weinheim, 2005. ISBN: 978-3-527-30363-2.

[28] G. Auer, W.D. Griebler, and B. Jahn. *Industrial Inorganic Pigments. Vol I-Raw Materials and Their Usage, G. Buxbaum and G. Pfaff (editors)*, chapter 2, pages 51–97. WILEY-VCH Verlag GmbH & Co. KGaA, Weinheim, 2005. ISBN: 978-3-527-30363-2.

[29] S. Croll. *Overview of Developments in the Paint Industry since 1930. In: Modern Paints Uncovered*, pages 17–29. The Getty Conservation Institute. T.J.S. Learner et al. (editors), Los Angeles, 2007. ISBN: 978-0-89236-906-5.

[30] Oil and Colour Chemists' Association, Australia. *Surface Coatings*, chapter 25, pages 288–304. Springer Science+Business Media, Dordrecht, 1983. ISBN: 978-94-011-6940-0.

[31] N.T. Burgos, A. López-Montes, E.M. Valero, J.L. Nieves, and M.R. Blanc. Characterization of the evolution of indigo blue by multispectral imaging. *Color Research & Application*, 47(2):486–497, 2022. DOI: 10.1002/col.22721.

[32] L. Legan, K. Retko, and P. Ropret. Vibrational spectroscopic study on degradation of alizarin carmine. *Microchemical Journal*, 127:36–45, 2016. DOI: 10.1016/j.microc.2016.02.002.

[33] L.M. Rader Bowers and S.J. Schmidtke Sobeck. Impact of medium and ambient environment on the photodegradation of carmine in solution and paints. *Dyes and Pigments*, 127:18–24, 2016. DOI: 10.1016/j.dyepig.2015.12.012.

[34] S.Q. Lomax and T. Learner. A Review of the Classes, Structures, and Methods of Analysis of Synthetic Organic Pigments. *Journal of the American Institute for Conservation*, 45(2):107–125, 2006. DOI: 10.1179/019713606806112540.

[35] Colour Index^{TM} published online by Society of Dyers and Colourists and American Association of Textile Chemists and Colorists. Last accessed February 2025. colour-index.com.

[36] RCSB PDB. Chemical Sketch Tool [Powered by Marvin JS by ChemAxon]. Last accessed April 2025. www.rcsb.org/chemical-sketch.

[37] A. Bosi, A. Ciccola, I. Serafini, M. Guiso, F. Ripanti, P. Postorino, R. Curini, and A. Bianco. Street art graffiti: Discovering their composition and alteration by FTIR and micro-Raman spectroscopy. *Spectrochimica Acta Part A: Molecular and Biomolecular Spectroscopy*, 225:117474, 2020. DOI: 10.1016/j.saa.2019.117474.

[38] J. La Nasa, B. Campanella, F. Sabatini, A. Rava, W. Shank, P. Lucero-Gomez, D. De Luca, S. Legnaioli, V. Palleschi, M.P. Colombini, I. Degano, and F. Modugno. 60 years of street art: A comparative study of the artists' materials through spectroscopic and mass spectrometric approaches. *Journal of Cultural Heritage*, 48:129–140, 2021. DOI: 10.1016/j.culher.2020.11.016.

[39] B.H. Berrie and S.Q. Lomax. *Studies in the History of Art. Monograph Series II. Conservation Research 1996/1997*, volume 57, chapter 3, pages 9–33. National Gallery of Art, Washington, 1997. ISBN: 089468-264-4.

[40] N. Eastaugh, V. Walsh, T. Chaplin, and R. Siddall. *The Pigment Compendium: A dictionary of historical pigments*, pages 29–30.203–204. Elsevier Butterworth-Heinemann, London, 2004. ISBN: 0-7506-57499.

[41] V. Radtke, P. Erk, and B. Sens. *Isoindoline Pigments*, pages 221–241. Wiley, 2009. DOI: 10.1002/9783527626915.ch14.

[42] S.Q. Lomax, M.R. Schilling, and T.J.S. Learner. *The identification of Synthetic Organic Pigments by FTIR and DMTS. In: Modern Paints Uncovered*, pages 105–117. The Getty Conservation Institute. T.J.S. Learner et al. (editors), Los Angeles, 2007. ISBN: 978-0-89236-906-5.

[43] D.G. Myers. The Color of Art Site Map - Pigments, Paints and Formulas. Last accessed February 2025. www.artiscreation.com/.

[44] A. Ciccola, M. Guiso, F. Domenici, F. Sciubba, and A. Bianco. Azo-pigments effect on UV degradation of contemporary art pictorial film: A FTIR-NMR combination study. *Polymer Degradation and Stability*, 140:74–83, 2017. DOI: 10.1016/j.polymdegradstab.2017.04.004.

[45] G. Poldi and S. Caglio. Phthalocyanine identification in paintings by reflectance spectroscopy. A laboratory and in situ study. *Optics and Spectroscopy*, 114(6):929–935, 2013. DOI: 10.1134/S0030400X13060143.

[46] C. Defeyt, J. Van Pevenage, P. Vandenabeele, T. Learner, and D. Strivay. *Distinction by Micro-Raman Spectroscopy and Chemometrical Analysis of Copper Phthalocyanine Blue Polymorphs in Oil-Based and Acrylic Paint Samples*, pages 105–116. Springer International Publishing, 2014.

[47] C.C. Leznoff and A.B.P. Lever. *Phthalocyanines: Properties and Applications*, volume 4. VCH Publishers Inc., New York, 1996. ISBN: 1-56081-916-2.

[48] D. Wöhrle, G. Schnurpfeil, S. Makarov, A. Kazarin, and O.N. Suvorova. Practical Applications of Phthalocyanines – from Dyes and Pigments to Materials for Optical, Electronic and Photo-electronic Devices. *Macroheterocycles*, 5(3):191–202, 2012. DOI: 10.6060/mhc2012.120990w.

[49] T. Sizun, M. Bouvet, Y. Chen, J.M. Suisse, G. Barochi, and J. Rossignol. Differential study of substituted and unsubstituted cobalt phthalocyanines for gas sensor applications. *Sensors and Actuators B: Chemical*, 159(1):163–170, 2011. DOI: 10.1016/j.snb.2011.06.067.

[50] N. Ishida and D. Fujita. Adsorption of Co-Phthalocyanine on the Rutile TiO_2(110) Surface: A Scanning Tunneling Microscopy/Spectroscopy Study. *The Journal of Physical Chemistry C*, 116(38):20300–20305, 2012. DOI: 10.1021/jp303152c.

[51] N.A. Kuznetsova and O.L. Kaliya. Oxidative photobleaching of phthalocyanines in solution. *Journal of Porphyrins and Phthalocyanines*, 16(07n08):705–712, 2012. DOI: 10.1142/S1088424612300042.

[52] R. Słota and G. Dyrda. UV Photostability of Metal Phthalocyanines in Organic Solvents. *Inorganic Chemistry*, 42(18):5743–5750, 2003. DOI: 10.1021/ic0260217.

[53] F. Ghani, J. Kristen, and H. Riegler. Solubility Properties of Unsubstituted Metal Phthalocyanines in Different Types of Solvents. *Journal of Chemical & Engineering Data*, 57(2):439–449, 2012. DOI: 10.1021/je2010215.

[54] A. Erdoğmuş and T. Nyokong. Synthesis of zinc phthalocyanine derivatives with improved photophysicochemical properties in aqueous media. *Journal of Molecular Structure*, 977(1-3):26–38, 2010. DOI: 10.1016/j.molstruc.2010.04.048.

[55] M. Anghelone, D. Jembrih-Simbürger, V. Pintus, and M. Schreiner. Photostability and influence of phthalocyanine pigments on the photodegradation of acrylic paints under accelerated solar radiation. *Polymer Degradation and Stability*, 146:13–23, 2017. DOI: 10.1016/j.polymdegradstab.2017.09.013.

[56] M. Anghelone, D. Jembrih-Simbürger, and M. Schreiner. Influence of phthalocyanine pigments on the photo-degradation of alkyd artists' paints under different conditions of artificial solar radiation. *Polymer Degradation and Stability*, 134:157–168, 2016.

[57] C.H. Lin and Y.F. Chang. Comparison and characterization of pigments and dyes by Raman spectroscopy. *Analytical Sciences*, 38(3):483–495, 2022. DOI: 10.2116/analsci.21SAR03.

[58] R.J. Gettens, H. Kühn, and W.T. Chase. *Artists' Pigments: A Handbook of Their History and Characteristics*, volume 2, chapter 3, pages 67–81. National Gallery of Art, A. Roy (editor), Washington, 1993. ISBN: 978-1-904982-75-3.

[59] C.S. Tumosa and M.F. Mecklenburg. The influence of lead ions on the drying of oils. *Studies in Conservation*, 50:39–47, 2005. DOI: 10.1179/sic.2005.50.Supplement-1.39.

[60] J.J. Hermans, K. Keune, A. Van Loon, and P.D. Iedema. *Metal Soaps in Art: Conservation and Research*, chapter 3, pages 47–67. Cultural Heritage Science, F. Casadio et al. (editors), Cham, 2019. ISBN: 978-3-319-90616-4.

[61] F.C. Izzo, M. Kratter, A. Nevin, and E. Zendri. A Critical Review on the Analysis of Metal Soaps in Oil Paintings. *ChemistryOpen*, 10(9):904–921, 2021. DOI: 10.1002/open.202100166.

[62] M. Cotte, E. Checroun, W. De Nolf, Y. Taniguchi, L. De Viguerie, M. Burghammer, P. Walter, C. Rivard, M. Salomé, K. Janssens, and J. Susini. Lead soaps in paintings: Friends or foes? *Studies in Conservation*, 62(1):2–23, 2017. DOI: 10.1080/00393630.2016.1232529.

[63] M. Laver. *Artists' Pigments: A Handbook of Their History and Characteristics*, volume 3, chapter 10, pages 295–355. National Gallery of Art, E.W. FitzHugh (editor), Washington, 1997. ISBN: 978-1-904982-76-0.

[64] X. Wu. *Titanium Dioxide: Advances and Applications*, chapter 9, pages 175–197. IntechOpen, H.M. Ali (editor), Rijeka, 2022. ISBN: 978-1-83969-476-9.

[65] A.J. Haider, Z.N. Jameel, and I.H.M. Al-Hussaini. Review on: Titanium Dioxide Applications. *Energy Procedia*, 157:17–29, 2019. DOI: 10.1016/j.egypro.2018.11.159.

[66] X. Chen and S.S. Mao. Titanium Dioxide Nanomaterials: Synthesis, Properties, Modifications, and Applications. *Chemical Reviews*, 107(7):2891–2959, 2007. DOI: 10.1021/cr0500535.

[67] R.F. Salzman, J. Xue, B.P. Rand, A. Alexander, M.E. Thompson, and S.R. Forrest. The effects of copper phthalocyanine purity on organic solar cell performance. *Organic Electronics*, 6(5-6):242–246, 2005. DOI: 10.1016/j.orgel.2005.09.001.

[68] Y.W. Song, M.Y. Kim, M.H. Chung, Y.K. Yang, and J.C. Park. NOx-Reduction Performance Test for TiO_2 Paint. *Molecules*, 25(18):4087, 2020. DOI: 10.3390/molecules25184087.

[69] E. Stanaszek-Tomal. Anti-Smog Building and Civil Engineering Structures. *Processes*, 9(8):1446, 2021. DOI: 10.3390/pr9081446.

[70] R. Kaegi, A. Ulrich, B. Sinnet, R. Vonbank, A. Wichser, S. Zuleeg, H. Simmler, S. Brunner, H. Vonmont, M. Burkhardt, and M. Boller. Synthetic TiO_2 nanoparticle emission from exterior facades into the aquatic environment. *Environmental Pollution*, 156(2):233–239, 2008. DOI: 10.1016/j.envpol.2008.08.004.

[71] N.S. Allen, M. Edge, A. Ortega, G. Sandoval, C.M. Liauw, J. Verran, J. Stratton, and R.B. McIntyre. Degradation and stabilisation of polymers and coatings: nano versus pigmentary titania particles. *Polymer Degradation and Stability*, 85(3):927–946, 9 2004. DOI: 10.1016/j.polymdegradstab.2003.09.024.

[72] B.A. van Driel, T.A. Wezendonk, K.J. van den Berg, P.J. Kooyman, J. Gascon, and J. Dik. Determination of early warning signs for photocatalytic degradation of titanium white oil paints by means of surface analysis. *Spectrochimica Acta Part A: Molecular and Biomolecular Spectroscopy*, 172:100–108, 2017. DOI: 10.1016/j.saa.2016.04.026.

[73] J. Dickens, A. Rava, M.P. Colombini, M. Picollo, and W. Shank. Keith Haring in Pisa and Melbourne: Controversy and conservation. *Studies in Conservation*, 61(sup2: LA Congress Preprints Modern Art):29–37, 2016. DOI: 10.1080/00393630.2016.1193691.

[74] N. Guarnieri, A. Di Benedetto, D. Comelli, F. Mirani, D. Dellasega, L. Pagnin, S. Goidanich, and L. Toniolo. Rapid chromatic alteration of Street Art: Mechanisms of deterioration of the painting materials of the 20 years of Freedom and Democracy mural. *Dyes and Pigments*, 239:112733, 2025. DOI: 10.1016/j.dyepig.2025.112733.

[75] H. Azizpour, M. Talebi, F.D. Tichelaar, R. Sotudeh-Gharebagh, J. Guo, J.R. van Ommen, and N. Mostoufi. Effective coating of titania nanoparticles with alumina via atomic layer deposition. *Applied Surface Science*, 426:480–496, 2017. DOI: https://doi.org/10.1016/j.apsusc.2017.07.168.

[76] H. Kohn. *Artists' Pigments: A Handbook of Their History and Characteristics*, volume 1, chapter 8, pages 169–186. National Gallery of Art, R.L. Feller (editor), Washington, 1986. ISBN: 978-1-904982-74-6.

[77] A. Kołodziejczak-Radzimska and T. Jesionowski. Zinc Oxide—From Synthesis to Application: A Review. *Materials*, 7(4):2833–2881, 2014. DOI: 10.3390/ma7042833.

[78] A. Moezzi, A.M. McDonagh, and M.B. Cortie. Zinc oxide particles: Synthesis, properties and applications. *Chemical Engineering Journal*, 185-186:1–22, 2012. DOI: 10.1016/j.cej.2012.01.076.

[79] J.J. Hermans, K. Keune, A. van Loon, and P.T. Iedema. An infrared spectroscopic study of the nature of zinc carboxylates in oil paintings. *Journal of Analytical Atomic Spectrometry*, 30(7):1600–1608, 2015.

[80] M. Baudys, J. Krýsa, M. Zlámal, and A. Mills. Weathering tests of photocatalytic facade paints containing ZnO and TiO_2. *Chemical Engineering Journal*, 261:83–87, 2015. DOI: 10.1016/j.cej.2014.03.112.

[81] A. Artesani, M.V. Dozzi, L. Toniolo, G. Valentini, and D. Comelli. Experimental Study on the Link between Optical Emission, Crystal Defects and Photocatalytic Activity of Artist Pigments Based on Zinc Oxide. *Minerals*, 10(12):1129, 2020. DOI: 10.3390/min10121129.

[82] L. Campanella, A. Casoli, M.P. Colombini, R. Marini Bettolo, M. Matteini, L.M. Migneco, A. Montenero, L. Nodari, C. Piccioli, M. Plossi Zappalà, G. Portalone, U. Russo, and M.P. Sammartino. *Chimica per l'arte.* Zanichelli, 2007. ISBN: 978-88-08–06853-8.

[83] M.R. Schilling, J. Mazurek, and T.J.S. Learner. *Studies of Modern Oil-Based Artists' Paint Mediaby Gas Chromatography/Mass Spectrometry. In: Modern Paints Uncovered*, pages 129–139. The Getty Conservation Institute. T.J.S. Learner et al. (editors), Los Angeles, 2007. ISBN: 978-0-89236-906-5.

[84] J. Mallégol, J. Lemaire, and J.L. Gardette. Drier influence on the curing of linseed oil. *Progress in Organic Coatings*, 39(2-4):107–113, 2000. DOI: 10.1016/S0300-9440(00)00126-0.

[85] S. Pizzimenti, L. Bernazzani, M.R. Tinè, V. Treil, C. Duce, and I. Bonaduce. Oxidation and Cross-Linking in the Curing of Air-Drying Artists' Oil Paints. *ACS Applied Polymer Materials*, 3(4):1912–1922, 2021.

[86] R.J. Meilunas, J.G. Bentsen, and A. Steinberg. Analysis of aged paint binders by FTIR spectroscopy. *Studies in Conservation*, 35(1):33–51, 1990. DOI: 10.1179/sic.1990.35.1.33.

[87] J.S. Mills and R. White. *The Organic Chemistry of Museum Objects*, chapter 3, pages 26–40. Butterworth, London, 1987. ISBN: 0-408-11810-5.

[88] R.T. Marcus. *Color for Science, Art and Technology*, chapter 2, pages 31–96. AZimuth. North-Holland, K. Nassau (editor), 1998. ISBN: 978-0-444-89846-3.

[89] J.E. Agudo, P.J. Pardo, H. Sánchez, Á.L. Pérez, and M.I. Suero. A Low-Cost Real Color Picker Based on Arduino. *Sensors*, 14(7):11943–11956, 2014. DOI: 10.3390/s140711943.

[90] A. Gilchrist and J. Nobbs. Colorimetry, Theory. In *Encyclopedia of Spectroscopy and Spectrometry (Third Edition)*, pages 328–333. Academic Press, J.C. Lindon et al. (editors), Oxford, 2017. DOI: 10.1016/B978-0-12-803224-4.00124-2.

[91] D.A. Skoog, F.J. Holler, and S.R. Crouch. *Principles of Instrumental Analysis (Seventh Edition).* Cengage Learning, Boston, USA, 2016. ISBN: 978-1-305-57721-3.

[92] S. Wartewig. Basic Principles of Vibrational Spectroscopy. In *IR and Raman Spectroscopy: Fundamental Processing*, chapter 4, pages 27–33. Wiley-VCH Verlag GmbH & Co. KGaA, Weinheim, 2003. ISBN: 978-3-527-302451-X.

[93] P. Larkin. *Infrared and Raman Spectroscopy: Principles and Spectral Interpretation.* Elsevier, P. Larkin (editor), Oxford, 2011. ISBN: 978-0-12-386984-5.

[94] P.R. Griffiths and J.A. de Haseth. Attenuated Total Reflection. In *Fourier Transform Infrared Spectrometry, second edition*, chapter 15, pages 321–348. John Wiley & Sons, Inc., 2007. ISBN 978-0-471-19404-0.

[95] HORIBA Scientific Application Notes. *Strain measurements of a Si cap layer deposited on a SiGe substrate determination of Ge content.* URL: www.horiba.com.

[96] K.F. Dombrowski, I. De Wolf, and B. Dietrich. Stress measurements using ultraviolet micro-Raman spectroscopy. *Applied Physics Letters*, 75(16):2450–2451, 1999. DOI: 10.1063/1.125044.

[97] G. Giorgi. Overview of Mass Spectrometric Based Techniques Applied in the Cultural Heritage Field. In *Organic Mass Spectrometry in Art and Archaeology*, chapter 2, pages 37–74. John Wiley & Sons, Ltd. M.P. Colombini, F. Modugno (editors), 2009. ISBN: 978-0-470-51703-1.

[98] J.C. Vickerman and D. Briggs. *ToF-SIMS: Materials Analysis by Mass Spectrometry, 2nd edition.* IM Publications LLP, 2013. ISBN 978-1-906715-17-5.

[99] S. De Rosa. *Low energy ion collisions as a tool for unveiling the HOPG anion intercalation mechanism.* PhD thesis, University of Roma Tre, 2020.

[100] J. Epp. X-ray diffraction (XRD) techniques for materials characterization. In *Materials Characterization Using Nondestructive Evaluation (NDE) Methods*, chapter 4, pages 81–124. Woodhead Publishing, G. Hübschen et al. (editors), 2016. ISBN: 978-0-08-100040-3.

[101] A. Ali, Y. Wai Chiang, and R.M. Santos. X-ray Diffraction Techniques for Mineral Characterization: A Review for Engineers of the Fundamentals, Applications, and Research Directions. *Minerals*, 12(2), 2022. DOI: 10.3390/min12020205.

[102] M. Sasges, J. Robinson, and F. Daynouri. Ultraviolet Lamp Output Measurement: A Concise Derivation of the Keitz Equation. *Ozone: Science & Engineering*, 34(4):306–309, 2012. DOI: 10.1080/01919512.2012.694322.

[103] F. Daynouri and J. Robinson. Evaluation of the Keitz Method for Quantifying the UV Output of Medium Pressure Mercury Lamps. *Ozone: Science & Engineering*, 34(4):310–314, 2012. DOI: 10.1080/01919512.2012.694327.

[104] L. Greenspan. Humidity fixed points of binary saturated aqueous solutions. *Journal of Research of the National Bureau of Standards - A. Physics and Chemistry*, 81A:89–96, 1977. DOI: 10.6028/jres.081A.011.

[105] P.W. Winston and D.H. Bates. Saturated solutions for the control of humidity in biological research. *Ecological Society of America*, 41(1):232–237, 1960. DOI: 10.2307/1931961.

[106] Atlante italiano della radiazione solare - enea. Last accessed April 2025. www.solaritaly.enea.it/index.php.

[107] D. Frederichi, M.H.N.O. Scaliante, and R. Bergamasco. Structured photocatalytic systems: photocatalytic coatings on low-cost structures for treatment of water contaminated with micropollutants—a short review. *Environmental Science and Pollution Research*, 28(19):23610–23633, 2021. DOI: 10.1007/s11356-020-10022-9.

[108] N. Doebelin and R. Kleeberg. Profex : a graphical user interface for the Rietveld refinement program BGMN. *Journal of Applied Crystallography*, 48(5):1573–1580, 2015. DOI: 10.1107/S1600576715014685.

[109] T. Cavaleri, P. Buscaglia, S. Migliorini, M. Nervo, G. Piccablotto, A. Piccirillo, M. Pisani, D. Puglisi, D. Vaudan, and M. Zucco. Pictorial materials database: 1200 combinations of pigments, dyes, binders and varnishes designed as a tool for heritage science and conservation. *Applied Physics A*, 123(419), 2017. DOI: 10.1007/s00339-017-1031-1.

[110] D. Scalarone and O. Chiantore. Separation techniques for the analysis of artists' acrylic emulsion paints. *Journal of Separation Science*, 27(4):263–274, 2004. DOI: 10.1002/jssc.200301638.

[111] B.A. Price, B. Pretzel and S.Q. Lomax (eds). Infrared and Raman Users Group Spectral Database. 2007 ed. Vol. 1 & 2. Philadelphia: IRUG, 2009. Infrared and Raman Users Group Spectral Database. Last accessed February 2025. www.irug.org.

[112] D. Lin-Vien, N.B. Colthup, W.G. Fateley, and J.G. Grasselli. *The Handbook of Infrared and Raman Characteristic Frequencies of Organic Molecules.* Academic Press, San Diego, 1991. ISBN: 978-0-12-451160-6.

[113] M. Bertasa, E. Possenti, A. Botteon, C. Conti, A. Sansonetti, R. Fontana, J. Striova, and D. Sali. Close to the diffraction limit in high resolution ATR FTIR mapping: demonstration on micrometric multi-layered art systems. *Analyst*, 142:4801–4811, 2017. DOI: 1039/C7AN00873B.

[114] E. Possenti, C. Colombo, M. Realini, C. Li Song, and Kazarian S.G. Insight into the effects of moisture and layer build-up on the formation of lead soaps using micro-ATR-FTIR spectroscopic imaging of complex painted stratigraphies. *Analytical and Bioanalytical Chemistry*, 413:455–467, 2021. DOI: 10.1007/s00216-020-03016-6.

[115] J. van der Weerd, A. van Loon, and J.J. Boon. FTIR Studies of the Effects of Pigments on the Aging of Oil. *Studies in conservation*, 50(1):3–22, 2005. URL: www.jstor.org/stable/25487713.

[116] A. Okasha, F. Gomaa, H. Elhaes, M. Morsy, S. El-Khodary, A. Fakhry, and M. Ibrahim. Spectroscopic analyses of the photocatalytic behavior of nano titanium dioxide. *Spectrochimica Acta Part A: Molecular and Biomolecular Spectroscopy*, 136, Part B:504–509, 2015. DOI: 10.1016/j.saa.2014.09.063.

[117] M. Lazzari and O. Chiantore. Drying and oxidative degradation of linseed oil. *Polymer Degradation and Stability*, 65(2):303–313, 1999. DOI: 10.1016/S0141-3910(99)00020-8.

[118] L. de Viguerie, P.A. Payard, E. Portero, Ph. Walter, and M. Cotte. The drying of linseed oil investigated by Fourier transform infrared spectroscopy: Historical recipes and influence of lead compounds. *Progress in Organic Coatings*, 93:46–60, 2016. DOI: 10.1016/j.porgcoat.2015.12.010.

[119] A. Schönemann and H.G.M. Edwards. Raman and FTIR microspectroscopic study of the alteration of Chinese tung oil and related drying oils during ageing. *Analytical and Bioanalytical Chemistry*, 400(4):1173–1180, 2011. DOI: 10.1007/s00216-011-4855-0.

[120] A. Colombini and D. Kaifas. Characterization of Some Orange and Yellow Organic and Fluorescent Pigments by Raman Spectroscopy. *In Proceedings of the 8th international conference of the Infrared and Raman Users' Group (IRUG), Vienna, Austria, 26-29 March 2008*, 7:14–21, 2010. ISSN: 1581-9280.

[121] N. C. Scherrer, Z. Stefan, D. Francoise, F. Annette, and K. Renate. Synthetic organic pigments of the 20th and 21st century relevant to artist's paints: Raman spectra reference collection. *Spectrochimica Acta Part A: Molecular and Biomolecular Spectroscopy*, 73(3):505–524, 2009. DOI: 10.1016/j.saa.2008.11.029.

[122] P. Vandenabeele, L. Moens, H.G.M. Edwards, and R. Dams. Raman spectroscopic database of azo pigments and application to modern art studies. *Journal of Raman Spectroscopy*, 31(6):509–517, 2000. DOI: 10.1002/1097-4555(200006)31:6%3C509::AID-JRS566%3E3.0.CO;2-0.

[123] P. Ropret, S.A. Centeno, and P. Bukovec. Raman identification of yellow synthetic organic pigments in modern and contemporary paintings: Reference spectra and case studies. *Spectrochimica Acta Part A: Molecular and Biomolecular Spectroscopy*, 69(2):486–497, 2008. DOI: 10.1016/j.saa.2007.03.050.

[124] F. Schulte, K.W. Brzezinka, K. Lutzenberger, H. Stege, and U. Panne. Raman spectroscopy of synthetic organic pigments used in 20th century works of art. *Journal of Raman Spectroscopy*, 39(10):1455–1463, 2008. DOI: 10.1002/jrs.2021.

[125] M. Corradini, L. de Ferri, and G. Pojana. Spectroscopic characterization of commercial pigments for pictorial retouching. *Journal of Raman Spectroscopy*, 52(1):35–58, 2021. DOI: 10.1002/jrs.5935.

[126] I.M. Bell, R.J.H. Clark, and P.J. Gibbs. Raman spectroscopic library of natural and synthetic pigments (pre- $\approx$ 1850 AD). *Spectrochimica Acta Part A: Molecular and Biomolecular Spectroscopy*, 53(12):2159–2179, 1997. DOI: 10.1016/S1386-1425(97)00140-6.

[127] A.M. Correia, R.J.H. Clark, M.I.M. Ribeiro, and M.L.T.S. Duarte. Pigment study by Raman microscopy of 23 paintings by the Portuguese artist Henrique Pousão (1859–1884). *Journal of Raman Spectroscopy*, 38(11):1390–1405, 2007. DOI: 10.1002/jrs.1786.

[128] E.M. Angelin, S. Babo, J.L. Ferreira, and M.J. Melo. Raman microscopy for the identification of pearlescent pigments in acrylic works of art. *Journal of Raman Spectroscopy*, 50(2):232–241, 2019. DOI: 10.1002/jrs.5431.

[129] K. Castro, M. P´erez-Alonso, M.D. Rodr´ıguez-Laso, N. Etxebarria, and J.M. Madariaga. Non-invasive and non-destructive micro-XRF and micro-Raman analysis of a decorative wallpaper from the beginning of the 19th century. *Analytical and Bioanalytical Chemistry*, 387(3):847–860, 2007. DOI: 10.1007/s00216-006-0593-0.

[130] J. Yan, W. Guangjun, N. Guan, L. Landong, L. Zhuoxin, and C. Xingzhong. Understanding the effect of surface/bulk defects on the photocatalytic activity of TiO_2: anatase versus rutile. *Physical Chemistry Chemical Physics*, 15:10978–10988, 2013. DOI: 10.1039/C3CP50927C.

[131] T. Ohsaka, F. Izumi, and Y. Fujiki. Raman spectrum of anatase, TiO_2. *Physical Chemistry Chemical Physics*, 7(6):321–324, 1978. DOI: 10.1002/jrs.1250070606.

[132] S. Calixto, C.F. Reyes, J. Medina-Valtierra, and M. Sánchez-Cárdenas. Formation of smooth and rough TiO_2 thin films on fiberglass by sol-gel method. *Journal of the Mexican Chemical Society*, 50(1):8–13, 2006. ISSN: 1665-9686.

[133] E.J. Ekoi, A. Gowen, R. Dorrepaal, and D.P. Dowling. Characterisation of titanium oxide layers using Raman spectroscopy and optical profilometry: Influence of oxide properties. *Results in Physics*, 12:1574–1585, 2019. DOI: 10.1016/j.rinp.2019.01.054.

[134] T. Sekiya, S. Ohta, S. Kamei, M. Hanakawa, and S. Kurita. Raman spectroscopy and phase transition of anatase TiO_2 under high pressure. *Journal of Physics and Chemistry of Solids*, 62(4):717–721, 2001. DOI: 10.1016/S0022-3697(00)00229-8.

[135] V. Košařová, D. Hradil, J. Hradilová, Z. Čermáková, I. Němec, and M. Schreiner. The efficiency of micro-Raman spectroscopy in the analysis of complicated mixtures in modern paints: Munch's and Kupka's paintings under study. *Spectrochimica Acta Part A: Molecular and Biomolecular Spectroscopy*, 156:36–46, 2016. DOI: 10.1016/j.saa.2015.11.027.

[136] F. Decremps, J. Pellicer-Porres, A.M. Saitta, J.C. Chervin, and A. Polian. High-pressure Raman spectroscopy study of wurtzite ZnO. *Physical Review B*, 65(9):092101, 2002. DOI: 10.1103/PhysRevB.65.092101.

[137] T.C. Damen, S.P.S. Porto, and B. Tell. Raman Effect in Zinc Oxide. *Physical Review*, 142(2):570–574, 1966. DOI: 10.1103/PhysRev.142.570.

[138] Y. Du, M.S. Zhang, J. Hong, Y. Shen, Q. Chen, and Z. Yin. Structural and optical properties of nanophase zinc oxide. *Applied Physics A*, 76:171–176, 2003. DOI: 10.1007/s003390201404.

[139] L. Burgio and R.J.H. Clark. Library of FT-Raman spectra of pigments, minerals, pigment media and varnishes, and supplement to existing library of Raman spectra of pigments with visible excitation. *Spectrochimica Acta Part A: Molecular and Biomolecular Spectroscopy*, 57(7):1491–1521, 2001. DOI: 10.1016/S1386-1425(00)00495-9.

[140] E. Manzano, J. García-Atero, A. Dominguez-Vidal, M.J. Ayora-Cañada, L.F. Capitán-Vallvey, and N. Navas. Discrimination of aged mixtures of lipidic paint binders by Raman spectroscopy and chemometrics. *Journal of Raman Spectroscopy*, 43(6):781–786, 2012. DOI: 10.1002/jrs.3082.

[141] S. Carlesi, M. Ricci, C. Cucci, J. La Nasa, C. Lofrumento, M. Picollo, and M. Becucci. Multivariate Analysis of Combined Fourier Transform Near-Infrared Spectrometry (FT-NIR) and Raman Datasets for Improved Discrimination of Drying Oils. *Applied Spectroscopy*, 69(7):865–876, 2015. DOI: 10.1366/14-07775.

[142] P. Vandenabeele, B. Wehling, L. Moens, H. Edwards, M. De Reu, and G. Van Hooydonk. Analysis with micro-Raman spectroscopy of natural organic binding media and varnishes used in art. *Analytica Chimica Acta*, 407(1-2):261–274, 2000. DOI: 10.1016/S0003-2670(99)00827-2.

[143] M. Gomez, D. Reggio, and M. Lazzari. Linseed oil as a model system for surface enhanced Raman spectroscopy detection of degradation products in artworks. *Journal of Raman Spectroscopy*, 50(2):242–249, 2019. DOI: 10.1002/jrs.5472.

[144] M. Krmpotić, D. Jembrih-Simbürger, Z. Siketić, N. Marković, M. Anghelone, T. Tadić, D. Plavčić, M. Malloy, and I.B. Radović. Identification of Synthetic Organic Pigments (SOPs) Used in Modern Artist's Paints with Secondary Ion Mass Spectrometry with MeV Ions. *Analytical Chemistry*, 92(13):9287–9294, 2020. DOI: 10.1021/acs.analchem.0c01630.

[145] N. Sugaya, M. Takahashi, K. Sakurai, N. Tanaka, I. Okubo, and T. Kawakami. Mass Spectrometric Analysis of Synthetic Organic Pigments. *Journal of AOAC INTERNATIONAL*, 101(5):1328—1340, 2018. DOI: 10.5740/jaoacint.18-0049.

[146] J. Russell, B.W. Singer, J.J. Perry, and A. Bacon. The identification of synthetic organic pigments in modern paints and modern paintings using pyrolysis-gas chromatography–mass spectrometry. *Analytical and Bioanalytical Chemistry*, 400:1473—1491, 2011. DOI: 10.1007/s00216-011-4822-9.

[147] N. Sonoda. Characterization of Organic Azo-Pigments by Pyrolysis-Gas Chromatography. *Studies in Conservation*, 44:195–208, 1999.

[148] E. Ghelardi, I. Degano, M.P. Colombini, J. Mazurek, M. Schilling, and T. Learner. Py-GC/MS applied to the analysis of synthetic organic pigments: characterization and identification in paint samples. *Analytical and Bioanalytical Chemistry*, 407:1415–1431, 2015. DOI: 10.1007/s00216-014-8370-y.

[149] T. Calligaro, A. Banas, K. Banas, I. Bogdanović Radović, M. Brajković, M. Chiari, A.M. Forss, I. Hajdas, M. Krmpotić, A. Mazzinghi, E. Menart, K. Mizohata, M. Oinonen, L. Pichon, J. Raisanen, Z. Siketić, Ž. Šmit, and A. Simon. Emerging nuclear methods for historical painting authentication: AMS-14C dating, MeV-SIMS and O-PTIR imaging, global IBA, differential-PIXE and full-field PIXE mapping. *Forensic Science International*, 336:111327, 2022. DOI: 10.1016/j.forsciint.2022.111327.

[150] Z.E. Voras, K. deGhetaldi, B. Baade, E. Gordon, G. Gates, and T.P. Beebe. Comparison of oil and egg tempera paint systems using time-of-flight secondary ion mass spectrometry. *Studies in Conservation*, 61(4):222–235, 2016. DOI: 10.1179/2047058414Y.0000000154.

[151] K. Keune and J.J. Boon. Enhancement of the static SIMS secondary ion yields of lipid moieties by ultrathin gold coating of aged oil paint surfaces. *Surface and Interface Analysis*, 36(13):1620–1628, 2004. DOI: 10.1002/sia.1996.

[152] C. Bouvier, S. Van Nuffel, and A. Brunelle. ToF-SIMS spectra of historical inorganic pigments: Lead-based pigments in positive polarity. *Surface Science Spectra*, 31:015003, 2024. DOI: 10.1116/6.0003507.

[153] C. Bouvier, S. Van Nuffel, and A. Brunelle. ToF-SIMS spectra of historical inorganic pigments: Lead-based pigments in negative polarity. *Surface Science Spectra*, 31:015005, 2024. DOI: 10.1116/6.0003560.

[154] A.L. Castro, P.J.A. Madeira, M.R. Nunes, F.M. Costa, and M.H. Florêncio. Titanium dioxide anatase as matrix for matrix-assisted laser desorption/ionization analysis of small molecules. *Rapid Communications in Mass Spectrometry*, 22(23):3761–3766, 2008. DOI: 10.1002/rcm.3795.

[155] B. Guan, W. Lu, J. Fang, and R.B. Cole. Characterization of Synthesized Titanium Oxide Nanoclusters by MALDI-TOF Mass Spectrometry. *Journal of the American Society for Mass Spectrometry*, 18(3):517–524, 2007. DOI: 10.1016/j.jasms.2006.10.021.

[156] M. Kasperkowiak, M. Kurowska, M. Zalas, and R. Frański. Laser Desorption/Ionization Mass Spectrometry as a Potential Tool for Evaluation of Hydroxylation Degree of Various Types of Titanium Dioxide Materials. *Materials*, 14(22):6848, 2021. DOI: 10.3390/ma14226848.

[157] C. Bouvier, S. Van Nuffel, and A. Brunelle. Tof-SIMS spectra of historical inorganic pigments: Copper-, zinc-, arsenic-, and phosphorus-containing pigments in negative polarity. *Surface Science Spectra*, 31:025002, 2024. DOI: 10.1116/6.0003723.

[158] T. Nguyen, N. Valle, J. Guillot, J. Bour, N. Adjeroud, Y. Fleming, M. Guennou, J.N. Audinot, B. El Adib, R. Joly, D. Arl, G. Frache, and J. Polesel-Maris. Elucidating the growth mechanism of ZnO films by atomic layer deposition with oxygen gas via isotopic tracking. *Journal of Materials Chemistry C*, 9(7):4307–4315, 2021. DOI: 10.1039/D0TC05439A.

[159] M. Bouslama, M. C. Amamra, Z. Jia, M. Ben Amar, K. Chhor, O. Brinza, M. Abderrabba, J.-L. Vignes, and A. Kanaev. Nanoparticulate TiO_2–Al_2O_3 Photocatalytic Media: Effect of Particle Size and Polymorphism on Photocatalytic Activity. *ACS Catalysis*, 2(9):1884–1892, 2012. DOI: 10.1021/cs300033y.

[160] P.M. Leukkunen, E. Rani, A.A. Sasikala Devi, H. Singh, G. King, M. Alatalo, W. Cao, and M. Huttula. Synergistic effect of Ni–Ag–rutile TiO_2 ternary nanocomposite for efficient visible-light-driven photocatalytic activity. *RSC Advances*, 10(60):36930–36940, 2020. DOI: 10.1039/D0RA07078E.

[161] E. Marconi, I. Luisetto, and L. Tortora. Green synthesis and characterization of titanium dioxide nanoparticles and their photocatalytic activity. *Acta IMEKO*, 13(3):1–6, 2024. DOI: 10.21014/actaimeko.v13i3.1775.

[162] J.M. Mora-Hernández, E.M. Arce-Estrada, L. Zarazúa-Villalobos, M. Estrada-Flores, J. Medina-Flores, and C. Reza-San Germán. Synthesis and characterization of wires-like ZnO structures grown on a graphite support by microwave irradiation. *Journal of Crystal Growth*, 426:141–146, 2015. DOI: 10.1016/j.jcrysgro.2015.06.006.

[163] M. Gancheva, M. Markova-Velichkova, G. Atanasova, D. Kovacheva, I. Uzunov, and R. Cukeva. Design and photocatalytic activity of nanosized zinc oxides. *Applied Surface Science*, 368:258–266, 2016. DOI: 10.1016/j.apsusc.2016.01.211.

[164] A. Privitera, S. Tuti, U.P. Laverdura, L. Duranti, E. Di Bartolomeo, A.R. Taddei, and A. Sodo. One-step nanoencapsulation of essential oils and their application in hybrid coatings: A sustainable long-lasting treatment of stone materials against biodeterioration. *Progress in Organic Coatings*, 196:108759, 2024. DOI: 10.1016/j.porgcoat.2024.108759.

[165] J. Delgado Rodrigues and A. Grossi. Indicators and ratings for the compatibility assessment of conservation actions. *Journal of Cultural Heritage*, 8(1):32–43, 2007. DOI: 10.1016/j.culher.2006.04.007.

[166] R. Mazzeo, S. Prati, M. Quaranta, E. Joseph, E. Kendix, and Galeotti M. Attenuated total reflection micro FTIR characterisation of pigment–binder interaction in reconstructed paint films. *Analytical and Bioanalytical Chemistry*, 392(1-2):65–76, 2008. DOI: 10.1007/s00216-008-2126-5.

[167] A. Lanzarotta. Approximating the Detection Limit of an Infrared Spectroscopic Imaging Microscope Operating in an Attenuated Total Reflection (ATR) Modality: Theoretical and Empirical Results for an Instrument Using a Linear Array Detector and a 1.5 Millimeter Germanium Hemisphere Internal Reflection Element. *Applied Spectroscopy*, 69(2):205–214, 2015. DOI: 10.1366/14-07538.

[168] P.A. Hayes, S. Vahur, and I. Leito. ATR-FTIR spectroscopy and quantitative multivariate analysis of paints and coating materials. *Spectrochimica Acta Part A: Molecular and Biomolecular Spectroscopy*, 133:207–213, 2014. DOI: 10.1016/j.saa.2014.05.058.

[169] K. Keune, F. Hoogland, J.J. Boon, D. Peggie, and C. Higgitt. Evaluation of the "added value" of sims: A mass spectrometric and spectroscopic study of an unusual naples yellow oil paint reconstruction. *International Journal of Mass Spectrometry*, 284(1-3):22–34, 2009. DOI: 10.1016/j.ijms.2008.10.016.

[170] Y. Orlova, R.E. Harmon, L.J. Broadbelt, and P.D. Iedema. Review of the kinetics and simulations of linseed oil autoxidation. *Progress in Organic Coatings*, 151:106041, 2021. DOI: 10.1016/j.porgcoat.2020.106041.

[171] A. Gnanaprakasam, V.M. Sivakumar, P.L. Sivayogavalli, and M. Thirumarimurugan. Characterization of TiO_2 and ZnO nanoparticles and their applications in photocatalytic degradation of azodyes. *Ecotoxicology and Environmental Safety*, 121:121–125, 2015. DOI: 10.1016/j.ecoenv.2015.04.043.

[172] C. Bouvier, S. Van Nuffel, P. Walter, and A. Brunelle. Time-of-flight secondary ion mass spectrometry imaging in cultural heritage: A focus on old paintings. *Journal of Mass Spectrometry*, 57(1), 2022. DOI: 10.1002/jms.4803.

[173] E. Marconi and L. Tortora. Synthesis of titania nanoparticles in W/O microemulsion: moving the production toward a green approach. In *Proceedings of the 2022 IMEKO TC4 International Conference on Metrology for Archaeology and Cultural Heritage*, pages 479–484. IMEKO, 2023. DOI: 10.21014/tc4-ARC-2023.091.

[174] D. Feldman. Polymer Weathering: Photo-Oxidation. *Journal of Polymers and the Environment*, 10(4):163–173, 2002. DOI: 10.1023/A:1021148205366.

[175] T. Kobayashi, F. Kurokawa, N. Uyeda, and E. Suito. The metal-ligand vibrations in the infrared spectra of various metal phthalocyanines. *Spectrochimica Acta Part A: Molecular Spectroscopy*, 26(6):1305–1311, 1970. DOI: 10.1016/0584-8539(70)80036-8.

[176] C. Defeyt, P. Vandenabeele, B. Gilbert, J. Van Pevenage, R. Cloots, and D. Strivay. Contribution to the identification of α-, β- and ϵ-copper phthalocyanine blue pigments in modern artists' paints by X-ray powder diffraction, attenuated total reflectance micro-fourier transform infrared spectroscopy and micro-Raman spectroscopy. *Journal of Raman Spectroscopy*, 43(11):1772–1780, 2012. DOI: 10.1002/jrs.4125.

[177] M.M. El-Nahass, K.F. Abd-El-Rahman, and A.A.A. Darwish. Fourier-transform infrared and UV–vis spectroscopes of nickel phthalocyanine thin films. *Materials Chemistry and Physics*, 92(1):185–189, 2005. DOI: 10.1016/j.matchemphys.2005.01.008.

[178] D. Verma, R. Dash, K.S. Katti, D.L. Schulz, and A.N. Caruso. Role of coordinated metal ions on the orientation of phthalocyanine based coatings. *Spectrochimica Acta Part A: Molecular and Biomolecular Spectroscopy*, 70(5):1180–1186, 2008. DOI: 10.1016/j.saa.2007.10.050.

[179] R. Seoudi, G.S. El-Bahy, and Z.A. El Sayed. FTIR, TGA and DC electrical conductivity studies of phthalocyanine and its complexes. *Journal of Molecular Structure*, 753(1-3):119–126, 2005. DOI: 10.1016/j.molstruc.2005.06.003.

[180] A.V. Ziminov, S.M. Ramsh, E.I. Terukov, I.N. Trapeznikova, V.V. Shamanin, and T.A. Yurre. Correlation dependences in infrared spectra of metal phthalocyanines. *Semiconductors*, 40(10):1131–1136, 2006. DOI: 10.1134/S1063782606100022.

[181] C. Cucci, G. Bartolozzi, M. De Vita, V. Marchiafava, M. Picollo, and F. Casadio. The Colors of Keith Haring: A Spectroscopic Study on the Materials of the Mural Painting *Tuttomondo* and on Reference Contemporary Outdoor Paints. *Applied Spectroscopy*, 70(1):186–196, 2016. DOI: 10.1177/0003702815615346.

[182] T.V. Basova, V.G. Kiselev, B.E. Schuster, H. Peisert, and T. Chassé. Experimental and theoretical investigation of vibrational spectra of copper phthalocyanine: polarized single-crystal Raman spectra, isotope effect and DFT calculations. *Journal of Raman Spectroscopy*, 40(12):2080–2087, 2009. DOI: 10.1002/jrs.2375.

[183] D.R. Tackley, G. Dent, and W.E. Smith. Phthalocyanines: structure and vibrations. *Physical Chemistry Chemical Physics*, 3(8):1419–1426, 2001. DOI: 10.1039/B007763L.

[184] W. Fremout and S. Saverwyns. Identification of synthetic organic pigments: the role of a comprehensive digital Raman spectral library. *Journal of Raman Spectroscopy*, 43(11):1536–1544, 2012. DOI: 10.1002/jrs.4054.

[185] L.T. Weng, P. Bertrand, G. Lalande, D. Guay, and J.P. Dodelet. Surface characterization by time-of-flight SIMS of a catalyst for oxygen electroreduction: pyrolyzed cobalt phthalocyanine-on-carbon black. *Applied Surface Science*, 84(1):9–21, 1995. DOI: https://doi.org/10.1016/0169-4332(94)00470-6.

[186] L. Li, Q. Tang, H. Li, W. Hu, X. Yang, Z. Shuai, Y. Liu, and D. Zhu. Organic thin-film transistors of phthalocyanines. *Pure and Applied Chemistry*, 80(11):2231–2240, 2008. DOI: 10.1351/pac200880112231.

[187] J. Bartolomé, C. Monton, and I.K. Schuller. Magnetism of Metal Phthalocyanines. In *Molecular Magnets: Physics and Applications*, pages 221–245. Springer Berlin Heidelberg, J. Bartolomé et al. (editors), Berlin, Heidelberg, 2014. ISBN: 978-3-642-40609-6.

[188] W.F. Zhang, Y.L. He, M.S. Zhang, Z. Yin, and Q. Chen. Raman scattering study on anatase TiO_2 nanocrystals. *Journal of Physics D: Applied Physics*, 33:912–916, 2000. DOI: 10.1088/0022-3727/33/8/305.

[189] C.A. Melendres, A. Narayanasamy, V.A. Maroni, and R.W. Siegel. Raman spectroscopy of nanophase TiO_2. *Journal of Materials Research*, 4(5):1246–1250, 1989. DOI: 10.1557/JMR.1989.1246.

[190] V. Swamy, B.C. Muddle, and Q. Dai. Size-dependent modifications of the Raman spectrum of rutile TiO_2. *Applied Physics Letters*, 89(16), 2006. DOI: 10.1063/1.2364123.

[191] H. Chang and P.J. Huang. Thermo-Raman studies on anatase and rutile. *Journal of Raman Spectroscopy*, 29(2):97–102, 1998.

[192] H. Zangeneh, A.A.L. Zinatizadeh, M. Habibi, Akia M., and M. Hasnain Isa. Photocatalytic oxidation of organic dyes and pollutants in wastewater using different modified titanium dioxides: A comparative review. *Journal of Industrial and Engineering Chemistry*, 26:1–36, 2015. DOI: 10.1016/j.jiec.2014.10.043.

[193] S. Hernández, D. Hidalgo, A. Sacco, A. Chiodoni, A. Lamberti, V. Cauda, E. Tresso, and G. Saracco. Comparison of photocatalytic and transport properties of TiO_2 and ZnO nanostructures for solar-driven water splitting. *Physical Chemistry Chemical Physics*, 17(12):7775–7786, 2015. DOI: 10.1039/C4CP05857G.

Acknowledgements

This Ph.D. has been a rewarding experience, though not without its challenges, and I am grateful to all those who have been part of it and helped make it possible.

First and foremost, I am deeply thankful to my supervisors, Prof. Luca Tortora (Università degli Studi Roma Tre) and Prof. Patrizio Antici (INRS – Institut national de la recherche scientifique), for their important support throughout the programme, as well as for their scientific guidance during the development of this Ph.D.
My deepest thanks go to Dr. Valerio Graziani for his invaluable advice and continuous encouragement. His expertise, generosity, and dedication have played a key role in the successful completion of this work.
I would like to express my sincere gratitude to the Surface Analysis Laboratory – INFN Roma Tre group, where I carried out most of my experimental research. Finding a second family within the laboratory has been one of the most meaningful aspects of this journey. My heartfelt thanks go to Dr. Eleonora Marconi, Dr. Marco Ruggieri, Giulia Iorio, Dr. Hussam Bouaamlat, Dr. Hajar Jabkhiro, Dr. Francesca Visone, Dr. Elisabetta Colantoni, Dr. Sacha Cormenier, and all the other students and researchers who have been part of the lab over these years and contributed to making this experience truly memorable.
Special thanks go to INRS for welcoming me into its institution in Canada as part of my cotutelle program, which offered valuable opportunities to expand my scientific expertise. In particular, I am grateful to Prof. Andreas Ruediger and Balasurya Senthilmurugan for their scientific collaboration and assistance throughout my research.
I also wish to express my profound thanks to Dr. Canan Yagmur Boynukara and Dr. Elias Catrix for being indispensable friends during my time in Canada—and beyond.
I would like to thank the Spectra Lab group at the Department of Science, Università degli Studi di Roma Tre, for their helpful assistance and collaboration, as well as for providing me with the opportunity to gain hands-on experience in Raman spectroscopy.

I am especially thankful to Prof. Armida Sodo, Dr. Antonella Privitera, and Dr. Michael Di Gioacchino for their expert guidance and for always warmly welcoming me into their laboratory.
I gratefully acknowledge INFN - Sezione di Roma Tre for providing the infrastructure and institutional support necessary for this work. In particular, I would like to thank Prof. Andrea Fabbri and Prof. Paolo Branchini, as well as all the technical staff for their valuable assistance.
I also wish to acknowledge the coordinators of the Ph.D. program in Science of Matter and Nanomaterials at Università degli Studi di Roma Tre, Prof. Marco Barbieri and Prof. Fabio Bruni, for their ongoing presence and encouragement throughout my doctoral journey, both academically and personally.

To all of you reading my thesis, my heartfelt thanks.

Agnese De Carlo